



**HAL**  
open science

# Advances in quantitative micro/nanoscale thermometry using scanning thermal microscopy

Tran Phong Nguyen

► **To cite this version:**

Tran Phong Nguyen. Advances in quantitative micro/nanoscale thermometry using scanning thermal microscopy. Thermics [physics.class-ph]. Université Bourgogne Franche-Comté, 2018. English. NNT : 2018UBFCD010 . tel-02096873

**HAL Id: tel-02096873**

**<https://theses.hal.science/tel-02096873>**

Submitted on 11 Apr 2019

**HAL** is a multi-disciplinary open access archive for the deposit and dissemination of scientific research documents, whether they are published or not. The documents may come from teaching and research institutions in France or abroad, or from public or private research centers.

L'archive ouverte pluridisciplinaire **HAL**, est destinée au dépôt et à la diffusion de documents scientifiques de niveau recherche, publiés ou non, émanant des établissements d'enseignement et de recherche français ou étrangers, des laboratoires publics ou privés.

NNT : AAAAUBFCYXXX

**THESE DE DOCTORAT DE L'ETABLISSEMENT UNIVERSITE BOURGOGNE FRANCHE-COMTE**

**PREPAREE A L'INSTISTUT FEMTO-ST**

Ecole doctorale n°ED 37

Sciences Pour l'Ingénieur et Microtechniques

Doctorat de Sciences pour l'ingénieur

Par

M. Tran Phong NGUYEN

Progrès en thermométrie quantitative aux échelles micro et nanométriques par  
microscopie thermique à balayage (SThM)

Thèse présentée et soutenue à Besançon, le 18 Janvier 2018

**Composition du Jury :**

Monsieur, Tessier, Gilles  
Monsieur, Dobson, Phillip  
Madame, Trannoy, Nathalie  
Monsieur, Vairac, Pascal  
Monsieur, Thiery, Laurent  
Monsieur, Teyssieux, Damien  
Monsieur, Hay, Bruno  
Madame, Gomès, Séverine

Professeur à l'Université Paris Descartes  
Maitre de conférences à l'Université de Glasgow  
Professeur à l'Université de Reims  
Professeur à l'ENSMM  
Maitre de conférences à l'Université de Franche-Comté  
Maitre de conférences à ENSMM  
Chargé de recherche au LNE  
Chargée de recherche CNRS au CETHIL, Lyon

Rapporteur  
Rapporteur  
Président du jury  
Examineur  
Directeur  
Codirecteur  
Invité  
Invité



*ADVANCES IN QUANTITATIVE  
MICRO/NANOSCALE THERMOMETRY USING  
SCANNING THERMAL MICROSCOPY*

**Tran Phong NGUYEN**  
**SPIM**

**This dissertation is submitted for the degree of Doctor of Philosophy**  
**April 2018**





*To my family and my friends*



*You cannot travel the path until you become the path itself*

*Siddhartha GAUTAMA*



## SUMMARY / ABSTRACT

English

Thermal characterizations at nano-scale remain a challenge since the emergence of nano-structured devices. Having advantages in term of lateral resolution compared to far field techniques, the scanning thermal microscopy has become an essential tool for local materials heat transport characterization. In the frame of the European Quantiheat Project, several laboratories have worked together trying to figure out and to obtain quantitative thermal measurements covering spatial scales from the micrometre to the nanometre.

This document contains six chapters with four main parts, in which micro-wire thermocouple based SThM probes have been used to enhance our knowledge in quantitative thermometry at this scale. This kind of probe has been developed and improved for several years. We demonstrate that it is adapted for measuring temperature of active samples as well as thermal conductivity of passive samples.

Through the dissertation, the last version of the microscope (hardware, software) and probe design are presented. Attached on a quartz tuning fork, the tip-sample contact force can be quantified. Placed in a vacuum chamber, this system permits a full control of predominant parameters on the measurement such as air pressure and contact force. Thanks to samples provided by Quantiheat partners, measurements in active and passive modes have been performed to demonstrate that quantitative measurements are feasible. By changing ambient conditions from primary vacuum to ambient pressure, the tip-sample heat transfer mechanisms have been analysed in detail to reveal the preponderant role of air and solid-solid contact conductions.

## Français

Les caractérisations thermiques à l'échelle nanométrique restent un défi depuis l'émergence de dispositifs nano structurés. Ayant des avantages en termes de résolution latérale par rapport aux techniques de champ lointain, la microscopie thermique à balayage est devenue un outil essentiel pour la caractérisation locale des propriétés thermiques des matériaux. Dans le cadre du projet européen « Quantiheat », plusieurs laboratoires ont travaillé ensemble pour essayer de comprendre et d'obtenir des mesures quantitatives couvrant les échelles spatiales allant du micro au nanomètre.

Ce document contient six chapitres avec quatre parties principales, dans lesquelles des sondes SThM à thermocouples microfilaires ont été utilisées pour améliorer nos connaissances en thermométrie quantitative à cette échelle. Ce type de sonde a été développé et amélioré pendant plusieurs années. Nous démontrons qu'il est adapté pour mesurer la température d'échantillons actifs ainsi que la conductivité thermique d'échantillons passifs.

Grâce à la thèse, la dernière version du microscope (matériel, logiciel) et la conception de la sonde sont présentés. Fixé sur un diapason en quartz, la force de contact pointe-échantillon peut être quantifiée. Placé dans une chambre à vide, ce système permet un contrôle complet des paramètres prédominants sur la mesure, tels que la pression de l'air et la force de contact. Les mesures en modes actif et passif ont pu être menées grâce aux échantillons fournis par les partenaires du projet « Quantiheat » afin de démontrer que des mesures quantitatives sont envisageables. En changeant les conditions ambiantes allant du vide primaire à la pression ambiante, les mécanismes de transfert de chaleur de l'échantillon-pointe ont été analysés en détail pour mettre en évidence le rôle prépondérant de l'air et des conceptions de contact solide-solide.

## ACKNOWLEDGEMENTS

This thesis is prepared at FEMTO-ST Institut, Besançon France, far away from my home town. I have a few people to thank. Firstly, I would like to express my gratitude to my advisor Dr. Laurent THIERY, with whom I worked for more than 3 years, who had read carefully and gave good advices to correct the manuscript. I appreciate the time and the chance that he gave me as a teacher and a good friend.

I would also like to thank my co-adviser Dr. Damien TEYSSIEUX for the pleasure he brings with his sense of humour, his advice and his support.

A thank to Pr. Pascal VAIRAC as the group leader, the time he spent for the project at FEMTO-ST

Somme of the materials used in this manuscript is the fruit of collaborating work with other establishments. I would like to thank Dr. Danick Briand and Dr. Etienne Lemaire from EPFL for the clean room fabrication of active samples and Dr. Bruno Hay, Dr. Alexandre Allard for their help on the analyze works in some of our data.

A special thank goes to the European Quantiheat project for the funding of this work as well as Dr. Séverine Gomès for her great work of coordinating the project, from which many samples are used.

I would also like to thank to the jury members, Pr. Nathalie Trannoy, Pr. Gilles Tessier and Dr. Phillip Dobson for spending their precious time, having been in Besançon for my defense.

I also express my deepest thanks to colleagues and friends in FEMTO-ST:

- Mr. Emmanuel Dordor, Dr. Roland Salut, Dr. Franck Lardet for their technical supports
- Dr. Sarah Benchabane, Dr. Sébastien Eprahsie for fruitful discussions.
- Alexia, Guillaume, Anurupa, TingTing, Nicolas, Huan Lan, Etienne, Gautier, Tintu, Xavier, Séverine, Xu Xiaolong, Stéfania, Raya, Yanfeng, Masha, Laetitia, Asma, David (INSA Lyon), Fatah, Nhat Binh, chi Thuy, Lien, chi Luyen, Thao, Huy, anh Duc for the great the times that we have spent together in Besançon.

Last but not least, I express my deepest gratitude to my parents and my brother. Without them, nothing likes it is now.



# CONTENTS

<b>1 INTRODUCTION .....</b>	<b>1</b>
1.1 FAR FIELD THERMAL MICROSCOPES.....	2
1.2 NEAR FIELD LOCAL PROBE FOR THERMAL MEASUREMENTS AND THESIS ARCHITECTURE .....	5
<b>2 STHM: STATE OF ART AND A REVIEW OF FEMTO-ST SYSTEM.....</b>	<b>8</b>
2.1 SPM METHODS AND DEVELOPMENT OF STHM .....	8
2.2 DIFFERENT TYPES OF STHM.....	14
2.2.1 Resistive probes.....	14
2.2.2 Thermocouple probes .....	17
2.2.3 Other methods .....	21
2.2.4 SThM quantitative measurements.....	21
2.3 FEMTO-ST STHM BASED MICROWIRE THERMOCOUPLE.....	26
2.3.1 Thermocouple principles and temperature measurement .....	26
2.3.2 Thermal conductivity measurement using 3-omega and 2-omega method .	27
2.3.3 Microwire thermocouple fabrication .....	31
2.3.4 Quartz Tuning Fork for contact detection.....	33
2.3.5 The development of FEMTO-ST SThM system .....	34
2.4 SUMMARY .....	36
<b>3 CONTACT FORCE CONTROL USING QTF AND REALISATION OF SECOND VERSION STHM SYSTEM.....</b>	<b>37</b>
3.1 FORCE SENSING TECHNIQUE .....	37
3.1.1 Static force sensing .....	37
3.1.2 Dynamic force sensing .....	38
3.2 QTF PRINCIPLE .....	40
3.2.1 Structure.....	40
3.2.2 SPM application .....	41
3.3 QTF TIP-SAMPLE CONTACT FORCE MODEL FOR THERMOCOUPLE.....	46
3.3.1 Single prong model .....	46
3.3.2 FEM simulation and comparison of different models.....	50
3.3.3 Two masses model.....	54
3.3.4 Experimental verification .....	57

3.4 FORCE CALCULATION USING QTF AND THERMOCOUPLE PROBE .....	62
3.5 SECOND VERSION OF STHM SYSTEM.....	64
3.6 SUMMARY.....	72
<b>4 TEMPERATURE MEASUREMENT AND CALIBRATION .....</b>	<b>73</b>
4.1 INTRODUCTION .....	73
4.2 SMALL SCALE TEMPERATURE MEASUREMENT .....	74
4.2.1 <i>Temperature measurements</i> .....	74
4.2.2 <i>Thermal configuration</i> .....	75
4.3 TEMPERATURE CALIBRATION DEVICES.....	77
4.3.1 <i>First generation device RTD and OPT</i> .....	77
4.3.2 <i>Second generation device</i> .....	86
4.4 INFLUENCE OF DIFFERENT FACTORS ON TEMPERATURES MEASUREMENT .....	92
4.4.1 <i>Influence of air and contact force on temperature measurement</i> .....	92
4.4.2 <i>Statistical study on different parameters</i> .....	94
4.5 THERMAL RESOLUTION ESTIMATION .....	97
4.6 APPLICATION ON MICRO-NANO SCALE THERMAL MEASUREMENTS.....	100
4.6.1 <i>Conpart spherical particles</i> .....	100
4.7 SUMMARY.....	107
<b>5 THERMAL CONDUCTIVITY MEASUREMENTS AND CALIBRATIONS .....</b>	<b>108</b>
5.1 INTRODUCTION .....	108
5.2 PROBE SIMULATION .....	110
5.2.1 <i>Analytical model</i> .....	110
5.2.2 <i>Numerical model with coupling harmonics and a comparison with analytical models</i> .....	119
5.3 PROBE CALIBRATION USING REFERENCE MATERIALS.....	124
5.3.1 <i>Calibrating materials</i> .....	124
5.3.2 <i>Under vacuum measurements</i> .....	126
5.3.3 <i>Ambient air measurements</i> .....	131
5.4 TIP-SAMPLE HEAT TRANSFER .....	140
5.4.1 <i>Tip-sample heat transfer analyze</i> .....	140
5.4.2 <i>Influence of different factors on the measurement</i> .....	146

5.5 SUMMARY .....	153
<b>6 CONCLUSIONS AND PERSPECTIVES .....</b>	<b>154</b>
6.1 CONCLUSIONS.....	154
6.2 PERSPECTIVES .....	156
6.2.1 <i>Thermo-mechanical measurements</i> .....	156
6.2.2 <i>Square wave frequency synthesis technique for thermal penetration measurement</i> .....	158
6.2.3 <i>Towards quantitative temperature measurements by a correction of thermal resistance</i> .....	159
6.2.4 <i>New probe generation based on optical fibre</i> .....	161
<b>7 REFERENCES .....</b>	<b>162</b>
<b>8 APPENDICES .....</b>	<b>174</b>
<b>APPENDIX 1 THERMOCOUPLE PRINCIPLES.....</b>	<b>175</b>
<b>APPENDIX 2 FABRICATION OF CALIBRATION DEVICES .....</b>	<b>179</b>
<b>APPENDIX 3 FISHER'S TEST .....</b>	<b>181</b>
<b>APPENDIX 4 UNCERTAINTY PROPAGATION .....</b>	<b>183</b>
<b>APPENDIX 5 COUPLING MODEL AND PYTHON SIMULATION CODE .....</b>	<b>185</b>

## LIST OF TABLES

Table 2-1: Time constant and cut-off frequency of micro-wire probes .....	25
Table 2-2: Conversion coefficients of thermocouple type S [81] .....	27
Table 3-1: Coefficient of conversion frequency shift to probe-sample stiffness values calculated by 3 models.....	57
Table 3-2: QTF frequency shift for “1-5 N/m” and “20-80 N/m” cantilever and the calculated stiffness.....	59
Table 3-3: QTF frequency shifts with different combinations.....	61
Table 3-4: The system equivalent stiffness and the thermocouple stiffness deduced from by 3 different experiments (with 1-5 N/m, 20-80 N/m cantilever and Silicon substrate) .....	62
Table 4-1: Characteristics of the calibration chips.....	79
Table 4-2: Characteristics of the second generation calibration chips.....	87
Table 4-3: The ratio $\tau$ values measured by localized RTD and optical techniques for different device designs .....	92
Table 4-4: Temperature measured by a 1.3 $\mu$ m probe at device different powers.....	93
Table 4-5: ANOVA table for the DOE for the temperature.....	95
Table 5-1: Physical parameters of Platinum and Platinum-10% Rhodium wire .....	114
Table 5-2: Cut-off frequency of thermocouples .....	117
Table 5-3: The uncertainty estimation of different parameters.....	119
Table 5-4: Thermo-physical parameters of reference materials (provided by LNE) ....	125
Table 5-5: Statistical results of the linear regression ( $V/\Delta V$ and $1/\lambda$ ).....	127
Table 5-6: Boundary condition of thermal constriction.....	128
Table 5-7: The fitting results and their statistical analysis.....	135
Table 5-8: The parameters of the equation 5-34 and 5-36 .....	136
Table 5-9: Thermal conductance components extracted from the measurements of PMMA and Si doped n++ .....	145
Table 5-10: ANOVA table for $\Delta T/T$ for the DOE applied to S-TH-Cal3 .....	147
Table 5-11: Equivalent conductivity calculated for every step.....	149
Table 5-12: Apparent resolution at different frequency .....	152
Table 8-1: Absolute Seebeck coefficient of materials at 0°C.....	175

Table 8-2: Characteristics of different types thermocouple..... 178  
Table 8-3: Analysis of variance..... 182

## LIST OF FIGURES

Figure 2-1: STM schematic and principle of tunnel junction .....	9
Figure 2-2: Working principle of AFM .....	10
Figure 2-3: AFM tips example .....	10
Figure 2-4: AFM approach curve .....	11
Figure 2-5: Schematic of FM-AFM (frequency modulation AFM).....	12
Figure 2-6: STM profiler [34] .....	13
Figure 2-7: SThM general schematic.....	14
Figure 2-8: Wollaston probe image [35] .....	15
Figure 2-9: Thermal resistive probe fabricated by Rangelow et al [37] .....	16
Figure 2-10: Resistive probe developed by Mills [38] and KNT SThM probe [40] .....	16
Figure 2-11: Thermo-resistive probe made by Wielgoszewski et al[41] .....	17
Figure 2-12: Thermo-resistive Silicon doped probe IBM[46].....	17
Figure 2-13: Thermocouple type K probe by Majumdar et al[32] .....	18
Figure 2-14: Thermocouple type S probe by Thiery[47],[48] .....	18
Figure 2-15: Thermocouple probe developed by Zhang [50] .....	19
Figure 2-16: Thermocouple probe developed by Mills[51] .....	19
Figure 2-17: Thermocouple probe developed by Kim group [54] .....	20
Figure 2-18: Thermocouple probe deposited on an optical fibre tip .....	20
Figure 2-19: Fluorescence particle attached on Tungsten tip [61] .....	21
Figure 2-20: Heat transfer mechanism of a SThM probe to surface[62] .....	22
Figure 2-21: Tip-sample heat transfer .....	23
Figure 2-22: Probe calibration principle using contact method .....	24
Figure 2-23: Cut-off frequency of thermocouple probes and Wollaston probes [81] ...	25
Figure 2-24: Measurement schematic of microwire thermocouple [81] .....	27
Figure 2-25: Three omega method .....	28
Figure 2-26: Thermal model of Wollaston probe [84] .....	29
Figure 2-27: Thermal model of microwire thermocouple [81].....	31
Figure 2-28: Thermocouple welding principle [81].....	32
Figure 2-29: Optical image of thermocouple probe .....	32

Figure 2-30: Quartz resonator (QTF) with its thermocouple probe and electrical connection principle. ....	33
Figure 2-31: Thermocouple junctions: a) 1.3 $\mu\text{m}$ probe and b) 5 $\mu\text{m}$ probe.....	34
Figure 2-32: The SThM system v1 [81].....	35
Figure 3-1: Tuning fork (left) and a tuning fork with thermocouple tip (right) .....	39
Figure 3-2: Quartz tuning fork with a capsule cover .....	39
Figure 3-3: 32.768 kHz QTF configuration [49] .....	40
Figure 3-4: QTF in AM mode .....	41
Figure 3-5: QTF in FM mode using a PLL.....	41
Figure 3-6: QTF response under electrical excitation [101] .....	42
Figure 3-7: Mechanical excitation technique[105] .....	43
Figure 3-8: Experimental setup and probe positioning [49].....	44
Figure 3-9: Amplitude and phase response of QTF with photo-thermal excitation.....	44
Figure 3-10: Connection configuration of thermocouple probe attached on the QTF ..	45
Figure 3-11: Frequency response of QTF with TC probe attached ( $f_0 = 32232$ Hz; $Q = 8000$ ) and QTF without TC probe ( $f_0 = 32756$ Hz; $Q = 16000$ ) .....	46
Figure 3-12: Beam presentative mechanical model when TC probe in contact.....	47
Figure 3-13: Effective mass-spring model of tuning fork in contact and out of contact with the sample .....	48
Figure 3-14: Comparison between a single beam mechanical model and an effective mass model .....	49
Figure 3-15: Static mode FEM simulation of QTF .....	51
Figure 3-16: Resonance modes of QTF .....	52
Figure 3-17: QTF vibration amplitude as function of its generating current[81] .....	53
Figure 3-18: QTF FEM model, stress and displacement results in frequency domain ...	53
Figure 3-19: Comparison between FEM model and effective mass-spring model.....	54
Figure 3-20: Two effective masses model [117] .....	55
Figure 3-21: Comparison of 3 different mechanical models for QTF .....	56
Figure 3-22: Cantilever stiffness measurement setup using a QTF .....	58
Figure 3-23: Frequency shift of QTF when AFM cantilever put in contact with a prong a) 1-5 N/m cantilever and b) 20-80 N/m cantilever .....	59

Figure 3-24: AFM cantilever in near contact with thermocouple probe.....	60
Figure 3-25: 1-5 N/m AFM cantilever approaching curve on QTF prong, 5 $\mu$ m thermocouple and 1 $\mu$ m thermocouple .....	61
Figure 3-26: Working scheme of dynamic AFM using QTF .....	63
Figure 3-27: Approach and retraction curve of a 1.3 $\mu$ m thermocouple on a Silicon substrate .....	64
Figure 3-28: 3D view of the second generation FEMTO-ST SThM system .....	64
Figure 3-29: FEMTO-ST SThM system in its vacuum chamber. Close view of the probe holder and samples.....	65
Figure 3-30: Passive mode configuration.....	66
Figure 3-31: Active mode configuration .....	67
Figure 3-32: SThM Application Interface .....	67
Figure 3-33: Noise measurements of thermocouple at low frequency.....	68
Figure 3-34: Quartz resonator (QTF) with its thermocouple probe new design .....	69
Figure 3-35: Static stability probe testing .....	69
Figure 3-36: Contact detection principle .....	70
Figure 3-37: Device structure and scanning thermocouple tip .....	71
Figure 3-38: Dynamic AFM measurements using QTF and thermocouple tip.....	71
Figure 4-1: Side-view (a) and top-view (b) of the micro-hotplate .....	74
Figure 4-2: Topography (a) and surface temperature map (b) of active micro-hotplate supplied with a DC current of 17mA (47mW).....	75
Figure 4-3: Tip-sample thermal configuration .....	75
Figure 4-4: (a) Schematic cross-section of the RTD device; (b) RTD design variations; (c) Schematic cross-section of the OPT device; (d) Cross-section of the standalone platinum membrane and its top view for the OPT device.....	78
Figure 4-5: (a) RTD device with heating area and two RTDs (b) RTD patterned using e-beam lithography; (c) (d) OPT device with standalone Pt membranes.....	79
Figure 4-6: RTD values measured as a function of temperature up to 400°C.....	80
Figure 4-7: Experimental results 5 $\mu$ m probe results and 1.3 $\mu$ m results .....	81
Figure 4-8: Extracted values of $\tau$ and $\phi$ for both probes .....	81
Figure 4-9: Experimental set-up of the SThM-NIR coupling measurement .....	82

Figure 4-10: Schematic of the SThM-NIR coupling measurement .....	82
Figure 4-11: a) NIR thermograph of OPT device (1 mm <sup>2</sup> membrane with heater area of 440×440 μm <sup>2</sup> ) without SThM probe contact. b) NIR thermograph of the same device when a 1.3μm diameter thermocouple probe put in contact c) subtraction image of NIR thermograph after contact and before contact, d) cross section of NIR thermographs and comparison with SThM measurement.....	83
Figure 4-12: Temperature measured at the centre of RTD and OPT devices using SThM probe (thin wires thermocouple with a diameter of 1.3 μm) for the two heaters areas (220x220μm <sup>2</sup> : 220 and 440x440μm <sup>2</sup> :440 in the legend).....	85
Figure 4-13: Thermograph (left), topography (middle) and RTD response RTD (right) while the probe is scanning on the surface of a RTD device .....	85
Figure 4-14: Schematic cross-section of the v2RTD device (left); Schematic cross-section of the v2OPT device (right).....	86
Figure 4-15: Calibration chips with heating area of 50x50 μm <sup>2</sup> and contact area of 10 x 10 μm <sup>2</sup> . From left to right: v2RTD design with Pt RTD; v2OPT design with the suspended platinum membrane; the full chip image of v2RTD device.....	87
Figure 4-16: Measurement points and slope extraction of electrical resistances versus temperature of 2 devices v2RTD .....	88
Figure 4-17: SThM thermograph (a), topography (b) and RTD temperature (c) while the probe is scanned on the device surface of heated with 1.61mW supplied power	88
Figure 4-18: Optical micrograph of an v2RTD large heater; v2RTD small heater.....	89
Figure 4-19: v2RTD large design: top left) SThM TC topography, top right) SThM TC temperature at 1.8 mW, bottom) Comparison between TC SThM probe on Vlarge and Vsmall respectively. ....	89
Figure 4-20: v2RTD device: RTD temperature as evolution of air pressure (left) and experimental results with a 1.3μm thermocouple under vacuum (2Pa) .....	90
Figure 4-21: a) NIR thermograph of v2OPT device (1 mm <sup>2</sup> membrane with heater area of 50×50 μm <sup>2</sup> ) without SThM probe contact. b) NIR thermograph of the same device when a 1.3μm diameter thermocouple probe put in contact c) subtraction image of NIR thermograph after contact and before contact, d) cross section of NIR thermographs and comparison with SThM measurement.....	91

Figure 4-22: RTD and tip probe temperature evolution when the probe approaches the surface.....	93
Figure 4-23: Comparison of 1.3 $\mu\text{m}$ and 5 $\mu\text{m}$ thermocouple probe approach curve on the .....	94
Figure 4-24: Visualization of the interaction effect between the probe size and the pressure, for the 3 values of contact force, for the temperature .....	96
Figure 4-25: Optical micrographs of a C4 device with a 600nm wide stripe .....	97
Figure 4-26: Topography and temperature distribution measured with a 1.3 $\mu\text{m}$ probe when a 6mA electrical current is injected in the device.....	97
Figure 4-27: Transverse scan on the centre of the device supplied with 6mA using a 1.3 $\mu\text{m}$ thermocouple SThM probe .....	98
Figure 4-28: Topography and temperature distribution measured with a 5 $\mu\text{m}$ probe when a 6mA electrical current is injected in the device.....	99
Figure 4-29: Transverse scan on the centre of the device supplied with 6mA using a 5 $\mu\text{m}$ thermocouple SThM probe .....	99
Figure 4-30: Conpart spherical particle coated with a thin film silver.....	100
Figure 4-31: v2RTD device and Conpart particle on top of the localized RTD.....	101
Figure 4-32: Tip-particle in contact image .....	101
Figure 4-33: Thermal configuration of coupling system v2RTD device, particle, thermocouple probe before contact (left) and in contact (right) .....	102
Figure 4-34: The approach curve on the v2RTD device surface without particle, with particle with and without coating.....	104
Figure 4-35: Conductance values and heat flux calculated from temperatures and device power .....	105
Figure 4-36: Conductance values and heat flux calculated from temperatures and device power at different device power.....	106
Figure 5-1: Side-view (a) and top-view (b) of the micro-hotplate .....	109
Figure 5-2: Topography and thermal maps in active mode of a portion of platinum heater on silicon nitride membrane with a 5 $\mu\text{m}$ thermocouple probe. The sample is passive .....	109
Figure 5-3: Thermocouple probe theoretical model .....	111

Figure 5-4: $2\omega$ temperature profile of the 1.3 $\mu\text{m}$ thermocouple probe under air and vacuum conditions .....	113
Figure 5-5: Comparison of theory and measurement of $2\omega$ and $3\omega$ response for 1.3 $\mu\text{m}$ thermocouple.....	115
Figure 5-6: SEM images of a 1.3 $\mu\text{m}$ thermocouple .....	116
Figure 5-7: Comparison of theory and measurement of $2\omega$ and $3\omega$ response for 5 $\mu\text{m}$ thermocouple.....	116
Figure 5-8: 1D finite volume model for a thermocouple probe .....	120
Figure 5-9: Mesh elements .....	120
Figure 5-10: Simulated temporal junction temperature of 1.3 $\mu\text{m}$ thermocouple and its FFT spectrum (non-contact and in-contact) .....	121
Figure 5-11: Simulated voltage response of 1.3 thermocouple .....	122
Figure 5-12: $2\omega$ temperature profile of the 1.3 $\mu\text{m}$ thermocouple under air and vacuum .....	122
Figure 5-13: Relative error between coupling model and identical wire analytical model for 1.3 $\mu\text{m}$ and 5 $\mu\text{m}$ thermocouple .....	123
Figure 5-14: $\Delta\theta/\theta$ ratio as function of probe length .....	124
Figure 5-15: $\Delta V/V$ and $V/\Delta V$ as function of thermal conductivity .....	126
Figure 5-16: Tip-sample heat transfer mechanism.....	127
Figure 5-17: Evolution of equivalent thermal conductance and resistance as function of sample conductivity .....	129
Figure 5-18: Index-A and B distribution calculated by Monte Carlo method.....	130
Figure 5-19: An example of the error estimation ( $V=150\mu\text{V}$ ; $\lambda=2.25\text{ W/mK}$ ) and relative error under vacuum calculated at different thermal conductivity.....	131
Figure 5-20: Radius contact schematic on different conductivity samples.....	132
Figure 5-21: COMSOL model of tip-sample heat transfer under air.....	133
Figure 5-22: System temperature simulations for low conductivity and high conductivity material .....	133
Figure 5-23: Normalised temperature on the sample surface (a) and thermal radius (b) at different thermal conductivity.....	134

Figure 5-24: $\Delta V/V$ and $V/\Delta V$ as function of thermal conductivity under air measurements and the fit curve.....	135
Figure 5-25: Evolution of equivalent thermal conductance and resistance under air as function of sample conductivity and its inversion respectively .....	135
Figure 5-26: The calculated conductance components (a) and evolution of thermal diameter as function of the inversion of sample conductivity .....	136
Figure 5-27: Index-A and B distribution calculated by Monte Carlo method.....	138
Figure 5-28: Index-A and C distribution calculated by Monte Carlo method.....	138
Figure 5-29: An example of the error estimation ( $V=111\mu V$ ; $\lambda=1.26 W/mK$ ) and relative error under vacuum calculated at different thermal conductivity.....	139
Figure 5-30: Global and local tip-sample heat transfer .....	140
Figure 5-31: Approach and retraction curves of the $1.3\mu m$ thermocouple tip on the sample. a) tip-sample equivalent stiffness and b) tip-sample equivalent conductance.....	141
Figure 5-32: Approach curve $100\mu m$ above the sample a) $2\omega$ temperature b) tip-sample thermal resistance and its zoom on the close contact zone c) and d).....	142
Figure 5-33: Comparison of conductance approach curve under air and vacuum measured by $1.3\mu m$ thermocouple probe on a Silicon substrate .....	144
Figure 5-34: The contact conductance components (air, solid-solid) and the thermal radius produced by air and solid-solid contact.....	144
Figure 5-35: Visualization of the interaction effect between the probe size and the pressure.....	146
Figure 5-36: Topography and $2\omega$ thermography .....	147
Figure 5-37: The thermal ratio and equivalent conductance on every layer step .....	148
Figure 5-38: Equivalent conductivity for every layer step .....	149
Figure 5-39: Optical image of the sample.....	150
Figure 5-40: Probe scanning schematic .....	150
Figure 5-41: Topography, amplitude and phase of $2\omega$ and $3\omega$ harmonics at $57Hz$ .....	151
Figure 5-42: amplitude and phase of $2\omega$ and $3\omega$ harmonics at $1237Hz$ .....	151
Figure 5-43: Normalized amplitude and phase at different frequencies .....	152
Figure 6-1: Thermo-mechanical coupling effect.....	157

Figure 6-2: Thermocouple voltage spectrum (in red) and QTF frequency shift spectrum in blue at different excitation current 0.5 – 15mA (upper plot) and 0mA (lower plot)..... 157

Figure 6-3: The correlation between QTF  $2\omega$  component frequency shift and  $2\omega$  voltage of thermocouple in contact with a silicon substrate ..... 158

Figure 6-4: Square wave signal and its frequency component..... 159

Figure 6-5: Different measuring schematics, from the left to the right: active sample measured by passive probe, passive sample measured by active probe and active sample measured by active probe in the future ..... 159

Figure 8-1: Seebeck effect..... 175

Figure 8-2: Peltier effect ..... 176

Figure 8-3: Thomson effect..... 176

Figure 8-4: Seebeck voltage of different type thermocouple in function of temperature (source: NIST) ..... 177

Figure 8-5: Temperature calibration with 0°C ..... 178

Figure 8-6: Illustration of the fabrication process detailing the two variations of designs: RTD and OPT device ..... 179

## LIST OF ABBREVIATIONS AND ACRONYMS

AFM	Atomic force microscope
AM-AFM	Amplitude modulation AFM
ANOVA	Analysis of variance
CCD	Charge coupled device
CR-AFM	Contact resonance AFM
DOE	Design of experiment
FEM	Finite element method
FM-AFM	Frequency modulation AFM
LPCVD	Low pressure chemical vapor deposition
MFM	Magnetic force microscope
NIR	Near infrared
PECVD	Plasma enhanced chemical vapor deposition
QTF	Quartz tuning fork
RTD	Resistance Temperature Detector
SEM	Scanning electron microscope
SMM	Scanning microdeformation microscope
SNOM	Near-field scanning optical microscope
SPM	Scanning probe microscopy
SThM	Scanning thermal microscope
STM	Scanning tunneling microscope
TC	Thermocouple
TCR	Temperature coefficient of resistance







# 1 INTRODUCTION

Thermal characterizing tools are always indispensable and gradually improved with the development of science and technology. One of the first temperature measurements was performed by Galilee in 1593. Temperature measurement is always indirect, in other words the temperature needs always to be measured through a multi-physics phenomenon (thermo-mechanic, thermo-electric, thermo-photonics...). The very first measurements were based on the thermal expansion of materials or thermal fusions are still widely used nowadays. The temperature scale systems developed by Celcius and Fahrenheit have created a base for an international “agreement” on temperature measurements. The precision of temperature measurements was improved by the inventions of electrical (resistance conversion, thermal electricity conversion or Johnson noise...) and optical methods. Thermal characterizations present in many fields, electronics, mechanics, chemistry, biology and every structure from the smallest to the biggest (eg. Biocell or nuclear plant). The emergence of nano technology and the progress of science in many fields have set new challenges for thermal characterization techniques.

Over the last decades, with the developing of micro/nano technology, the size of structures are getting smaller and smaller, to economize material, energy or to exploit the properties that can only appear at these scales (quantum dot, quantum well). According to Moore law[1], the density of transistor double every two years, which means that size of electronic details (transistor) should reduce to few nanometres. New thermal management materials also achieved great advances (eg. the composite

of graphene or carbon nanotube with high thermal conductivity)[2][3][4]. The thermal investigations at the micro or nano scale are therefore pushed to their limits by the demands of high precision , high stability, and high resolution (thermal, lateral) measurements[5][6].

## 1.1 Far field thermal microscopes

As other conventional microscopes, thermography methods can also be divided in two groups: far-field and near-field thermography. In far-field microscope, beams (light beam, electron beam...) are focused on the object and the detection is performed from distance. Many far-field methods were developed for small scale thermal characterization thermometry. Each of them has their own advantages or limits. Depending on the needs of sample investigations, the suitable technique is chosen or even a combination of different techniques can be considered.

- *Infrared or near infrared thermography*

This method allows us to measure the temperature of objects thanks to Plank's law of emission:

$$\frac{dE(\lambda,T)}{d\lambda} = \frac{8\pi hc\lambda^{-5}}{\exp\left(\frac{hc}{k_B T\lambda}\right)-1} \quad (1-1)$$

Every object with a temperature above 0K emits radiation at specific wavelength which can be detected by infrared detectors. Many works have focused on the conversion from infrared emission to temperature map for which the main uncertainty source is due to the emissivity. Besides, the lateral resolution of such a far field technique remains limited around 1.5 $\mu$ m due to the spectral length of the detected radiations. Several researches have shown that the use of CCD camera working on visible zone (0.4 – 1 $\mu$ m) can improve the spatial resolution down to 500nm with a high temperature sensitivity near 0.1K. The works of Damien Teyssieux and colleagues [7][8] investigated on this wavelength band, showing that the temperature is less dependent on uncertainty of emissivity. However, measurements must be performed at more than 300°C typically.

- *Thermoreflectance* [9]

The reflectivity of materials depends also on temperature via its reflection coefficient as described in the equation:

$$\frac{\Delta R}{R} = \left( \frac{1}{R} \frac{\delta R}{\delta T} \right) \Delta T = \kappa \Delta T \quad (1-2)$$

Here  $\kappa$  is the coefficient of thermo-reflectivity of the sample. In this method, a low power laser beam is sent to a heated sample (by Joule effect or laser heating), the reflected part being measured by a photodetector or a CCD camera[10][11]. The working wavelength of this technique is much shorter compared to infrared or near infrared range, which allows to improve the thermal resolution to 250nm with a sensitivity of 10mK [12].

- *Raman spectroscopy*

Raman scattering is an inelastic scattering of photons from materials excited by an incident light. There is an exchange in energy between material and photon so that two components are emitted: Stokes with the frequency of  $(\omega_j + \Delta\omega_s)$  and anti-Stokes with the frequency of  $(\omega_j - \Delta\omega_{as})$  compared to incident light  $(\omega_j)$ . The shift of light frequency depends on the materials but not on the excitation light which gives a possibility to analyse material compositions. The temperature measurements can be performed by calculating the ratio between the intensity of Stokes and anti-Stokes components[13].

$$\frac{I_s}{I_{as}} = C \exp\left(\frac{h\omega_j}{kT}\right) \quad (1-3)$$

Authors have announced a thermal resolution of 10K and a spatial resolution of 1 $\mu$ m[14][15]. Although the thermal resolution and spatial resolution are low, the large temperature range, from 300K to 700K still presents some advantages.

- *Photoluminescence*

This technique was developed by Kolodner and his colleagues[16][17]. The EuTTA (europium theonyltrifluoroacetate) is dissolved in a solution of a polymer such as PMMA and then deposited on the investigated sample. The sample with fluorescence

deposit layer is exposed to ultraviolet. The fluorescence response is then measured by an optical system with a CCD camera. A thermal resolution of 0.08K and spatial resolution of 700nm is announced.

## 1.2 Near field local probe for thermal measurements and thesis architecture

- *Limits of far field thermal measurements and SThM advantages*

As describe from the last part, several standard far-field microscope techniques were listed. The resolution of these thermal microscopes is always restrained by physical limit known as diffraction limit. The Rayleigh criterion affirms the impossibility of obtaining a spot with dimension smaller than the half wavelength on the focal length of lens[18].

$$\Delta x_{min} = \frac{\lambda_{min}}{2} \quad (1-4)$$

Moreover, the thermal optical phenomena such as the emittance or the reflectance are sometimes also very sensible to other parameters (nature of materials, temperature itself). The measurements remain complicated when the influence of these parameters rests undetermined.

Another form of high-resolution microscopy is known as near-field techniques. These techniques investigate the short-range interaction between a miniature tip and the sample. In particular, the scanning thermal microscope (SThM) developed over the last 20-30 years is becoming popular and promising for nanoscale thermography. Based on SPM techniques, SThM helps to improve the lateral resolution by overcoming the diffraction limit.

The general idea is based on classical contact “touch to sense” method. The thermometer tip size is reduced as much as possible to have the same size or smaller to the measured micro nano-object which also helps to minimize measurement disturbances. At these small scales, some physical laws need to be modified (eg. classical Fourier’s law, Hertz elastic contact theory...), surface forces such as frictions, capillary force or electrostatic force becoming dominant over the solid-solid body contact force or gravitational force. The simple approximation of thermal phenomenon is not valid anymore and still need to be studied.

This is the main objective of the QUANTIHEAT project which includes many laboratories in Europe. These laboratories together are trying to develop several protocols for SThM from calibration methods (active, passive samples) to theory

problems in order to perform reliable quantitative measurements, and possible applications on industrial samples or devices.

SThM measurements can be divided in two groups. The first concerns the measurement of the temperature fields of a surface using a miniature thermometer tip and the second corresponds to the characterization of the thermal properties of solid materials. The latter requires an active thermal probe, from which the heat dissipation to the sample provides relevant data, to deduce some local thermophysical quantities [18], [19].

In FEMTO-ST, a temperature probe based on microwire thermocouple was developed more than 20 years ago. More recently, we have shown that a 2-wire micro-thermocouple can operate in these two modes of measurement [20], [21]. In the most common available systems, a thermometer is integrated on a micro-fabricated cantilever whose deflection is optically detected to derive the contact force between the probe tip and the surface. Here, an attachment of a thermocouple probe on a quartz tuning fork (QTF) force sensor allows the control of tip-sample contact force.

- *Thesis structure:*

This thesis financed by the Quantiheat project, reports a study of many parameters such as contact force, probe size, pressure using the consortium's protocol and samples. Through a dedicated calibration procedure, the objective is to study and to understand the heat transfer mechanisms between thermocouple probe and a sample under a specified condition to finally perform quantitative thermal measurements.

The thesis is divided in four main parts, the first part reviews the development of SThM microscopes. Different type of SThM probe and their characteristics will be presented, followed by a review of our microwire thermocouple probe, previously designed for the microscope system.

The second part focuses on force control system using QTF in dynamic frequency modulation mode as force detection. A theoretical model is compared to a numerical Comsol simulation. The force estimation and a comparison with a first AFM experiment results is presented through samples topography images. First noise and stability tests in laboratory environment and details on the new FEMTO-ST microscope setup are given.

The third part is dedicated to temperature measurement in passive mode for which series of active devices have been manufactured in EPFL. Thermocouple probes have been used to test and develop such temperature calibration tools. SThM temperature measurements are compared with different methods of local thermoresistor or near infrared thermography. Using these devices, a full study of the influence of different parameters on temperature measurements is also presented. A specific application using one of these devices under vacuum environment is performed to study heat transfer through metalized polymer microparticle. Moreover, a measurement on a thin submicron hot string was performed to study the probe spatial resolution.

In part four, we describe AC active mode to measure the thermal conductivity. A comparison of different thermal models of TC probe in 2-omega mode (simple analytical model, 2 wires analytical model and a numerical finite volume model) is proposed. Influence of different parameters (force, pressure, probe sizes) on the measurement is presented giving complement information for heat transfer mechanism study. A calibration process using bulk materials is performed under ambient air and vacuum conditions based on simple models: three fitting constants in air and two fitting constants under vacuum.

## 2 SThM: STATE OF ART AND A REVIEW OF FEMTO-ST SYSTEM

The early first modern optical microscope was believed to be developed by Hans Lippershey in 1590. This led to many breakthroughs by the possibility to image many small objects in particular biotechnology. As briefly described in the introduction, the resolution of optical microscopes is limited by about a half of wavelength[18]. Despite the contribution of the optical techniques, the development of science always boosts to new microscopy technique with higher resolution. This is why a first scanning electron microscope (SEM) was invented in 1931 by Davisson and Calbick. In 1980s, a new concept of microscopy was presented by which diffraction limit was overcome. This is scanning probe microscopy (SPM) where the resolution is directly related to the probe size.

This chapter is a review of SThM as a part of scanning probe technique. A history of SThM (from the development of scanning probe microscopy to the emergence of many SThM tip probes) is presented. The quantifying of SThM measurements and the of tip-sample heat transfer models from literature are presented. The last part of the chapter will be dedicated to FEMTO-ST SThM system from the development history to the last version.

### 2.1 SPM methods and development of SThM

- *History of SPM methods*

As a revolution of microscopy technique, the inventors of scanning tunnel microscope[22][23], Binnig and Rohrer from IBM-Zurich won the Nobel Prize in physics in 1982. The STM exploits the tunnel current between a very fine metallic tip and a conductive sample. The resolution of STM can reach atomic scale (0.2 nm) allowing distinction of atoms on the images. The tunnel effect can be illustrated by using a simple model of tunnel junction (Figure 2-1). A voltage is applied across two electrodes. When one electrode is brought close to the other, a tunnel current can be detected if the distance of two electrodes is small enough. The tunnel current is given by

$$I \propto \exp\left(-\frac{2}{h}\sqrt{2m\phi}d\right) \quad (2-1)$$

where  $m$  is the electron mass,  $\phi$  is the difference between the kinetic energy and the height of potential barrier, and  $d$  is the distance between the tip and the sample.

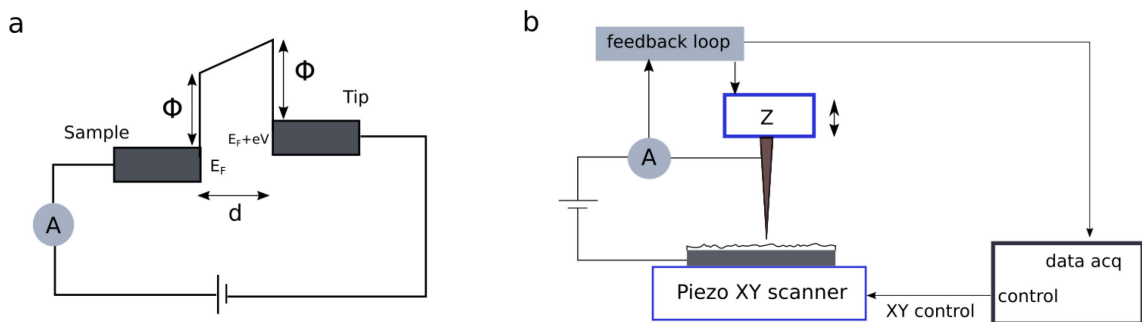


**Figure 2-1: STM schematic and principle of tunnel junction**

This is the first microscope based on near field technique. It has inspired many other types of microscope with different applications. Later, in 1986 the invention of atomic force microscope (AFM) overcomes the drawback of conductive sample restriction[24]. The principle used is the short-range interaction force between tip and surface such as the Van der Waals force.

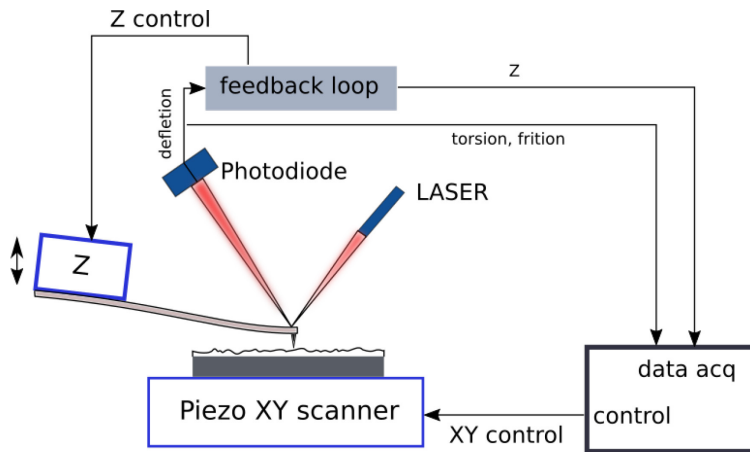


**Figure 2-2: Working principle of AFM**

The AFM uses a flexible cantilever with a stiffness varying from 0.01 N/m to several tens N/m which limits the damage of tip or sample. Depending on the investigated sample and the scanning mode, the tip type is chosen. The cantilever deflection is generally detected by an optical system made of a laser and photodiode quadruple as described in the Figure 2-2. The laser beam is reflected from cantilever onto the photodetector. The tip deflection can be therefore precisely measured and the tip-surface distance or force can be controlled. Figure 2-3 shows the SEM images of two representative AFM probes. The first (left image) [25] is a very stiff cantilever ( $k=20\text{-}80\text{N/m}$ ) with a very fine tip allowing to increase the force sensitivity. The second (right image) is a more flexible cantilever, provided from Veeco that minimizes the contact force and avoids tip damage.

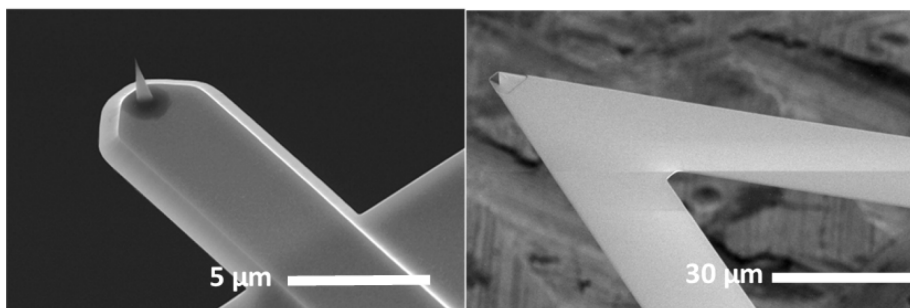


**Figure 2-3: AFM tips example**

The AFM approach curve (Figure 2-4) illustrates different force levels when the tip approaching a surface. Based on this curve, many AFM scanning modes were developed.

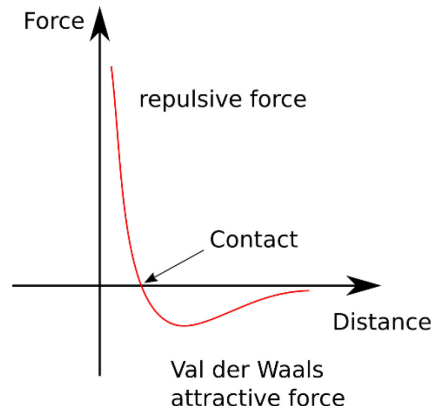


**Figure 2-4: AFM approach curve**

The AFM resolution does not only depend on tip radius but also on the scanning mode. There are three main operating modes of AFM microscope: contact mode, tapping mode (amplitude modulation) and non-contact mode (usually dynamic force AFM with frequency modulation). In contact mode, the AFM detects the repulsive force of tip and sample. The contact of tip and sample is guaranteed, the force is controlled constant by a feedback loop on Z axis throughout the scan. In tapping mode, the cantilever is excited at its resonance frequency[26],[27]. The amplitude of this oscillation is recorded by the photodiode. When the tip approaches and interacts with the surface, its amplitude decreases. The set point on oscillation amplitude allows the tip-surface distance control. The contact to the surface is minimized to avoid tip damage and increase the resolution. In noncontact mode, the Van der Waals attractive force is detected when the tip is close to the sample (2nm)[28].

The Van der Waal force is a very weak interaction force and very hard to measure in static mode. Dynamic mode sensing method was developed taking advantages of lock-in amplifier to increase the signal-to-noise ratio. An excitation is sent to the cantilever to make it vibrate near its resonance frequency. The detection principles can be AM/PM (amplitude/phase modulation which is similar to tapping mode) or FM (frequency modulation). As resonance frequency of a cantilever is modified due to the

interaction force of tip and sample, Albrecht and colleagues developed a method called frequency modulation exploiting the advantages in frequency domain (high signal/noise ratio and high stability)[29],[30]. An automatic gain control (AGC) is integrated to stabilize the oscillation amplitude and the interaction force.

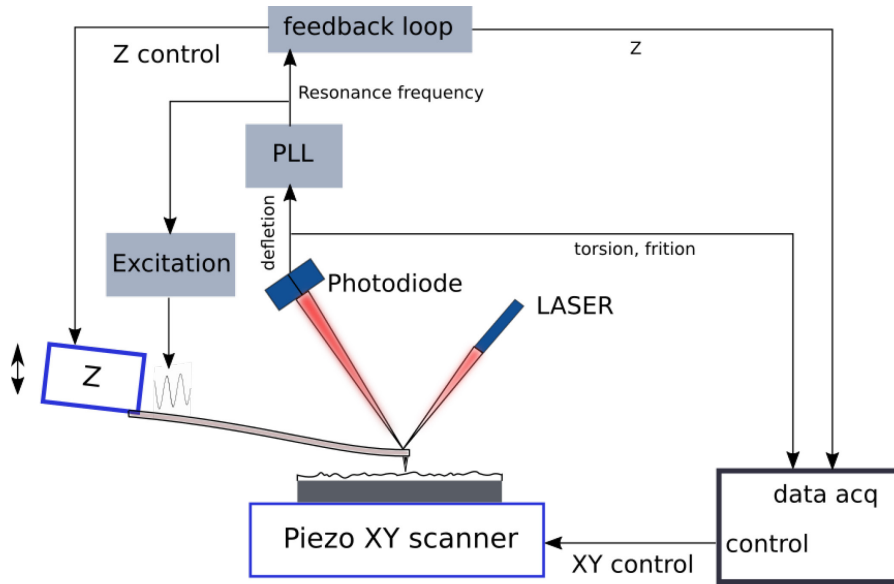


**Figure 2-5: Schematic of FM-AFM (frequency modulation AFM)**

Because of thermal noise, a minimum force gradient can be detected as described in the equation below:

$$\frac{\partial F}{\partial z_{min}} = \sqrt{\frac{4k.k_B T.B}{\omega_0 Q \langle z_{osc}^2 \rangle}} \quad (2-2)$$

where B is the bandwidth of measurement, T is the temperature, k is cantilever stiffness,  $k_B$  is Boltzmann constant,  $\langle z_{osc}^2 \rangle$  is mean-square of oscillation and Q is quality factor of the cantilever. The resolution is largely improved using this frequency modulation mode for AFM. A very high resolution scan under ultrahigh vacuum was performed firstly by Giessibl [31] on a Si(111)-(7x7) surface.

Based on the AFM principle, other scanning probe technologies were developed using many different tip-surface interaction physics such as magnetic (MFM)[32], mechanical (SMM, CR-AFM)[33], local electrical properties (Kevin Probe)[34], and especially thermal[35] which is the main discussion subject of this work.

- *Development of SThM*

The first near field local thermography technique was developed in 1986 by Williams and Wickramasinghe[36], they called it “scanning thermal profiler”. Based on STM ideas, this microscope controls a constant heat flux (instead of tunnel current) to maintain a specific distance between tip and sample. The sample topography can be therefore reconstructed. In 1992, Another thermal based on AFM technique was attributed by Nonnenmacher and Wickramasinghe.[37]

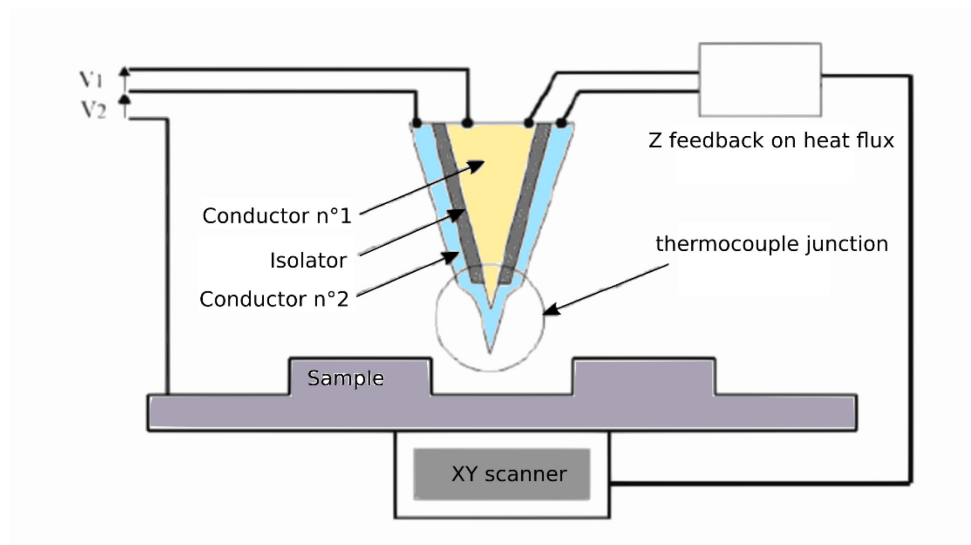


**Figure 2-6: STM profiler [37]**

Majumdar and al [35] developed a thermal imaging technique based on AFM technology which can obtain a topography and thermography image simultaneously. They called the technique Scanning Thermal Microscopy (SThM). The SThM principle is described in Figure 2-7. When the thermal tip scans over the sample, the Z axes piezo-actuator and the cantilever deflection control system takes the responsibility of contact force sensing (which is similar to any conventional AFM system), the thermometer integrated on the tip will record simultaneously the sample thermal information. The system is therefore able to obtain at the same time topography and thermography.

The general principle remains valid for almost all SThM systems (Figure 2-7). However, different types of sensor tip were developed. The contact detection might be a

cantilever or a dynamic force detection resonator as described earlier in AFM force detection principle. In the next part, different types of SThM probe based on various principles will be presented.

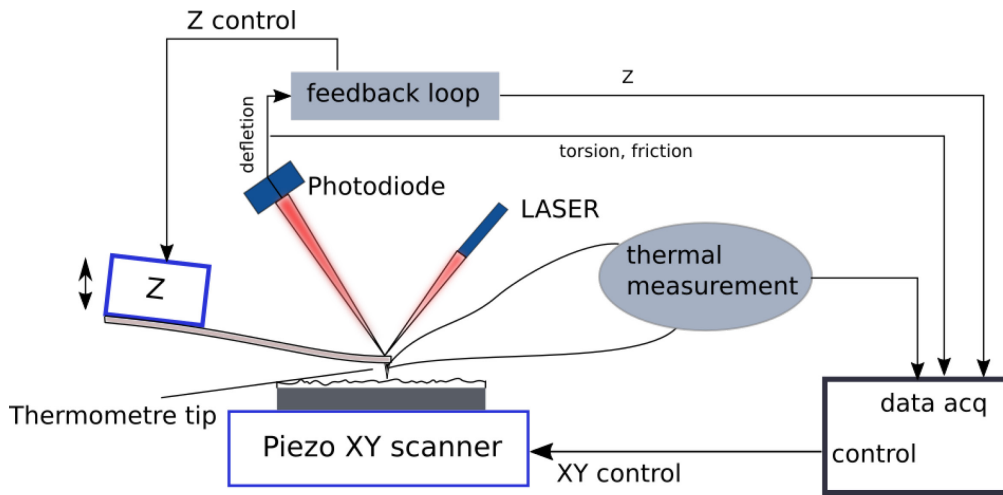


**Figure 2-7: SThM general schematic**

## 2.2 Different types of SThM

As briefly presented in the introduction, many effects connected to thermal physics have been discovered as thermoelectric effect, thermal-resistance, fluorescence or thermal-expansion... Here we present the state of art on different thermal probes. Each of them is different in fabrication process, geometry, leading to different theoretical modelling, thermal sensitivity and lateral resolution.

### 2.2.1 Resistive probes

The resistive probes use thermal resistance effect:

$$R(T) = R_0(1 + \alpha(T - T_0)) \quad (2-3)$$

where  $R$  is the resistance at temperature  $T$ ,  $R_0$  is the resistance at temperature  $T_0$  and  $\alpha$  is the temperature coefficient of resistance (TCR). In this equation, the resistivity of materials changes with the changing of temperature. The temperature obtained is the integration of the whole sensor probe temperature; fabricator of this type of probe needs a model to infer the tip temperature.

The probe fabrication can be divided in two different techniques. The first based on microfabrication process performed notably for Wollaston wire. The second is thin film lithography process which has a big advantage on mass production and tip reproducibility.

In 1805, William Hyde Wollaston proposed a cold drawing process to obtain a silver wire cladding of 75 $\mu\text{m}$  diameter with a Platinum thin core of 0.75-5  $\mu\text{m}$  diameter in middle. The same principle was extended to Platinum-10%Rhodium alloy. A resistive probe 200  $\mu\text{m}$  based on Wollaston wires was proposed by Dinwiddie[25]and Pylkki [38]. This probe is well-known as “Wollaston thermal probe”. The silver cladding is removed by chemical attack. The thin Platinum or Platinum-10%Rhodium core is used as a resistive thermometer. The probe design is depicted in the Figure 2-8 in which the silver outer part is used as an AFM cantilever, a mirror is glued on the probe lever for AFM laser signal reflection. For mechanical stabilization, the wires are attached at the end by a drop of glue.

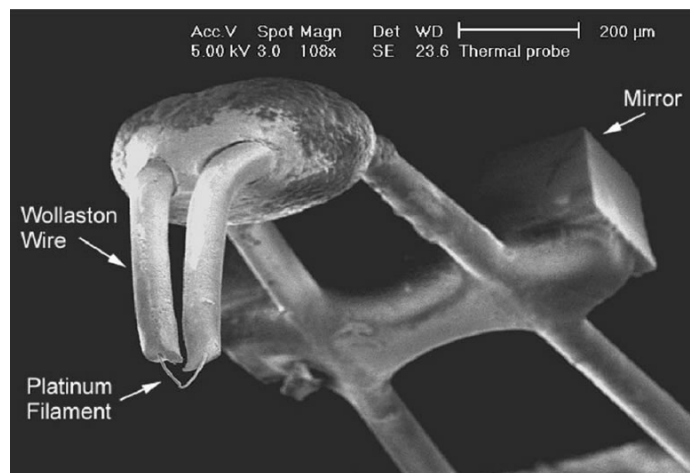


**Figure 2-8: Wollaston probe image [25]**

Since the tip size is quite large, the probe lateral topographical resolution is limited around 1  $\mu\text{m}$  [39]. The Wollaston probe is still widely used by SThM user community because of their thermal sensitivity, stability and the relative simplicity of the model for microscale thermal quantitative measurements.

To improve the thermal resolution, it is essential to reduce thermal probe size. Rangelow and colleagues [40] have put a thin platinum resistive wire (100 nm)

between two electrodes using focus ion beam etching and deposition. The tip radius obtained is around 20nm which can improve the lateral resolution to 20 nm and 1mK in thermal resolution.

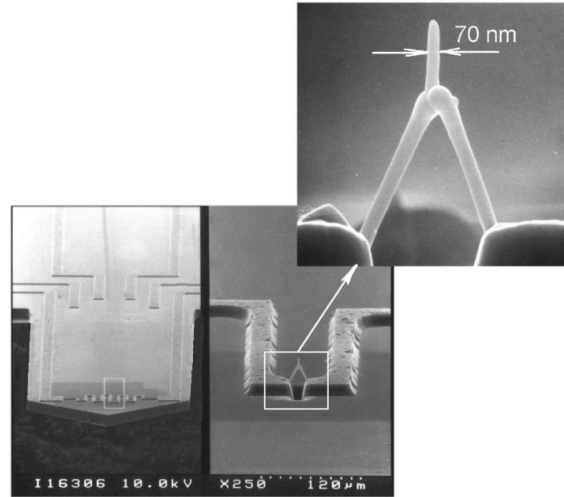


**Figure 2-9: Thermal resistive probe fabricated by Rangelow et al [40]**

Another way for probe size reducing is using a thin film lithography process. Mills et al in have used a thin film resistive on Silicon Nitride tip [41] (figure 2-10a) for a thermal scan to detect voids subsurface. A new batch-fabricated version of this probe is presented and commercialized by Kelvin Nano Technology called KNT probe[42],[43].

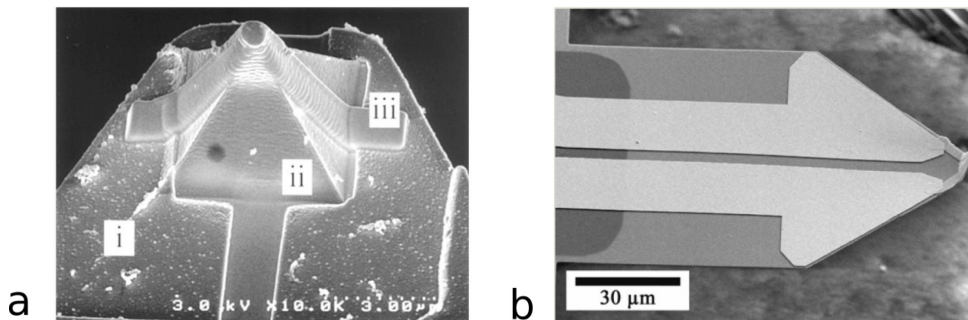


**Figure 2-10: Resistive probe from Digital Instrument [41] and KNT SThM probe [43]**

This is also one of the most wide-used probes in many laboratories. The probe is composed of Silicon nitride thin film cantilever and Palladium deposited resistive tip. The thin film  $\text{SiN}_x$  cantilever possesses low thermal conductivity to minimize the thermal perturbation on the measurement.

Another SThM probe was developed by Wielgoszewski et al [44]. A platinum thin film is deposited on Silicon Nitride cantilever. After lithography fabrication, the probe V shape tip is refined by FIB, the tip radius can attend 100nm. The authors have announced a topographic resolution of 100nm using this tip.

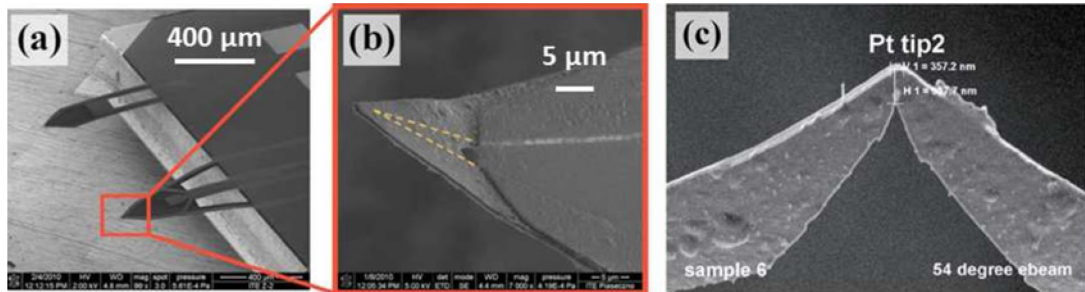


**Figure 2-11: Thermo-resistive probe made by Wielgoszewski et al[44]**

In 2002, King et al developed an AFM cantilever for thermomechanical writing and reading[45]. The U-shape cantilever includes 2 high-doped legs and low-doped resistor element at the end on the tip base which creates a localized heat source when the current crosses. Later, thermal characterizations using this probe proved its high resolution[46]. The authors have announced a well-controlled heat flux (tip sample in active mode) under ultrahigh vacuum with very high resolution [47] of around 10-20 nm, [48] and quantitative temperature measurement.

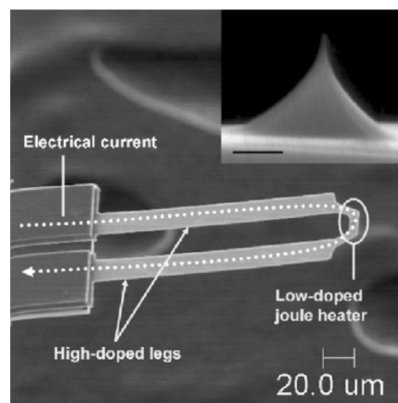


**Figure 2-12: Thermo-resistive Silicon doped probe IBM[49]**

## 2.2.2 Thermocouple probes

Thermocouple probes measure temperature information using thermoelectricity effect. Junction temperature values are converted directly from thermocouple voltages due to Seebeck coefficient.

$$dV = SdT \quad (2-4)$$

The thermocouple probes can be classified into two types. The first is the microwire probe formed by two different metal wires of which the Seebeck coefficient is well-known and then the tip temperature does not need to be calibrated. The second is thin film probe fabricated in clean room process. The Seebeck coefficient of thin film probe should be calibrated due to possible impurity inclusion during process and the thin film size effect on electrical (and thermal) properties.

The first micro wire thermocouple for SThM was presented by Majumdar et al[35]. A 25  $\mu\text{m}$  of diameter type K thermocouple (Nickel-Chromium/Nickel-Alumel) was used. To reduce the tip size, the thermocouple wire is refined by chemical treatment (10 $\mu\text{m}$  of diameter). A diamond tip is added to thermocouple junction to obtain a finer tip. In fact, diamond is a very hard material with high thermal conductivity and electrical insulator.

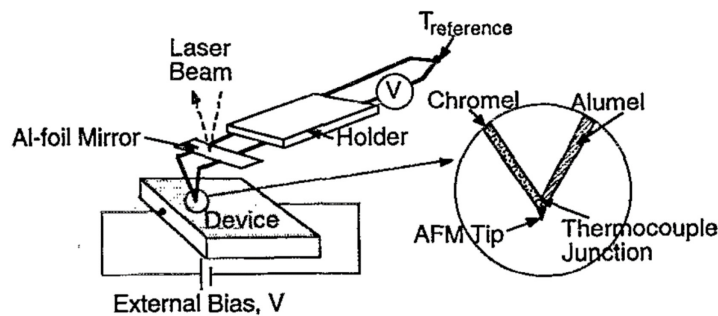


**Figure 2-13: Thermocouple type K probe by Majumdar et al[35]**

Thinner thermocouple probes were presented by Thiery and al[50],[51]. The authors have used two “Wollaston” wires to perform the micro-thermocouple of which the diameter can attend 5, 2.5, 1.3 or 0.5 $\mu\text{m}$ .

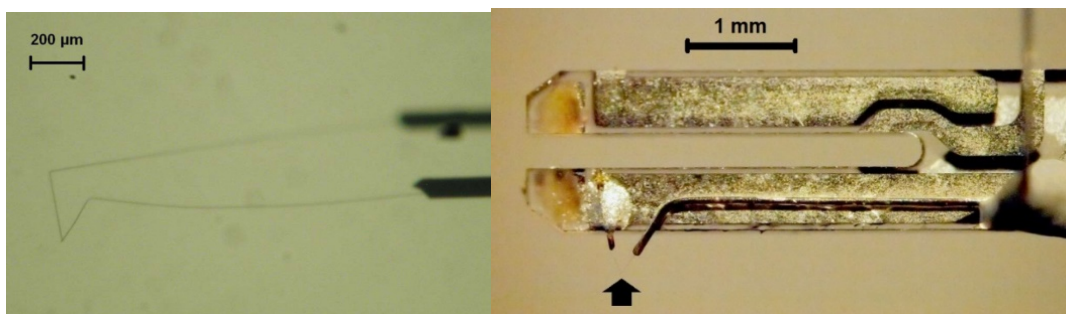


**Figure 2-14: Thermocouple type S probe by Thiery[50],[51]**

As proposed by Bontempi and al, the probe can be integrated on a quartz tuning fork for contact detection[52]. One thermocouple connector can be connected to a quartz tuning fork electrode using electrically conductive adhesive while the second is glued along the middle of a prong (neutral axis) after insulating its surface. Figure 2-14 shows the tuning fork with its thermocouple probe.

Zhang et al [53] have presented a thermocouple probe deposited on tip probe. The thermocouple junction has the curvature radius around 200nm. However, the tip and cantilever was made in silicon, highly thermally conductive (148 W/m.K), which reduces the probe thermal sensitivity.

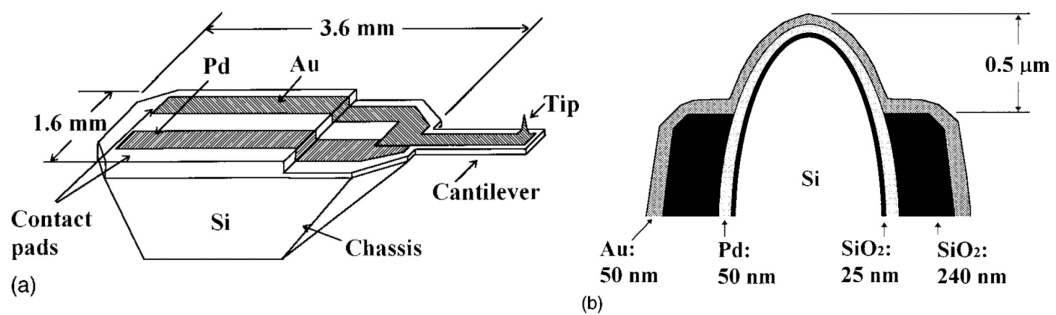


**Figure 2-15: Thermocouple probe developed by Zhang [53]**

Mills et al in 1998 have developed a Palladium – Gold thermocouple on a Silicon Nitride (SiN) cantilever[54]. SiN is a very low thermal conductivity material ( $0.17 \text{ Wm}^{-1}\text{K}^{-1}$ ). The tip curvature obtained is around 30 nm. The authors announced the resolution of around 40 nm.

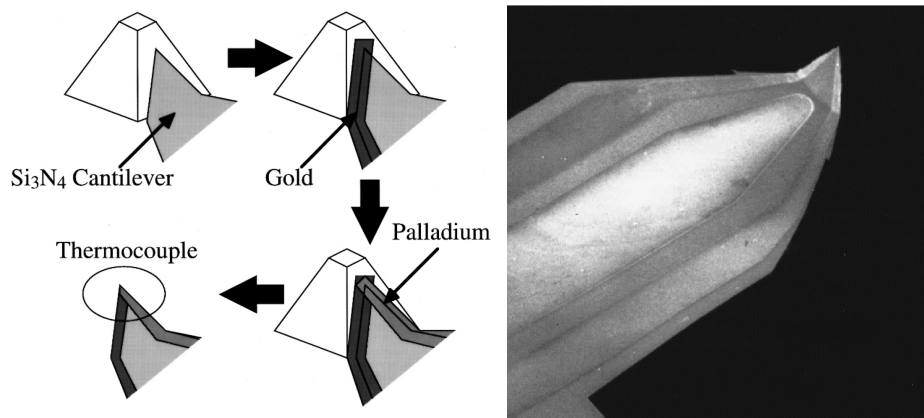


**Figure 2-16: Thermocouple probe developed by Mills[54]**

At Berkeley University, Shi and Majumdar developed a SiO<sub>2</sub> pyramid and cantilever on which they deposited 2 two layers of metal (Cr and Pt) separated by a silicon oxide insulating layer[55],[56]. Another thermocouple probe (Au and Cr) was developed also by several thin film depositions on SiO<sub>2</sub> tip. The AFM reflector element is moved away from the heating zone to avoid the laser perturbation [57]. The authors performed double scan technique[57] or null-point technique[58] to obtain quantitative temperature measurements.

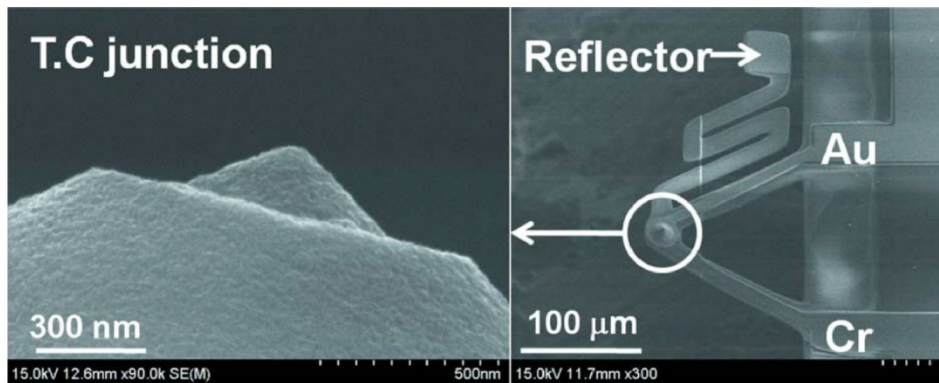


**Figure 2-17: Thermocouple probe developed by Kim group [57]**

On the same principle, Thiery has deposited thermocouple on a fine tip made from optical fiber [59]. The tip radius achieved can be less than 1 μm. The two metal Ni-Cr and Cr-Al is isolated by a SiO<sub>2</sub> layer.

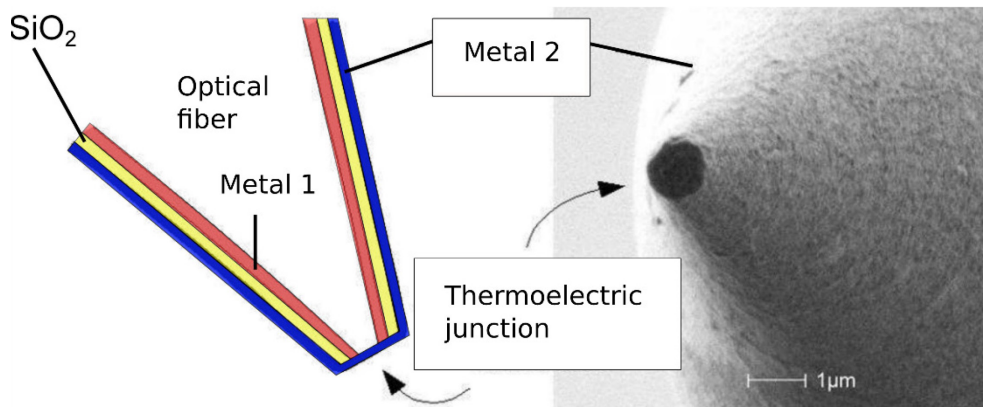


**Figure 2-18: Thermocouple probe deposited on an optical fibre tip [59]**

### 2.2.3 Other methods

Another way to overcome the optical diffraction limit is near field optical method (Near Field Optical Thermometry)[60] which is based on the use of a SNOM (Scanning Near-Field Optical Microscope). An optical fibre with a small tip and aperture are used to collect the optical information from sample. The tip-sample distance is much smaller than the wavelength of the light therefore the resolution of technique is not limited by Rayleigh criterion. A surface temperature measurement was performed by Goodson et al[61].

Aigouy et al have developed another technique in which a fluorescent nano-particle is attached on a STM tungsten tip[62]. The particle diameter is around 300nm which give a high resolution for this method (Figure 2-19).

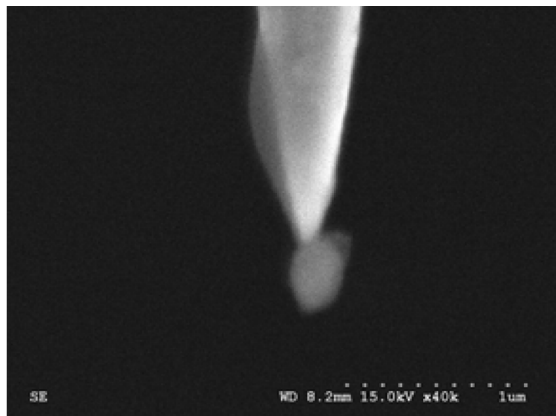


**Figure 2-19: Fluorescence particle attached on Tungsten tip [63]**

However, this method has a difficulty on measurement reproducibility due to the particle forms and the hard possibility to attach them at the same place. The particle excited by a laser can emit a fluorescence light of which the intensity depends on the temperature. There are many types of particle can be used for thermometry technique such as Er/Yb-doped or CdSe/ZnS[64].

### 2.2.4 SThM quantitative measurements

- *Tip-surface interaction*

A thermal local measurement by contact method depends on many factors due to the thermal, mechanical interactions between a small tip and the sample surface. The complex study of these contributions on the tip-sample heat transfer was performed by many research groups and still under development. The thermal configuration of the whole probe can be described in Figure 2-20.

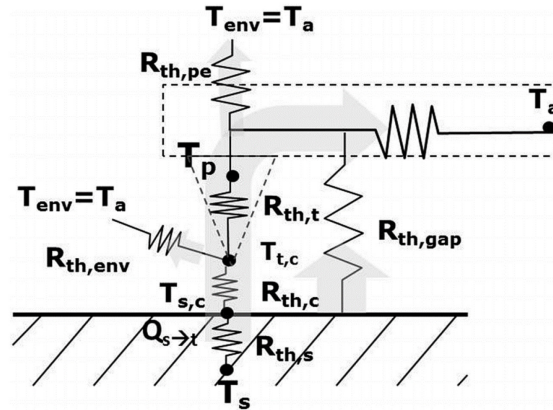


**Figure 2-20: Heat transfer mechanism of a SThM probe to surface[65]**

As described in the model, there are many parameters influencing the equivalent thermal conductance and then thermal contrast images. The cantilever conductance can cause a thermal perturbation which leads to an image distortion when the tip scans over the sample[66]. Measurements were performed in different environments (vacuum[47], [48],[67], liquid[68], gas[69]) to eliminate or quantify the influence of air. Concerning the tip-sample heat transfer, the heat flux from the tip to the sample can be represented by an equivalent thermal conductance[70][71] (the inversion of resistance).

$$\Phi = G_{eq}\Delta T \quad (2-5)$$

The equivalent thermal conductance  $G_{eq}$  can be decomposed in 2 contributions: contact conductance  $G_c = 1/R_c$  and sample spreading  $G_s = 1/R_s$  conductance[72],[73].

$$\frac{1}{G_{eq}} = R_{eq} = R_c + R_s \quad (2-6)$$

The contact depends on many different heat transfer mechanisms[74],[65],[75]: thermal radiation conductance  $G_{ra}$ , air conductance  $G_{air}$ , even  $G_w$  the conductance of water meniscus [76] and mechanical contact conductance  $G_{mc}$ .

$$\frac{1}{G_c} = R_c = \frac{1}{G_{air} + G_{ra} + G_{mc} + G_w} \quad (2-7)$$

The sample conductance  $G_s$  (the inversion of resistance) can be expressed in the following term[65]:

$$G_s = Kb\lambda_s \quad (2-8)$$

where  $b$  is the effective thermal contact radius,  $K$  is geometrical factor of tip-sample and  $\lambda_s$  is the thermal conductivity of sample.

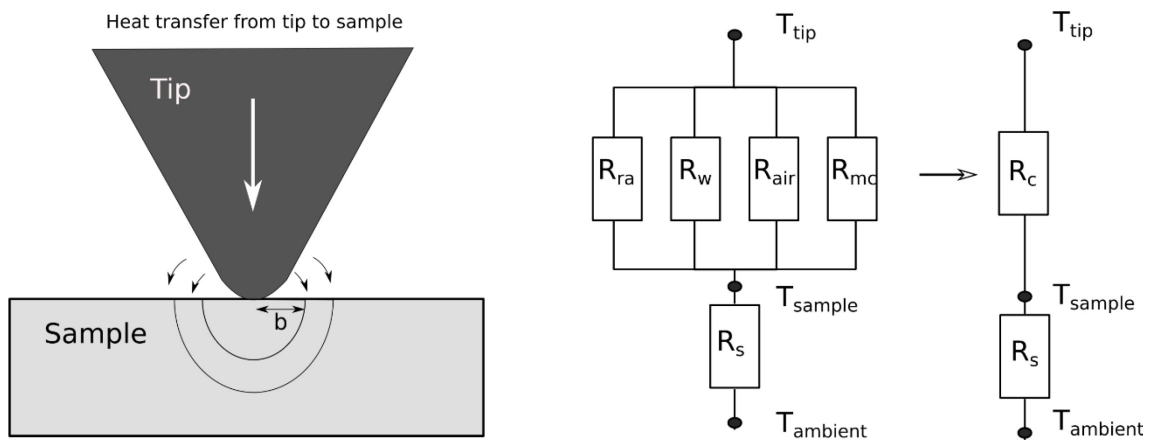


**Figure 2-21: Tip-sample heat transfer**

For quantitative measurements, these factors need to be quantified especially  $G_c$  and  $b$ . The contact conductance  $G_c$  can be influenced by material properties, topography details, roughness, force and environment condition. For example, a topography artifact appears when the probe scans over a hollow or convex details (holes, steps peaks...)[77]. In this case, the thermal contact radius  $b$  and the contact conductance  $G_c$  are modified when the probe falls into a surface defect. Many works concentrated on the influence of topography on thermography. Klapetek and al [78] have developed a numerical correction on thermography taking to account the tip and sample geometry. Yunfei Ge and al developed a topography-free sample for probe evaluation[79].

The modelling of  $b$  is tricky and must consider many factors especially measurements under air condition. In nanoscale measurements, solutions in ballistics regime should be considered [80],[81],[82]. Measurements under controlled environment are performed for example in ultra-high vacuum or different air pressures to study small scale tip-sample heat transfer. The quantifying of thermal contact area is also one of the objectives of this thesis in the next chapters.

- *Probe calibration*

Probe calibration bases on the probe characteristics. One of the most wide-known method is the dipping the probe in a liquid [66] bath or a high temperature oven if one is looking for high temperature ( $>300^{\circ}\text{C}$ ) information.

A fragile micro-wire thermocouple is likely unsupportable dipping in a liquid bath. In fact another method was used by Majumdar [74] and Thiery [59] using a well-known thermocouple type K or type S for reference temperature. The thermocouple is welded on a hot plate; a thermal tip is then glued on the thermocouple. Since the thermal contact is considered as perfect, the probe temperature is assumed to be equal to the temperature measured by the thermocouple.

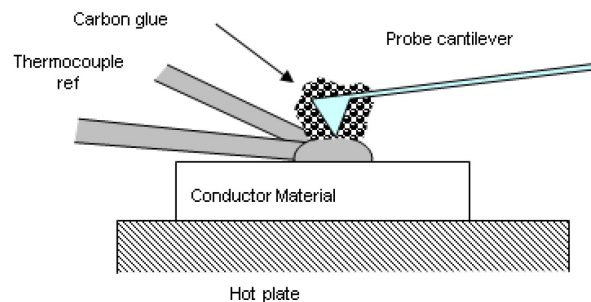


**Figure 2-22: Probe calibration principle using contact method**

However, for small scale measurements, hot objects with tiny thermal mass are considered. Then, the measuring tool itself (SThM probe) can interfere with the thermal measurement and the contact resistance may become dominant. Some active devices were developed for probe evaluation at micro and nano scale [66], [83]. One of these devices will be presented in the chapter 4 of this document.

The thermal probe time constant is also an important parameter which expresses how long it takes for the probe to reach thermal equilibrium. The scan speed is totally depended on this parameter. The dynamic method can be used to measure the time constant value. Among possible thermal excitation methods, Joule heating in which the probe takes the role of the heating and sensing element, or external laser flash heating are the most used. The excitation function may be sinusoid, a high intensity pulse or a step function.

Figure 2-23 depicts time constant measurement using Joule heating sinusoid excitation whose frequency is changed while magnitude and phase are stored. The time constant is calculated using the cut-off frequency, which correspondent to the -3dB drop of the magnitude. The relation between the time constant  $\tau$  and the cut off frequency  $f_c$  is given by:

$$f_c = \frac{1}{2\pi\tau} \quad (2-9)$$

It is clearly shown that this time constant depends mainly on the probe size and its materials. A study of cut-off frequency is described in Table 2-1 using Joule heating and  $2\omega$  Seebeck measurements for thermocouple or  $3\omega$  measurements for resistive probes.

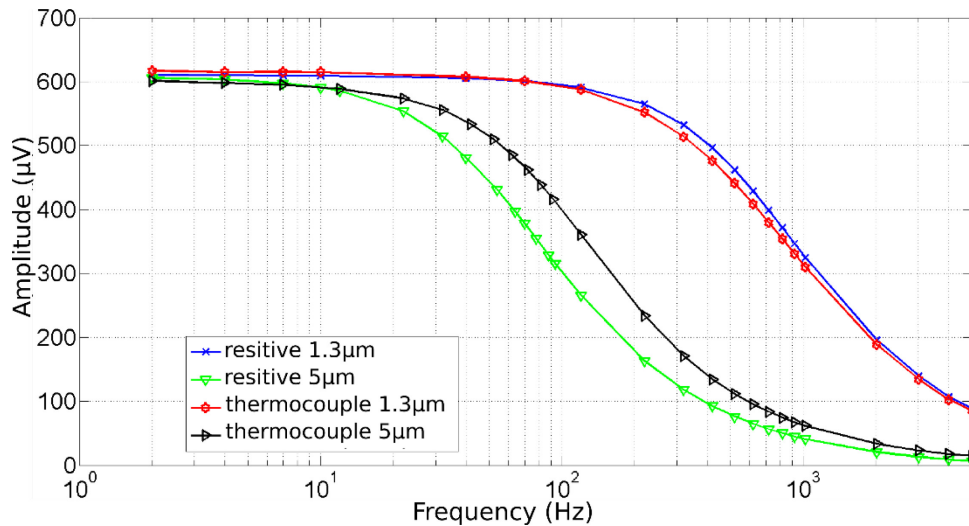


Figure 2-23: Cut-off frequency of thermocouple probes and Wollaston probes [84]

Type	Diameter ( $\mu\text{m}$ )	Time constant (ms)	Cut-off frequency (Hz)
K	25	30 ms	5
	12.5	8 ms	20
	7.6	3 ms	53
S	5	1250 $\mu\text{s}$	125
	1.3	180 $\mu\text{s}$	880

Table 2-1: Time constant and cut-off frequency of micro-wire probes

## 2.3 FEMTO-ST SThM based microwire thermocouple

This work focuses on the study of microwire thermocouple probes made by Thiery as presented earlier in Figure 2-14. In this part, the principles of thermoelectric effects (Seebeck effect, Joule effect and Peltier effect) are recalled. Then the probe detection mode (active, passive) as well as the earlier FEMTO-ST SThM system design is described.

### 2.3.1 Thermocouple principles and temperature measurement

The thermocouple measurements based on the thermo-electricity principles are known as Seebeck, Thomson, Peltier and Joule effects (Appendix 1). The thermocouple voltage (Seebeck voltage) can be used to deduce the hot junction temperature if reference temperature is predetermined.

The conversion is established through a polynomial function relating Seebeck voltage to temperature or inversely temperature to Seebeck voltage.

$$E = \sum_{i=0}^n c_i T^i ; T = \sum_{i=0}^n b_i E^i \quad (2-10)$$

Usual thermocouples are named under a capital letter for example “A type”. Here in this work, the choice of a S type thermocouple is due to the existence of the thinnest wires ever fabricated, known as “Wollaston wires”, corresponding to Platinum and Platinum-10%Rhodium alloy. As a result, the probe can attend a relatively small size for a local thermal measurement. The S type thermocouple is also considered having the highest stability at high temperature. It possesses also a very large working range (from -50°C to 1768°C). To convert the voltage signal of the thermocouple to temperature, a polynomial function is used in which the reference temperature is equal to 0°C, as given in the Table 2-2 below.

Coefficients $X_n$	$T^\circ \rightarrow E (X \rightarrow c)$	$E \rightarrow T^\circ (X \rightarrow b)$
$X_0$	0	-0.122638580254693
$X_1$	5.40313308631	0.186645256034229
$X_2$	1.2593428974 e-2	-7. 829973449446437 e-5
$X_3$	-2.32477968689 e-5	6.588579925468409 e-8
$X_4$	3.22028823036 e-8	-4.160178200931134 e-11

$X_5$	$-3.31465196389 \text{ e-11}$	$1.815268176321127 \text{ e-14}$
$X_6$	$2.55744251786 \text{ e-14}$	$-5.427735397174568 \text{ e-18}$
$X_7$	$-1.25068871393 \text{ e-17}$	$1.116245567777319 \text{ e-21}$
$X_8$	$2.71443176145 \text{ e-21}$	$-1.574101642114063 \text{ e-25}$

**Table 2-2: Conversion coefficients of thermocouple type S [84]**

An advantage of a thermocouple is that the measured temperature is located only at the junction, considered as a sensing point. A temperature measurement using the Wollaston wire thermocouple is somewhat different to standard thermocouple since the cold (reference) junction corresponds to the massive Silver cladding whose temperature remains at ambient as described in the Figure 2-24. The temperature of the hot junction can be deduced using the polynomial coefficients of Table 2-3 and the reference correction, as described in Alexia Bontempi's PhD thesis[84].

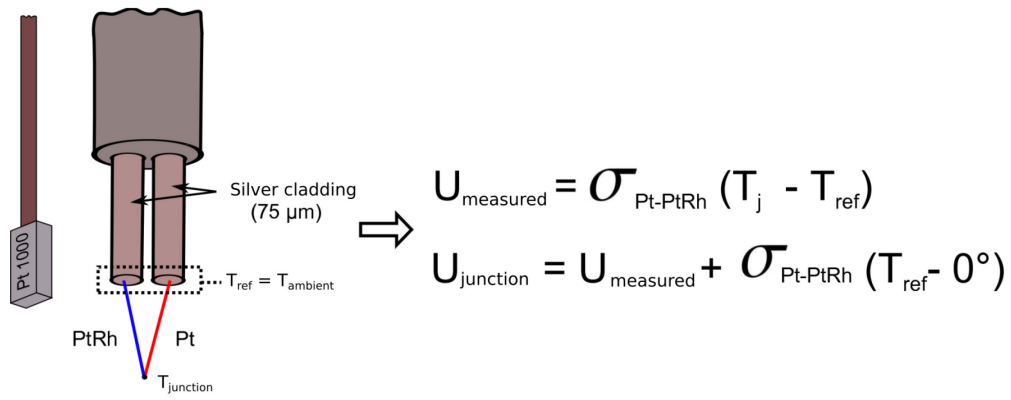


**Figure 2-24: Measurement schematic of microwire thermocouple [84]**

### 2.3.2 Thermal conductivity measurement using 3-omega and 2-omega method

In addition to passive mode allowing to measure temperature, the microwire thermocouple probe can also work well in active mode using AC current excitation. The measurement method called 2-omega method is a modified version of the well-known 3-omega method for thermal conductivity.

- *Three omega method for a thin wire deposited on a substrate*

This technique was developed by Cahill in 1990[85]. A thin film hot metal wire is deposited on a sample. This wire is used as a heater as well as a thermometer. An AC current with angle frequency of  $\omega$  is supplied to the wire and the output voltage is analysed in frequency domain instead of time domain compare to earlier techniques.

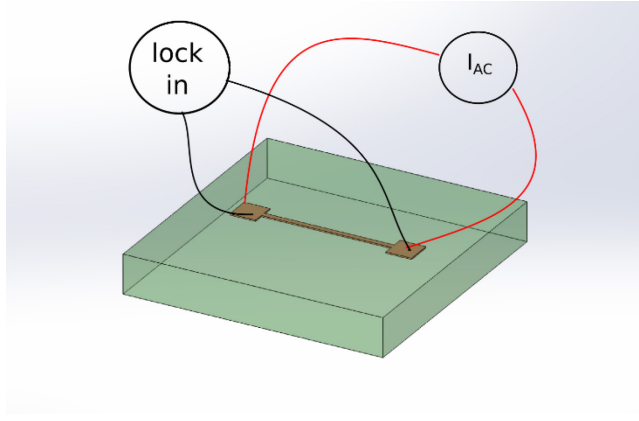


**Figure 2-25: Three omega method**

An approximation of temperature field solution in cylindrical coordinate from distance  $r = (x^2 + y^2)^{\frac{1}{2}}$  through the substrate can be deduced if we consider the penetration depth  $|1/q| \gg r$ :

$$\Delta T(r) = \frac{P}{i\pi\lambda_e} \left( \frac{1}{2} \ln\left(\frac{a}{r^2}\right) + \ln(2) - 0.5772 - \frac{1}{2} \ln(2\omega) - \frac{i\pi}{4} \right) \quad (2-11)$$

where  $\frac{P}{l}$  is the power per unit length of Joule heating,  $\lambda_e$  is thermal conductivity of substrate and  $q = \sqrt{\frac{2i\omega}{a}}$  where  $a$  is thermal diffusivity of the sample.

The temperature oscillates at  $2\omega$  frequency and generates a voltage output at  $3\omega$  frequency as shown in the equation below.

$$V = iR = i_0 \cos(\omega t) R_0 (1 + TCR * \Delta T(2\omega)) \quad (2-12)$$

$$\Rightarrow V_{3\omega} = \frac{i_0 R_0 * TCR * \Delta T_{2\omega}}{2} \cos(3\omega t + \phi) \quad (2-13)$$

A three-omega voltage exhibits a linear behavior with logarithm of frequency[85]. The experimental measurements can be fitted with theory using the Equation 2-11 to deduce thermal conductivity and thermal diffusivity of the sample.

- *Three omega method for SThM*

Inspired by the  $3\omega$  method for metal wire deposited on a substrate, Gomès et al presented a SThM measurement method using AC excitation [86]. Lefèvre et al [87],[88] developed an analytical model to quantify  $3\omega$  measurement for Wollaston thermal resistive probe to measure thermal conductivity.

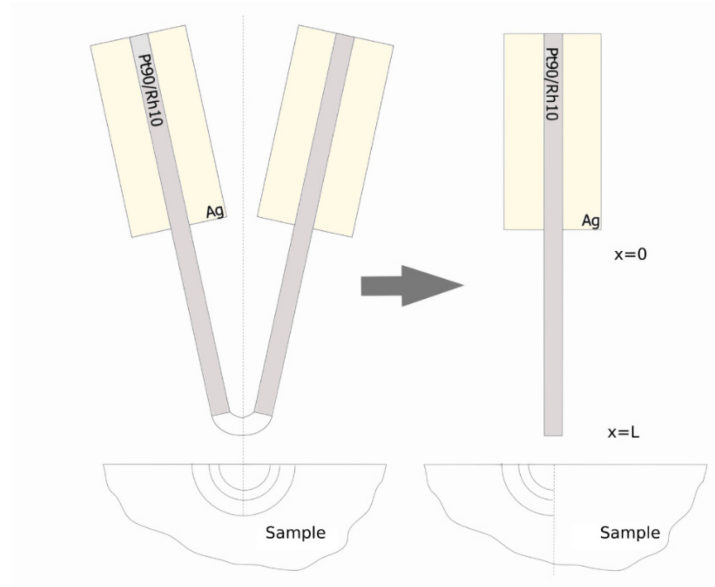


**Figure 2-26: Thermal model of Wollaston probe [87]**

A thermal model of cylinder homogenous wire is considered, the  $2\omega$  temperature amplitude is described following the equation[87]

$$\frac{2i\omega}{a_s} \theta_{s2\omega} = \frac{\rho_e l_0^2}{2\lambda_s S_s^2} - \frac{hp_s}{\lambda_s S_s} \theta_{s2\omega} + \frac{d^2 \theta_{s2\omega}}{dx^2} \quad (2-14)$$

To solve the equation, they introduced a boundary condition with an equivalent thermal conductance to the sample.

$$\begin{cases} \theta(0) = 0 \\ G\theta(L) - \lambda_s S \frac{d\theta(L)}{dx} = 0 \end{cases} \quad (2-15)$$

The solution of the equation 2-14 gives temperature contribution along the whole length of the Wollaston wire (from 0 to L). The average value  $\overline{\theta_{2\omega}}$  can be expressed by equation 2-16 after integrating  $\theta_{2\omega}$  from 0 to L.

$$\overline{\theta_{2\omega}} = \frac{J}{Lm^3} \frac{(4e^{mL-2} + mL e^{2mL} - mL - 2e^{2mL}) \frac{Geq}{kmS} + (mL + mL e^{2mL} - e^{2mL} + 1)}{(e^{2mL} - 1) \frac{Geq}{kmS} + (1 + e^{2mL})} \quad (2-16)$$

This value  $\overline{\theta_{2\omega}}$  can be extracted by measuring the  $3\omega$  Voltage using a lock-in amplifier and corresponding to:

$$V_{3\omega} = \frac{i_0 R_0 * TCR * \overline{\theta_{2\omega}}}{2} \quad (2-17)$$

The equivalent thermal conductance  $G_{eq}$  can also be extracted from electrical measurement of  $3\omega$  voltage. From the equation 2-6, 2-8, the equivalent thermal conductance can be separated in two parts: thermal spreading conductance in the sample and tip-sample thermal contact conductance.

$$\frac{1}{G_{eq}} = \frac{1}{2b\lambda_s} + \frac{1}{G_c} \quad (2-18)$$

The sample equivalent thermal conductivity  $\lambda_s$  can be measured through a  $3\omega$  voltage ratio if we consider thermal contact area and thermal contact resistance are constant or defined.

- *Two omega method for thermocouple SThM*

A  $2\omega$  method has been developed for thermocouple probes which have presented the advantages of measuring directly the tip temperature (junction temperature)  $\theta_{2\omega}$  instead of an integration on the whole probe  $\overline{\theta_{2\omega}}$  [21]. This technique brings the sensing point closer to the sample and the tip (junction) temperature is extracted directly through the Seebeck's voltage measurement. Another advantage of thermocouple wire is the V-form of cylindrical micro-wire thermocouple allowing to simplify the theoretical model similar to the Wollaston resistive probe. Finally, different harmonics can be measured simultaneously (eg. the  $2\omega$  issues from Seebeck effect, the  $3\omega$  harmonic generated from thermoresistive effect).

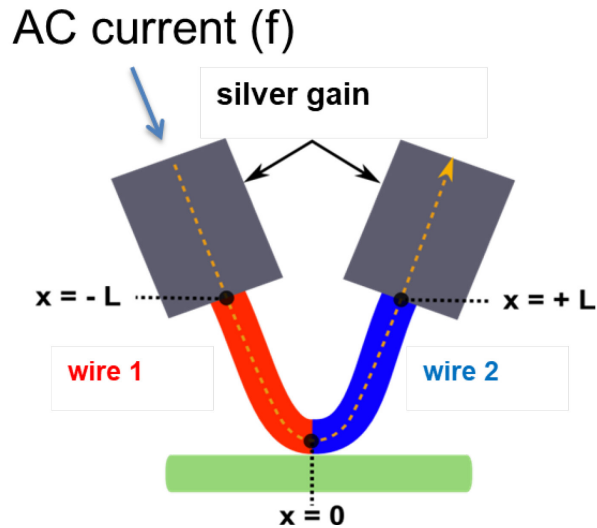


**Figure 2-27: Thermal model of microwire thermocouple [84]**

A model will be presented for thermocouple probe taking account of the different parameters of two metal wires.

### 2.3.3 Microwire thermocouple fabrication

Macroscale thermocouples are widely used in many industrial applications. The work of Thiery at FEMTO-ST Institute [89] led to reduce the thermocouple size from  $25\mu\text{m}$  to  $5\mu\text{m}$ ,  $1.3\mu\text{m}$  or even  $0.5\mu\text{m}$  of diameter for microscale thermal applications.

In any case, the metal microscale core to make thermocouple is covered by a silver gain of diameter  $75\mu\text{m}$ . Depending on of the intended thermocouple length, the silver is removed by dipping in a chemical solution (50% nitride acid – 50% water). The exposure time is around 10s with 2V applied between the electrodes.

The most classical techniques to weld the wires together such as gas or oxy fuel welding are no longer applicable for small scale thermocouple. The thermocouple junction can be obtained by welding two wires using an electrical sparking technique by capacitive discharge[90]. This method allows attending a localized fusion between two thin metal wires by creating an electrical spark when these wires approaching each other or in contact. The principle schematic is described in the Figure 2-28.

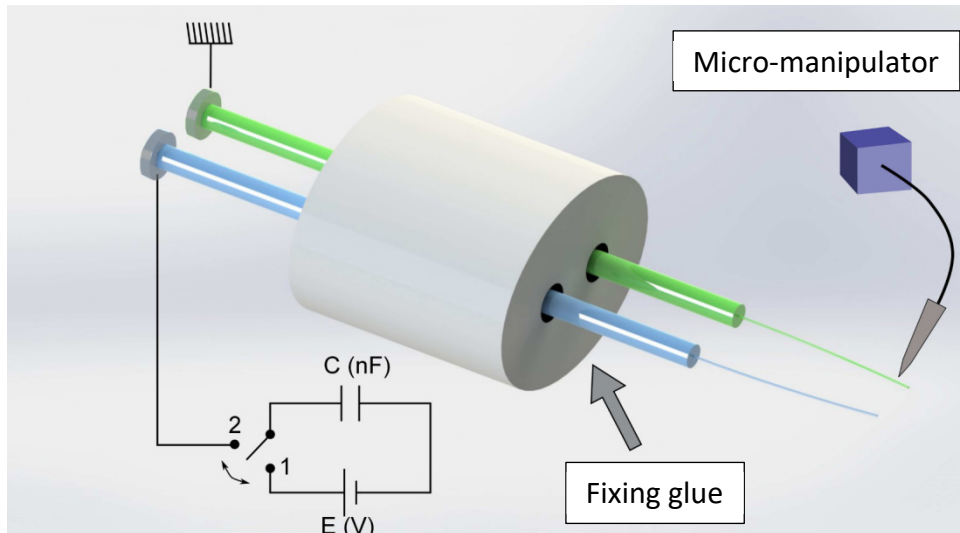


**Figure 2-28: Thermocouple welding principle [84]**

Because the Platinum core wire is thin and very flexible, the fabrication is made with a help of a pneumatic micro-manipulator and a joystick to limit the vibration and a binocular for magnifying the vision.

The fusion zone obtained due to the short circuit when the switch changes from the position 1 to the position 2. The capacitive discharge energy  $\frac{CV^2}{2}$  is one of the important parameters for the quality of the junction. This parameter can be justified by changing the capacitance or the charging voltage values. For instance,  $200V_{DC}/125nF$  and  $200V_{DC}/75nF$  is needed for the thermocouple type K ( $12.7\ \mu\text{m}$  and  $7.6\ \mu\text{m}$  respectively) or  $80\ V_{DC}/4nF$  and  $20V_{DC}/4nF$  for thermocouple type S ( $5\ \mu\text{m}$  and  $1.3\ \mu\text{m}$  respectively). These parameters are indicative and they can be changed due to laboratory environment (temperature, cleanness, humidity...) or wire geometry (length, uniformity...).

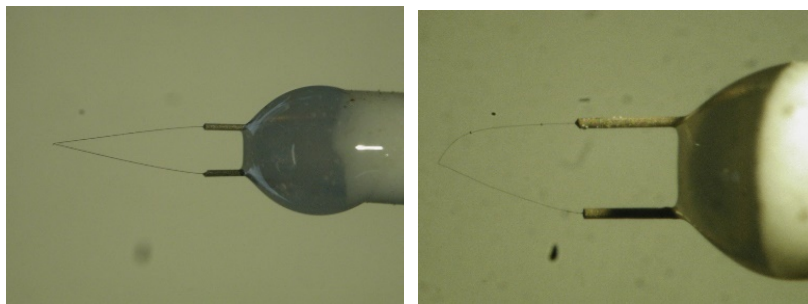


**Figure 2-29: Optical image of thermocouple probe**

### 2.3.4 Quartz Tuning Fork for contact detection

To complete the SThM probe, different combinations of thermal and force sensors has been developed. The most spread are micro-fabricated cantilevers on which a thermal sensor is deposited. For these techniques, the most common contact detection principle remains the optical deflectometer, which is only available if the probe tip is stiff enough, but that is not the case of a micro-thermocouple junction.

A Quartz Tuning Fork (QTF) has been proposed for the first time in 1994 by Karrai and Grober to control the tip-to-sample distance [91],[92]. The contact is detected by tracking the QTF resonance frequency that is shifted when a mechanical coupling occurs. This piezoelectric element can be found as a force sensor in several AFM systems[93],[94].

A QTF can be excited by three different means: electrically, mechanically and photo-thermally. Bontempi et al[83] have extended the use of S-type micro-thermocouple from passive to active mode by integrating it on a QTF. The excitation of the QTF resonator is provided by a modulated laser diode whose energy generates vibration by means of photo-thermo-elastic conversion process. Contrary to AFM cantilever which does not provide a quality factor higher than 700, the QTF quality factor is around 8000 allowing a reliable tip-to-sample distance control mechanism in scanning probe microscopes.

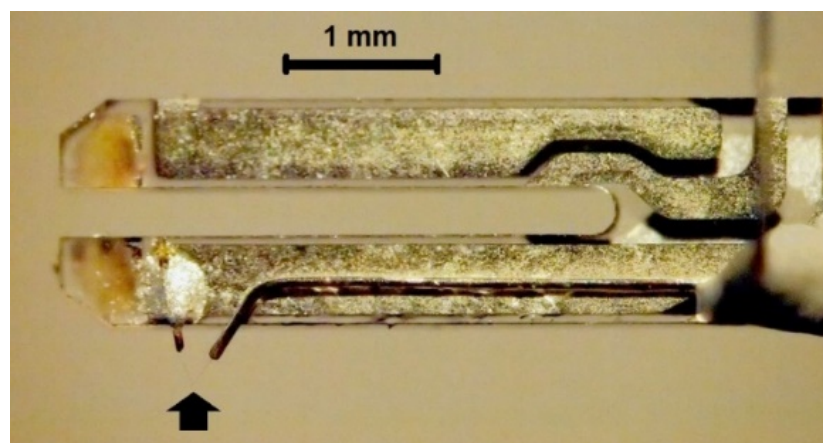


**Figure 2-30: Quartz resonator (QTF) with its thermocouple probe and electrical connection principle.**

Let us recall that Wollaston wires are used to perform a S type thermocouple junction of different available diameters: 5 $\mu\text{m}$ , 2.5  $\mu\text{m}$  and 1.3  $\mu\text{m}$ . Then, since two “Wollaston” wires are used to perform the microthermocouple, one was connected to an electrode using electrically conductive adhesive while the second was glued along the middle of a prong (neutral axis) after insulating its surface. Figure 2-30 shows the tuning fork with its thermocouple probe. The arrow of Figure 2-30 shows the location of the welded wires after being removed from the silver cladding by means of electrochemical attack. To insure a quasi-punctual contact between the thermocouple tip and the sample surface, the junction is reshaped by means of focused ion beam etching (FIB). The SEM (scanning electronic microscope) image of two different sizes thermocouple 1.3  $\mu\text{m}$  and 5 $\mu\text{m}$  after FIB etching is shown on the Figure 2-31.

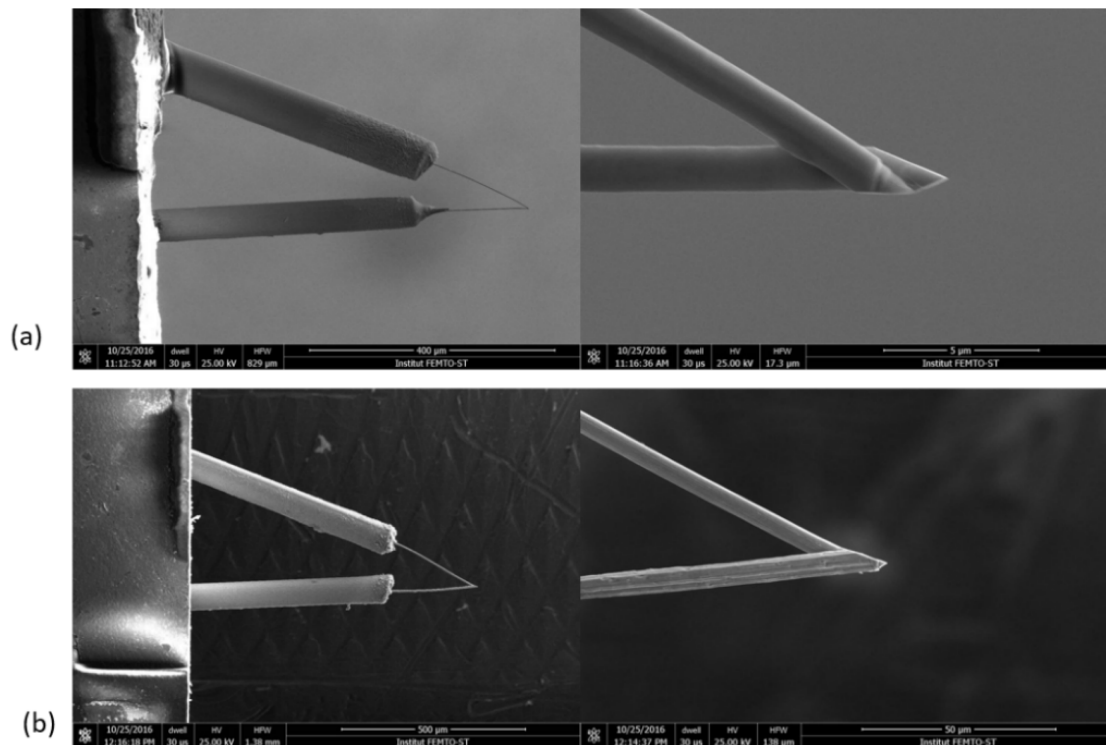


**Figure 2-31: Thermocouple junctions: a) 1.3  $\mu\text{m}$  probe and b) 5  $\mu\text{m}$  probe.**

### 2.3.5 The development of FEMTO-ST SThM system

- *First version FEMTO-ST SThM*

The first SThM system at FEMTO-ST was developed by Alexia Bontempi on a heavy marble support[84]. This system includes 3 manual stages with long travel range of

15mm. A nano-positioning in 3 axis XYZ Nanocube “Physik Instrument” which possesses 10nm of resolution and 100 $\mu$ m of working range. The system is automatically controlled by computer with a Visual Basic program.

A vision system is provided by a CCD camera with a long working range objective. A scan is made by measuring point by point on a surface. The reflection of thermocouple probe on the surface and manual movement system allow the preposition the thermocouple probe toward the sample. The PI Nanocube plays a role of piezo-scanner with small movement steps.

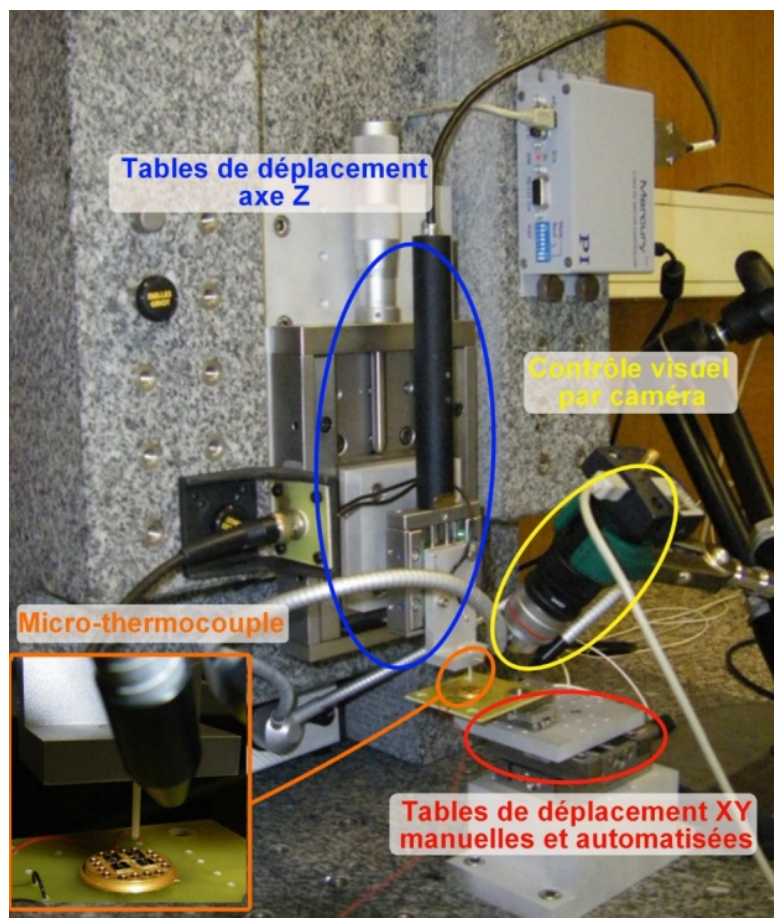


**Figure 2-32: The SThM system v1 [84]**

This system works well for probe testing and passive measurements however it has presented some limits. PI Nanocube, that uses a resistive positioning sensor, suffers from high thermal drift that drastically limits the accurate control of contact force and tip position. The needs of measurement under vacuum have made the marble support

with all positioning stages too voluminous. In the frame of this work, a SThM second version system is redesigned with the objectives: thermal measurement under vacuum, higher resolution  $< 1\text{nm}$  and control from distance all the component including prepositioning SThM probe.

## 2.4 Summary

This chapter has presented the developing of SThM as SPM tool for micro and nano-scale characterisation. It appeared as one of the most promising tool at these scales which is not restrained by optical diffraction limit. However, as a “contact” measuring method, the SThM technique presents its own problems, especially the interfering with measured object. Through more than 20 years of development, the researches invested on this tool to attempt on performing quantitative measurements. Many theoretical calculations as well as experimental technique developed have tried to clarify tip-sample heat transfer interaction. This work presents a research on SThM based micro-wire thermocouple associated on a QTF as force sensor. The first measurement principles and basic tests were presented. In the next chapters, a new microscope setup will be presented. Calibration measurements in active mode and passive mode under a control environment will be deeper studied. Combined to theoretical model, we have investigated and tried to understand the factors involved in the heat transfer mechanisms of our specific probe.

# 3 CONTACT FORCE CONTROL USING QTF AND REALISATION OF SECOND VERSION SThM SYSTEM

Contact force control is essential for SThM to quantify the interaction between tip and surface. Nowadays, the force sensor is fully developed for macro-scale. At nanoscale, the weak force measurement remains challenging. In this chapter, we will present the quartz tuning fork (QTF) as a dynamic force sensor for our SThM application, and how to estimate the contact force by different mechanical models. Three models are used: a very simple one beam model, a two masses model and a finite element method (FEM) simulation. This chapter will also present the advantages and the application of a QTF force sensor associating a thermocouple probe and a photo-thermal excitation principle. The realization of the custom-build SThM system will be described and test results presented to demonstrate the stability of the setup in laboratory environment.

## **3.1 Force sensing technique**

### 3.1.1 Static force sensing

There are two fundamental principles of force sensing at these scales. Firstly, the static method, the force can be measured by determining the displacement of a reference

object which has a predefined stiffness (a cantilever for example). As presented in the first chapter, the most wide-used force sensing method for SPM technique is a cantilever with an optical system (laser and photodiode) of measuring displacement. This system presents some disadvantages such as the difficulty on alignment, the complexity of the design because of voluminous components. These may become difficulties if one wants to integrate the system in a vacuum chamber or scanning electron microscope (SEM) chamber. The opto-deflection system also brings a serious problem to SThM technique due to its thermal perturbation on the sensor.

The problem can be solved using a piezo-resistive or capacitive detection cantilever [95],[96]. In this type of cantilever, local piezo resistors or capacitors are integrated. They can be used to measure local stress and strain through the resistivity or capacity change. These measurements can be converted into force. However, these solutions make the fabrication process more complicated and expensive especially for SThM where a thermometer is already integrated.

### 3.1.2 Dynamic force sensing

This technique uses a resonator for force sensing. The resonator oscillates near its resonance frequency. Dynamic AFM cantilevers can be used, these cantilevers are attached to a piezo actuator for excitation. This technique has considerably increased the sensitivity of the force sensor[97][31].

However, the technique still uses an optical system (laser + photodiode or interferometer) to measure the oscillation amplitude[98]. The quality factor is still low which is a drawback that affects signal-to-noise ratio. Another well-known resonator for SPM technique is the quartz tuning fork used the first time by Karrai[92]. The tuning fork AFM[99] can also easily obtain an atomic-resolution due to its high stiffness ( $\approx 20000 \text{ N/m}$ ) and high quality factor. Figure 3-1 shows a tuning fork and a tuning with thermocouple tip.

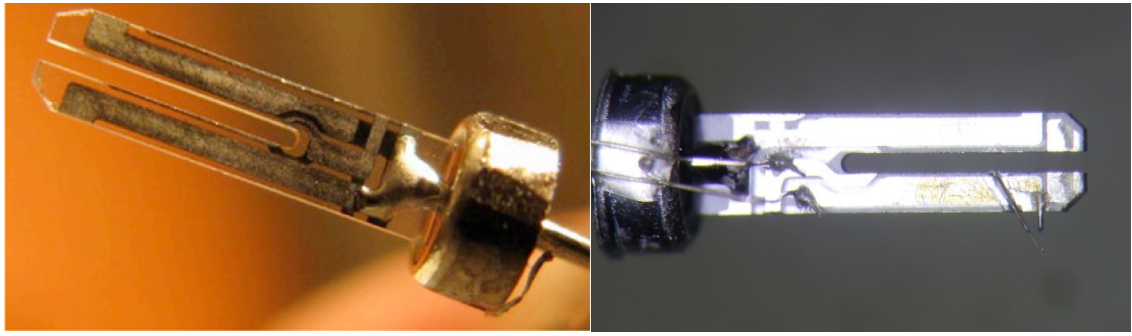


**Figure 3-1: Tuning fork (left) and a tuning fork with thermocouple tip (right)**

Compared to other conventional small scale force sensing tools such as AFM, piezo-resistive cantilever[95] or a force sensing MEMS device[100], the tuning fork presents a large range of force sensing[101] which is very useful for our application with many different thermocouple sizes.

As reference resonator for watch, the quartz tuning fork possesses a very high quality factor around 10 000 in air ambient and 100 000 under vacuum. It is therefore very convenient for SPM technique with a high signal noise ratio in air. The research on the application of QTF has been performed by many groups. The quartz tuning fork has been used in many kinds of scanning probe system such as SNOM[102], noncontact mode AFM with an atomic resolution and Qplus sensor in advanced STM[98]. Besides, they possess a self-sensing system which is an advantage for designing and performing of a compact system. Moreover, their large, rigid structures but highly sensitive are very convenient for the integration of our homemade SThM probe.



**Figure 3-2: Quartz tuning fork with a capsule cover**

The QTF is also very cheap because of their mass production for resonator application in electronic. Many different QTF with different resonance frequency are available (20 kHz, 100 kHz and the 32.768 kHz one being the most popular). These resonators are packaged inside a canister to maintain a vacuum environment and can be used as a common electronic device.

## 3.2 QTF principle

### 3.2.1 Structure

The work concerning this thesis used a very common QTF, at 32.768 kHz, available in many electronic stores. This one has been chosen due to its large size. Its quality factor ( $Q$ ) is on the order of  $10^5$ . When the canister packaging is removed,  $Q$  drops to  $1.5 \times 10^4$  typically due to air density damping effect. Figure 3-3 shows the geometry of the QTF without its metallic canister and its dimensions  $A = 5.95 \text{ mm}$ ,  $L = 3.65 \text{ mm}$ ,  $T = 580 \text{ }\mu\text{m}$ ,  $W = 320 \text{ }\mu\text{m}$ .

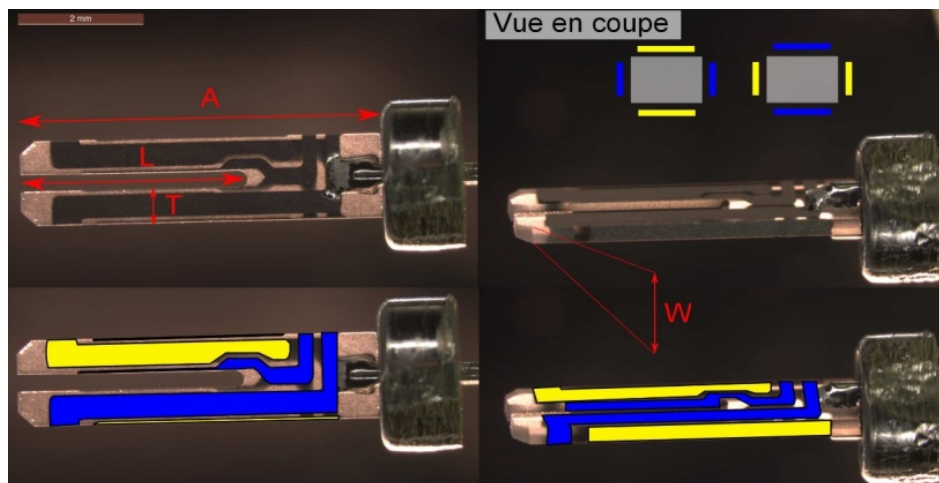


**Figure 3-3: 32.768 kHz QTF configuration** [52]

The prong material is quartz whose Young modulus and mass density are respectively:  $E = 78.7 \times 10^9 \text{ N/m}^2$  and  $\rho = 2650 \text{ kg/m}^3$ . Quartz is a piezoelectric material. Under a mechanical constraint, the electrical field is polarized. The two silver electrodes represented by the blue and yellow area allow to access QTF electrical response when

subjected to mechanical strain. They are deposited symmetrically on the two hands of tuning fork in order to keep the symmetrical balance and obtain the highest efficiency.

### 3.2.2 SPM application

As other standard dynamic force AFM techniques, quartz tuning fork technique for SPM application has the same principle. It can be used in amplitude modulation mode (AM) or frequency modulation mode (FM). In the first mode, the QTF sensor is excited at its resonance frequency, a lock-in amplifier is used to measure amplitude and phase of the oscillation as showed in the Figure 3-4.

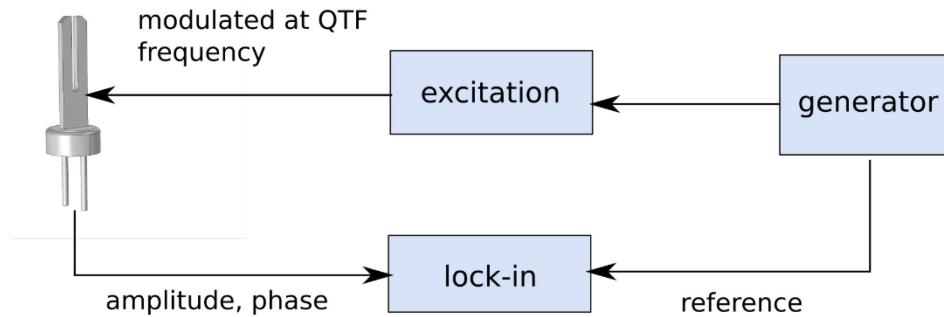


**Figure 3-4: QTF in AM mode**

In the second technique, a phase lock-loop (PLL) is used. In fact, the PLL is the excitation system and the feedback loop maintains the phase value by modifying the excitation frequency. The PLL controller can measure the resonant frequency of the tuning fork which is very useful for the force quantification. The force gradient  $\frac{\partial F}{\partial z}$  can be deduced from the resonance frequency shift[31].

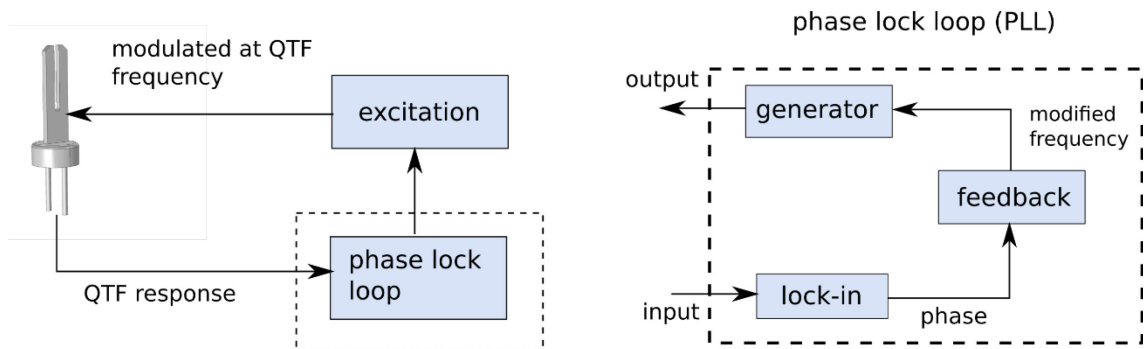


**Figure 3-5: QTF in FM mode using a PLL**

Selecting FM mode presents another advantage on settling time over the AM mode[29]. For the AM mode configuration, the time constant  $\tau = Q/\pi f_0$  (where Q is the quality factor of resonator,  $f_0$  is the resonance frequency) depends on the quality factor. There is a trade-off between the signal-to-noise ratio (which increases when Q increases) and the settling time. In FM mode, the time constant  $\tau \approx 1/f_0$  depends only on the resonance frequency[29]. Therefore, we can take advantage of narrow bandwidth (high quality factor) without reducing the sensing speed. This FM mode is also very stable when the oscillation amplitude is stabilized by an Automated Gain Controller (AGC)[103]. A QTF can be excited by different means for example: electrically, mechanically and photo-thermally.

- *Electrical excitation*

In electrical mode, the piezoelectric nature of the QTF, with its eight opposite electrodes, allows both exciting and detecting oscillations at a chosen resonance mode. The setup is then simplified with respect to external detection such as optical cantilever deflection. However, each resonance mode is followed by an anti-resonance because of the electrical capacitance which includes the contribution of the electrodes patterned along the prongs.

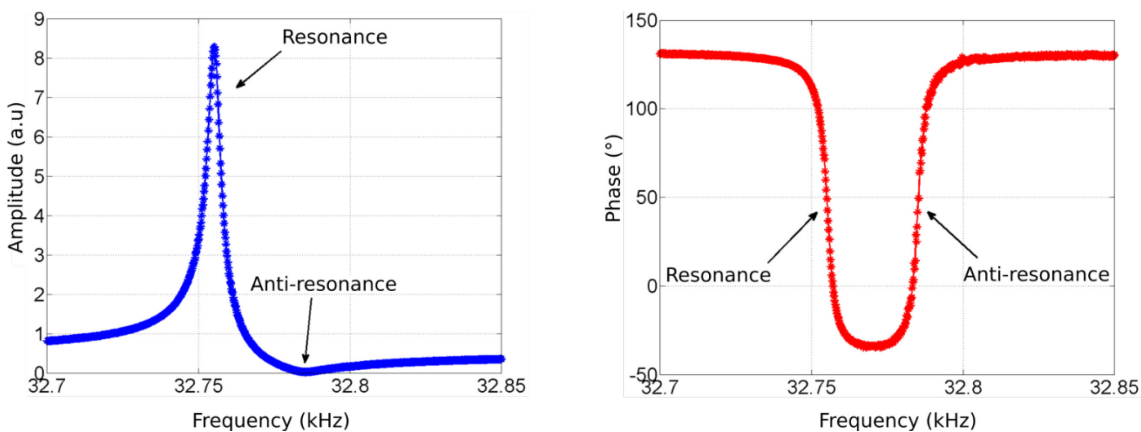


**Figure 3-6: QTF response under electrical excitation [104]**

With a high parasitic capacitance (cable, electrodes, instrument), the resonance and the anti-resonance frequencies become closer and the quality factor is decreased. Karrai and Grober lowered this parasitic capacitance effect by placing electronics very

close to the QTF[105]. However, this can be done by adding a compensated capacitance in the electrical circuit[106],[107].

- *Mechanical excitation*

To counteract the anti-resonance and capacitance problems, mechanical excitation requires the use of a vibrating actuator on which the QTF is embedded[108]. Thus, one prong being usually glued on it, the quality factor drops to a few hundreds. This configuration is well-known with the name “q-Plus” using for SPM technique in ultrahigh vacuum where one prong is fixed [109]. The low Q factor can be only used when the probe tip is not subjected to deformation such as tungsten tip AFM or in the case of near-field optical microscope based on optical fibre tips not for our flexible thermocouple tip.

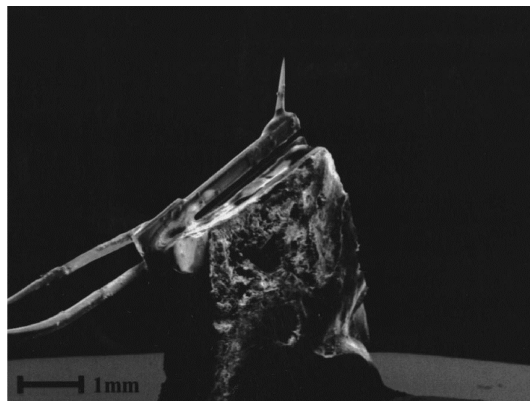


**Figure 3-7: Mechanical excitation technique[108]**

- *Photothermal excitation*

Bontempi et al [104] pointed out the advantages of using a photo-thermal excitation in terms of contact detection and experimental setup flexibility. The lack of anti-resonance is the main advantage for SPM application. The experimental setup is presented in Figure 3-8. Photothermal excitation on tuning fork is a multi-physics phenomenon. Photo-thermal effect appears when a laser beam wavelength is modulated at the QTF resonance frequency focused on its prongs base area. In our setup a diode laser with the wavelength of 637 nm (LP637-SF70 Thorlabs) is used. Optical energy is brought to the tuning fork and converted into heat. This local heating

produces a thermal expansion known as a thermo-mechanical or photo-thermo-elastic conversion effect that generates an elastic wave. An electrical response appears due to the piezo-electric properties of quartz which is demodulated by a lock-in amplifier.

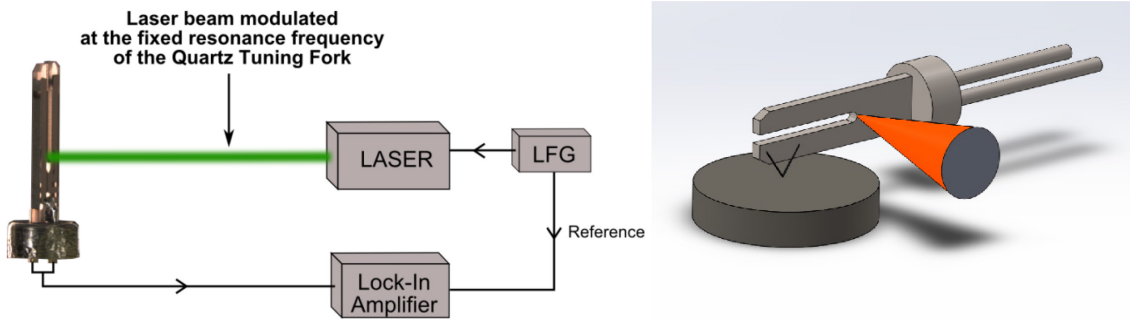


Figure 3-8: Experimental setup and probe positioning [52]

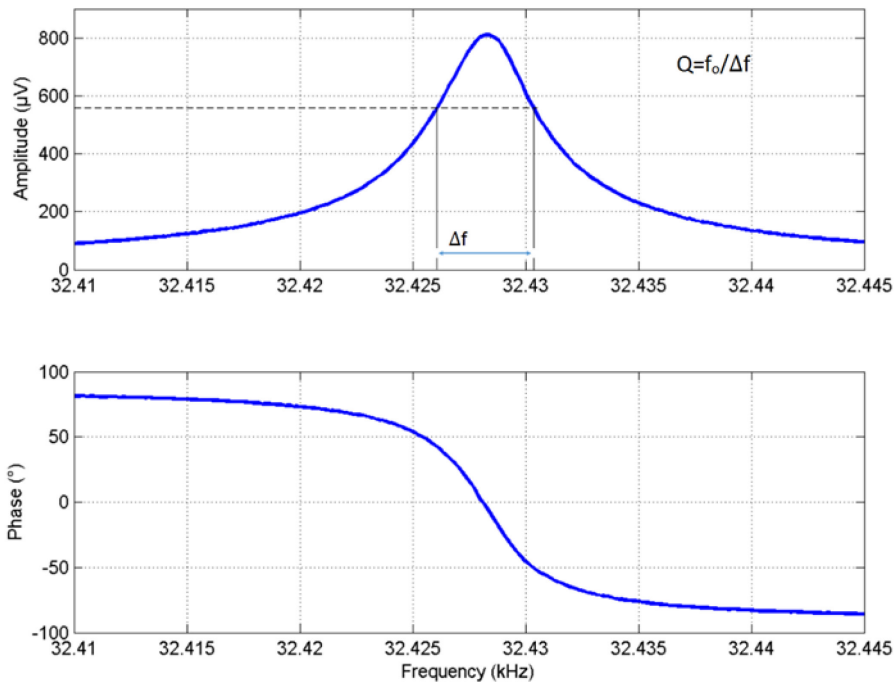
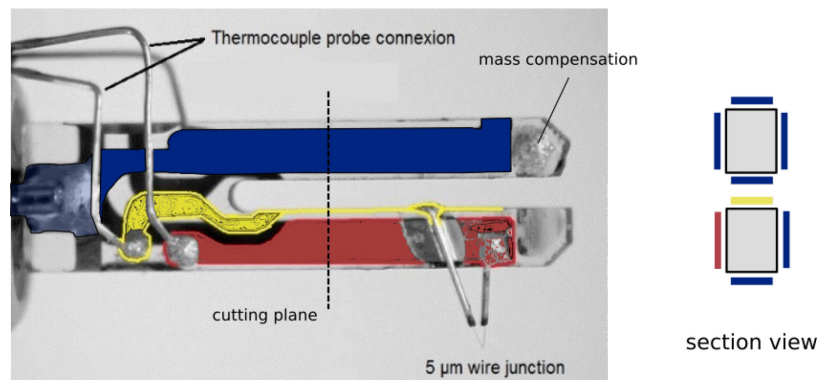


Figure 3-9: Amplitude and phase response of QTF with photo-thermal excitation

Amplitude and phase are given by the lock-in amplifier at certain frequency. The contact detection throughout the scan is commonly done by tracking the phase change (instead of unstable amplitude tracking) of QTF. As seen on the Figure 3-9, the lack of phase rotation compared to an electrical excitation helps to avoid a much more

complicated setup with a double frequency measurements[110]. The anti-resonance and its associated phase rotation are suppressed and possible parasitic capacitance has no effect on measurement chain. Besides, the mechanical drawback is avoided since the resulting quality factor remains in the range 2000 to 8000 depending on the fabrication quality of the probe.

This excitation method is also an advantage comparing to electrical method when integrating a SThM tip. Among the eight available electrodes of a QTF, two electrodes are disconnected and reserved for the thermocouple connections. The photo-thermal excitation doesn't have any influence on the equilibrium of the tuning fork when two faces of the electrodes are disconnected which is not the case for electrical excitation. The bonding area is placed far from the constraint zone of the tuning fork (Figure 3-10) and a mass compensation made by silver is attached on the other prong (without probe) to keep the quality factor as high as possible.



**Figure 3-10: Connection configuration of thermocouple probe attached on the QTF**

The quality factor ( $Q$ ) of the probe can be easily measured using the piezoelectric voltage output when varying the excitation frequency of the modulated laser beam. Figure 3-11 depicts the magnitude and phase of this signal from which a quality factor near 8000 has been calculated for the QTF attached SThM probe.

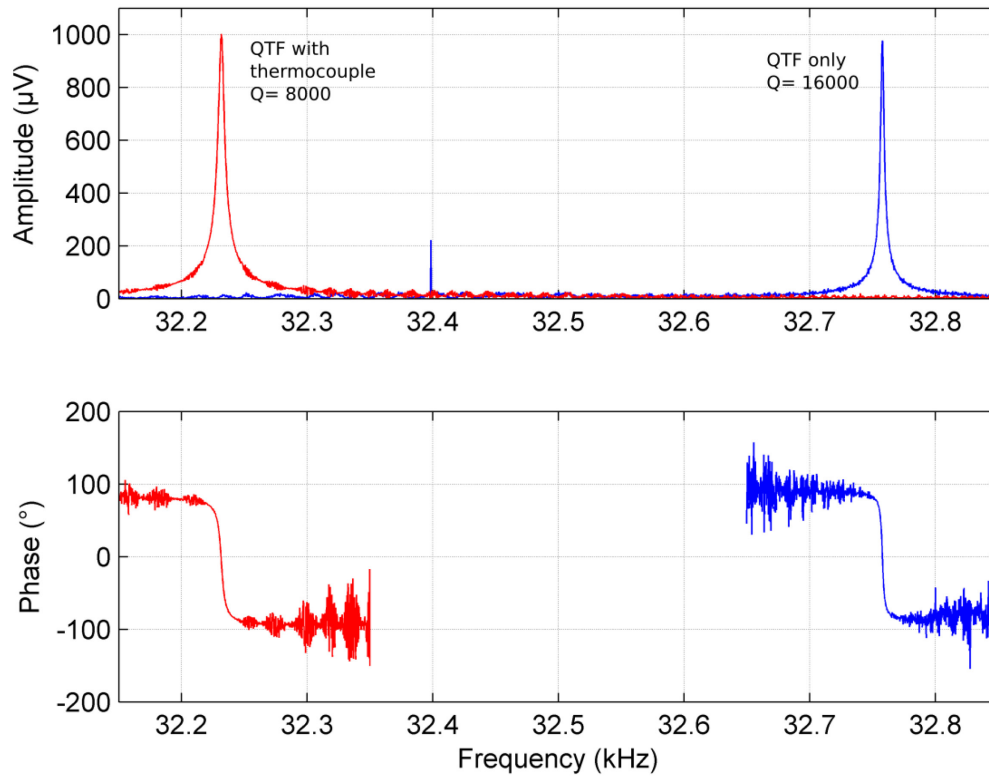


**Figure 3-11: Frequency response of QTF with TC probe attached ( $f_0 = 32232$  Hz;  $Q = 8000$ ) and QTF without TC probe ( $f_0 = 32756$  Hz;  $Q = 16000$ )**

### 3.3 QTF tip-sample contact force model for thermocouple

The main problem of a tuning fork is the quantitative force measurement due to its complicated structure. The tuning fork is a very sensitive force sensor, a very small change in force, mass adding or environment viscosity can influence the result. A realistic model to describe its mechanical behaviour is essential. In this part, a simple effective mass-spring model (in which the spring stiffness is calculated by FEM simulation) is presented then a comparison of this model with a two masses model and FEM model is shown.

#### 3.3.1 Single prong model

- *Dynamic beam model*

The tuning fork can be modelled as a clamped dynamic single prong which is similar to a dynamic AFM cantilever[111],[112]. When the tip is put in contact with the sample, we can consider it as a clamped beam with excitation at one end and a system spring-damping representing probe-sample equivalent stiffness at the other end. This is a well-known model for contact resonance AFM[113], SMM[33].

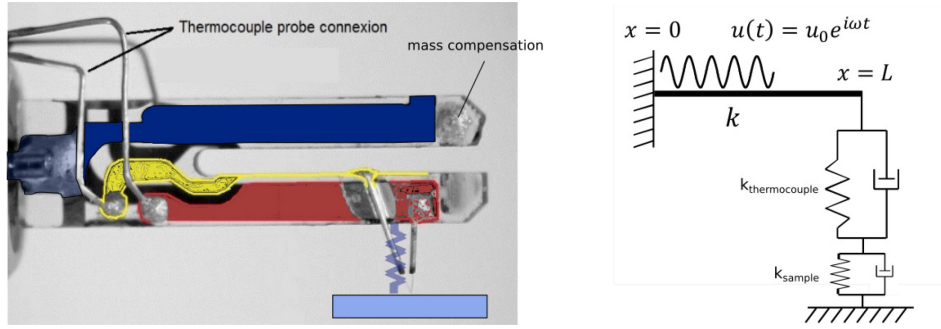


**Figure 3-12: Beam presentative mechanical model when TC probe in contact**

The phenomenon can be described by this equation[114],[103]:

$$EI \frac{\partial^4 y}{\partial x^4} + \eta_{air} \rho A \frac{\partial y}{\partial t} + \rho A \frac{\partial^2 y}{\partial t^2} = 0 \quad (3-1)$$

With the boundary condition

$$y = u; \quad \partial y / \partial x = 0 \quad (3-2)$$

At the base of the beam ( $x = 0$ ) and

$$\partial^2 y / \partial x^2 = 0; \quad EI(\partial^3 y / \partial x^2) = K_{eq} y + \gamma(\partial y / \partial t) \quad (3-3)$$

At the end of the cantilever beam with  $x = L$ .  $E, I, \rho, A$  in the equation are the Young's modulus, moment inertia, density and cross-section of the cantilever respectively. The  $K_{eq}$  is the equivalent stiffness calculated from the thermocouple stiffness  $k_{thermocouple}$  and the sample equivalent stiffness  $k_{sample}$ . The sample equivalent stiffness can be calculated from Hertz's contact[115]:

$$k_{sample} = \sqrt[3]{6E^*{}^2 R F_N} \quad (3-4)$$

where  $R$  is the tip radius,  $E^*$  is the equivalent Young's modulus of the tip and the sample described by:

$$\frac{1}{E^*} = \frac{1-\nu_t^2}{E_t} + \frac{1-\nu_s^2}{E_s} \quad (3-5)$$

In this case, this sample stiffness can be neglected because the thermocouple is much more flexible compared to a hard surface.

$$\frac{1}{K_{eq}} = \frac{1}{k_{thermocouple}} + \frac{1}{k_{sample}} \quad (3-6)$$

The solution of the equation (3-3) gives the displacement at the end of the beam depending on two parameters: contact stiffness  $K_{eq}$  and damping coefficient  $\gamma$ .

$$y_L = u_0 \frac{\alpha^3 EI (\cos(\alpha L) + \cosh(\alpha L))}{\alpha^3 EI (1 + \cos(\alpha L) \cosh(\alpha L)) + (k_{eq} + i\omega\gamma) (\sin(\alpha L) \cosh(\alpha L) + \cos(\alpha L) \sinh(\alpha L))} \quad (3-7)$$

In which the eigenvalues  $\alpha$  is given by this formula:

$$\alpha_n^4 = (\omega_n^2 - i\omega_n \eta_{air}) \rho A / EI \quad (3-8)$$

- *Simplify effective mass-spring oscillator*

This one prong model can be simplified when we consider a harmonic cantilever oscillation and an effective mass-spring system (Figure 3-13).

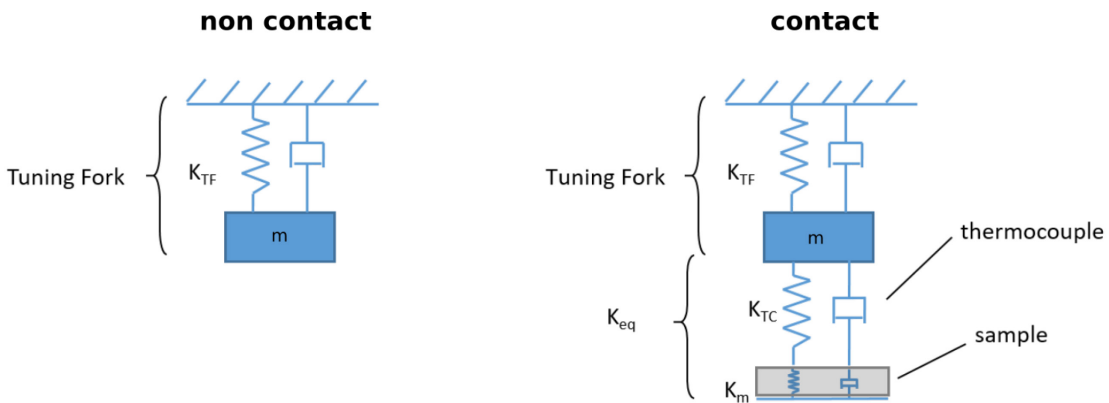


**Figure 3-13: Effective mass-spring model of tuning fork in contact and out of contact with the sample**

The resonance frequency  $f_0$  is calculated from:

$$f_0 = \frac{1}{2\pi} \sqrt{\frac{k}{m}} \quad (3-9)$$

If the oscillation amplitude is small and  $\Delta f$  is small compared to  $f_0$ , we consider that the static force is much larger than the dynamic force. The force gradient or tip-sample stiffness can be therefore derived from the frequency shift as the following equation[116]:

$$K_{eq}(z) = 2k_{TF} \frac{\Delta f}{f_0} \quad (3-10)$$

where  $k_{ts}$  is the force gradient between tip and sample,  $k_{TF}$  is the stiffness of tuning fork sensor,  $\Delta f$  is the frequency shift and  $f_0$  is the resonance frequency of tuning fork without interaction with the sample.

The tuning fork spring value can be determined considering its prong as clamped mechanics beam. The stiffness constant is defined as the following expression:

$$k_{TF} = \frac{EW}{4} \left(\frac{T}{L}\right)^3 \quad (3-11)$$

Applying the tuning fork dimensions  $E, W, T, L$ , the tuning fork spring constant is estimated around 24850 (N/m). A comparison of dynamic beam solution and effective mass-spring approximation has been made using geometry values of tuning fork presented in the Figure 3-14. The result depicts the frequency shift as a function of different tip-sample equivalent stiffness. The small difference in the results shows the validity of the simple effective model.

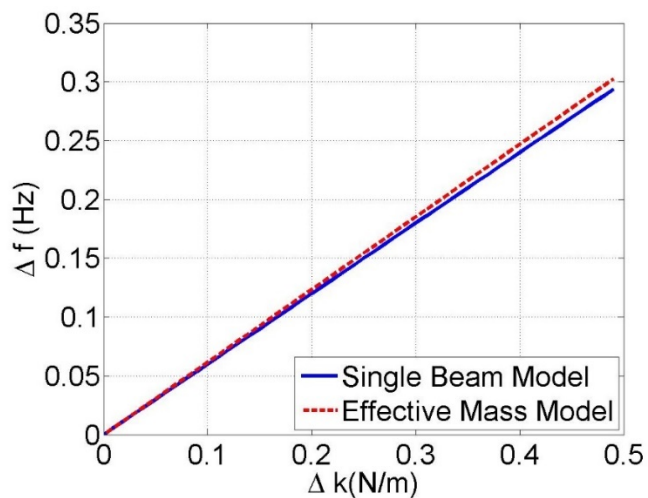


**Figure 3-14: Comparison between a single beam mechanical model and an effective mass model**

From the equation 3-9, we can calculate the coefficient of conversion  $\chi$  that relies  $\Delta f$  to  $k_{eq}$ :  $\chi$  is around  $1.52 N/m.Hz$ . This configuration is broadly applied for any single AFM cantilever or Qplus sensor in which one prong of the tuning fork is fixed. However, to preserve the tuning fork a high Q-factor, the other prong should be free for the equilibrating. The stiffness estimation by single beam formula is not valid anymore[117].

### 3.3.2 FEM simulation and comparison of different models

- *Recalculate prong stiffness*

The frequency shift during the tip-sample interaction can be easily measured using a PLL system. However, the main problem of tuning fork modelling is its calibration of effective stiffness. The calibration of tuning fork spring constant can be obtained by performing static measurement or dynamic experiments (thermal noise[118], adding mass[119]...) or a finite element method (FEM) model. Here, a FEM model is built using COMSOL Multiphysics to simulate tuning fork stiffness. In the present simulation, a 3D model was used. The quartz Young's modulus and mass density given in section 3.2.1 can be found in literatures [92]. The mesh used is automatically built using "fine option" so that maximum and minimum element sizes are around  $468\mu m$  and  $58\mu m$  respectively. As shown in Figure 3-15, the element density of the prongs joining area has been increased since the gradient constraint is here the most important. In the model, the QTF base is clamped, a force  $F = 0.1 N$  is applied at the end of one prong. As the constraint appears mostly on the separate zone between the base and two prongs, the element density is increased on that zone. Simulation result gives a displacement of  $4.865 \times 10^{-6} m$ . This value can be used to modify the stiffness value of tuning fork and recalibrate the force measurement using Hooke's law.

$$F = -k\Delta x \quad (3-12)$$

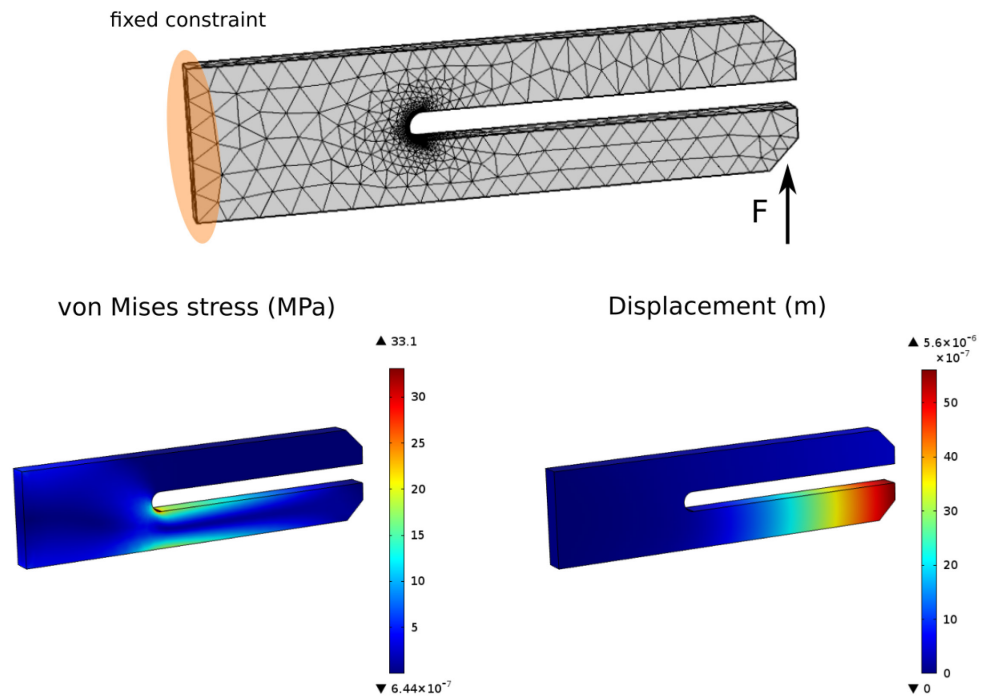


**Figure 3-15: Static mode FEM simulation of QTF**

The stiffness value calculated is about  $20,552 \text{ N/m}$  in static mode. This is around 15% different compared to the value calculated by a single beam formula.

- *Frequency domain simulation*

The eigenfrequencies of the structure are simulated using eigenfrequency mode of COMSOL Multiphysics software. The resonance modes found from the simulation are presented in the Figure 3-16. The two main modes are described in many publications as in-phase mode at 28.399 kHz and anti-phase mode at 32.688 kHz. In “in-phase” mode, the two prongs move in the same direction while in “anti-phase”, they move symmetrically in the opposite direction as seen in the Figure 3-16.

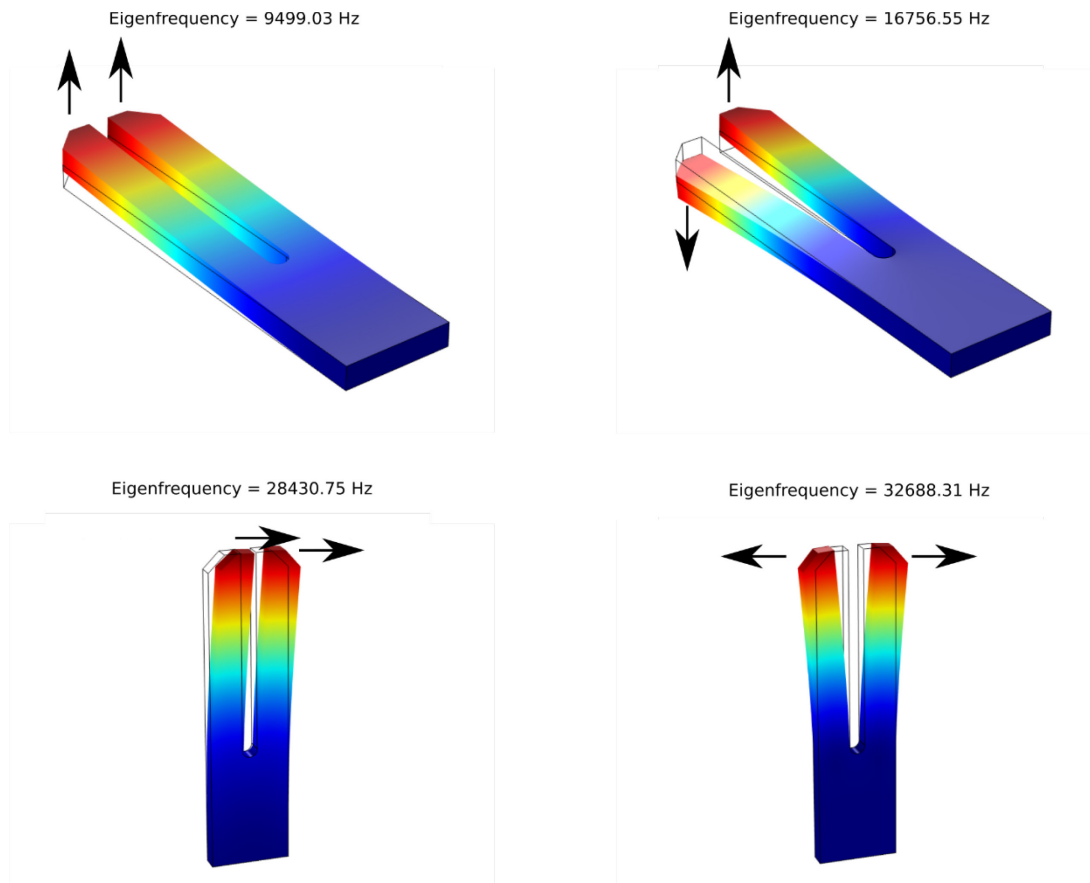


**Figure 3-16: Resonance modes of QTF**

The mode called “anti-phase” at 32,688 Hz is the chosen mode because it generates the strongest electrical response. Actually, this is the equilibrated mode in which the centred mass does not move during the vibration, and therefore preserving the quality factor.

The tip-sample stiffness is also simulated by this FEM COMSOL model in active frequency domain. Instead of a thermo-elastic excitation quite complicated to simulate (comprising photo-thermal and mechanical phenomena), a simplification is made by applying a mechanical vibration (sinusoidal applied force). In her PhD work, Alexia Bontempi measured the tuning fork displacement using an interferometer setup [84]. The calibration coefficient was introduced around  $5.33 \text{ pA/pm}$ . If the measuring device has input impedance of  $10 \text{ MOhm}$ , the coefficient can be converted to  $53.3 \text{ }\mu\text{V/pm}$ .

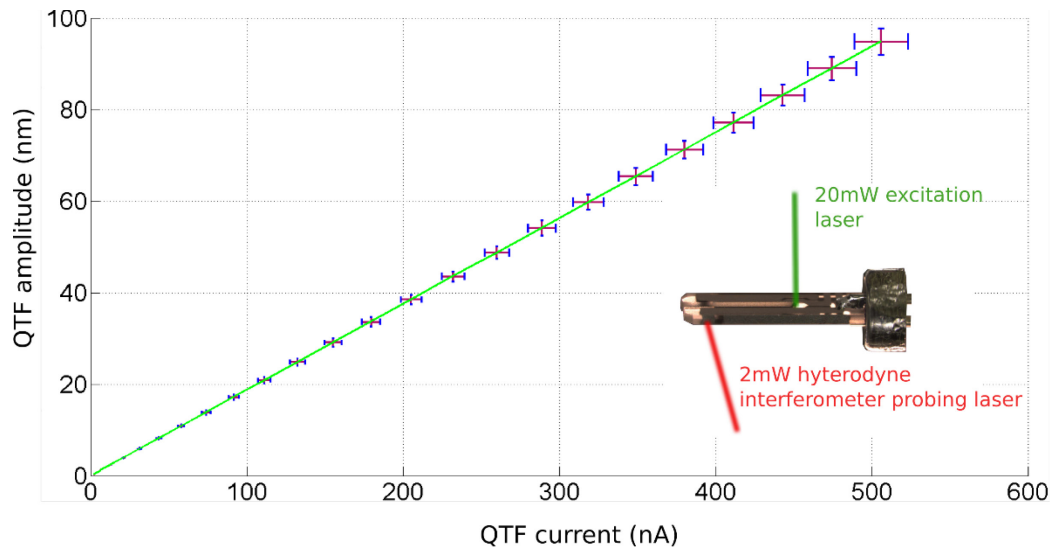


**Figure 3-17: QTF vibration amplitude as function of its generating current[84]**

The amplitude of the excitation force of around 10nN is set so that the displacement amplitude is close to the experimental value around 100pm. The stress and strain in the tuning fork structure are then calculated. It is visible that this tuning fork structure presents three high constraint zones from the base of the two prongs. In fact, the tuning fork can only generate a good electrical response when the laser beam excites on these zones.

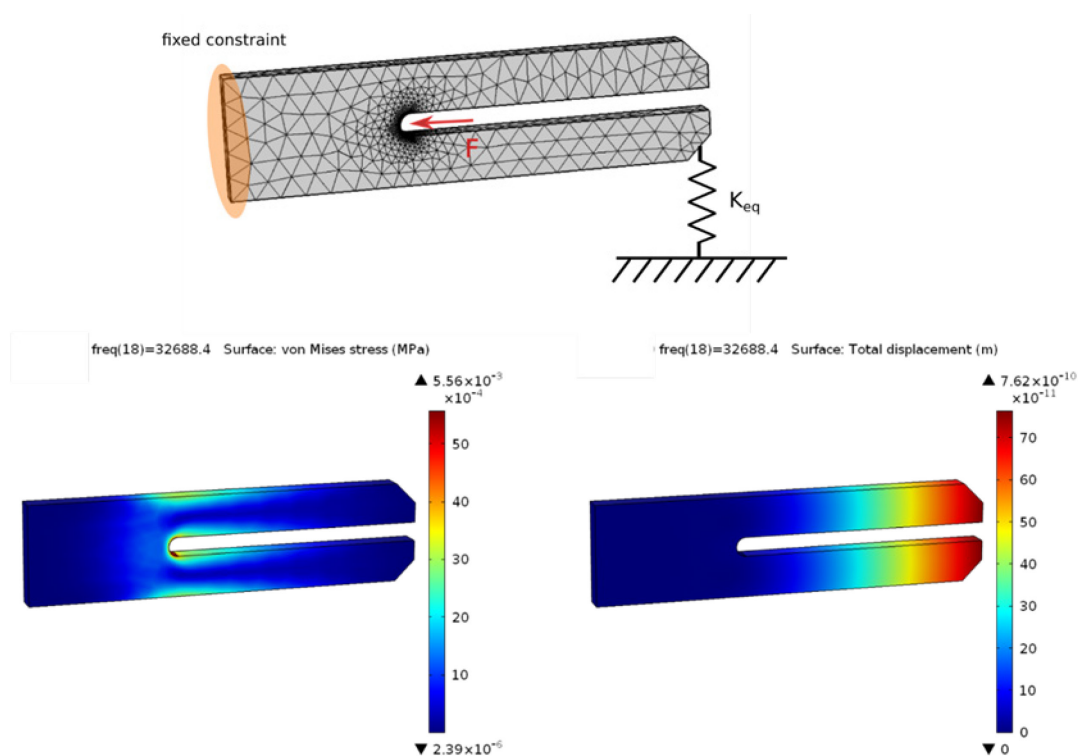


**Figure 3-18: QTF FEM model, stress and displacement results in frequency domain**

To simulate the contact force, a spring is added to one end of the prong representing tip-sample interaction stiffness. A comparison of frequency shift using this FEM model and a very simple effective mass-spring model (using the stiffness correction  $20,552 \text{ N/m}$ ) is depicted in the Figure 3-19. The result shows a difference of more than 100% between the two models. In this simulation, COMSOL parameters remain unchanged except the calculation mode performed in frequency domain.

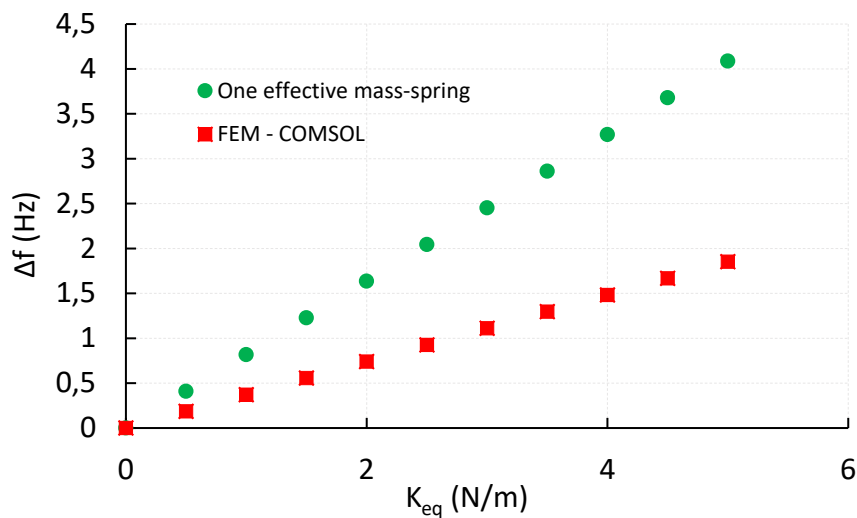


**Figure 3-19: Comparison between FEM model and effective mass-spring model**

The results demonstrate that the simplified one effective mass model does not consider the influence of the other prong of tuning fork which leads to an important error.

### 3.3.3 Two masses model

In the one effective-mass model, the movement of the other beam is not considered. Castellanos and al had also shown that this simplified model can produce an error of more than 100%. They proposed another model which takes account of the symmetrical movement of the other prong[117]. In this model, another virtual spring  $k_c$  and mass  $m$  are added representing the interaction between the two prongs as depicted in the Figure 3-20.

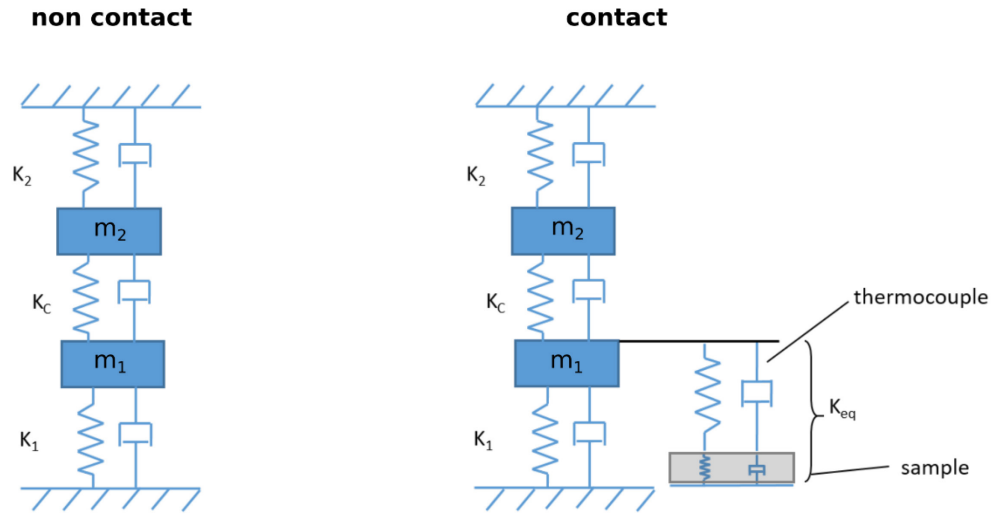


**Figure 3-20: Two effective masses model [120]**

The dynamics equation of the “non contact” system can be written as:

$$\begin{cases} m_1 \ddot{x}_1 + (k_1 + k_c)x_1 - k_c x_2 = 0 \\ m_2 \ddot{x}_2 + (k_2 + k_c)x_2 - k_c x_1 = 0 \end{cases} \quad (3-13)$$

where  $x_1, x_2, \dot{x}_1, \dot{x}_2$  are the position and the acceleration of the mass  $m_1$  and  $m_2$ ,  $k_1$  and  $k_2$  are the stiffness of the tuning fork prongs. The damping parts can be considered as a virtual part of the stiffness. However, these parameters are very difficult to determine. To simplify the calculation, we consider that they have no influence on the frequency shift. Indeed, the damping factors only have great influence on the quality factor. Here, we consider the two prongs are identical which means  $m_1 = m_2 = m$  and  $k_1 = k_2 = k$ . The eigenvalues of this system are calculated using the following terms:

$$\det \begin{vmatrix} k + k_c - \omega^2 m & -k_c \\ -k_c & k + k_c - \omega^2 m \end{vmatrix} = 0 \quad (3-14)$$

The solution provides two values of angular frequency  $\omega$  which represent two resonance modes of the quartz tuning fork.

$$\begin{cases} \omega_{\text{in-phase}}^2 = \frac{k}{m} \\ \omega_{\text{anti-phase}}^2 = \frac{k+2k_c}{m} \end{cases} \quad (3-15)$$

From the eigenfrequencies calculated using FEM model in previous part, we have an “in-phase” mode  $f_0 = 28399.23 \text{ Hz}$  and an “anti-phase” mode  $f_0 = 32671.95 \text{ Hz}$ .

Using the stiffness calculated from the static simulation mode  $k = 20552 \text{ N/m}$ , we can easily obtain  $k_c = 3324.69 \text{ N/m}$  and  $m = 6.44 \text{ mg}$ .

In contact position, an equivalent spring  $k_{eq}$  is added in parallel to the spring  $k_1$  as described in Acosta's thesis[120] for tuning fork force sensor. The modified dynamic equation becomes:

$$\begin{cases} m_1 \ddot{x}_1 + (k_1 + k_c + k_{eq})x_1 - k_c x_2 = 0 \\ m_2 \ddot{x}_2 + (k_2 + k_c)x_2 - k_c x_1 = 0 \end{cases} \quad (3-16)$$

Solving the eigenvalues of this equation system, we obtain:

$$\omega^2 = \frac{2k+2k_c+k_{eq} \pm \sqrt{4k_c^2+k_{eq}^2}}{2m} \quad (3-17)$$

The ratio of frequency square between contact and non-contact modes is written:

$$\frac{f^2}{f_0^2} = 1 + \frac{k_{eq}-2k_c + \sqrt{4k_c^2+k_{eq}^2}}{2k+4k_c} \quad (3-18)$$

The Figure 3-21 described the simulation results of QTF using three different models: one effective mass-spring model, FEM Comsol simulation and two masses model with virtual stiffness between these moving masses. It shows that the results obtained from the effective mass-spring model are very far from the other models. The difference between FEM-Comsol simulation and the two masses model is around 18%.

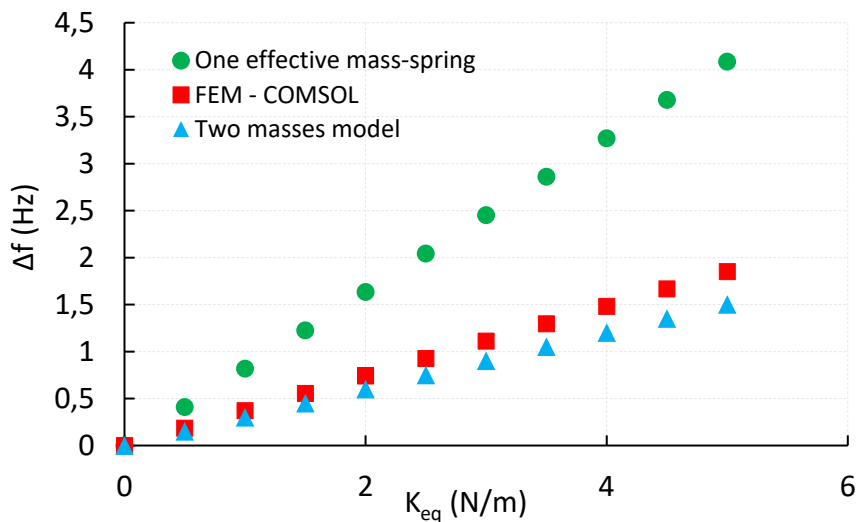


**Figure 3-21: Comparison of 3 different mechanical models for QTF**

The coefficient of conversion  $\chi$  (N/m. Hz) to calculate the equivalent stiffness from the frequency shift is defined.

$$k_{eq} = \chi \cdot \Delta f \quad (3-19)$$

The tip-sample stiffness coefficient results calculated by different models are summarized in the Table 3-1.

Model	Coefficient of conversion
One effective mass	1.52
FEM	2.7
Two masses	3.33

**Table 3-1: Coefficient of conversion frequency shift to probe-sample stiffness values calculated by 3 models**

As shown in the Table 3-1, the result from FEM simulation and the two masses model is close. Consequently, it seems more relevant to choose the coefficient  $\chi = 2.7$  (FEM value) for the QTF as a SThM force sensor in our application from now.

### 3.3.4 Experimental verification

One experimental setup was performed to verify the force measured by a tuning fork. The tuning fork is calibrated using predetermined AFM cantilever stiffness. The QTF with its thermocouple probe is placed on an AFM sample support. It is excited by a 10mW laser beam wavelength of 637 nm (LP637-SF70 Thorlabs). The QTF resonance frequency is tracked by a homemade numerical PLL (Figure 3-5). This PLL consists of a lock-in amplifier (EG&G 5210), a function generator (33220A Agilent) and a feedback digital application on the computer. The computer application receives the phase value from the lock-in amplifier and sends the modified frequency values to the function generator. There is always a trade-off between the tracking speed and the frequency resolution. The resolution of this homemade frequency tracking system is around 0.05 Hz with a tracking speed of about 100 Hz/s.

AFM measurement and QTF frequency shift measurements are performed simultaneously to compare the response. Here, two different AFM cantilevers with

two stiffness are used. The experiments are performed on QTF prong and two different thermocouple probe sizes ( $1.3\mu\text{m}$  and  $5\mu\text{m}$  of diameter).

- *Verification with AFM cantilever stiffness*

The AFM cantilever is firstly put in contact with a QTF's prong (without probe measurement) as described in the figure 3-23. The tuning frequency shift and AFM approach curve are obtained.

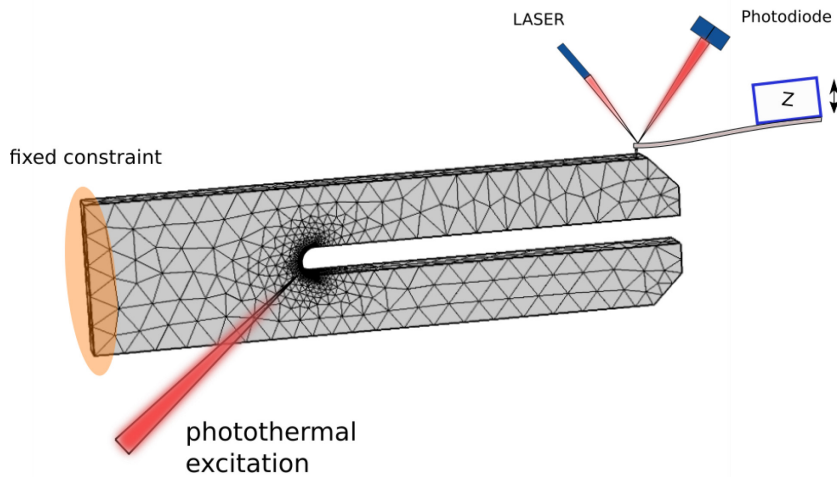


**Figure 3-22: Cantilever stiffness measurement setup using a QTF**

The measurements were made using two cantilevers. The constant stiffness of the first is in the range  $1 - 5\text{ N/m}$ , and the second presents a stiffness in the range  $20 - 80\text{ N/m}$ . These are not reference cantilevers with a precise stiffness value since they are provided by the manufacturer Veeco with a large uncertainty range. Figure 3-23 describes the frequency shift of the QTF when the two cantilevers are put in contact with a QTF prong (Figure 3-22). The error bars are calculated by 30 times measurements in contact and out of contact. Two different force levels (AFM set point) were set to show the influence of the force on the stiffness measurement.

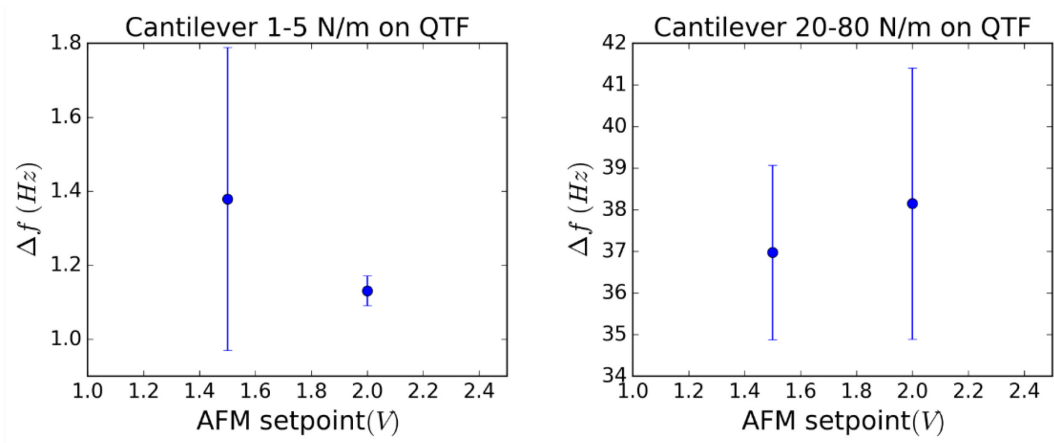


**Figure 3-23: Frequency shift of QTF when AFM cantilever put in contact with a prong a) 1-5 N/m cantilever and b) 20-80 N/m cantilever**

As a result of mechanical theory, the frequency shift is only sensitive to the force gradient which means the cantilever stiffness and not on the force magnitude. The quartz tuning fork measurements are also stable enough considering the standard deviation of the measurements.

The results are summarized in the table below. Cantilever stiffness is deduced using the coefficient of conversion  $\chi = 2.7$ .

Cantilever stiffness	1-5 N/m	20-80 N/m
Frequency shift (Hz)	1 – 1.8	35 – 41
Measured Coefficient $\chi$	1 - 2.8	0.57 - 1.95
Measured stiffness (N/m)	2.7 – 4.86	94.4 – 110.7

**Table 3-2: QTF frequency shift for “1-5 N/m” and “20-80 N/m” cantilever and the calculated stiffness**

The measured stiffness for “1-5 N/m” cantilever is 2.7-4.86 N/m which is in accordance with the value provided by the manufacturer. For “20-80 N/m” cantilever, the measured stiffness is 94.4-110.7 N/m which is outside the range provided by the manufacturer. The results are coherent when comparing measured and Comsol simulated  $\chi$  values. However, the uncertainty range of cantilever stiffness does not give us a more precise value of  $\chi$ .

- *On thermocouple measurement*

The cantilever stiffness measured in the previous part can be used as complement information for the coupling measurement AFM cantilever and thermocouple SThM probe shown in Figure 3-24. The AFM cantilever is now placed directly on the thermocouple tip (Figure 3-24).

The system stiffness  $k_{eq}$  consists of a cantilever stiffness  $k_{can}$  and the thermocouple stiffness  $k_{tc}$  such:

$$\frac{1}{k_{system}} = \frac{1}{k_{can}} + \frac{1}{k_{tc}} \quad (3-20)$$

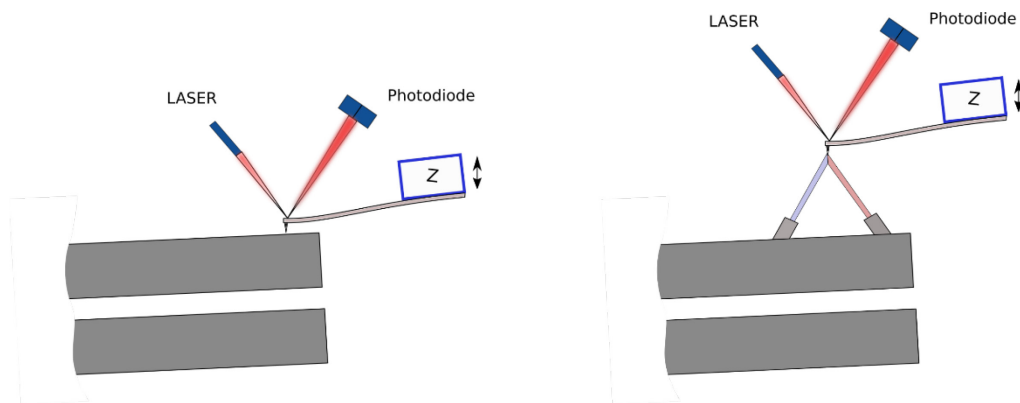


**Figure 3-24: AFM cantilever in contact with QTF and thermocouple probe**

Figure 3-25 shows the approaching curve of 1-5 N/m AFM cantilever on the QTF prong, 5 $\mu$ m of diameter and 1.3 $\mu$ m of diameter thermocouple probe. Concentrating on the linear slope of the curves, the QTF and TC5 (5 $\mu$ m of diameter thermocouple) presents almost the same slope values while the TC1 curve presents a smaller slope (which means lower stiffness). From these curves and the consequence of the equation 3-19, we can also conclude that the measurement is only sensitive when the stiffness values of AFM cantilever and TC probe are closed to each other. The horizontal parts of these curves and the contact zone demonstrate the contact quality between the AFM tip and the sample. For example, regarding the retraction period of the red curve in the Figure 3-25, a mechanical interaction between AFM cantilever and 1.3 $\mu$ m thermocouple probe shows unstable movements when the AFM tip out of contact.

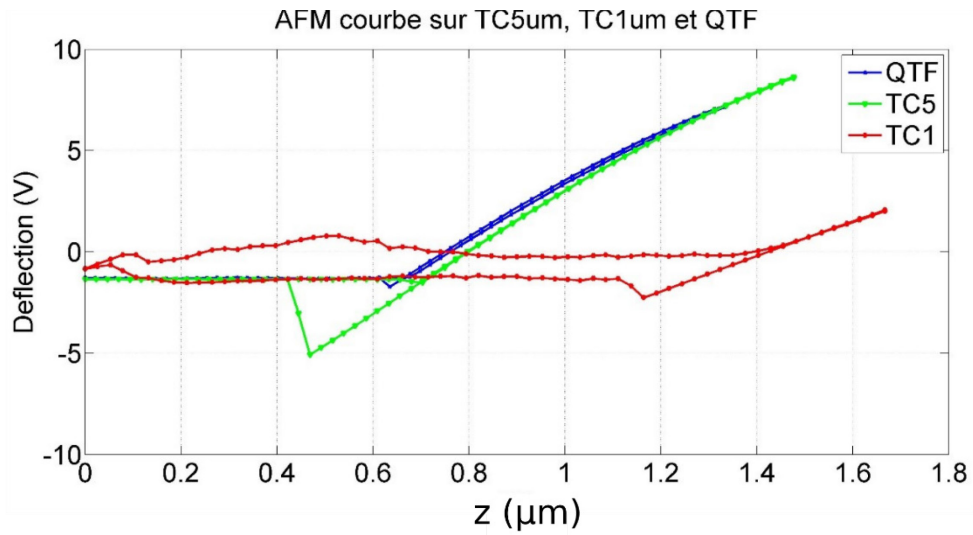


**Figure 3-25: 1-5 N/m AFM cantilever approaching curve on QTF prong, 5µm thermocouple and 1µm thermocouple**

The frequency shift of QTF when 1-5 N/m and 20-80 N/m cantilever put in contact with TC1 probe and TC5 probe respectively are summarized in the Table 3-3. A complementary information is provided when the TC probes are touching a hard surface such as a silicon substrate.

	Cantilever 1-5 N/m	20-80 N/m	Si substrate
1.3 µm TC	0.25 – 0.4 (Hz)	1.1 – 1.2 (Hz)	0.7 (Hz)
5 µm TC	2 – 3 (Hz)	14 – 17 (Hz)	30 – 41 (Hz)

**Table 3-3: QTF frequency shifts with different combinations**

From these frequency values, the system stiffness is converted using the coefficient of conversion from the last part (Table 3-1). The thermocouple stiffness is then calculated from the equation 3-19.

Method	Stiffness measured	TC 1µm	TC 5µm
Cantilever 1-5 N/m	$k_{system} (N/m)$	0.68 – 1.08	7.29 – 8.1
	$k_{thermocouple} (N/m)$	0.91 – 1.8	negative
Cantilever 20-80	$k_{system} (N/m)$	2.97 – 3.24	37.8 – 45.9

N/m	$k_{thermocouple} (N/m)$	3.05 – 3.35	57.4 – 89.3
Silicon substrate	$k_{system} (N/m)$	1.89	81 – 110.7
	$k_{thermocouple} (N/m)$	1.89	81 – 110.7

**Table 3-4: The system equivalent stiffness and the thermocouple stiffness deduced from by 3 different experiments (with 1-5 N/m, 20-80 N/m cantilever and Silicon substrate)**

The stiffness values obtained by three different experiments for the 1.3  $\mu\text{m}$  thermocouple are close to each other. In worst case, around 50% of difference is noticed. In fact, at this scale, many degrees of uncertainty occur such as the contact quality of two objects, the difficulty on positioning, the angle of cantilever... Concerning the 5 $\mu\text{m}$  thermocouple stiffness value, the first measurement using 1-5 N/m cantilever presents a negative value, which can explain the low sensitivity of this coupling (AFM, TC probe) system. Indeed, the cantilever stiffness is much smaller than TC 5 $\mu\text{m}$  stiffness. However, the other measurements using 20-80 N/m cantilever and silicon substrate show rational results, when we have a stiffer cantilever or very stiff surface.

### 3.4 Force calculation using QTF and thermocouple probe

- *Force quantification procedure*

The tuning fork force quantification procedure can be depicted in the Figure 3-26. The PLL input receives the electrical response from the QTF and sends the excitation signal from its output to a laser. It also takes the responsibility for QTF resonance frequency tracking. The frequency shift is sent to the computer and processed by the software. Based on this information, the software makes calculations and gives commands to the piezo stages.

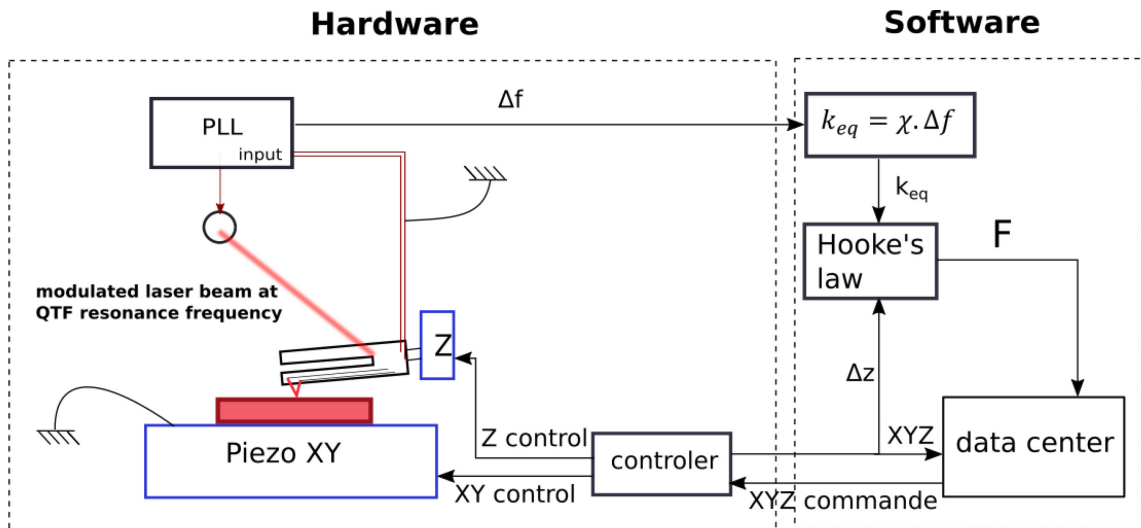


**Figure 3-26: Working scheme of dynamic AFM using QTF**

The extraction of thermocouple stiffness is described in the last section. This information is used as in the Figure 3-26 to calculate the contact force thanks to the Hooke's law.

$$F = k_{eq}\Delta z \quad (3-21)$$

An example result is depicted in the figure 3-27 showing approach curves of a  $1.3\mu\text{m}$  thermocouple on a silicon surface. The QTF thermocouple probe is moved down toward the sample. When the tip jumps in contact with the sample, a QTF frequency step suddenly appears. This represents the abruptly change in stiffness. The probe is then pushed more into the silicon sample. The frequency shift increases slightly due to the tip deformation and the slight change of probe stiffness (remember we consider the thermocouple probe as a spring however this spring may not be perfect). The retraction curve is exactly on the same way of approaching curve. At the beginning however, a hysteresis appears due to the repulsive force. The error bar on resonance frequency has been obtained by recording 30 consecutive values at every 4nm Z step. The error bar of the stiffness and the force plot is calculated by an error propagation method. These force values are indicative as explained in the previous section since many influencing factors occur. At the present, we still do not have an effective tool for an adequate force calibration, such as a high precision microbalance or a calibrated reference cantilever.

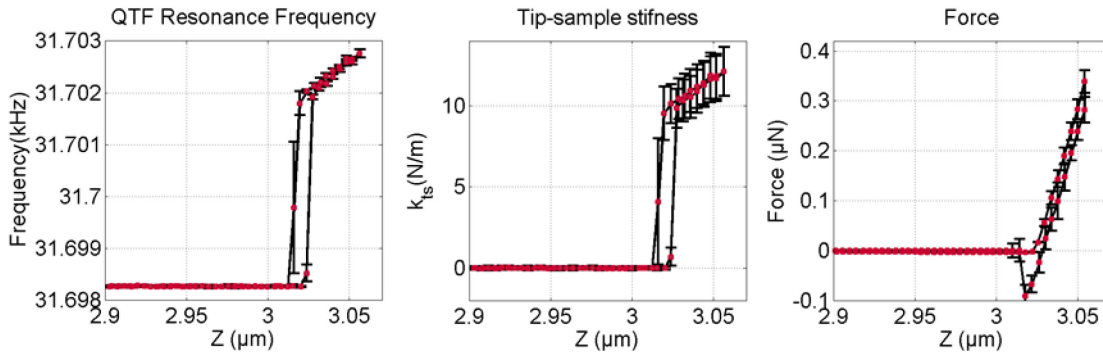


**Figure 3-27: Approach and retraction curve of a 1.3 μm thermocouple on a Silicon substrate**

### 3.5 Second version of SThM system

The new design with massive massive aluminium structure allows increasing the mechanical stability as well as thermal stability. The new system associates horizontal X-Y piezo-actuators (PI P-542.2 XY) with a very high resolution (0.4 nm) movement on which samples are placed. The probe holder is fixed on an independent Z axis, a piezo-actuator PI P-753 with a very high resolution of 0.05 nm (see Figure 3-28). These piezo stages are equipped of capacitive positioning sensors which provide a very high stability, and are controlled through a digital controller (PI E-727.3). The large course stepper motors of 25 mm (PI VT-80) on XY axis and on Z axis (PI M-112) are equipped for the probe prepositioning. These motorized stages can be used for a large scale scan, up to several millimetres.

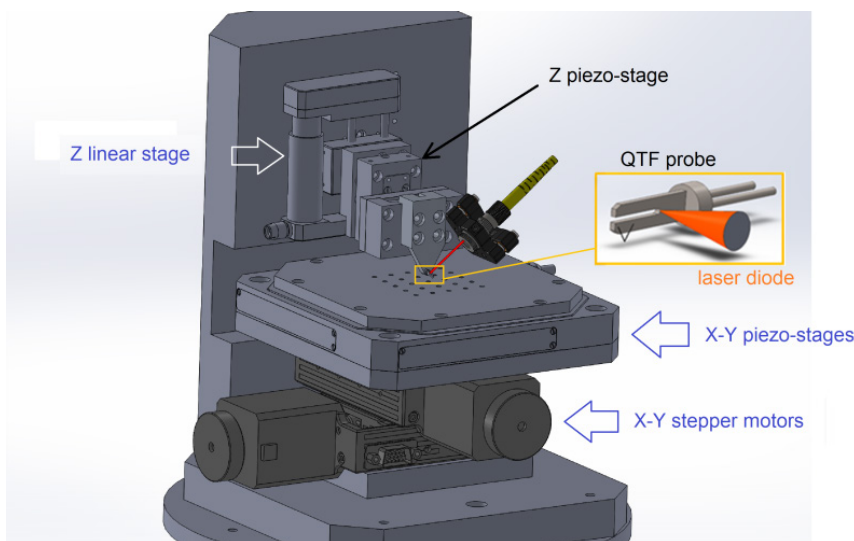


**Figure 3-28: 3D view of the second generation FEMTO-ST SThM system**

Since the system is more compact with an overall size of 140x140x250 mm, a major evolution of the setup is given by the possibility to operate in a vacuum chamber (Figure 3-29). The chamber is connected to a vacuum pump which can attend 1Pa level. The whole microscope and vacuum chamber is placed on a suspended air compression table for mechanical stabilization and vibration filtering.

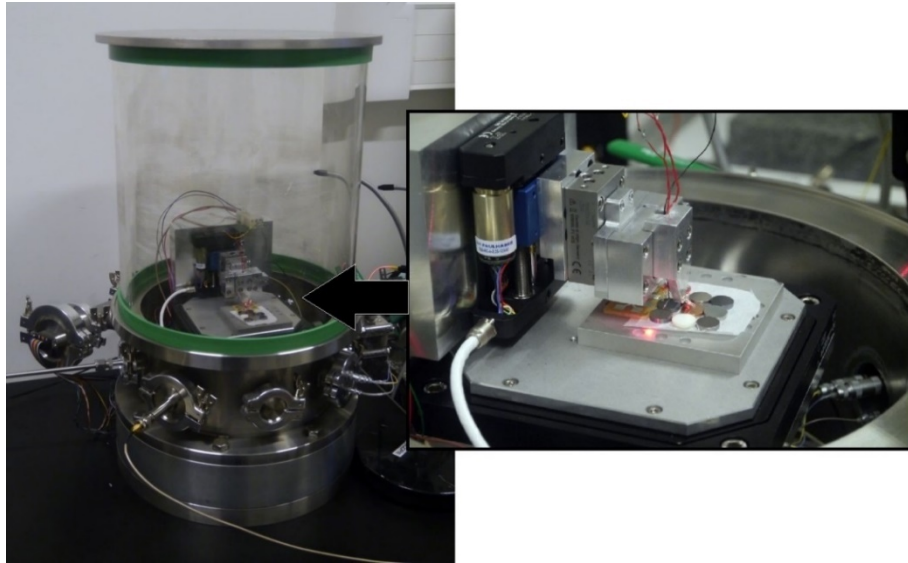


**Figure 3-29: FEMTO-ST SThM system in its vacuum chamber. Close view of the probe holder and samples**

The experimental setup is presented in Figure 3-30. A laser beam is modulated at the QTF resonance frequency and focused on its prongs base area. The dissipation of heat generates an elastic wave due to photo-thermoelastic conversion. Subsequently, piezoelectric conversion provides a voltage which is demodulated by a lock-in amplifier. Magnitude and phase signals are extracted at the same frequency. A PLL for QTF resonance frequency tracking can be a combination of this lock-in amplifier (E&EG 5210) and a function generator (33220A Agilent) for which a numerical PID feedback loop is programmed to lock the oscillation phase by modifying the oscillation frequency. A commercial PLL Zurich Instrument (HF2LI), which has a faster tracking speed, is planned to be used.

As mentioned previously, the SThM thermocouple probe can work in passive and active modes with two different configurations as in the Figure 3-30 and Figure 3-31. The positioning system (piezo actuators and QTF contact detection) takes the responsibility of scanning or force control for geometrical information. In passive mode, a power current is supplied to a heat-able sample, the Seebeck voltages can be measured using a nanovoltmeter Keithley 2182. The temperature is then converted from these voltage values.

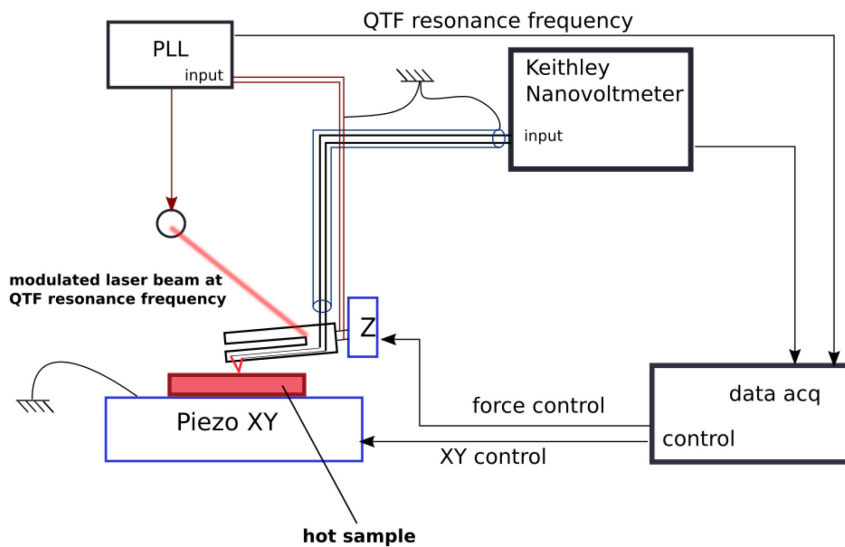


**Figure 3-30: Passive mode configuration**

In active mode ( $2\omega$ ,  $3\omega$  method) described in the Figure 3-31, samples used are passive (ambient temperature) whereas the thermocouple is heated with an AC current at frequency  $f$  by a current source. Then, different electrical harmonics ( $2\omega$  and  $3\omega$ ) are measured by lock-in amplifiers SR850. When the contact occurs, the probe's temperature is affected by the thermal conductance with the sample surface, notably related to its thermal conductivity. The wire connections are protected from electromagnetic field by metal cover which is connected to the ground.

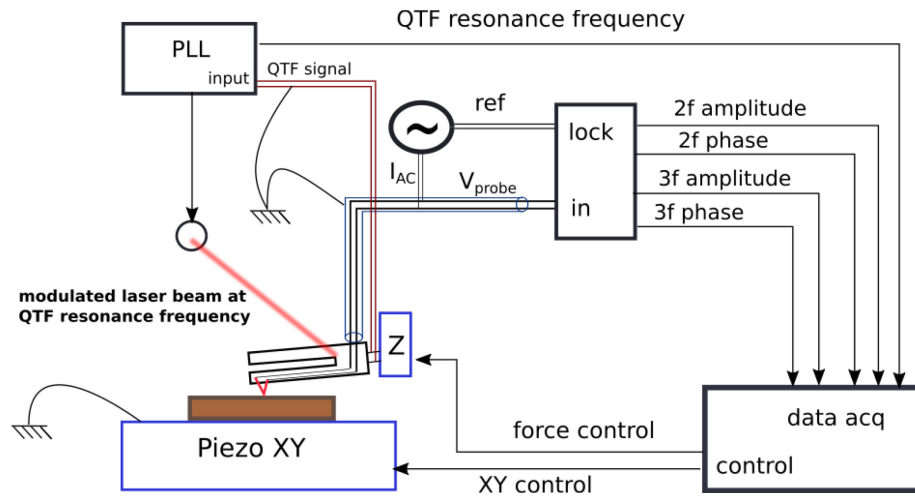


Figure 3-31: Active mode configuration

- Software interface and testing

The whole system is controlled automatically via a computer using a homemade Visual Basic Application. This gives a free access to any information or programs any complicated task that a commercial SPM is not able to provide.

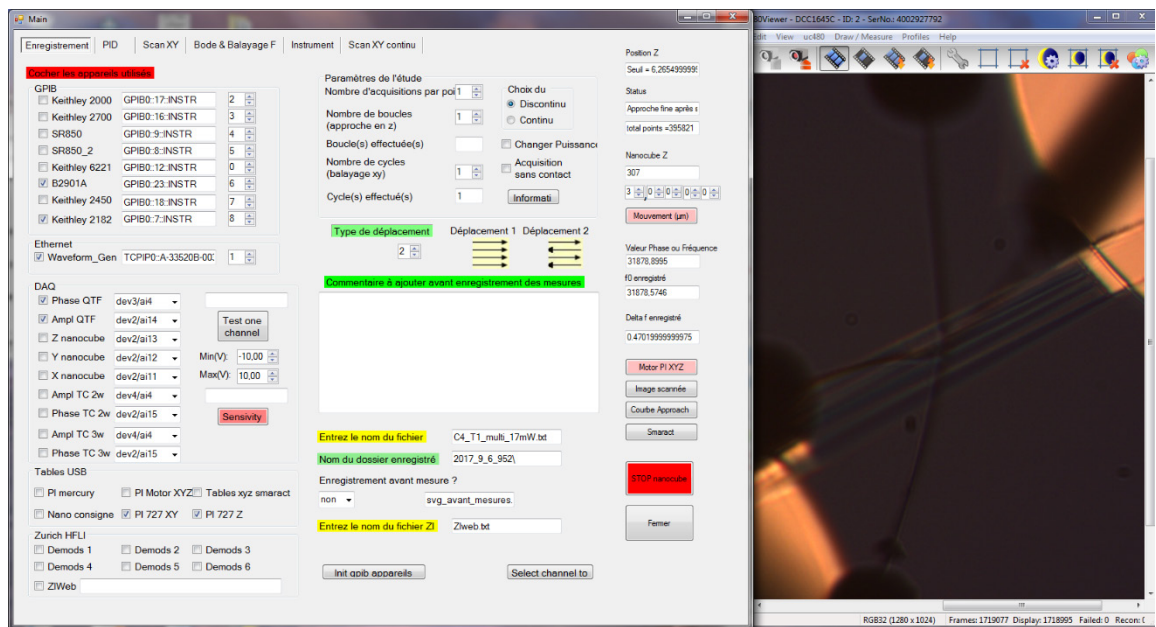
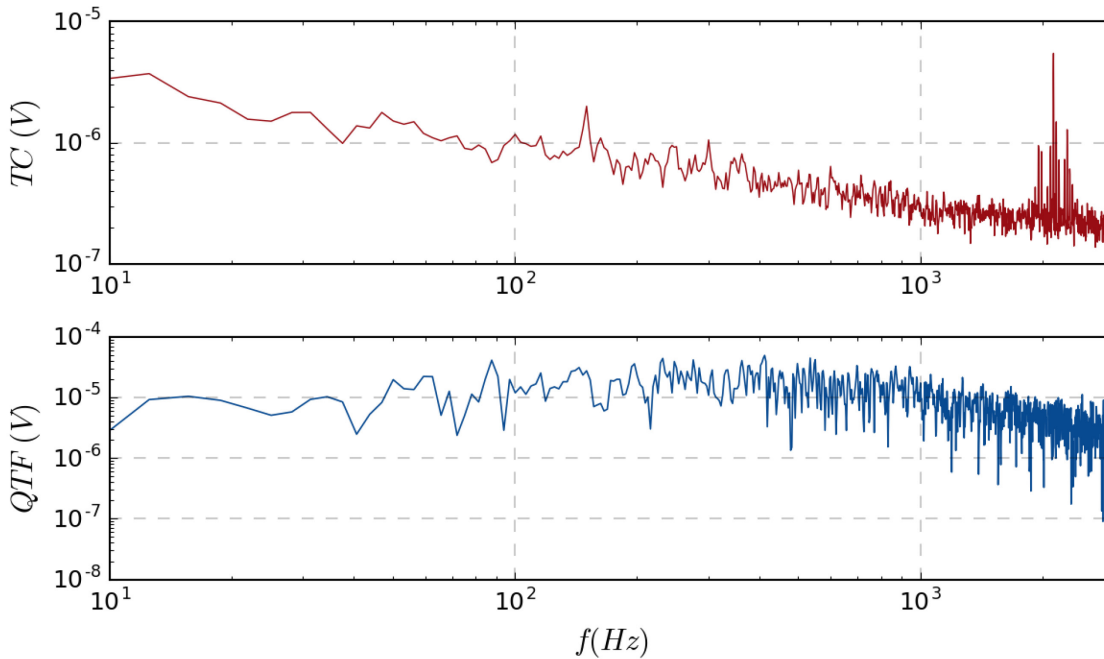


Figure 3-32: SThM Application Interface

To evaluate the system performance, the ground noise of thermocouple and QTF is measured as shown in the Figure 3-33. At low frequency the noise level of thermocouple is around  $1\mu\text{V}$  (which can be converted to 0.2K of temperature resolution) at 100Hz while the noise level of QTF possesses one higher order magnitude at around  $10\mu\text{V}$ .



**Figure 3-33: Noise measurements of thermocouple at low frequency**

It is necessary to isolate electrically the QTF electrodes from thermocouple connectors in order to reduce resistive and electronic noise of the connected apparatus. As presented earlier, the photothermal excitation on QTF has shown many advantages, notably the possibility to suppress some QTF's electrodes without affecting the piezo-electrical signal level.

A new probe design has been made as depicted in the Figure 3-34. The first design (Figure 2-30) used a common connector between thermocouple and QTF. In the new probe version, we have separated thermocouple connectors from QTF. Each are electrically connected with a dedicated electrode to minimize the embedded mass and then keep the QTF quality factor high enough, equaling 10000 in air and 25000 under vacuum. Probe tip distance to QTF's prong is also increased (around 1 mm) to reduce the thermal perturbation between the QTF's prong and the sample.

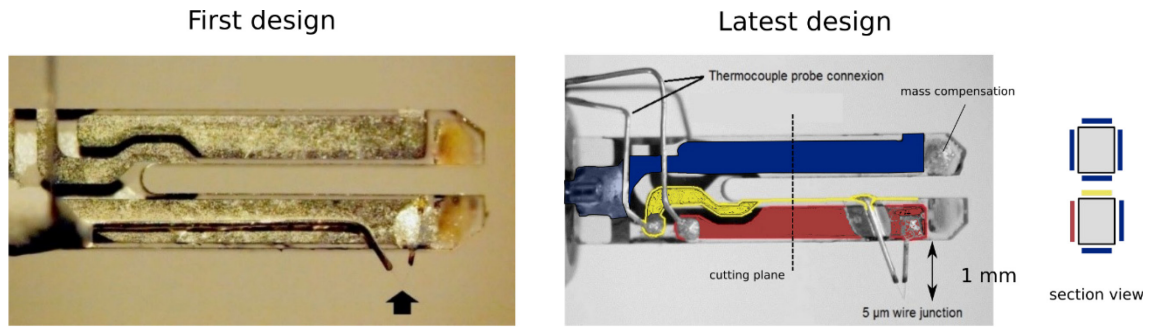


**Figure 3-34: Quartz resonator (QTF) with its thermocouple probe new design**

The probe stability under laboratory environment has been tested in active mode (Figure 3-35). The  $2\omega$  thermal signal is measured using a lock-in amplifier mean while the ambient temperature is recorded using a Pt1000 sensor. The results in Figure 3-35 represent a long-time measurement of 86 hours (5220 minutes). In this 3-days measurement, the ambient temperature depicts 3 periods with a small shift of around 0.01K/hour. There is a correlation between  $2\omega$  voltage and the temperature of laboratory environment. The standard deviation of  $2\omega$  voltage is measured around  $0.19 \mu\text{V}$  (about 0.03 K) while the difference between the maximum and the minimum values is around  $1\mu\text{V}$ . This proves a very high thermal stability and low noise of the whole system and laboratory environment.

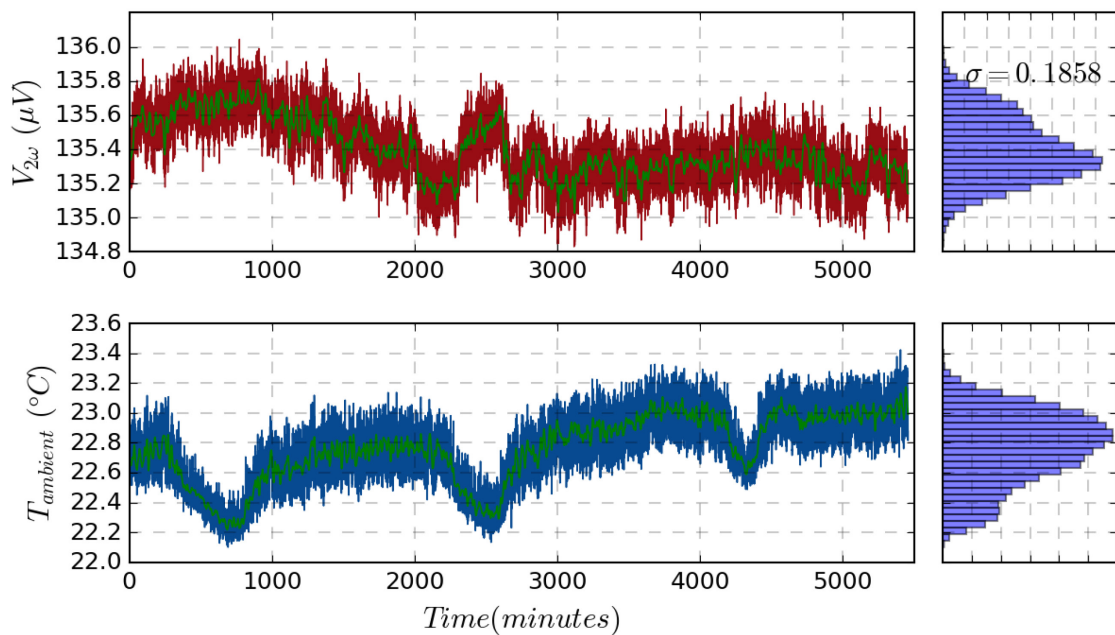


**Figure 3-35: Static stability probe testing**

- *Dynamic AFM demonstration*

Unlike conventional AFM in which the force relates directly to the measured cantilever deflection, the QTF frequency measurement can only extract the tip-sample stiffness information (force gradient  $\partial F/\partial z$ ) which is indirect and not linear as the force function. Complement information on the deflection  $\Delta z$  is needed (equation 3-20). It is a very difficult task to provide this deflection information and maintain a stable contact at the same time especially when the surface is not smooth and the profile changes abruptly which can easily influence the tip-sample stiffness.

Here, every topography scan performed by this system is discontinuous which means that the probe must be brought to contact and out of contact after the measurement for every pixel. This limits the scanning speed. However, this technique can protect the probe from damage.

When the probe approaches the sample surface, the contact sign is set once the QTF frequency value increases higher than the set point value ( $f_1 > \text{set point } f$ ) Figure 3-36. The set point is chosen so that it is a lot smaller than the typical shift value. Right after the contact, the probe is pressed a little more into the surface which can be considered as a deflection  $\Delta z$  for force calculation.

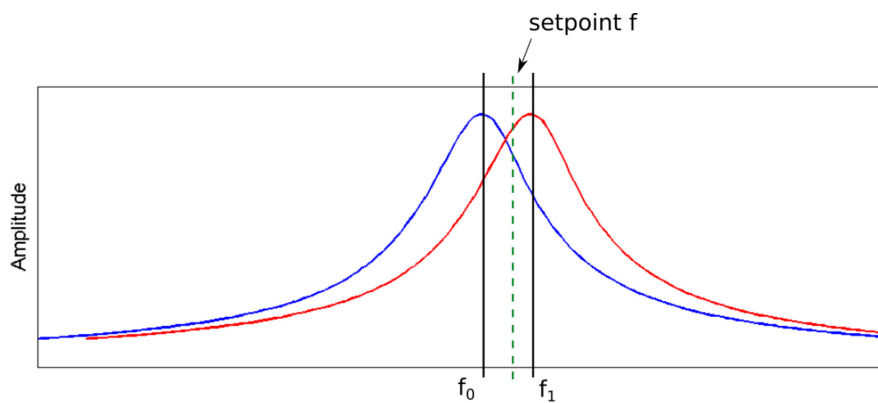


**Figure 3-36: Contact detection principle**

A topography scan demonstration is shown by making measurements on a thin film device using a thermocouple tip. The device is composed of thin film structure with different altitude layers. This device will be used for thermal calibration and described in the next chapter. On the Figure 3-37, the white layer structure is made of platinum

thin film. The bigger structure in pink is also platinum thin film deposition but buried in a Silicon Nitride membrane.

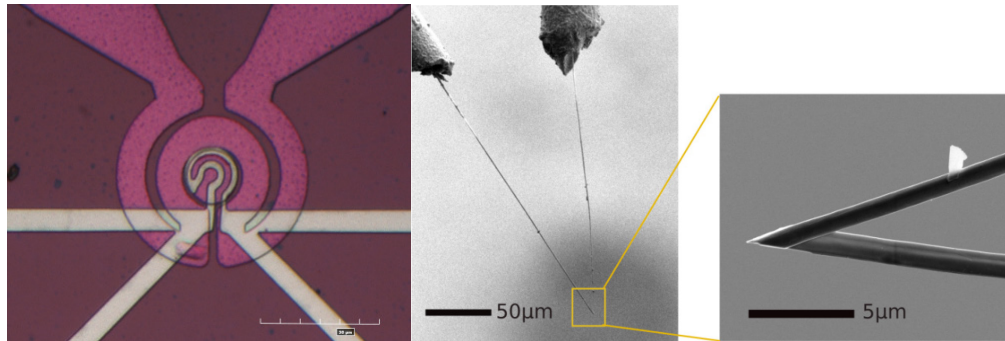


**Figure 3-37: Device structure and scanning thermocouple tip**

Every layer has its own height level; a demonstration scan on this surface shows the device structure consisting of different layers at difference heights. The image resolution depends on the mechanical stability, the sensitivity of the QTF and tip system but here mainly on the probe stiffness and the tip size.

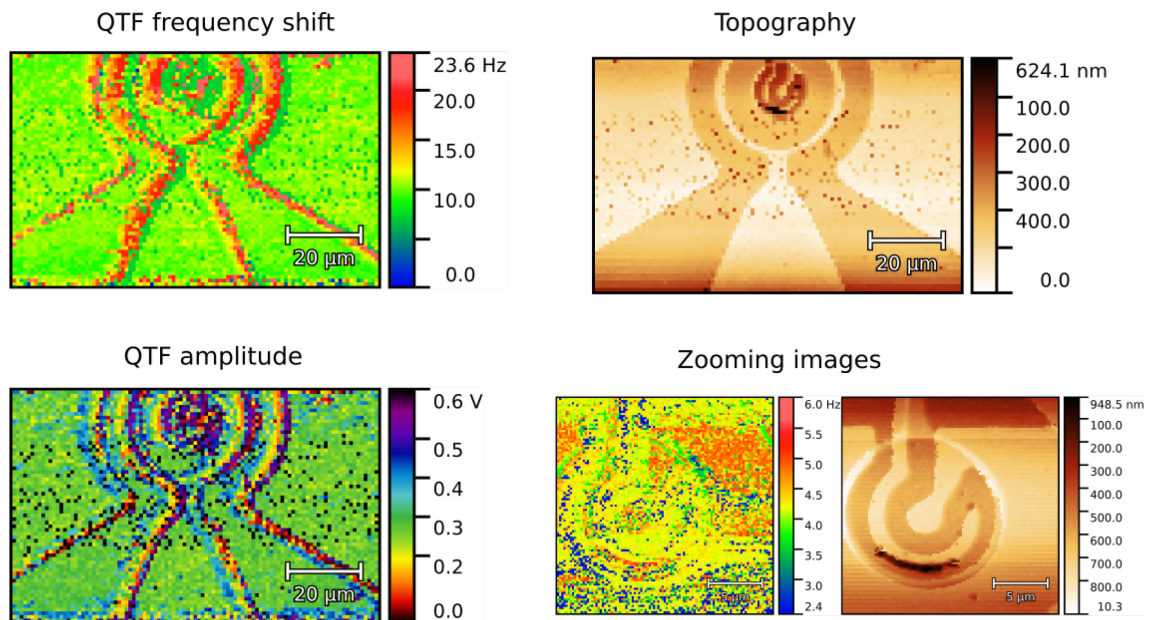


**Figure 3-38: Dynamic AFM measurements using QTF and thermocouple tip**

In addition to topography, images from QTF signal such as its resonance frequency and its oscillating amplitude also depicts the mechanical interaction between the probe and the surface. While the frequency shift shows the stiffness information between the tip and the sample, the amplitude image depicts the damping behaviours. This shows also the mechanical properties of the tip-surface coupling system although not very clearly. As seen in the Figure 3-38, the boundary between the layers appears due to artifacts where mechanical properties differ from smooth areas. Moreover, the difference of mechanical properties between the different materials is vaguely distinguishable (Figure 3-38 zooming images).

### **3.6 Summary**

This chapter has presented the control of the contact force, which is one of the most important parameters in SThM technique. The quantitative force measurement using QTF can be done by measuring its frequency shift and deflection. A dynamic AFM using photothermal excited QTF has been developed toward the SThM purpose. A FEM force model has been developed, however the real case presents many more complicated phenomena (nanoscale friction, tip angle...). A more sophisticated force calibration setup should be developed in order to calibrate the QTF force sensor behaviour. Through the chapter, the whole microscope system is also presented, with the hardware and the developed software.

# 4 TEMPERATURE MEASUREMENT AND CALIBRATION

## 4.1 Introduction

As mentioned earlier, one of the most important applications of SThM is mapping the temperature of the heated surface. In the last chapters, we described the SThM systems: the development (conception, basic theory, measurement system) and all necessary conditions (force control, environment control, nanoscale displacement). In this chapter, the passive mode that allows to measure temperatures using the thermocouple probe is studied and discussed. This measured temperature is only a manifestation of sample temperature through a tip-sample heat transfer theory [35]. The actual sample temperature is therefore hard to determine. As a result, a series of probe calibration and evaluation devices based on different principles have been developed to estimate the difference between tip and device surface temperature. Micro-hotplate devices made of a platinum heater suspended on a thin silicon nitride ( $\text{SiN}_x$ ) membrane integrating specific features for SThM calibration have been designed. An evaluation using different probes, controlling parameters is proposed. High temperature, large size and small size scans are performed to show the versatility of this microscope. Finally, a study of lateral resolution is also presented using a thin Platinum line of 600nm width with 1.3 $\mu\text{m}$  and 5 $\mu\text{m}$  thermocouples, illustrating the influence of the probe size notably.

## 4.2 Small scale temperature measurement

### 4.2.1 Temperature measurements

The first demonstration was made on an electrothermal low power consumption device (micro-hotplate) which is composed of a thin insulating membrane of silicon nitride (500 nm thick) and a 150nm suspended platinum heater. Hotplates are used for different types of microsystems such as actuators, flow sensors, gas sensors[121],[122]. Figure 4-1 presents the sample side view with the probe setup (a) and a top view of the platinum heater on the silicon nitride membrane (b). The platinum heater is supplied with a DC current. The probe is operated in passive mode (measuring the Seebeck voltage without current excitation). A scan is performed on the membrane surface (1mm x 1 mm) to extract a temperature map of the whole device surface.

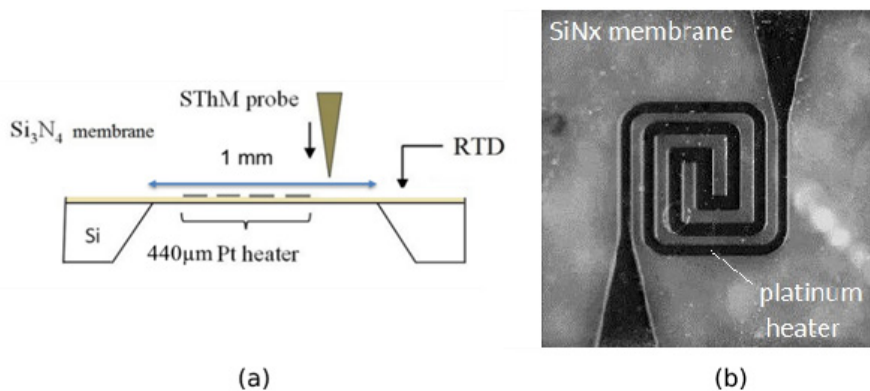


**Figure 4-1: Side-view (a) and top-view (b) of the micro-hotplate**

Absolute tip temperature is obtained using the S type thermocouple Seebeck conversion law. The temperature map of the device and the topography obtained (Figure 4-2) when the heater operates have shown the sensitivity of a QTF in terms of force detection and the high stability of the thermocouple at very high temperature ( $\sim 400^\circ\text{C}$ ). As presented earlier, the tip temperature is not the actual temperature of the surface. The SThM measurements need calibrations tools for small scale measurement. During the contact, different temperatures are involved due to the heat sink effect of the probe and the different thermal resistances encountered. In fact, the probe-

sample system thermal resistances must be considered. The temperature results of the scan need to be corrected or at least evaluated.

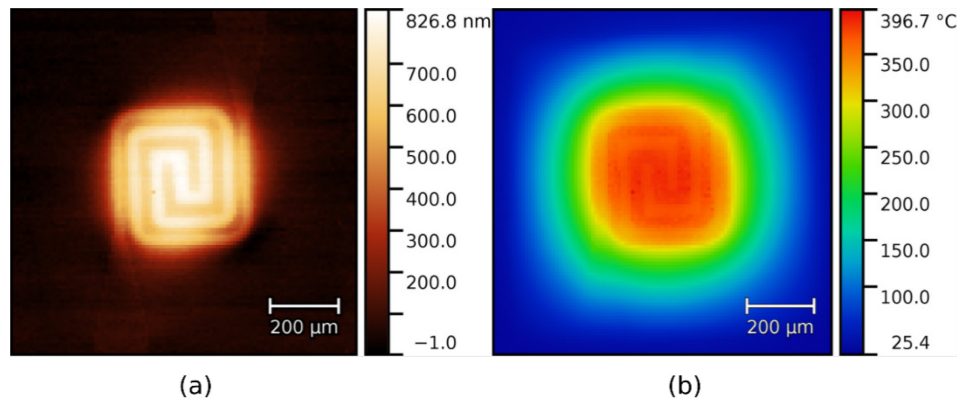


**Figure 4-2: Topography (a) and surface temperature map (b) of active micro-hotplate supplied with a DC current of 17mA (47mW)**

#### 4.2.2 Thermal configuration

When measuring a surface temperature by contact with any SThM probe, various thermal effects are encountered. Figure 4-3 shows the temperatures at different locations when the probe is in contact with a surface at thermal equilibrium:  $T_s$  is the actual surface temperature (before contact),  $T_m$  the modified temperature after contact, underneath the probe tip,  $T_p$  is the temperature measured by the probe and  $T_a$  is the ambient one.

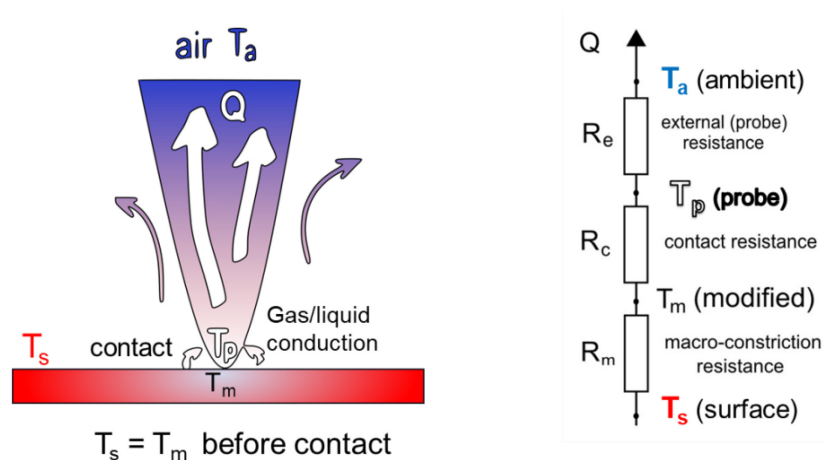


**Figure 4-3: Tip-sample thermal configuration**

According to the heat flux that is dissipated from the surface to ambient through the tip, during the measurement, any probe provides a value that relies on its own characteristics ( $R_e$ ), the tip-to-surface contact ( $R_c$ ) and the surface disturbance effect ( $R_m$ ) which is analogous to the usual macro-constriction effect[35],[51].

In order to characterize any SThM probe, two parameters can be used. The first represents the “thermal response” and is defined by the expression:

$$\tau = \frac{T_p - T_a}{T_s - T_a} \quad (4-1)$$

The second is expressed by a ratio:

$$\phi = \frac{T_m - T_p}{T_p - T_a} \quad (4-2)$$

The  $\phi$  ratio gives an indication of the contact quality of the tip probe since it is related to the contact thermal resistance between the tip of the probe and the surface [51]. The measurement of these ratios gives a first quantification of the probe quality in terms of measurement error. A perfect SThM probe should exhibit a thermal response  $\tau$  equal to unity since  $T_p$  and  $T_s$  are equal, whereas the  $\phi$  ratio should be null (negligible contact resistance). The thermal response  $\tau$  corresponds to a correction factor related to the coupling effects between the probe and the considered sample surface.

In order to monitor and calibrate the SThM probe/surface interactions in temperature measurement mode, active calibration samples are required. The calibration methodology was already presented using standard hotplates not specifically designed for that purpose[51]. We will report in the next parts on optimized devices with low power consumption and integrated temperature sensor to precisely adjust and measure temperature on a localized area on which the probe tip is put in contact. These calibration devices are dedicated to estimate the thermal resistance between the SThM tip and hot surface contact and to evaluate the perturbation induced by the probe on the heat dissipation when the contact measurement is performed.

## 4.3 Temperature calibration devices

We report here on silicon micromachined heating devices fabricated at “Ecole Polytechnique Fédérale de Lausanne”, Switzerland (EPFL) by E.Lemaire and D.Briand which are adapted for metrological study and calibration of SThM probes and operating at high temperature. Their complete thermo-electro-mechanical characterization was performed. The devices operate at low power, 8 mW to reach 300°C for the most efficient design, and they can be powered at least up to 500°C. Their membranes remain mechanically stable, with no significant deformation occurring, up to 250°C. We have specifically designed two types of devices: the first one implements a localized resistive temperature sensor (RTD) on the heating surface and the second one consists of standalone platinum membranes in the centre of the heated region. A membrane only made of platinum was implemented to facilitate the calibration by optical thermography. Although a contact area remains quasi-punctual (some tens of nanometres square), the resulting thermal perturbation area is much larger[83], a localized area of  $10 \times 10 \mu\text{m}^2$  can be used therefore to directly derive the temperature of a perturbed area below the probe tip. In the first concept (RTD device), a localized resistive temperature detector (RTD) quantifies the relative temperature decrease that occurs when the SThM probe is in contact with the RTD surface, acting as a heat sink. Both measurement concepts are dedicated to calibrate SThM probes and to quantify the heat flux and temperature accurately. The functionality of both calibration platforms was demonstrated by coupling SThM, RTD and infrared measurements.

### 4.3.1 First generation device RTD and OPT

#### 4.3.1.1 Device design

For the first design (called “RTD Device”), the platinum RTDs have been patterned using UV (RTDuv) and e-beam lithography (RTDeb). Due to its spatial resolution, the latter technique allows to fabricate RTDs with a higher resistance value per area and therefore with a higher sensitivity. The second design (called “OPT Device” for Optical thermography) implements standalone and thin (about 150 nm- thick) membrane of platinum (Pt) located in the middle of suspended silicon nitride membrane.

When the SThM probe is approaching the platinum hot membrane, the influence of the SThM probe on the temperature distribution of the membrane can be observed using near-infrared thermography. The RTD integrated on the heated surface of the RTD device allows measuring the local temperature. This measured temperature value corresponds to  $T_s$  when the tip of the probe is not in contact and  $T_m$  when it is in contact.

The designs and dimensions of the calibration chips are detailed in Figure 4-4. The designs were developed to have a simple fabrication process, when using standard photolithography, one patterning step for the heater together either with the RTD or the standalone Pt membrane. Figure 4-4 presents the cross-sections of the devices (Figure 4-4a and Figure 4-4c), the designs of the RTDs (Figure 4-4b) and of the standalone Pt-membrane (Figure 4-4d).

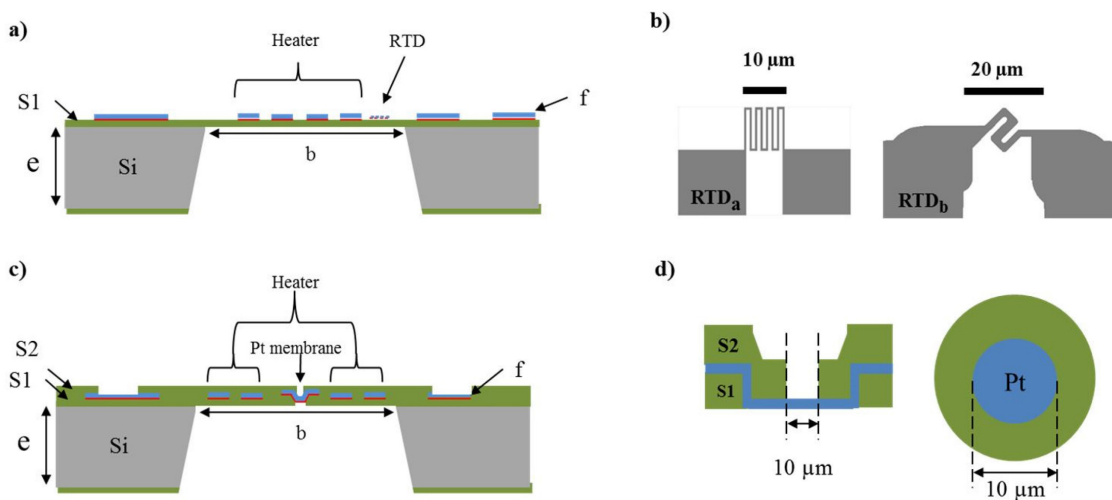


**Figure 4-4: (a) Schematic cross-section of the RTD device; (b) RTD design variations; (c) Schematic cross-section of the OPT device; (d) Cross-section of the standalone platinum membrane and its top view for the OPT device (images provided by E. Lemaire from EPFL)**

The main dimensions of the structures are detailed in Table 1. The silicon nitride membrane has an area of  $1 \times 1 \text{ mm}^2$  and the heaters were implemented with two different areas:  $220 \times 220 \text{ μm}^2$  and  $440 \times 440 \text{ μm}^2$ . The fabrication process is presented in Appendix 2. In the Figure 4-5 the devices optical images are presented.

	Material	Thickness (nm)	Area ( $\mu\text{m}^2$ )
RTD <sub>eb</sub>	Ta + Pt	d = 6 + 50	10 x 10
RTD <sub>uv</sub>	Ta + Pt	d = 15 + 150	10 x 10
Standalone Pt membrane	Ta + Pt	f = 15 + 150	25 $\pi$
Membrane	SiN (layer S1)	S1 RTD = 500 S1 OPT = 200	1000 x 1000
	SiN (layer S2)	S2 = 300	
Heater	Ta + Pt	f = 15 + 150	220 x 220 and 440 x 440
Chip	Si	e = 390 $\times 10^3$	3000 x 3000

**Table 4-1: Characteristics of the calibration chips**

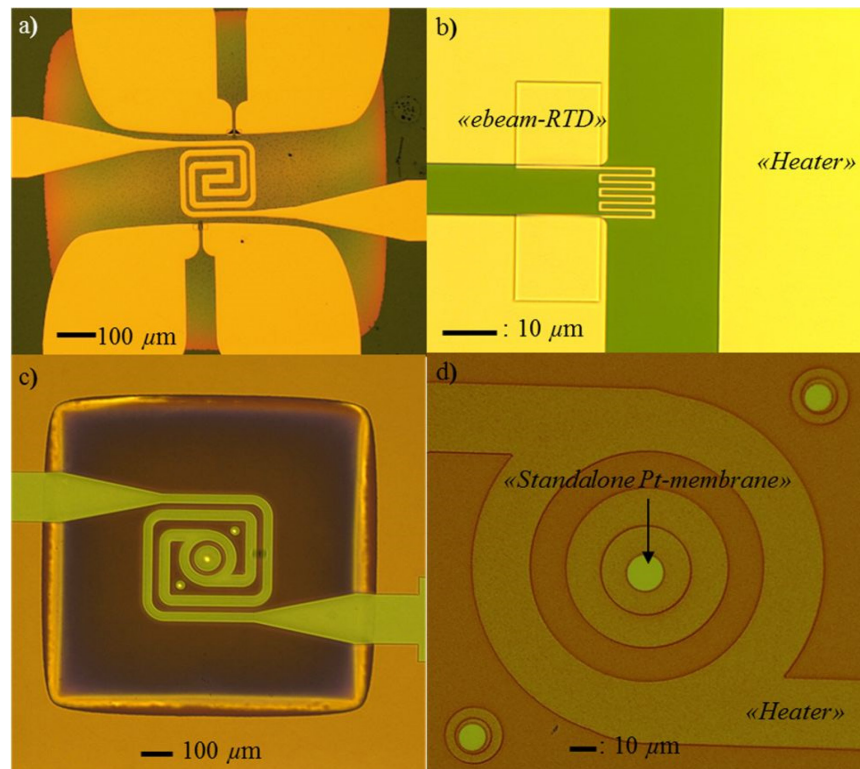


**Figure 4-5: (a) RTD device with heating area and two RTDs (b) RTD patterned using e-beam lithography; (c) (d) OPT device with standalone Pt membranes (images provided by E. Lemaire from EPFL)**

#### 4.3.1.2 Device characterisation and SThM probe evaluation procedure

- *RTD measurements*

The RTD designs patterned using standard lithography provides typical resistance values between 12 and 100  $\Omega$ , while the RTD fabricated using e-beam lithography exhibits higher resistance values (250-400  $\Omega$ ), and therefore a higher sensitivity (considering a comparable TCR). The temperature dependence of the two different RTDs implemented was characterized. A dedicated setup including a source meter (Keithley 2450) and high temperature oven (Vulcan 3-130) was used to measure the resistance value of the RTDs as a function of temperature in a range from 30 to 400°C, as depicted in Figure 4-6. The TCR values of the RTDs were found to be 0.00267 K<sup>-1</sup> and 0.00316 K<sup>-1</sup> for the RTD<sub>eb</sub> and RTD<sub>uv</sub>, respectively, with an estimated relative error of 1.5%. This error takes account of the temperature uncertainty (Pt100 located near the chip in the oven) and the electrical resistance measurement connector correction. Despite its lower TCR value, the e-beam RTD<sub>eb</sub> exhibits a mean sensitivity of 0.7  $\Omega$ .K<sup>-1</sup> in comparison to 0.06  $\Omega$ .K<sup>-1</sup> for RTD<sub>uv</sub> because of their higher resistance value.

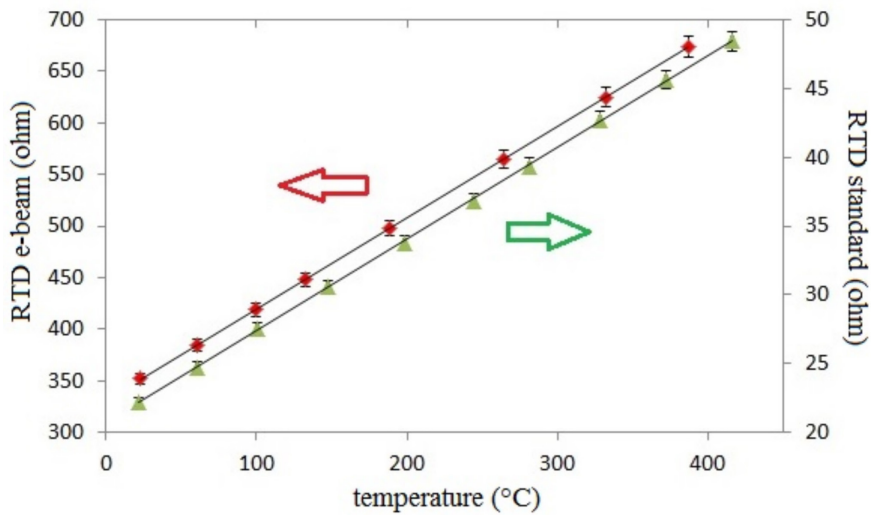


**Figure 4-6: RTD values measured as a function of temperature up to 400°C (figure generated by L. Thiery)**

- *SThM probe evaluation (RTD device)*

Functionality of the calibration chip was validated with coupled SThM and RTD temperature measurements. Measurements have been performed at different supplied power and the resulting points led to fitted curves as shown in the Figure 4-7. Left and right figures present the extracted curves from the measurement points of the 5  $\mu\text{m}$  and 1.3  $\mu\text{m}$  probe respectively.

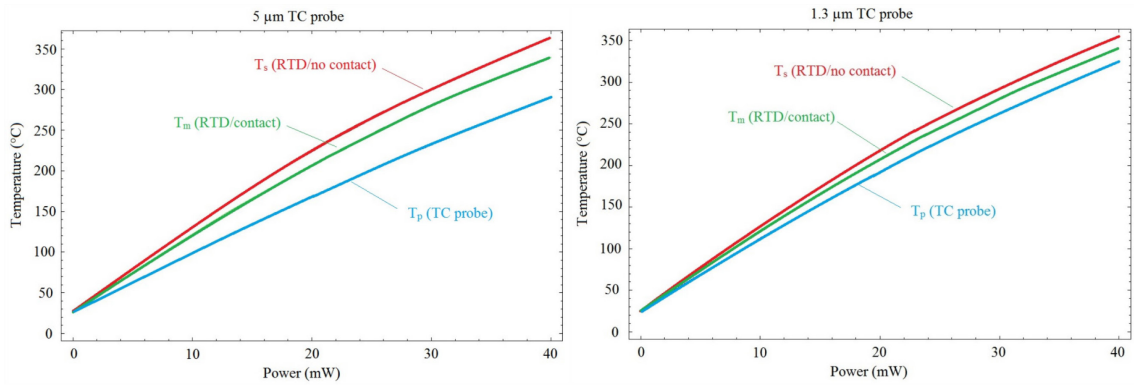


**Figure 4-7: Experimental results 5  $\mu\text{m}$  probe results and 1.3  $\mu\text{m}$  results (figure generated by L. Thiery)**

From these curves and knowing the ambient temperature, one can easily calculate the thermal response  $\tau$  of both probes, and their ratio  $\phi$  (Figure 4-8). It is interesting to notice the difference between the two probes due to their size. A perfect probe would indicate a thermal response equal to 1 whereas a  $\phi$  ratio near zero.

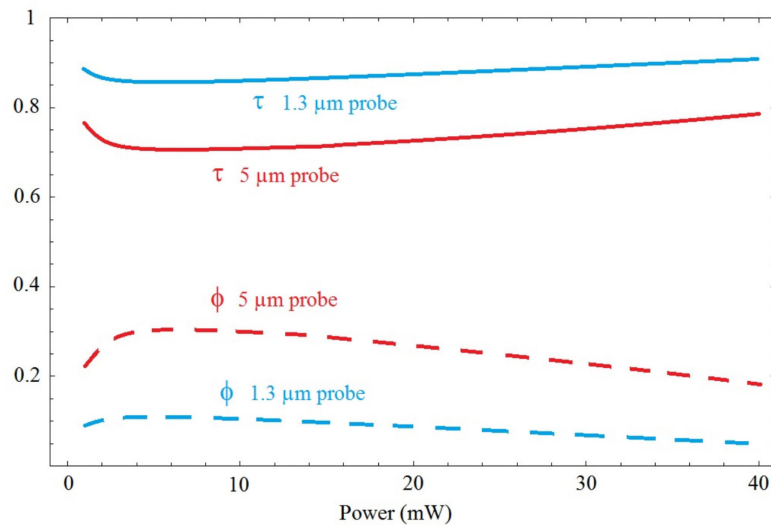


**Figure 4-8: Extracted values of  $\tau$  and  $\phi$  for both probes (figure generated by L. Thiery)**

Among the series of measurements, we observe that 5 $\mu\text{m}$  probes provide similar values whereas the 1.3  $\mu\text{m}$  exhibits large dispersion probably due to the uncertainty on its actual location regarding the RTD.

- *SThM probe evaluation (OPT device)*

Scans on OPT devices have also been performed with the SThM probe coupled with NIR optical imaging[7]. In this configuration, the SThM tip is landed on the topside of the standalone platinum target whereas the NIR microscope objective is on the backside. We confirmed that the standalone Pt-membrane placed at the centre of the device could be scanned at several temperatures without any mechanical robustness issue.

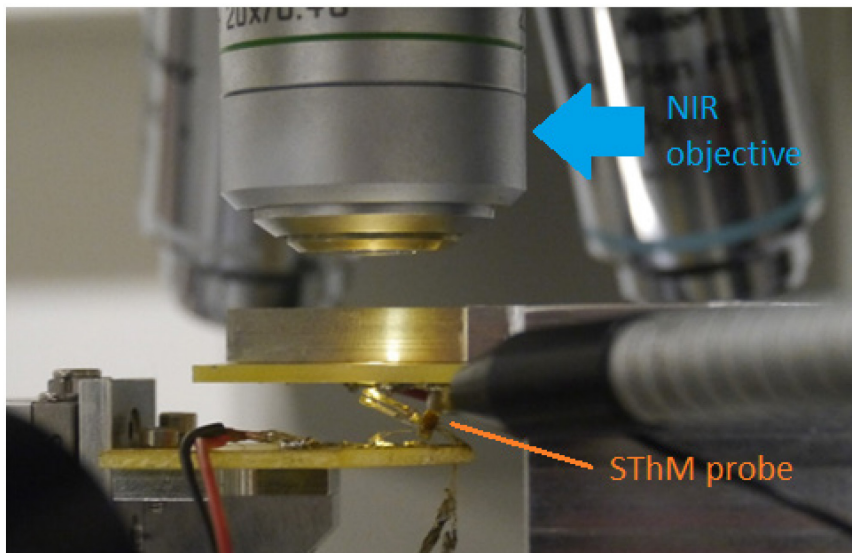


Figure 4-9: Experimental set-up of the SThM-NIR coupling measurement

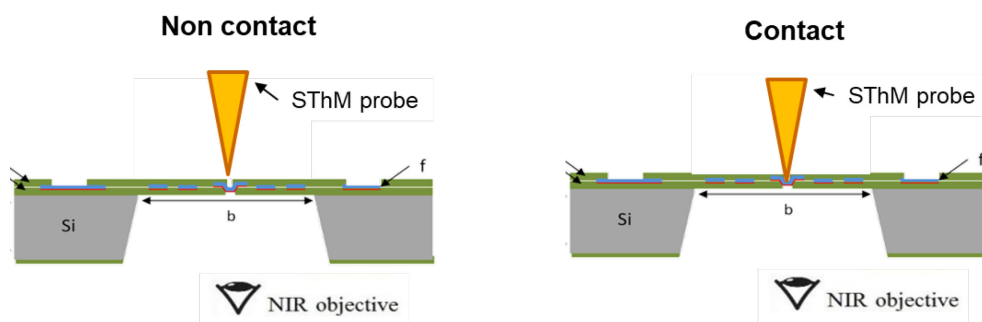
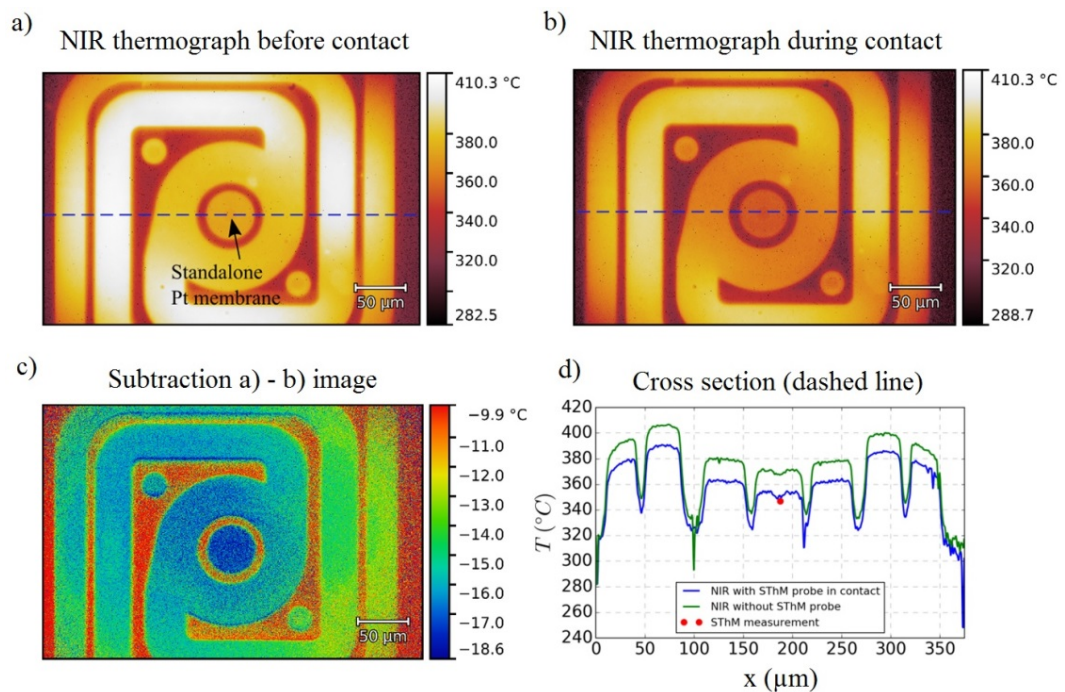


Figure 4-10: Schematic of the SThM-NIR coupling measurement

The results are presented on Figure 4-11 for a heater dissipated power of 46 mW. Indicated temperatures of Figure 4-11a and b have been calculated using an emissivity value of 0.1. This explains the important variations of apparent temperature (artefact) observed in Figure 4-11 (a, b and d) due to the very low emission by the silicon nitride layers in the optical spectrum range considered here. Consequently, only the temperature difference of Figure 4-11c thermograph obtained by subtracting Figure 4-11b from Figure 4-11a can be considered as relevant. A major effect is revealed in Figure 4-11 c and d: a global homogeneous cooling of the active part of the membrane (heater) whereas the thermocouple tip contact area corresponds typically to the area of the standalone membrane. Surprisingly, this confirms that the surface temperature of such a device remains homogeneous, and the fact that the size of the surface RTD or the optical target is not critical.



**Figure 4-11: a) NIR thermograph of OPT device (1 mm<sup>2</sup> membrane with heater area of 440×440 μm<sup>2</sup>) without SThM probe contact. b) NIR thermograph of the same device when a 1.3μm diameter thermocouple probe put in contact c) subtraction image of NIR thermograph after contact and before contact, d) cross section of NIR thermographs and comparison with SThM measurement.**

In this example, the extracted thermal response  $\tau$  value gives 0.97 that is different to previous measurements (with the RTD device) due to the hypothesis on platinum film emissivity and the fact that the device is not identical. It is clear that a step of platinum film emissivity calibration has to be performed before any quantitative measurement. Without this, only qualitative comparison studies of different SThM probes could be performed.

- *The drawbacks of this first generation device*

The temperature evolution with respect to the power dissipation for the two areas of heaters used in this study (220x220 $\mu\text{m}^2$  and 440x440 $\mu\text{m}^2$ ) was measured by SThM at the center of the heater using thin wires thermocouples with a correction from the ratio  $\tau$  measured. The results are shown in Figure 4-12 for the RTD and OPT devices. According to these results, the RTD device with heating areas of 220 x 220  $\mu\text{m}^2$  and 440 x 440  $\mu\text{m}^2$  consumes 20 mW and 36 mW, at 300°C respectively, while the OPT device exhibits slightly lower power consumption. The breakdown power of the hotplates was also characterized. This test was performed by applying a voltage ramp with steps of 50mV for 50ms until the structure broke. The RTD device can be powered up to 120 mW and 265 mW before destruction of the membrane for the heating areas of 220 x 220  $\mu\text{m}^2$  and 440 x 440  $\mu\text{m}^2$ , respectively. The power to breakdown the OPT device was of 54 mW and 108 mW for heating areas of 220 x 220  $\mu\text{m}^2$  and 440 x 440  $\mu\text{m}^2$ , respectively. This smaller value compared to the RTD device is due to the use of a PECVD nitride layer less temperature resistant. The temperatures reached at breakdown are far higher than the maximum operating temperature expected for these chips, with a typical operation between room temperature up to 300°C and a maximum temperature of operation lower than 500°C.

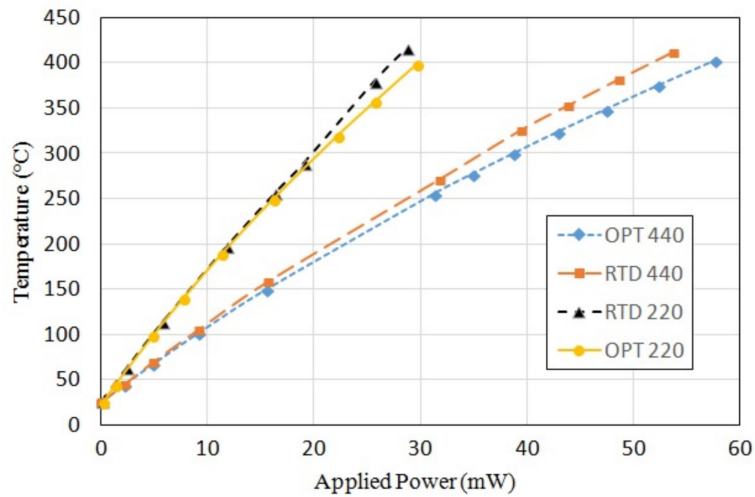


**Figure 4-12: Temperature measured at the centre of RTD and OPT devices using SThM probe (thin wires thermocouple with a diameter of 1.3  $\mu\text{m}$ ) for the two heaters areas ( $220 \times 220 \mu\text{m}^2$ : 220 and  $440 \times 440 \mu\text{m}^2$ :440 in the legend)**

Functionality of the calibration chip was validated with coupled SThM and RTD temperature measurements for all these devices. The resistance values of the RTD were simultaneously recorded with temperature information while the probe is scanned on the surface in order to study the perturbation of the probe on different regions of the device surface (Figure 4-13). When the probe scans on RTD's area or when it moves toward the heater, it makes a large perturbation on the surface as predicted.

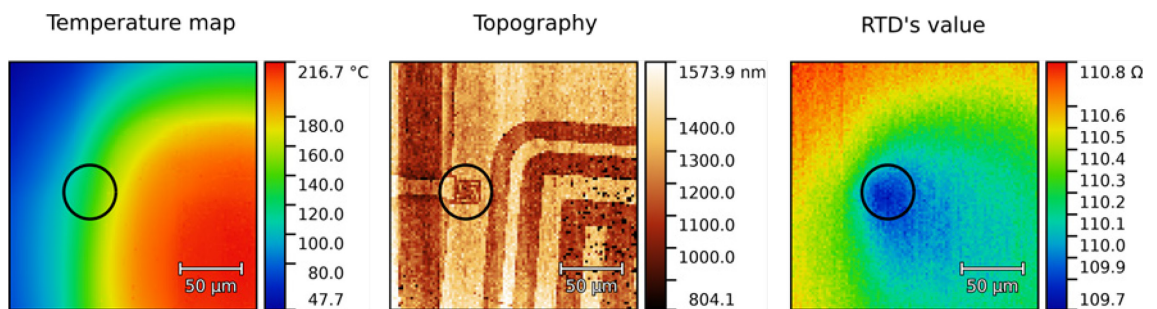


**Figure 4-13: Thermograph (left), topography (middle) and RTD response RTD (right) while the probe is scanning on the surface of a RTD device**

However, the devices also present drawbacks which can be noted from the experiment in Figure 4-13. First, there exists a temperature gradient of around 10°C on the RTD area due to its location far from the centre. This may imply a significant error on the  $\tau$  value depending on the tip position. Second, the heater size is still large so that the power consumption remains important and the sensitivity could be improved.

### 4.3.2 Second generation device

An optimized technology platform including second generation two chip designs for SThM probes characterization and calibration are reported to solve the drawbacks of the first generation. The designs developed in this work exhibit low-power consumption and uniform circular temperature distribution over the SThM contact area. The minimization of device size leads to the minimization of the power consumption which is crucial for increasing the thermal sensitivity. By an appropriate combination of the platinum and silicon nitride layers, the calibration chips designs can be realized in the same fabrication run. The sensing areas are moved to the chip center with a uniform temperature distribution.

#### 4.3.2.1 Device design

The calibration chips are made of a platinum heater, with an area of  $50 \times 50 \mu\text{m}^2$  sandwiched in a suspended silicon nitride membrane, and a SThM contact area of  $10 \times 10 \mu\text{m}^2$ , as shown in Figure 4-14. The total chip size and membrane size are kept similar to the first generation device. On top of the heating area and centered, the “v2RTD device” has a RTD patterned locally and centered on top of the heating area (Figure 4-14). The RTD provides the actual surface contact temperature, which allows monitoring the thermal contact efficiency of the SThM probe when in contact with the chip.

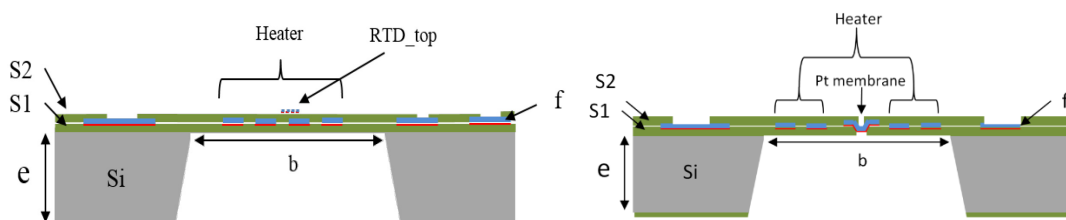


**Figure 4-14: Schematic cross-section of the v2RTD device (left); Schematic cross-section of the v2OPT device (right) (images provided by E. Lemaire from EPFL)**

	Material	Thickness (nm)	Area ( $\mu\text{m}^2$ )
RTD	Ta + Pt	$d = 10 + 140$	$25\pi$
Standalone Pt membrane	Ta + Pt	$f = 10 + 140$	$25\pi$
Membrane	SiN (layer S1)	S1 RTD = 200	$1000 \times 1000$
	SiN (layer S2)	S2 = 400	
Heater	Ta + Pt	$f = 15 + 135$	$25 \times 25\pi$
Chip	Si	$e = 390 \times 10^3$	$3000 \times 3000$

**Table 4-2: Characteristics of the second-generation calibration chips**

The RTD design is equipped with four-terminal connectors, which helps to eliminate the uncertainty of connection resistance and TCR calibration. The 2nd design (v2 opt device) consists of a suspended circular standalone platinum membrane (150 nm-thick / 10  $\mu\text{m}$ -wide) defined in the heater layer. These designs are depicted in the Figure 4-15.

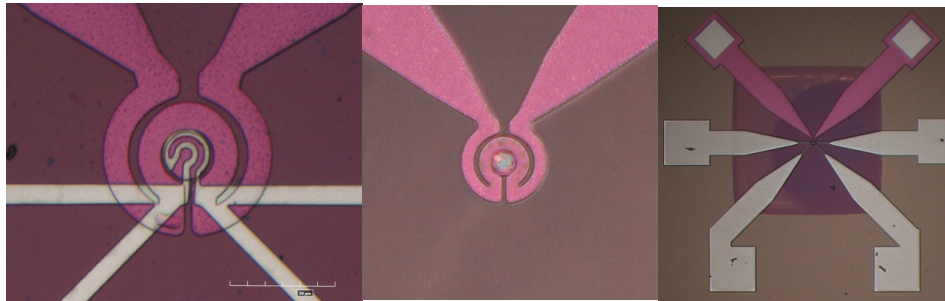


**Figure 4-15: Calibration chips with heating area of  $50 \times 50 \mu\text{m}^2$  and contact area of  $10 \times 10 \mu\text{m}^2$ . From left to right: v2RTD design with Pt RTD; v2OPT design with the suspended platinum membrane; the full chip image of v2RTD device (images provided by E. Lemaire from EPFL)**

#### 4.3.2.2 Device characterisation

- *RTD calibration*

Devices have been electro-thermally characterized by determining the temperature coefficient of the resistors. The Figure 4-16 presents the evolution RTD resistances as a function of temperature of two different chips of the same design and fabrication process. The resistance is slightly different between two chips due to the non-

uniformity of the layers produced from the fabrication; however, the slopes of the two lines are almost the same.

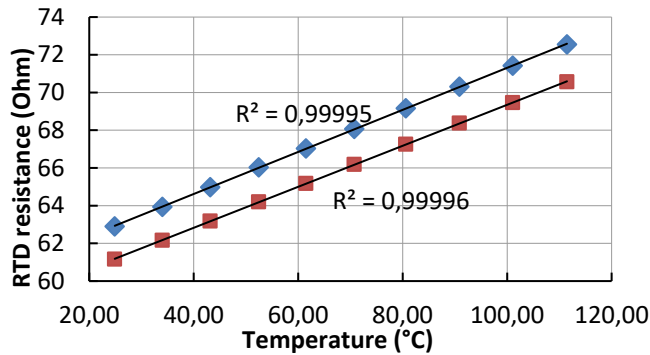


**Figure 4-16: Measurement points and slope extraction of electrical resistances versus temperature of 2 devices v2RTD.**

- *SThM scans*

Scan demonstration is also made on the device. Figure 4-17 presents scan results on the v2RTD device (temperature and topography maps) at 1.61mW power supply and the temperature at the center of the device versus power. In this figure, SThM measurements are not corrected so that the difference between the probe ( $T_p$ ) and the actual surface temperatures ( $T_s$ ) clearly appears.

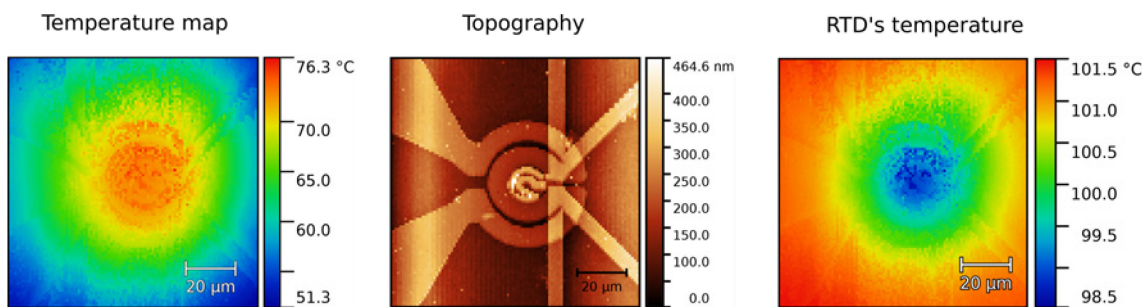


**Figure 4-17: SThM thermograph (a), topography (b) and RTD temperature (c) while the probe is scanned on the device surface of heated with 1.61mW supplied power**

Compared to the first generation RTD device, the temperature for the v2RTD device is more homogenous on the whole area of the RTD. The probe's perturbation on the surface measured by RTD's value can also be considered as constant inside RTD's area.

- Comparison with a larger heater size

A device with larger heater has also been made to verify the size effect on measurements. This device has the same size as the first generation device however the RTD has been moved to the center of the heater with four-terminals.

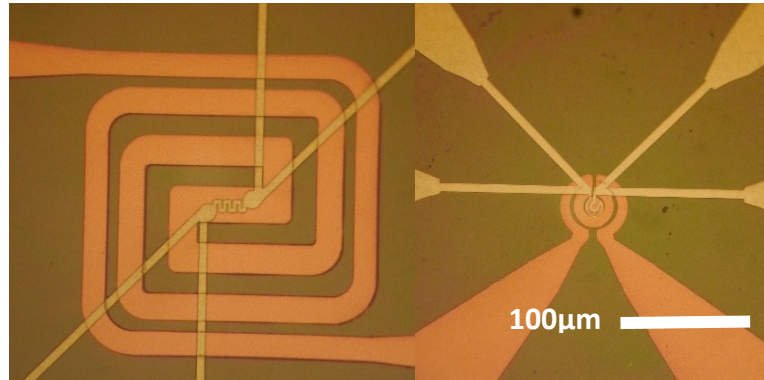


Figure 4-18: Optical micrograph of an v2RTD large heater; v2RTD small heater

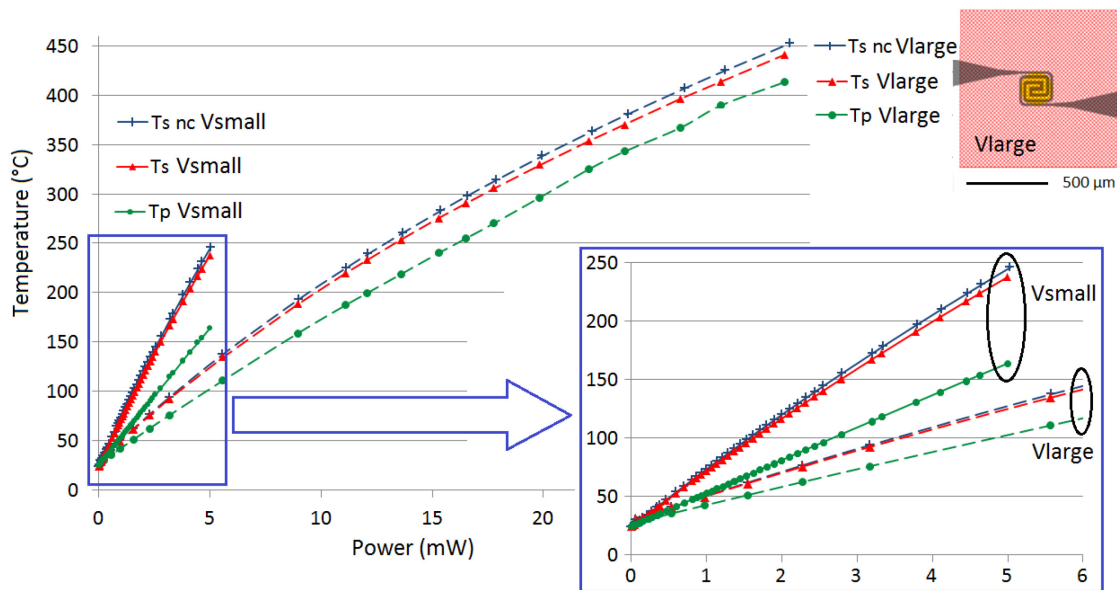


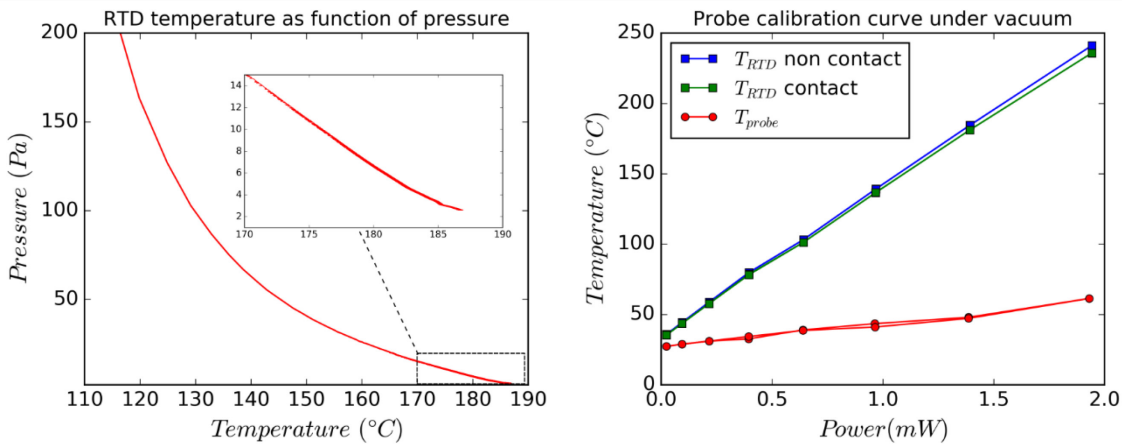
Figure 4-19: v2RTD large design: top left) SThM TC topography, top right) SThM TC temperature at 1.8 mW, bottom) Comparison between TC SThM probe on Vlarge and Vsmall respectively.

Figure 4-19 shows a comparison made on the central point with respect to a previous version of device (called Vlarge) for which the larger heater ( $220 \times 220 \mu\text{m}^2$ ) is shown on the figure (same RTD sensor not plotted). It clearly shows a large reduction of power consumption and subsequently a greater sensitivity in the measurement of the

thermal perturbation, as shown in the zoomed blue area. The mean values of the thermal responses of the SThM probe  $\tau = \frac{T_p - T_a}{T_s - T_a}$  were found to be 0.79 and 0.6 for Vlarge and Vsmall, respectively.

- *Vacuum measurements*

To evaluate the role of air on the device temperature, the RTD temperature is recorded (with 3.5 mA device supply current) with the evolution of pressure. The temperature increases to its maximum at the minimum pressure due to the elimination of air convection from the heat transfer of the device. It is noted that the primary vacuum doesn't eliminate totally the air convection due to the accumulation of low pressure air molecular heat transport on the large area membrane. The RTD temperature can therefore vary 2 °C/Pa with the variation of pressure.



**Figure 4-20: v2RTD device: RTD temperature as evolution of air pressure (left) and experimental results with a 1.3µm thermocouple under vacuum (2Pa)**

The 1.3µm thermocouple probe response is also tested under vacuum. The  $\tau$  ratio is much lower than the  $\tau$  measured in air which can be explained by the fact that air plays a very important role on the heat transportation. A very low tip-sample equivalent conductance measured around  $1.8 \times 10^{-7} W/K$  will be shown in the section 4.6.1 also explains the low thermal response  $\tau$ , near 0.15.

- *SThM NIR coupling measurement*

Similar to the first generation device, the v2 OPT device is also calibrated by a coupling measurement (NIR and SThM). For this measurement, calculated temperatures have been made using an emissivity value of 0.1. Results are shown in the Figure 4-21. The  $\tau$  ratio (0.79) measured for this device is also smaller than the one of the last generation device due to its smaller size.

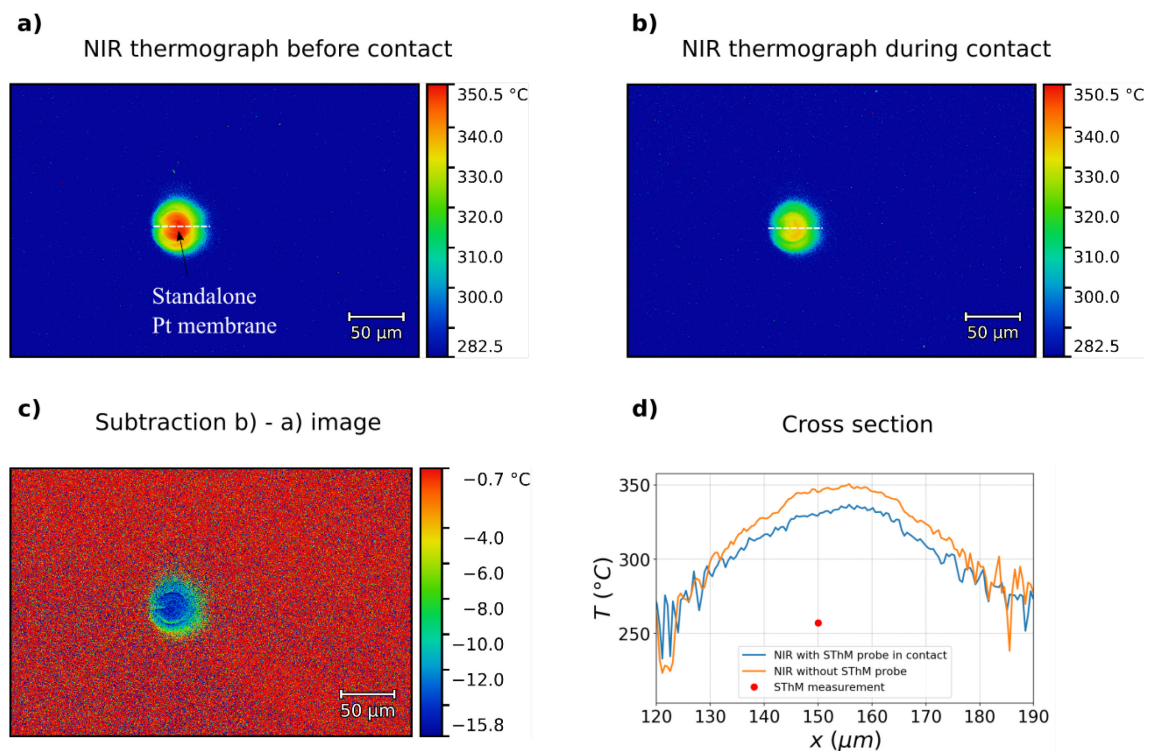


**Figure 4-21: a) NIR thermograph of v2OPT device (1 mm<sup>2</sup> membrane with heater area of 50×50  $\mu\text{m}^2$ ) without SThM probe contact. b) NIR thermograph of the same device when a 1.3 $\mu\text{m}$  diameter thermocouple probe put in contact c) subtraction image of NIR thermograph after contact and before contact, d) cross section of NIR thermographs and comparison with SThM measurement**

We have presented thermocouple calibrations on different devices using the two techniques. The results obtained are showed in Table 4-3. As can be seen from the table, the ratio  $\tau$  decreases with the decreasing of device size. The difference between the two techniques may come from the uncertainty of thin film platinum emissivity

(which is chosen equal to 0.1 for the entire image). The v2RTD device will be chosen for the probe evaluation under different conditions its size and high sensitivity.

	RTD device			OPT device		
Name	V1	V2 large	V2 small	V1	V2 large	V2 small
Size (μm <sup>2</sup> )	220x220	220x220	50x50	440x440	220x220	50x50
τ	0.86	0.79	0.6	0.95	0.82	0.72

**Table 4-3: The ratio τ values measured by localized RTD and optical techniques for different device designs**

## 4.4 Influence of different factors on temperatures measurement

### 4.4.1 Influence of air and contact force on temperature measurement

In this last section, we focus on the v2RTD device (Figure 4-15) to study the tip-sample heat transfer temperature measurement at different heater powers. The probe and RTD temperatures are recorded while the probe is approaching the device surface from 2μm above the surface down to contact. The measurements were performed at three different supplied currents notably at 2, 3, 4 mA, corresponding to 0.375, 0.868, 1.611 mW of device power and 41.72, 66.21, 100.96 °C of RTD non-contact temperature (the probe being very far from the sample).

Figure 4-22 illustrates the recorded thermocouple tip temperature and RTD temperature when the probe approaches the device surface. The temperatures (tip and RTD) are noted changing as a linear dependence of the distance, which is satisfy the Fourier’s law of heat conduction through air between two objects. From the Figure 4-22, only a small temperature step is detected the moment before contact. This also means the solid-solid conductance does not play an important role on the tip-sample conductance:  $\frac{\Delta T_{probe\ jump\ in\ contact}}{T_{probe\ in\ contact} - T_{amb}} < 2\%$ . It is also interesting to notice the after-contact zone at different device power, which can lead to a conclusion that the contact force does not have a big influence on the measurement (with the presence of air) especially at high temperature.

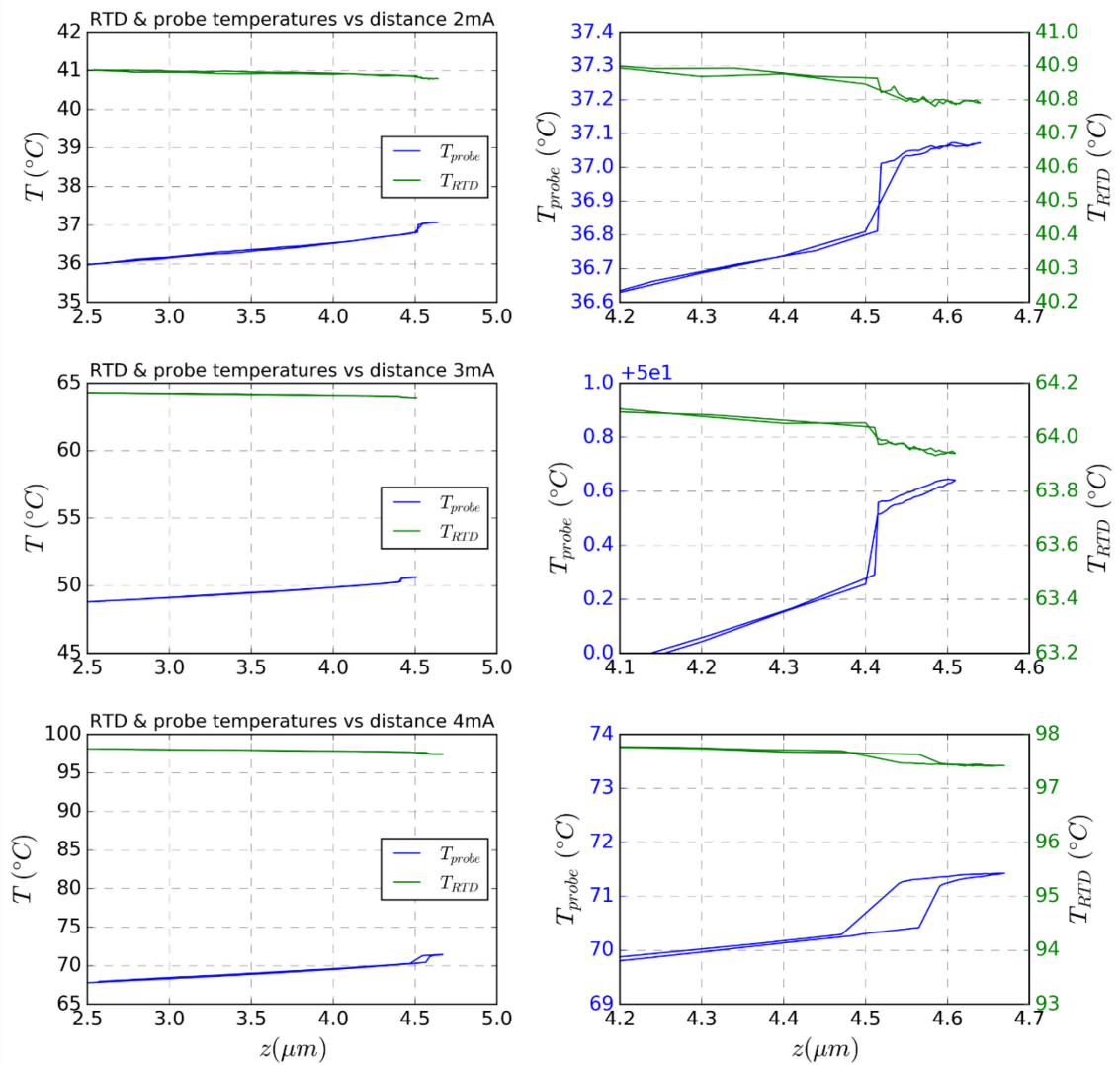


**Figure 4-22: RTD and tip probe temperature evolution when the probe approaches the surface**

Temperature (°C)	2 mA	3 mA	4 mA
RTD temperature	41.72	66.21	100.96
RTD temperature contact	40.8	63.95	97.5
$\Delta T$ RTD jump in contact	0.04	0.06	0.15
Tip temperature	37.05	50.5	71.3
$\Delta T$ tip jump in contact	0.2	0.3	0.7

**Table 4-4: Temperature measured by a 1.3 $\mu$ m probe at device different powers**

A bigger 5 $\mu\text{m}$  probe is also tested with this device to show the influence of the probe size on the measured temperature. Figure 4-23 shows temperature approach curves of 1.3 $\mu\text{m}$  probe and 5 $\mu\text{m}$  probe. As noted in the figure, the thermal response of the 5 $\mu\text{m}$  probe ( $\tau = 0.25$ ) is much lower to the  $\tau$  of 1.3 $\mu\text{m}$  probe (0.64). The 5 $\mu\text{m}$  probe also generates a larger perturbation on the device surface so that the RTD temperature decreases of 10 $^{\circ}\text{C}$  compared to 2.3 $^{\circ}\text{C}$  when a 1.3 $\mu\text{m}$  thermocouple is used.

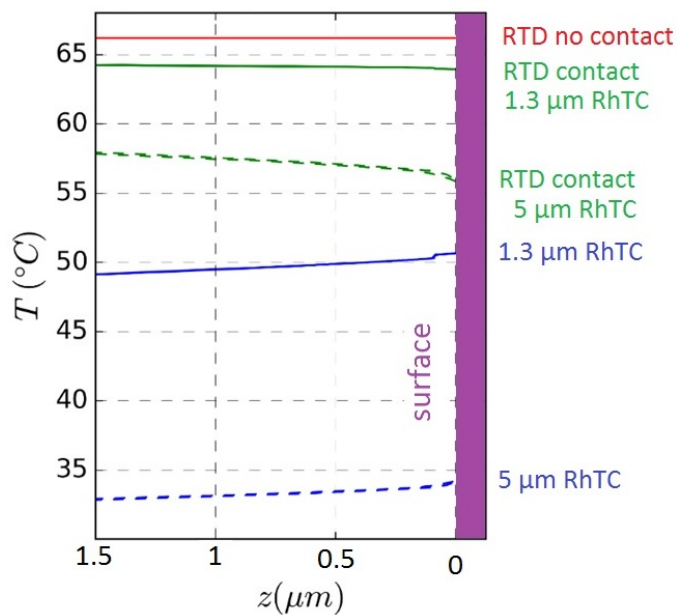


**Figure 4-23: Comparison of 1.3 $\mu\text{m}$  and 5 $\mu\text{m}$  thermocouple probe approach curve on the v2RTD chip surface**

#### 4.4.2 Statistical study on different parameters

To evaluate the influence of different parameters, a test plan was designed for the temperature measurements by changing the control factors (probe sizes, contact force and air pressure). The RTD temperature was fixed at 100 $^{\circ}\text{C}$  while a series of measurements were performed. Three different probes with diameters of 1.3, 2.5 and 5 $\mu\text{m}$  were used, called S1, S2 and S3 respectively. Measurements were performed at four different levels of pressure (1, 100, 5000, 100000 Pa) and three different forces applied for each probe:

- 1.3  $\mu\text{m}$  probe:  $F1=24\text{nN}$ ,  $F2=730\text{nN}$ ,  $F3 =1200\text{nN}$ ,

- 2.5  $\mu\text{m}$  probe:  $F_1=43\text{nN}$ ,  $F_2=432\text{nN}$ ,  $F_3 =1296\text{nN}$ ,
- 5  $\mu\text{m}$  probe:  $F_1=400\text{nN}$ ,  $F_2=4000\text{nN}$ ,  $F_3 =12000\text{nN}$ .

The force level is different depending on the probe due to the difficulty to maintain the same force level between three different probe sizes.

The experimental data were analysed at LNE, France (Laboratoire National de métrologie et d'Essais). A Fisher's test has been performed for each effect, which consists in the comparison between the mean squares associated with the considered effect and the mean squares associated with the residuals (more information on the Fisher's test can be found in the Appendix 3). If this ratio is too large, the test concludes that the effect is significant. Otherwise, it is assumed that the deviations observed for the effect are no greater than the residual error and the effect is not significant. The decision is then taken as a function of the p-value. An effect is considered as significant if the associated p-value is lower than 0.05.

ANOVA for selected factorial model - Temperature					
Analysis of variance table [Classical sum of squares - Type II]					
	Sum of		Mean	F	p-value
Source	Squares	df	Square	Value	Prob > F
Model	3959.24	13	304.56	59.3	< 0.0001
A-Probe size	1652.55	2	826.27	160.9	< 0.0001
B-Pressure	1620.92	3	540.31	105.2	< 0.0001
C-Contact force	55.56	2	27.78	5.4	0.0145
AB	398.50	6	66.42	12.9	< 0.0001
Residual	92.43	18	5.14		
Lack of Fit	81.96	14	5.85	2.2	0.2273
Pure Error	10.48	4	2.62		
Cor Total	4051.67	31			

**Table 4-5: ANOVA table for the DOE for the temperature**

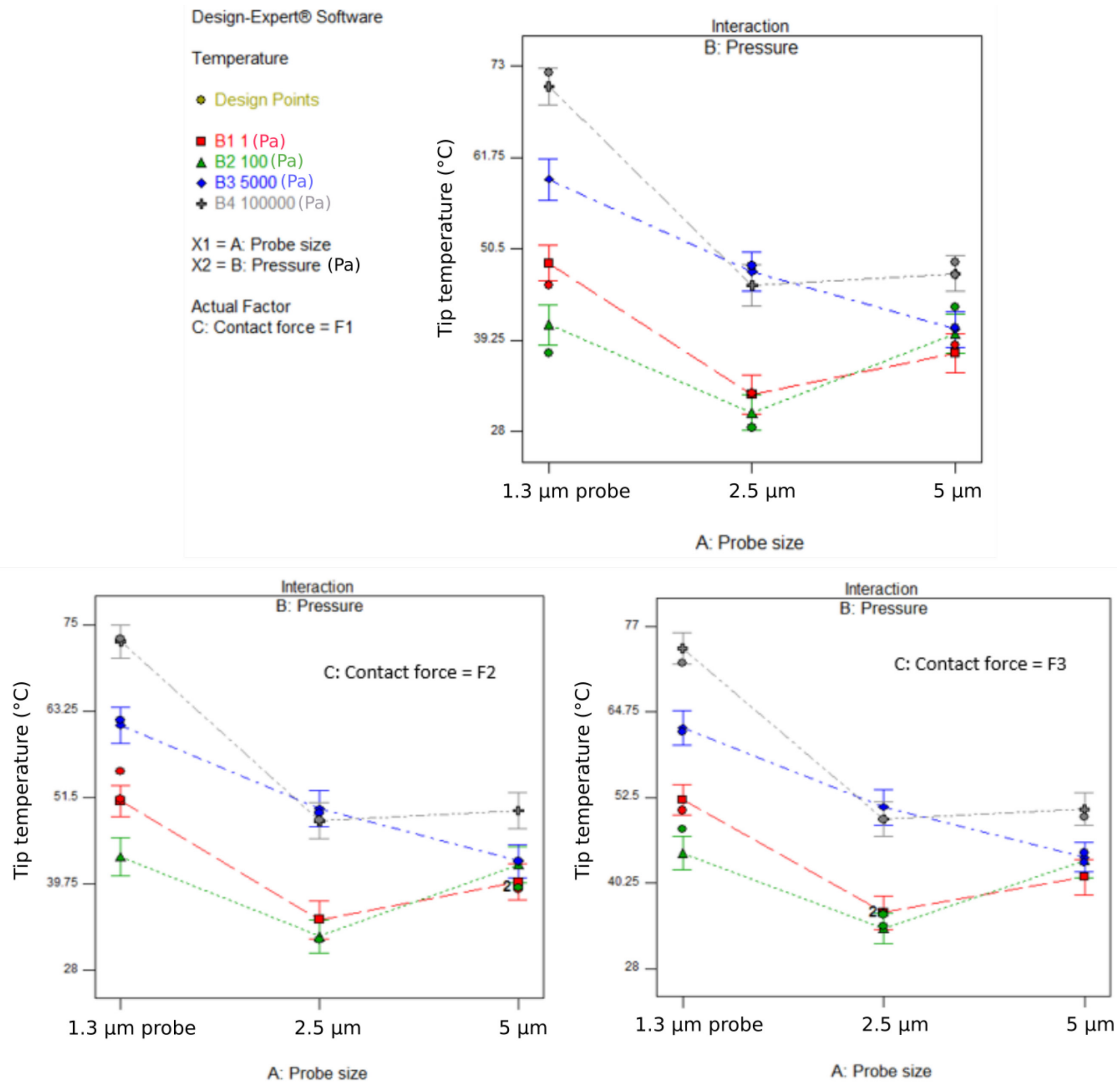
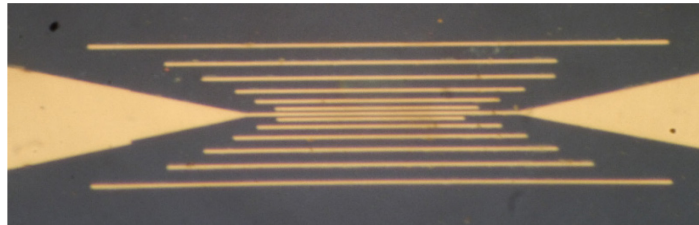


**Figure 4-24: Visualization of the interaction effect between the probe size and the pressure, with 3 values of contact force, for the temperature (figure provided by LNE)**

The probe size, the pressure and the contact force are all influential to the measured temperature. However, the main effects are the probe size and the pressure. Additionally, there exists an interaction between these two factors, as illustrated in Figure 4-24. The higher voltage values are obtained for the atmospheric pressure and the probe size S1. The probe size S1 is also the one for which the spread in the temperature is the highest, while for the probe size S3, the voltage values are much closer to each other. This is a consequence of the interaction: the effect of pressure is higher for probe size S1 than for probe size S3. This is related to the fact that the solid-solid contact conductance of the 5μm (S3) probe is larger than the one of 1.3μm probe. The contact force also has influence on the measurements but not as significant as the other parameters, noting that the different between force levels is very large.

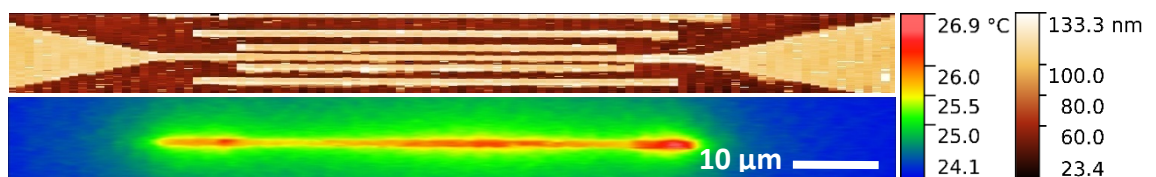
## 4.5 Thermal resolution estimation

To test the resolution of the probes, scans have been made on the sub-micron Ta/Pt wires device. For that, it is necessary to have localized heat sources with reduced lateral heat spreading on the surface. The device consists of a central line which can be heated by a supplied electrical current and many other unconnected lines taking role of thermal dissipaters. These wires were therefore fabricated in EPFL by e-beam on a silicon substrate, having a high thermal conductivity, on which a 200nm  $\text{Al}_2\text{O}_3$  passivation layer has been deposited. Lateral heat spreading is then reduced and temperature abruptly drops outside the wires. Optical micrograph of the device structure is shown in Figure 4-25.



**Figure 4-25: Optical micrographs of a C4 device with a 600nm wide stripe**

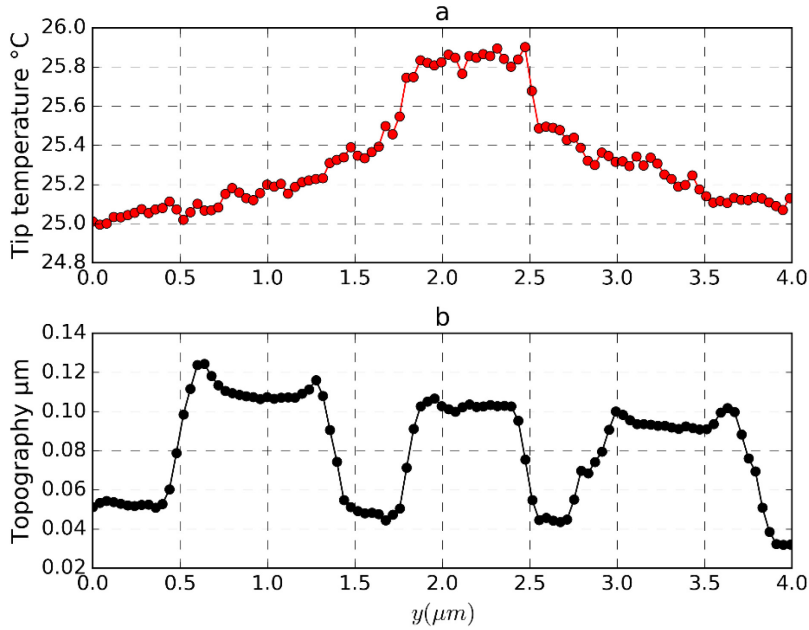
The measurements were performed with 1.3 $\mu\text{m}$  and 5 $\mu\text{m}$  thermocouple probes. We show in Figure 4-26 the temperature distribution of the device measured by a 1.3 $\mu\text{m}$  thermocouple when an electrical current is injected. The temperature elevation is clearly visible on the stripe showing the localization of heat in its immediate vicinity.



**Figure 4-26: Topography and temperature distribution measured with a 1.3 $\mu\text{m}$  probe when a 6mA electrical current is injected in the device**

As the room temperature was recorded at 23.5 $^{\circ}\text{C}$ , the triangular pad temperatures remain close to the room temperature (0.6 $^{\circ}\text{C}$  higher). As can be seen in Figure 4-26 and Figure 4-27, the topography of unconnected lines are not subjected to any artefact

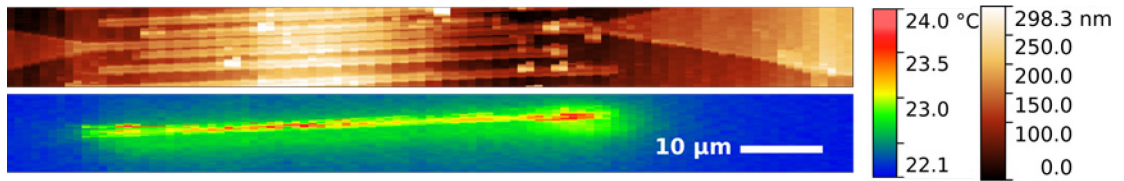
in relation to heat diffusion. Due to the thermal dissipative influence of the non-connected metal lines, the temperature distribution of the central line can be separated into three elevated temperature areas. The first two areas are located at the two ends of the heated line where the missing of the dissipative line is noted. The other area is located at the center due to the heat accumulation phenomenon.



**Figure 4-27: Transverse scan on the centre of the device supplied with 6mA using a 1.3 $\mu\text{m}$  thermocouple SThM probe**

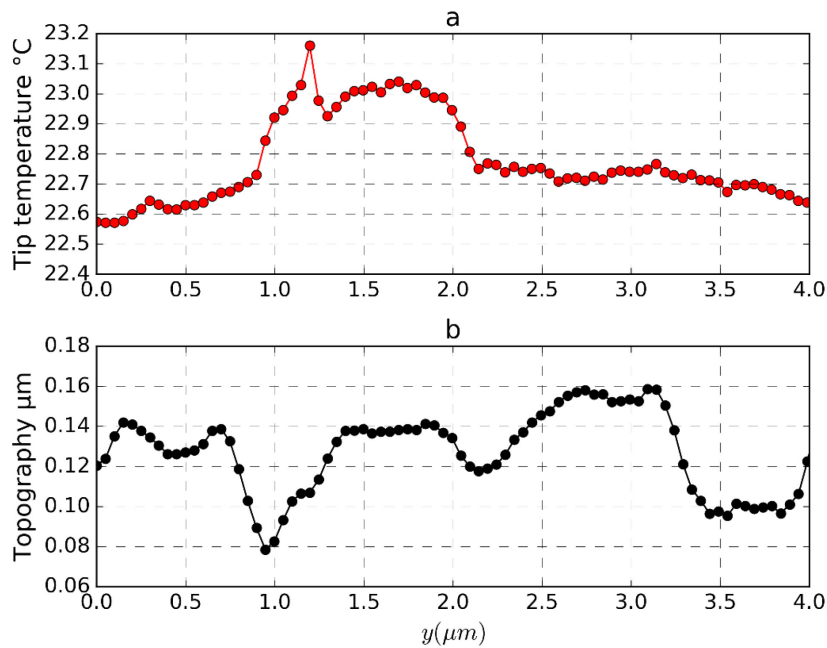
The thermal resolution of the probe can be verified due to the Y cross-section of the thermography and topography Figure 4-27. The iteration is 40nm between 2 points in the graphs of Figure 4-27, leading to an apparent resolution near 100nm.

Figure 4-28 shows thermography and topography of the device measured by the 5 $\mu\text{m}$  thermocouple. The images are in general close to the measurements performed by 1.3 $\mu\text{m}$  thermocouple however the resolution is degraded compare to Figure 4-26. The heat diffusion is strongly damped away from the heated line because of the large thermal mass of 5 $\mu\text{m}$  thermocouple.



**Figure 4-28: Topography and temperature distribution measured with a 5µm probe when a 6mA electrical current is injected in the device**

In addition to the thermal resolution, the topography resolution of this probe is also degraded which is caused by its larger tip curvature radius. The resolution of this probe is estimated around 500nm.



**Figure 4-29: Transverse scan on the centre of the device supplied with 6mA using a 5µm thermocouple SThM probe**

As previously described, there are still some uncertainties on the actual surface temperature ( $\tau$  ratio). However, due to the high thermal conductivity and mass of the silicon substrate, the measured temperature should not be very far from the actual value. At the moment, we don't have an effective tool to insure quantitative

measurements which is a very hard task. The idea of a quantitative temperature measurement based on a correction of heat flux (active probe) will be discussed in the perspective part of this document.

## 4.6 Application on micro-nano scale thermal measurements

### 4.6.1 Conpart spherical particles

In this part, a coupling measurement of the device v2RTD with thermal probe is proposed to characterize spherical polymer particles that can be metal coated (Figure 4-30) by the Norwegian company “Conpart”. These particles have been used as thermal conductive fillers[123], so that the thermal transport of a polymer composite network of these particles is of great interest.

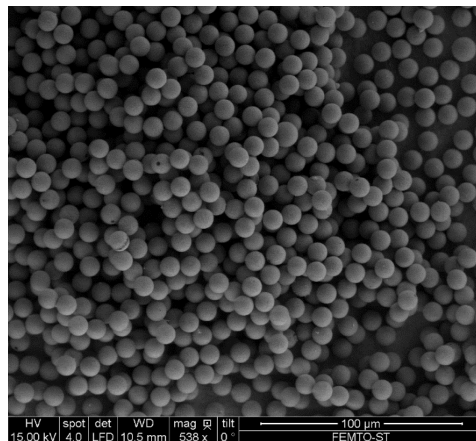


**Figure 4-30: Conpart spherical particle coated with a thin film silver**

The thermal behaviour of a single particle is also very important. In this part, a combination of a v2RTD device and a thermocouple probe has been used under vacuum to characterize these particles. The last generation V2 gen2 calibration device described in the last section is chosen for this experiment. The Figure 4-31 shows the SEM image of the v2RTD device and the micro particle of 10 μm of diameter placed on the top of RTD (localized resistive thermal detector) in order to measure the

temperature underneath the spherical particle. The particle was moved to the position using a pneumatique micro-manipulator.

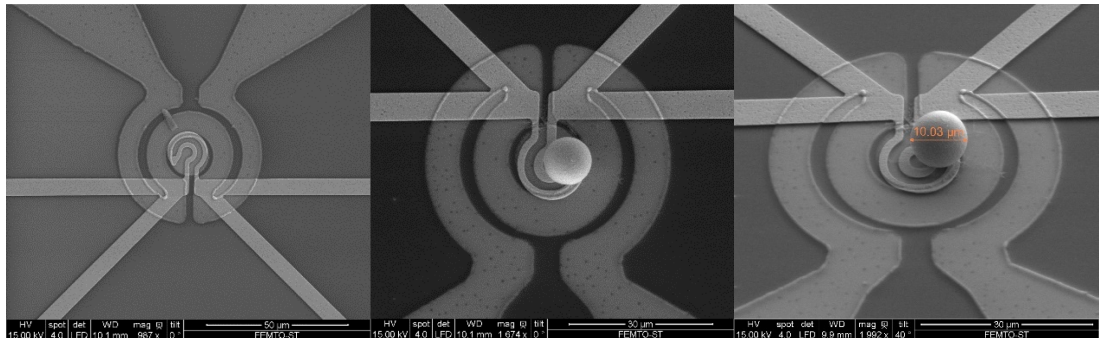


**Figure 4-31: v2RTD device and Conpart particle on top of the localized RTD**

The probe is prepositioned and moved to the top of the micro particle as illustrated in the Figure 4-32 to measure the temperature on its top. On this image, the optical reflection image of the particle and the probe on the device surface (Figure 4-32) give a better indication of probe-tip location. After the prepositioning, the whole system is placed under vacuum (1-4 Pa) to remove convective dissipation from measurements and simplify the thermal balance analysis.

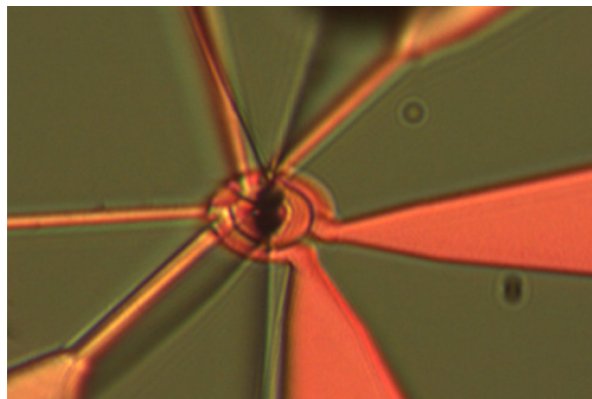


**Figure 4-32: Tip-particle in contact image**

A simple thermal model can be used when the probe is in two different positions (Figure 4-33): before contact and during contact. Before contact, as described the

equation 4-3, the Joule power generated by the device is equal to the heat conduction evacuated through the membrane to ambient.

$$P_{membrane} = u \times i = (T_{RTD} - T_a)/R_{membrane} \quad (4-3)$$

$$\Rightarrow R_{membrane} = (T_{RTD} - T_a)/u \times i \quad (4-4)$$

where  $P_{membrane}$  is the heat evacuated through the membrane,  $u, i$  are the device supplied voltage and current respectively,  $T_{RTD}$  is the RTD temperature (the temperature at the centre of the device),  $T_a$  is the ambient temperature and finally  $R_{membrane}$  is the thermal resistance of the device membrane.

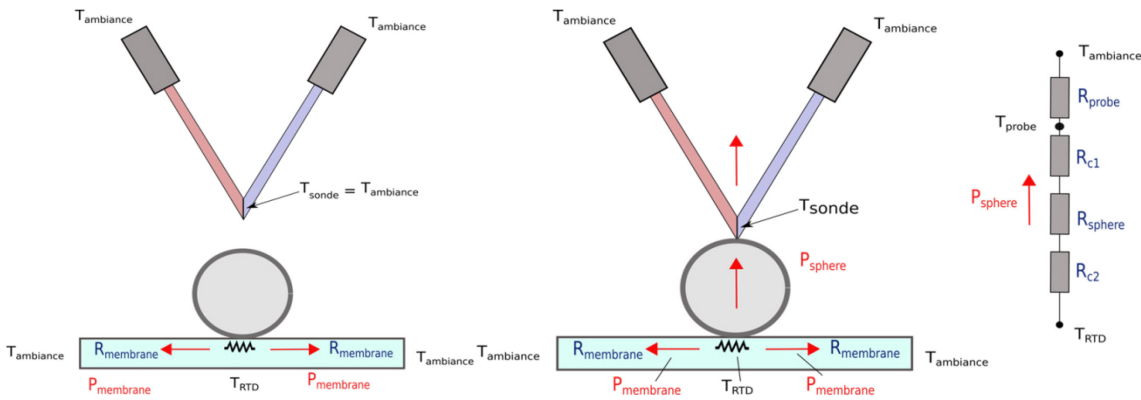


**Figure 4-33: Thermal configuration of coupling system v2RTD device, particle, thermocouple probe before contact (left) and in contact (right)**

During the contact, the device power is now separated into two parts. The first is heat conduction  $P'_{membrane}$  through the surrounding membrane to ambient. The second part is the heat conduction  $P_{particle} = P_{probe}$  through the probe to ambient.

$$u' \times i = P_{particle} + P'_{membrane} \quad (4-5)$$

$$\Rightarrow P_{particle} = u' \times i - P'_{membrane} \quad (4-6)$$

where  $u'$  is the device voltage during the contact,  $i$  is the device supplied current.

The heat conduction through the membrane during contact  $P'_{membrane}$  is given in the following term.

$$P'_{membrane} = (T'_{RTD} - T_a)/R_{membrane} \quad (4-7)$$

where  $T'_{RTD}$  is the RTD temperature during contact and  $R_{membrane}$  is the thermal resistance of the membrane which is considered unchanged before and during contact.

The equivalent resistance defined is the sum of the contact resistance  $R_{c2}$  between the v2RTD device and the particle, the thermal resistance of the particle and the contact resistance  $R_{c1}$  between the particle and the probe.

$$R_{eq} = R_{c2} + R_{particle} + R_{c1} = (T'_{RTD} - T_{probe})/P_{particle} \quad (4-8)$$

The probe thermal resistance can be also deduced by the following term

$$R_{probe} = (T_{probe} - T_a)/P_{particle} \quad (4-9)$$

The experiment was repeated with three different cases. The first is made on the blank device without particle on which the SThM is put on. The second is the experiment on the spherical polymer particle coated 200nm silver thin film and the third is the experiment on the polymer particle without coating. The tip-sample approach curves are depicted in the Figure 4-34 where the blue, green and red curves represent the measurements with blank device, silver coating particle and particle without coating respectively.

The device voltage, current, probe temperature, RTD temperature information are recorded and plotted in the Figure 4-34. From the curves plotted, the temperature remains constant before the contact which demonstrates that the air convection between the tip and the heat source is eliminated.

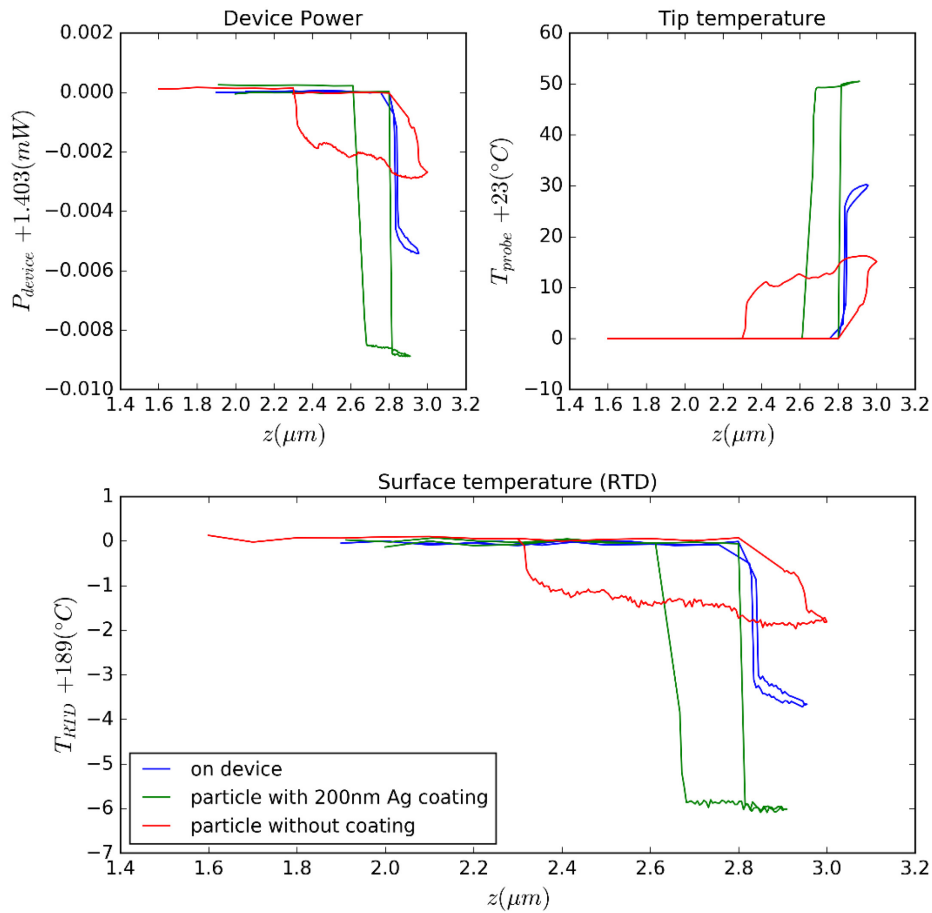


**Figure 4-34: The approach curve on the v2RTD device surface without particle, with particle with and without coating**

After contact, the curve behaviour depends totally on the mechanical properties of the contact. A larger hysteresis can be due to a more adhesive surface which is logical regarding to the mechanical properties of materials (polymer particle, polymer coated particle and v2RTD surface).

All useful information such as the equivalent conductance  $G_{eq}$  ( $1/R_{eq}$ ), the probe conductance  $G_{probe}$ , the heat flux through the membrane  $P_{membrane}$  and the heat flux go through the particle  $P_{particle}$  are calculated and depicted in the Figure 4-35.

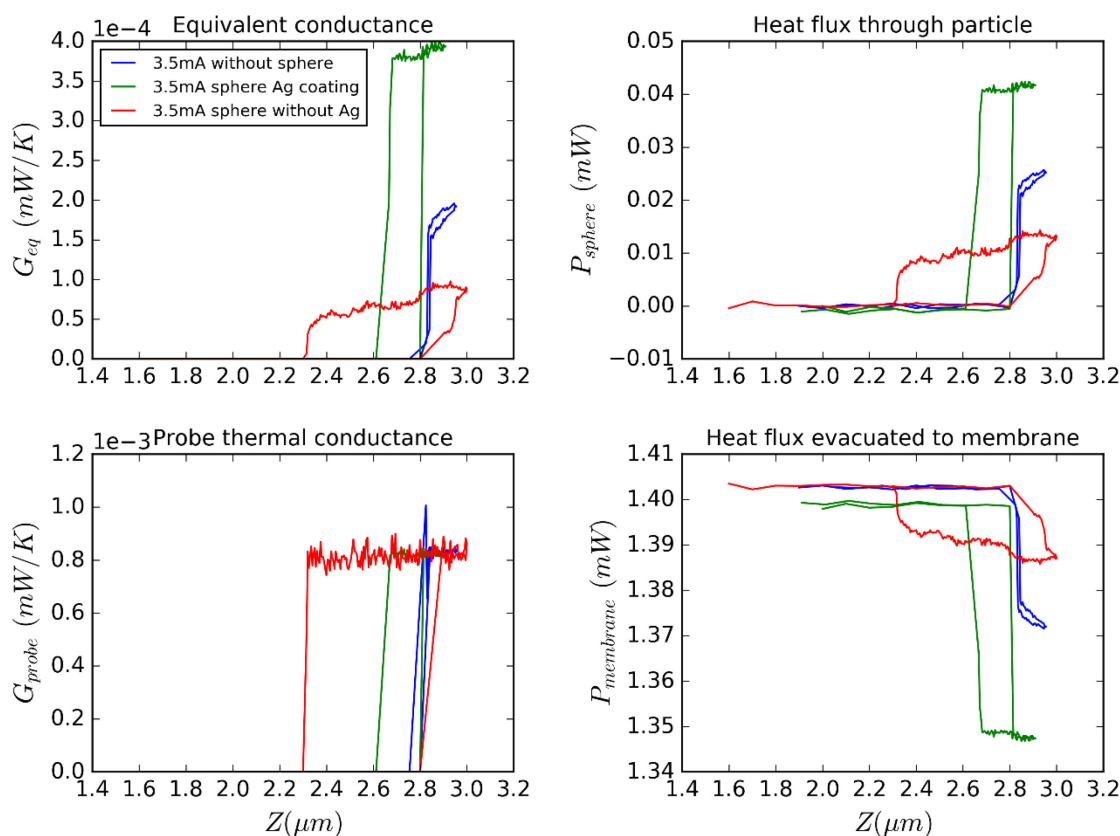


**Figure 4-35: Conductance values and heat flux calculated from temperatures and device power**

The equivalent conductance of the silver coated particle is the highest among all, proving that the efficiency of such particles as a thermal interface material. Indeed, compared to the blank device case (without particle measurement), we can clearly note that the equivalent conductance of the silver coated particle around  $4 \times 10^{-4}$  ( $\text{mW}/\text{K}$ ) is two times higher than the tip-device conductance, near  $1.7 \times 10^{-4}$  ( $\text{mW}/\text{K}$ ),  $G_{eq\ particle} \approx 2 \times G_{eq\ tip-sample}$ . This can be explained by the fact that the contact resistance is greatly reduced  $R_{c\ tip-device} \gg R_{c\ particle-device} + R_{c\ tip-particle}$ . In the polymer particle without coating case, the equivalent conductance  $G_{eq\ particle\ no\ coating}$  is the lowest compare to the other case. To verify the results, the thermal conductance of the probe is also calculated around  $8 \times 10^{-4}$  ( $\text{mW}/\text{K}$ ), this value practically unchanged for all the measurements. Complementary measurements have been performed at different device powers (different temperature level) notably at 1.5, 2.5, 3.5 mA, corresponding to 0.2167,

0.644, 1.403 mW of device power and 59, 105, 189 °C of RTD temperature respectively. This comparison at different power is depicted in the Figure 4-36.

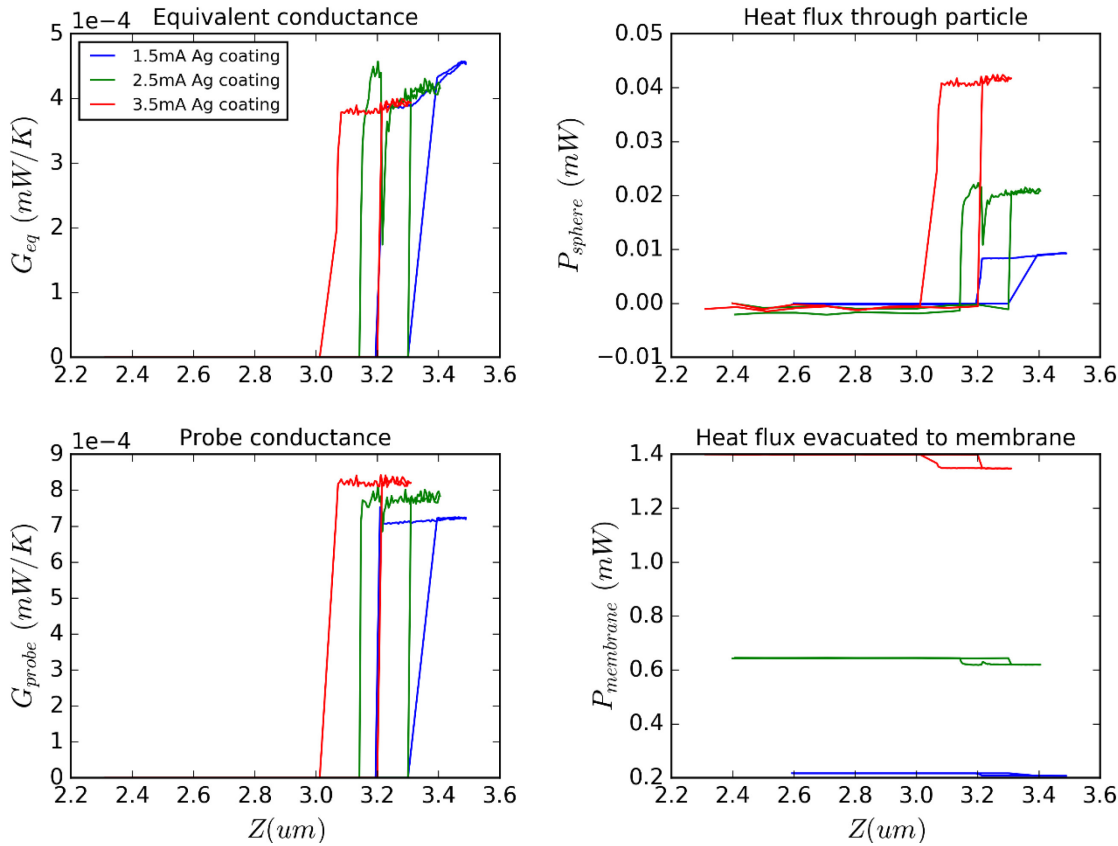


**Figure 4-36: Conductance values and heat flux calculated from temperatures and device power at different device power**

The equivalent conductance and the probe conductance stay unchanged which is concordant to the heat transfer theory in solid. The hysteresis value is noted relatively similar, which means that the tip-particle mechanical behavior does not significantly change.

The measurements were performed and compared at three different cases: blank device, device with coated particle and device with non-coated particle. The results obtained have shown the advantages of using this coated particle as a thermal interface material to reduce the thermal contact resistance. In fact, the adhesive force of the particle is also high which proves a good tip-particle and particle-device mechanical contact. Indeed, SThM probe measurements clearly show that the thermal

contact is even better with silver coated particle than without any particle. However, with the experiment we can only deduced an equivalent conductance (resistance). The sub-conductance (contact, particle) still rest undetermined. A thermal model should be considered to calculate these terms.

## 4.7 Summary

This chapter has discussed the temperature measurements using thermocouple probes. Different calibration devices were developed in order to evaluate probe-sample thermal transfer principally under air. The calibration processes were performed using two different techniques: localized RTD sensor and optical NIR. The optimized RTD design (v2RTD) is used then to study the influence of different parameters on the measurements. Using a localized temperature sample, measurements have been made with different 1.3 $\mu\text{m}$  and 5 $\mu\text{m}$  thermocouple probes, allowing comparing their apparent thermal resolution.

The coupling measurement system thermocouple probe calibration devices are also helpful for the thermal characterization of a micro structure (in this case a micro particle).

Although the high resolution (around 100nm) obtained compared to optical methods, the temperature measurements are still not quantitative. The quantification of SThM measurements is a complicated task. The probe temperature changes depending on the probe size, the sample size, materials... The only way to obtained quantitative measurements is the correction of heat flux to the sample.

# 5 THERMAL CONDUCTIVITY MEASUREMENTS AND CALIBRATIONS

## 5.1 Introduction

The thermal conductivity appears classically in the Fourier law of heat transfer in solid.

$$q = -kA \frac{\partial T}{\partial x} \quad (5-1)$$

Measurement techniques of  $k$  generally consist of a heat excitation source and of which the heat flux can be controlled or at least estimated for a given measured temperature gradient. In SThM technique, the thermal probes are at the same time the heat source (Joule effect) and temperature sensor. The thermal conductivity must be deduced from the cooling effect when the tip is put on the sample. Since steady measurements are not possible with a thermocouple, an alternative current is supplied to the thermocouple probe. It is then possible to extract two thermal components: the  $2\omega$  thermoelectric voltage that corresponds to the junction temperature, called  $2\omega$  method and the  $3\omega$  voltage derived from the resistive effect and the mean probe temperature ( $3\omega$  method). If the chosen frequency of this current is low, the measured  $2\omega$  temperature is identical to the DC temperature variation. In this chapter, the probe's thermal behaviors and the tip-sample heat transfer principle are studied.

Measurements are performed under air and vacuum to understand the influence of mechanical contact and air on the thermal measurements.

In Figure 5-2, a demonstration scan ( $100 \times 100 \mu\text{m}^2$ ) represented by the yellow rectangle was made on a sample surface of a  $\text{SiN}_x$  membrane (500nm) and platinum portion deposited on the membrane (Figure 5-1). The sample, described in the previous chapter, is a micro hotplate, used here as a passive sample. The thermocouple probe is heated by a sinusoidal current, and the probe tip temperature is extracted at the double frequency and the triple frequency which provides its mean temperature.

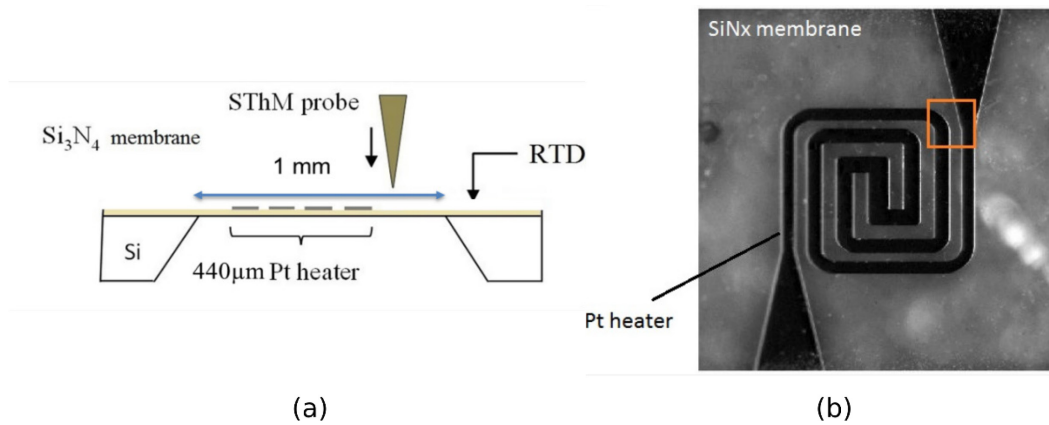


**Figure 5-1: Side-view (a) and top-view (b) of the micro-hotplate**

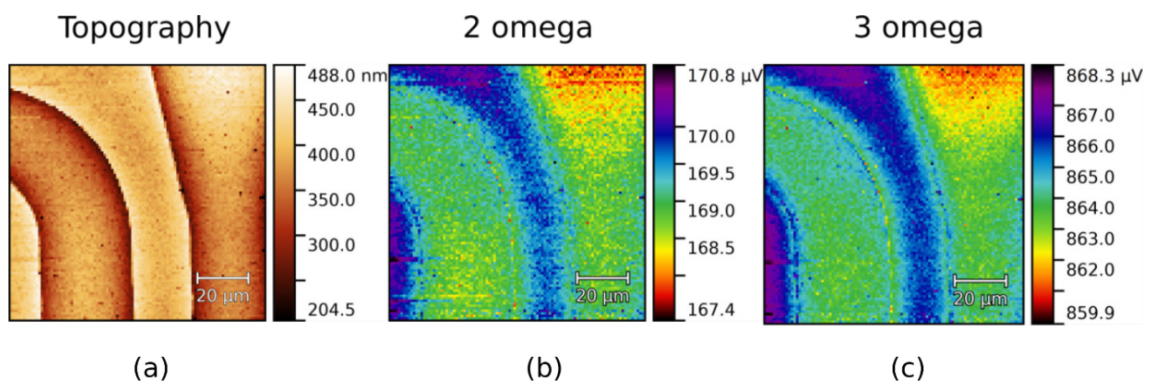


**Figure 5-2: Topography and thermal maps in active mode of a portion of platinum heater on silicon nitride membrane with a  $5 \mu\text{m}$  thermocouple probe. The sample is passive**

Figure 5-2b and c depicts the thermal contrast obtained from  $2\omega$  and  $3\omega$  components respectively. At a constant current, the tip temperature generally decreases when it approaches the platinum step due to the higher thermal conductivity of platinum (71.6 W/mK) compare to  $\text{SiN}_x$  (10 W/mK). At the boundary of two materials, the tip temperature is irregularly high or low due to the topographical artefacts. A stronger cooling is measured in the middle of platinum step, far away from silicon nitride membrane due to maximum heat diffusion into the sample.

SThM is very powerful to study thermal conductivity contrast at small scale due to its high resolution. However, looking at the thermograph (Figure 5-2), there still remains many questions to deepen in.

- First is the quantification of the thermograph. The Figure 5-2b and c represent probe temperatures (tip's temperature and average temperature) at every pixel. One of the most challenging goals of SThM technique is to convert this information into the sample local thermal conductivity.

- Second is how local we are. The thermographs are shown with "high definition" between Platinum portion and  $\text{SiN}_x$ . However, they are not totally thermal information because the topography artefacts appear at the boundary between two materials. The probe temperature is affected with details far away at the order of  $10\mu\text{m}$ . The thermal diffusion range in air and in solid is so large that may influence the SThM resolution.

As briefly presented in the second chapter, tip-sample heat transfer can be decomposed into two conductance components. First is sample spreading conductance  $G_s$  (thermal constriction) through an area with radius  $b$  (thermal contact radius). Second is thermal contact conductance  $G_c$  through the interface between the tip and the sample. Using a series of different bulk materials, this chapter is trying to clarify these terms by a simple theoretical analytical model for thermocouple probe and a thermal contact model under vacuum and air. Measurements on reference small scale samples will be also presented to demonstrate the microscope performance.

## 5.2 Probe simulation

### 5.2.1 Analytical model

- *Probe modelling*

Remind from the second chapter that the thermocouple active measurement is AC mode measurements. The thermocouple probe is cylindrical microwire. As a result, a simple 1D probe model can be used for this thermocouple probe. The simple model permits to study easily the influences of measurement parameters.

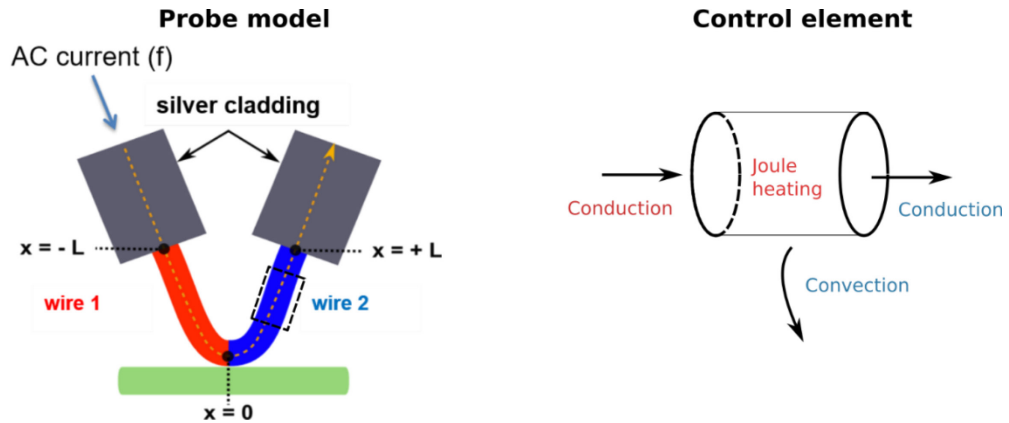


**Figure 5-3: Thermocouple probe theoretical model**

A control element is considered using balanced energy for the thermal equation. The energy exchanges are the conduction along the wire, the convection with the air ambient and the body Joule heating[21].

$$\lambda S \frac{\partial^2 T(x,t)}{\partial x^2} - hp(T(x,t) - T_0) + \frac{\sigma_0(1+\alpha(T(x,t)-T_0))}{S} I(t)^2 = \rho c S \frac{\partial T(x,t)}{\partial t} \quad (5-2)$$

Where  $\lambda$  is the thermal conductivity,  $h$  is the coefficient of convection,  $\sigma$  is the electrical resistivity,  $\alpha$  is the temperature coefficient of resistance,  $\rho$  is the material density,  $c$  is the heat volume capacity of the wire material;  $S$  and  $p$  are the section area and perimeter of the wire respectively.

The parameters of Platinum and Platinum-10%Rhodium applied on two different wires lead to the system of partial derivative equations below (if  $\alpha$  is considered negligible).

$$\begin{cases} \frac{\partial^2 \theta(x,t)}{\partial x^2} - \frac{hp}{\lambda_1 S} \theta(x,t) + \frac{\sigma_1}{\lambda_1 S^2} I(t)^2 = \frac{\rho_1 c_1}{\lambda_1} \frac{\partial \theta(x,t)}{\partial t}, & (-L \leq x < 0) \\ \frac{\partial^2 \theta(x,t)}{\partial x^2} - \frac{hp}{\lambda_2 S} \theta(x,t) + \frac{\sigma_2}{\lambda_2 S^2} I(t)^2 = \frac{\rho_2 c_2}{\lambda_2} \frac{\partial \theta(x,t)}{\partial t}, & (0 \leq x \leq L) \end{cases} \quad (5-3)$$

As described before in the chapter 2, the temperature oscillates at the double frequency ( $2\omega$ ) of the excitation current  $I(t) = I_0 \cos(\omega t)$ . The probe temperature in

function of  $x$  dimension and  $t$  time can be separated  $T(x, t) = T(x)e^{2i\omega t}$  and  $I(t) = I_0$  the equation then become

$$\begin{cases} \frac{\partial^2 \theta(x)}{\partial x^2} - \frac{hp}{\lambda_1 S} \theta(x) + \frac{\sigma_1}{2\lambda_1 S^2} I_0^2 = \frac{2i\omega \rho_1 c_1}{\lambda_1} \theta(x), & (-L \leq x < 0) \\ \frac{\partial^2 \theta(x)}{\partial x^2} - \frac{hp}{\lambda_2 S} \theta(x) + \frac{\sigma_2}{2\lambda_2 S^2} I_0^2 = \frac{2i\omega \rho_2 c_2}{\lambda_2} \theta(x), & (0 \leq x \leq L) \end{cases} \quad (5-4)$$

The solution of this equation is given by:

$$\begin{cases} \theta_1(x) = \frac{\sigma_1}{2\lambda_1 S^2 m_1^2} I_0^2 + A_1 e^{m_1 x} + B_1 e^{-m_1 x}, & (-L \leq x < 0) \\ \theta_2(x) = \frac{\sigma_2}{2\lambda_2 S^2 m_2^2} I_0^2 + A_2 e^{m_2 x} + B_2 e^{-m_2 x}, & (0 \leq x \leq L) \end{cases} \quad (5-5)$$

With

$$m_1 = \sqrt{\frac{hp}{\lambda_1 S} + 2i \left( \frac{\omega}{a_1} \right)}; \quad m_2 = \sqrt{\frac{hp}{\lambda_2 S} + 2i \left( \frac{\omega}{a_2} \right)} \quad (5-6)$$

Where  $a$  is the thermal diffusivity  $a = \lambda/\rho c$ . The boundary condition is selected at  $x=0$ ,  $x=-L$  and  $x=L$  to find the constants  $A_1, B_1, A_2, B_2$ .

At  $x = 0$ , the temperature continuity of two wires at the junction gives the first term of the Equation (5-7). The energy balance at the junction permits to deduce the second term (5-7), in which the interaction between the probe and the sample is represented by a heat flux to the sample  $\Phi = G\theta(0)$  where  $G$  is the equivalent tip-sample thermal conductance, the thermal conduction and finally a Joule heating due to the junction electrical resistance  $R_j$ . The boundary condition is therefore become:

$$\begin{cases} \theta_1(0) = \theta_2(0) \\ G\theta_1(0) - \lambda_2 S \frac{d\theta_2(0)}{dx} = \frac{R_j I_0^2}{2} - \lambda_1 S \frac{d\theta_1(0)}{dx} \end{cases} \quad (5-7)$$

At  $x = \pm L$ , the silver cladding diameter is 20 times larger than the thermocouple wire which can play a role of a thermal mass reservoir. The silver cladding thermal conductance  $G_{Ag}$  is many order magnitudes larger than the probe conductance. The  $2\omega$  temperature must be close to the ambient temperature.

$$\theta_1(-L) = \theta_2(L) = 0 \quad (5-8)$$

Solving the equation, the constants values  $A_1, B_1, A_2, B_2$  obtained give an access to the probe temperature profile  $\theta(x)$ . Figure 5-4 described the temperature profile of thermocouple probe before and during the contact, under air and vacuum conditions. The calculation was made using the materials parameters provided in the Table 5-1.

The dash curves represent the calculation when we consider the two wires of the thermocouple as identical (with average values of Platinum and Platinum-Rohdium are used), we call here an identical wires model. In her PhD manuscript, A. Bontempi also shown that this representative identical wire model does not differ (<2%) compared to the 2-wires model [84] when only the junction temperature is considered. This model is useful since it simplifies analytical expressions and also reduces error sources by reducing the number of terms whose identification remains problematic. Figure 5-4 depicts the  $2\omega$  temperature distribution along a  $1.3\mu\text{m}$  thermocouple probe wires under air and vacuum conditions.

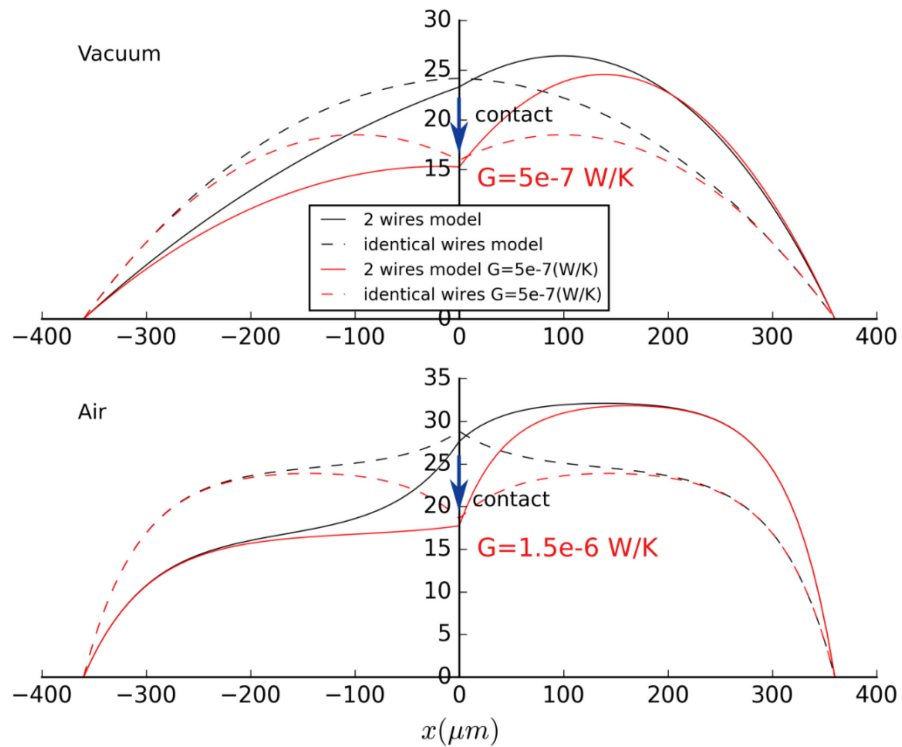


**Figure 5-4:  $2\omega$  temperature profile of the  $1.3\mu\text{m}$  thermocouple probe under air and vacuum conditions**

The parameters used are:

- An excitation RMS current of 3.4 mA at 57 Hz; a coefficient of convection  $h = 6500 \text{ W} \cdot \text{m}^{-2} \cdot \text{K}^{-1}$ ; a thermal conductance  $G = 5 \times 10^{-7} \text{ (W/K)}$  in the contact case under vacuum.

- An excitation RMS current of 1 mA at 57Hz; a coefficient of convection  $h = 1 \text{ W.m}^{-2}.\text{K}^{-1}$ ; a thermal conductance  $G = 1.5 \times 10^{-6} \text{ (W/K)}$  in the contact case under vacuum.

	Platinum	Platinum-10%Rhodium	Average
Conductivity ( $\text{W.m}^{-1}.\text{K}^{-1}$ )	71.6	52.0	61.8
Density ( $\text{kg.m}^{-3}$ )	21500.0	19970.0	20735.0
Specific heat capacity ( $\text{J.kg}^{-1}.\text{K}^{-1}$ )	133.0	144.1	138.55
Electrical resistivity ( $\text{Ohm.m}$ )	$9.81 \times 10^{-8}$	$19.0 \times 10^{-8}$	$14.41 \times 10^{-8}$

**Table 5-1: Physical parameters of Platinum and Platinum-10% Rhodium wire**

For thermocouple probe measurements, only the junction  $2\omega$  temperature  $\theta_{2\omega}$  and the average  $2\omega$  temperature  $\overline{\theta_{2\omega}}$  can be measured through the second and the third harmonics ( $V_{2\omega}, V_{3\omega}$ ) of the probe voltage respectively. The temperature at thermocouple junction and the average temperature can be expressed in the following terms.

$$\theta_{2\omega}(0) = \frac{1}{2} I_0^2 \frac{\left\{ \begin{array}{l} R_j S m_1 m_2 [ch(L(m_1 - m_2)) - ch(L(m_1 + m_2))] + 4\sigma_2 m_1 sh(m_1 L) \dots \\ + 4\sigma_1 m_2 sh(m_2 L) - 2\sigma_2 m_1 [sh(L(m_1 - m_2)) + sh(L(m_1 + m_2))] \dots \\ - 2\sigma_1 m_2 [sh(L(m_2 - m_1)) + sh(L(m_1 + m_2))] \end{array} \right\}}{\left\{ \begin{array}{l} S\lambda_1 m_1 [sh(L(m_1 - m_2)) - sh(L(m_1 + m_2))] \dots \\ S m_1 m_2 \left\{ \begin{array}{l} + S\lambda_2 m_2 [sh(L(m_2 - m_1)) - sh(L(m_1 + m_2))] \dots \\ + Gch(L(m_1 - m_2)) - Gch(L(m_1 + m_2)) \end{array} \right\} \end{array} \right\}} \quad (5-9)$$

$$\overline{\theta_{2\omega}} = \frac{1}{2L} \int_{-L}^L \theta_{2\omega}(x) dx \quad (5-10)$$

- *Probe calibration*

The  $V_{2\omega}$  and  $V_{3\omega}$  can be converted from the  $\theta_{2\omega}(0)$  and the  $\overline{\theta_{2\omega}}$  values and vice versa by the following relation.

$$\left\{ \begin{array}{l} \theta_{2\omega} = \frac{V_{2\omega}}{S_{Seebeck}} \\ \theta_{3\omega} = \frac{2V_{3\omega}}{\alpha R I_0} \end{array} \right. \quad (5-11)$$

S represents the Seebeck coefficient of the junction at its mean temperature.

The use of the identical wires model allows us to simplify the term (5-9) and (5-10) by considering:  $\sigma = \sigma_1 = \sigma_2$ ;  $\lambda = \lambda_1 = \lambda_2$ ;  $m = m_1 = m_2$ .

$$\theta_{2\omega}(0) = \frac{1}{2} I_0^2 \frac{R_j \sinh(mL) + \frac{4\sigma}{5m} [\cosh(mL) - 1]}{2\lambda Sm \cosh(mL) + G \sinh(mL)} \quad (5-12)$$

$$\overline{\theta_{2\omega}} = \frac{1}{2} \frac{I_0^2 \sigma}{S^2 km^2} \left\{ \frac{2G - m(GL - 2\lambda S) \sinh(mL) - m(GL - 2\lambda S) \cosh(mL)}{mL [2\lambda Sm \cosh(mL) + G \sinh(mL)]} \right\} \quad (5-13)$$

The junction temperature  $\theta_{2\omega}(0)$  and the average temperature  $\overline{\theta_{2\omega}}$  terms allows to calibrate the probe characteristics (L and R) without contact ( $G=0$ ). A similar methods of probe identification was also proposed by Lefèvre et al for a Wollaston resistive probe[88].

In the Figure 5-5, a comparison of the experimental results with theoretical simulation using an identical wire model for 1.3 $\mu\text{m}$  of diameter thermocouple probe under vacuum and under air when the probe is far from the contact. The  $2\omega$  and  $3\omega$  harmonic responses are measured and simulated at low frequency of 9Hz with different intensities. Their frequency responses are also plotted in the Bode diagram. The probe's fitting parameters used is also coherent with the SEM images of the 1.3 $\mu\text{m}$  thermocouple probe Figure 5-6 with  $L=360\mu\text{m}$ ,  $R=0.65\mu\text{m}$ .

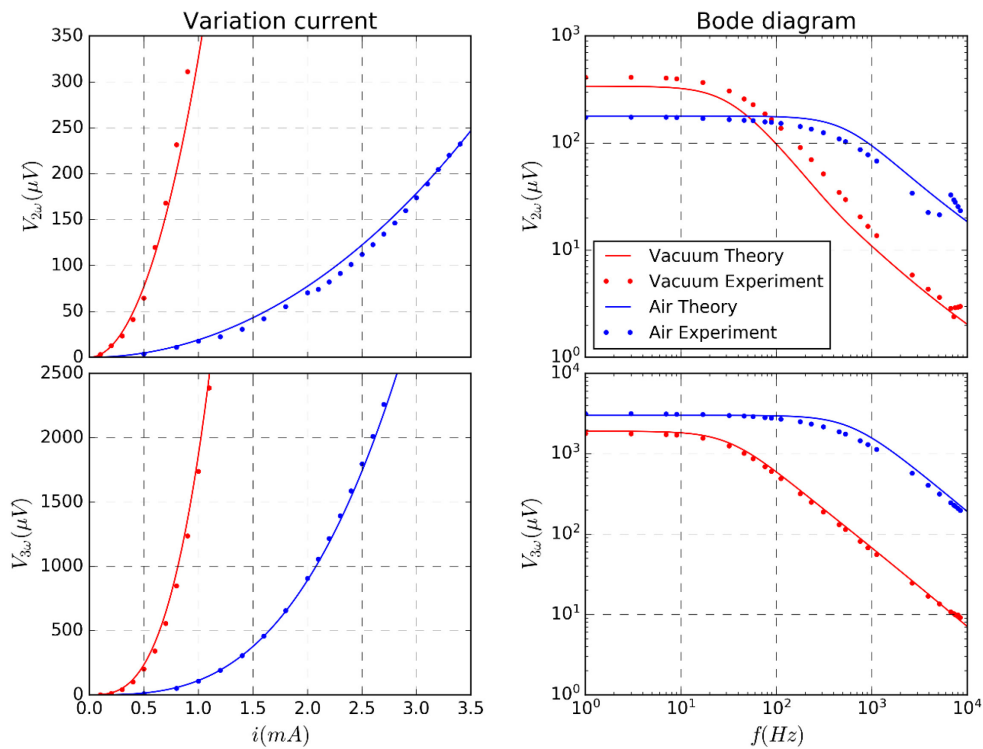


**Figure 5-5: Comparison of theory and measurement of  $2\omega$  and  $3\omega$  response for 1.3  $\mu\text{m}$  thermocouple**

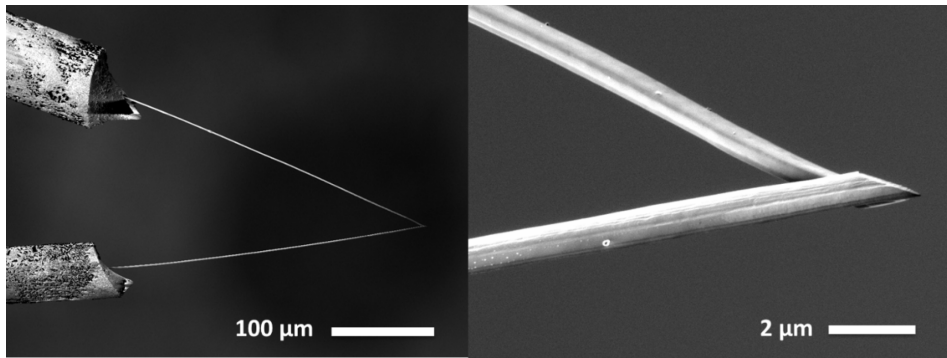


**Figure 5-6: SEM images of a 1.3 $\mu\text{m}$  thermocouple**

The same fitting process was also made with a 5 $\mu\text{m}$  probe, providing coherent results. Figure 5-7 represents the fitting curves for a 5 $\mu\text{m}$  thermocouple probe with  $L=345\mu\text{m}$ ,  $R=2.5\mu\text{m}$ ,  $R_j = 0.9 \text{ Ohm}$  with a supplied current. The convective coefficient in air is changed to  $h = 2300 \text{ W} \cdot \text{m}^{-2} \cdot \text{K}^{-1}$  due to the probe's size effect.

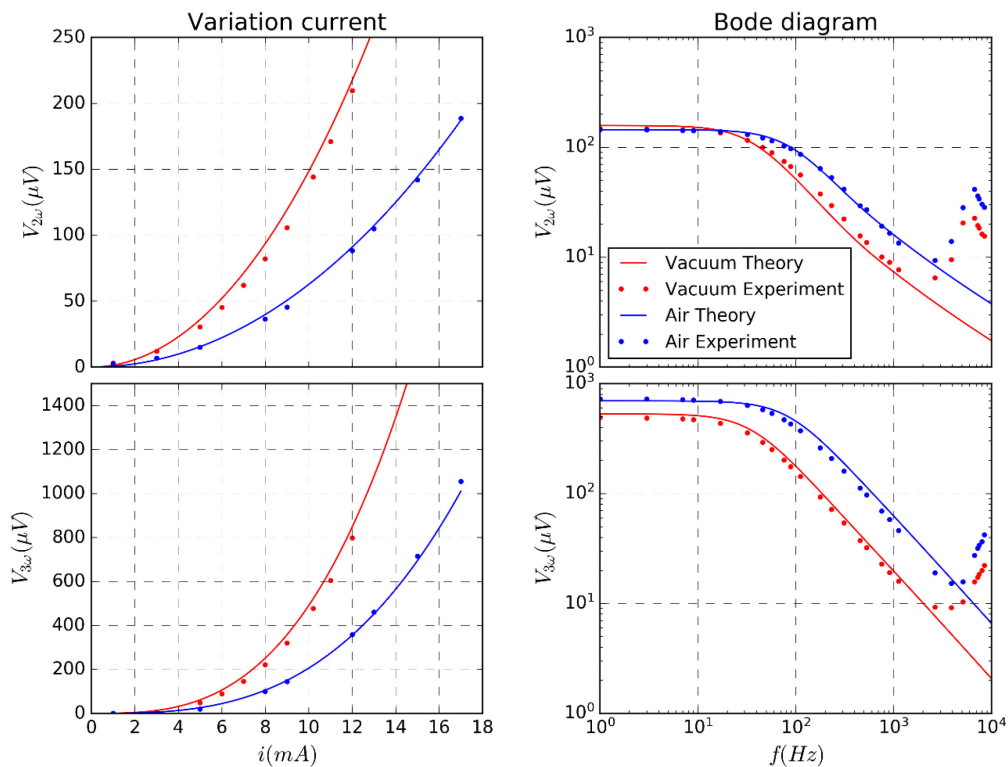


**Figure 5-7: Comparison of theory and measurement of  $2\omega$  and  $3\omega$  response for 5  $\mu\text{m}$  thermocouple**

The probe time constant is higher for the 5 $\mu$ m thermocouple and decreases when we change from air to vacuum due to the missing of air on heat excavation. We can also deduce the cut-off frequency from the time constant (Table 5.2).

	<b>T1</b>	<b>T5</b>
Vacuum (Hz)	100	57
Air (Hz)	1000	200

**Table 5-2: Cut-off frequency of thermocouples**

- *What we measure?*

We have shown that the probe thermal response (junction and mean wires temperatures) to an excitation can be measured and simulated under air and vacuum with  $G=0$  (non-contact). To measure the tip-sample conductance when the tip is in contact, it is practical to propose a dimensionless ratio deduced directly from the measurements (non-contact and contact). We introduce here a ratio  $(\theta_{nc} - \theta_c)/\theta_c$ . Where  $\theta_{nc}$  is the probe  $2\omega$  temperature at thermocouple junction when the probe is far from the sample (non-contact  $G = 0$ ) and  $\theta_c$  is the temperature when the probe is put in contact with a sample ( $G \neq 0$ ). From equation (5-9), this ratio presents a linear behaviour with the thermal conductance  $G$  through a constant  $\kappa$ .

$$\frac{\theta_{nc} - \theta_c}{\theta_c} = \kappa G \Rightarrow \frac{V_{2\omega \text{ non contact}} - V_{2\omega \text{ contact}}}{V_{2\omega \text{ contact}}} = \kappa G \quad (5-14)$$

The term  $\kappa$  gives a practical direct conversion to the equivalent conductance. Calculated from (Eq 5-9 and 5-14)  $\kappa$  can be given by the following formula for a 2-wire model.

$$\kappa = \frac{[\cosh(L(m_1 - m_2)) - \cosh(L(m_1 + m_2))]}{S\lambda_1 m_1 [\sinh(L(m_1 - m_2)) - \sinh(L(m_1 + m_2))] + \dots + S\lambda_2 m_2 [\sinh(L(m_2 - m_1)) - \sinh(L(m_1 + m_2))]} \quad (5-15)$$

While (Eq 5-16) shows the  $\kappa$  expression extracted from the identical wire model, the simplification of this term is more practical for probe study and simulation and decrease the systematic error to calculate the equivalent thermal conductance.

$$\kappa = \frac{\tanh(mL)}{2\lambda m S} \quad (5-16)$$

If we define the probe conductance  $G_p = \lambda S/L$ . The equation 5-16 will become.

$$\kappa = \frac{\tanh(mL)}{2G_p mL} \quad (5-17)$$

The term  $\kappa$  is only determined by the probe geometrical factor (L, R...) and thermophysical properties but not by the probe's temperature and the contact resistance.

This AC measurement configuration should be performed at low frequency excitation below the cut-off frequency or around the cut-off frequency to obtain the highest phase sensitivity. Indeed, when the frequency increases the absolute value of  $\kappa$  decreases to zero which reduce the microscope sensitivity. On the other hand, the phase value of  $\kappa$  increased can lead to interesting phase information of the sample.

$$\omega \rightarrow \infty, \left| \frac{\tanh(mL)}{2G_p mL} \right| \rightarrow 0, \arg\left(\frac{\tanh(mL)}{2G_p mL}\right) = 90^\circ \quad (5-18)$$

- *The uncertainty of measurements*

The uncertainty of  $\kappa$  can be estimated through a propagation error process (Appendix 4)

$$\delta_\kappa = \sqrt{(\delta_{mS})^2 + \left( \left| \frac{mL}{\tanh(mL)} [1 - \tanh^2(mL)] \right| \delta_{mL} \right)^2} \quad (5-19)$$

with

$$\delta_{mS} = \sqrt{(\delta_R/2)^2 + (2\delta_R)^2 + (\delta_h/2)^2} \quad (5-20)$$

$$\delta_{mL} = \sqrt{(\delta_R/2)^2 + (\delta_L)^2 + (\delta_h/2)^2} \quad (5-21)$$

The uncertainty values of R and L can be easily defined through SEM images with a high resolution however after calibration process this value can be modified. The calibrated values can be different compared to the measured values but not higher than 5%. The coefficient of convection error in the (Eq 5-20, 5-21) only appears when there is no correlation between the thermal convection and the size effect. However, the correlation is established through the calibration process described previously. This error is still added here to carefully estimate the total error. The value of the coefficient of convection measured by L. Thiery [124] for resistive wire are around  $2300 \text{ W.m}^{-2}.\text{K}^{-1}$  and  $6500 \text{ W.m}^{-2}.\text{K}^{-1}$  for  $1.3\mu\text{m}$  and  $5\mu\text{m}$  of diameter

respectively. The uncertainty values of  $\delta V$  is measured through the  $V_{2\omega}$  standard deviation of the setup.

Probe	Condition	$\delta R$	$\delta L$	$\delta h$	$\delta \kappa$	$\delta V$	$\delta G$
T1	Vacuum	5%	5%	0	10.4%	7.6%	12.9%
	Air	5%	5%	10%	11.4%	2.1%	11.6%
T5	Vacuum	5%	5%	0	10.7%	3%	11.1%
	Air	5%	5%	10%	11.5%	1.5%	11.6%

**Table 5-3: The uncertainty estimation of different parameters**

### 5.2.2 Numerical model with coupling harmonics and a comparison with analytical models

In the precedent analytical model, we have considered that the electrical resistivity does not depend on the temperature. However, Gomès et al have shown that this approximation can lead to an error of 10% in the calculation of the Wollaston probe temperature due to a significant temperature coefficient of resistance for Platinum and Platinum-10%Rhodium alloy. A more complicated approach must then be considered for which the electrical resistivity is also a function of temperature such  $\sigma = \sigma_0(1 + \alpha\Delta T)$ . Introducing this new term leads to a coupling effect that create a temperature variations at many harmonics  $2n\omega$  [19] (Appendix 5). The equation can be solved analytically using a matrix of n equations for n harmonics which is complicated for a two different wires thermocouple probe.

- *Model*

A simpler approach consists in a numerical calculation in time domain, followed by a Fourier transform to return the harmonic values. A 1D finite volume model is built (Figure 5-8) and solved using Numpy packages for Python using Crank-Nilcoson method (Appendix 5). The probe is separated into two parts with different parameters from material properties representing the two different wires.

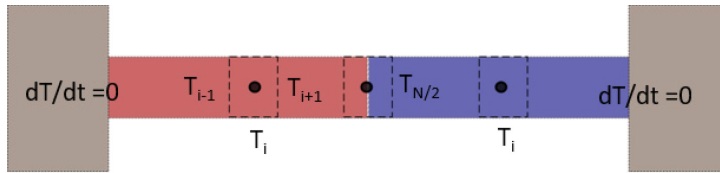


**Figure 5-8: 1D finite volume model for a thermocouple probe**

They are subdivided into  $N$  elements where  $N$  is an odd number. Figure 5-9 depicts the mesh elements schematic that describe the energy exchange of one element with others and with the environment. The temperature of each element is considered as homogenous. The normal element case described the heat exchange of the element  $i$  when  $i$  is not the boundary element from the base or the junction  $i \neq 1, N, (N - 1)/2$ . The centred element  $i = (N - 1)/2$  represents the thermocouple junction. This element is divided into two different parts with a heat exchange through equivalent conductance. Similar to analytical model, here, the constant temperature boundary condition at the tip base (with  $= 1, N$ ) is chosen.

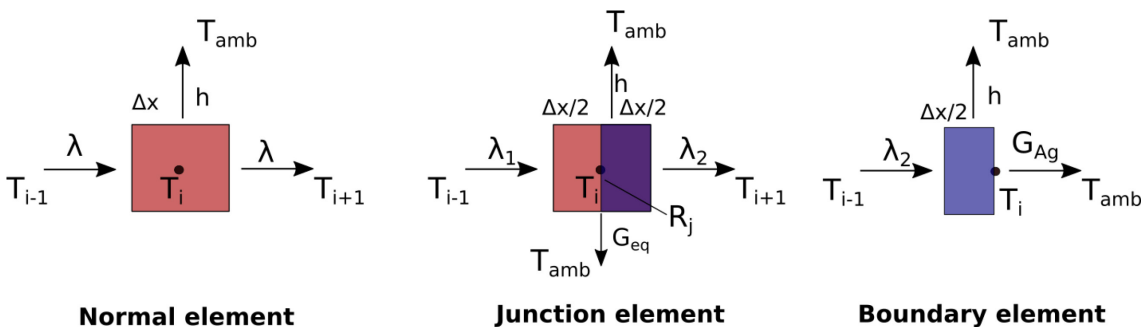


**Figure 5-9: Mesh elements**

Normal elements along the probe wire has a length of  $\Delta x$ . The relation below is obtained when considering the energy balance of these elements. The material properties are chosen accordingly to the element location,

$$S\rho c\Delta x \frac{dT(i)}{dt} = \frac{\lambda[T(i-1)+T(i+1)-2T(i)]}{\rho c\Delta x^2} + hp\Delta x(T_{amb} - T(i)) \dots \quad (5-22)$$

$$\dots + \frac{\sigma\Delta x(1+\alpha(T(i)-T_{amb}))I^2}{S}$$

The boundary condition is described in the Equation (5-16) for the thermocouple junction and the Equation (5-17) for the thermocouple base.

$$S\rho c\Delta x \frac{dT(i)}{dt} = \frac{k_2 S [T(i+1) - T(i)]}{\Delta x} + \frac{k_1 S [T(i-1) - T(i)]}{\Delta x} + hp\Delta x (T_{amb} - T(i)) \quad (5-23)$$

$$\dots + G(T_{amb} - T(i)) + R_j I^2 + \frac{\sigma \Delta x (1 + \alpha(T(i) - T_{amb})) I^2}{s}$$

$$T(1) = T(N) = T_{amb}, \quad (if G_{Ag} \rightarrow \infty) \quad (5-24)$$

- **Results**

Figure 5-10 depicts the temperature temporal solutions at the junction of 1.3µm thermocouple under vacuum condition with a supplied current of 1mA, 57Hz. The parameters used in the simulation is exactly same as those used for analytical model in the last section 5.2.1. The solution was made with a mesh of 101 elements and a timespan of 20 periods. The stabilization time is estimated around 20ms from the calculation. For a lock-in amplifier technique, it takes at least 5 oscillating periods to takes a reliable measurement, waiting time for a measurement is therefore at least 60ms. A Fourier transform of the junction temperature shown the presence of different harmonics  $2\omega, 4\omega, 6\omega, 8\omega \dots$

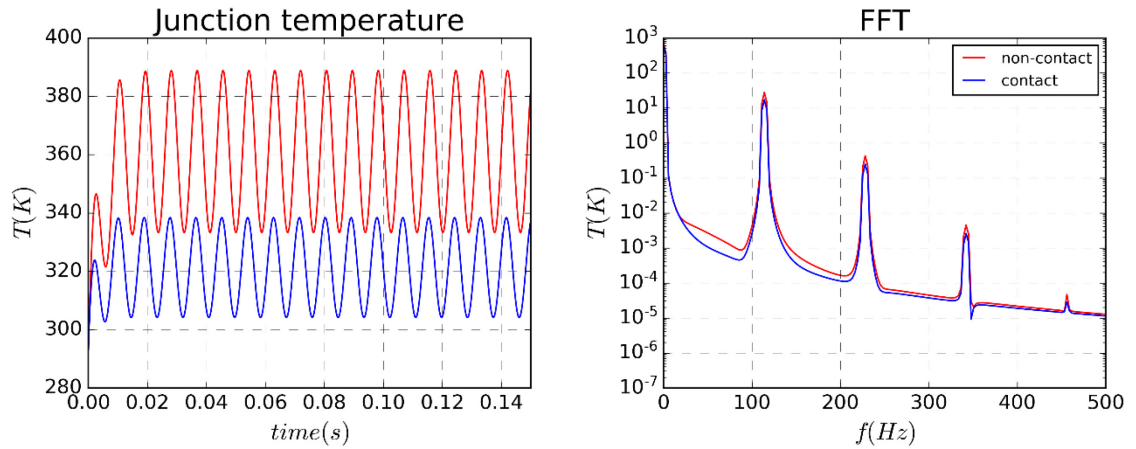


**Figure 5-10: Simulated temporal junction temperature of 1.3µm thermocouple and its FFT spectrum (non-contact and in-contact)**

The thermocouple voltage is given in the following term by combining the Seebeck voltage and the Joule voltage.

$$V_{tc} = \frac{T_{junction}}{S_{Seebeck}} + IR(1 + \alpha(\bar{T} - T_{amb})) \quad (5-25)$$

Figure 5-11 depicts the time evolution of probe voltage in and out of contact and its Fourier transform in frequency domain. The appearance of odd and even harmonics is

an error source to the analytical models however it can also give more information to the SThM measurement.

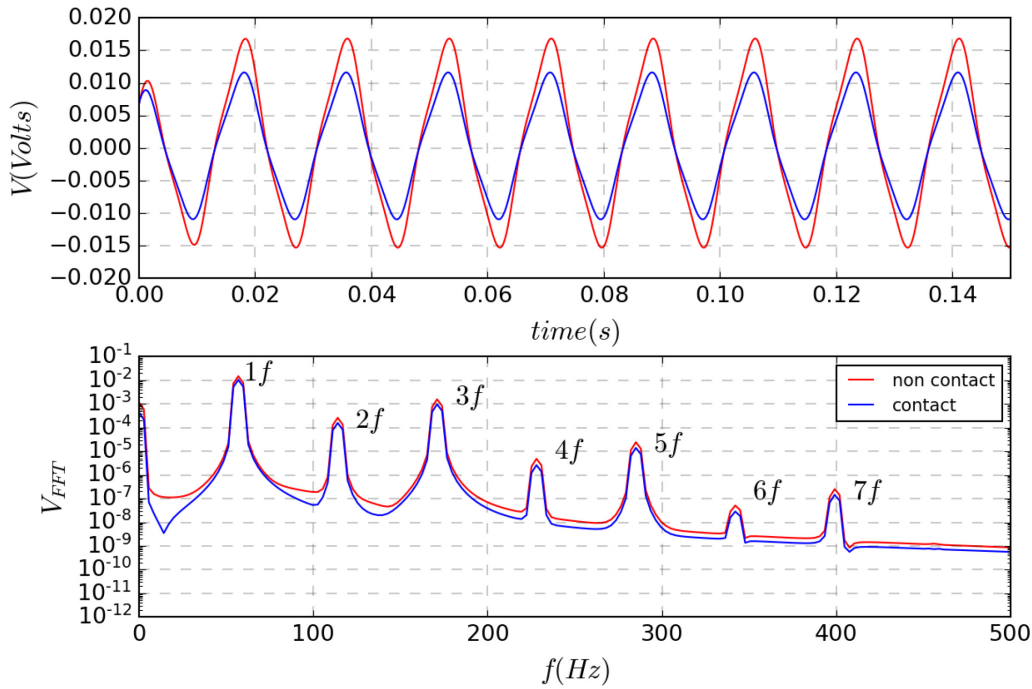


Figure 5-11: Simulated voltage response of 1.3 thermocouple

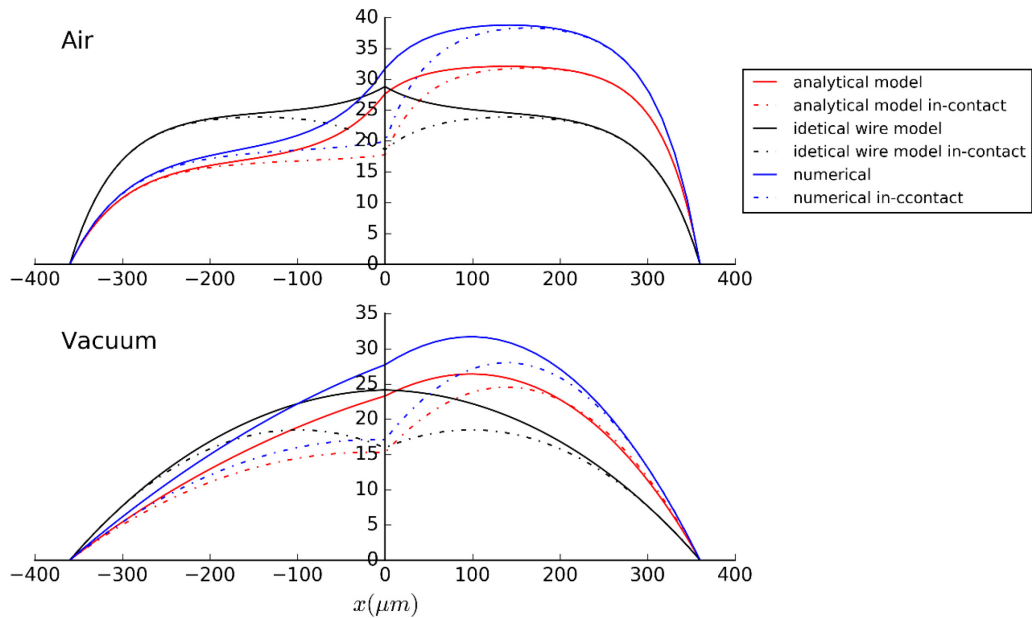


Figure 5-12:  $2\omega$  temperature profile of the  $1.3\mu\text{m}$  thermocouple under air and vacuum

The Figure 5-12 describes the temperature profile calculated by different models (numerical model with coupling effect, 2 wires analytical model and identical wires analytical model) with the same supplied current as in the Figure 5-10.

- *Discussion*

The results give an error of around 10% between the non-coupling analytical model and a coupling numerical model for usual levels of current. The error in vacuum is higher than in air that is logical when considering the effect of a higher time constant under vacuum and a longer thermal diffusion.

Figure 5-13 shows the ratio  $\Delta\theta/\theta$  relative error calculated for the  $1\mu\text{m}$  probe and the  $5\mu\text{m}$  probe under vacuum and air. Errors increase with the rise of probe temperature from around 1% to 100%.

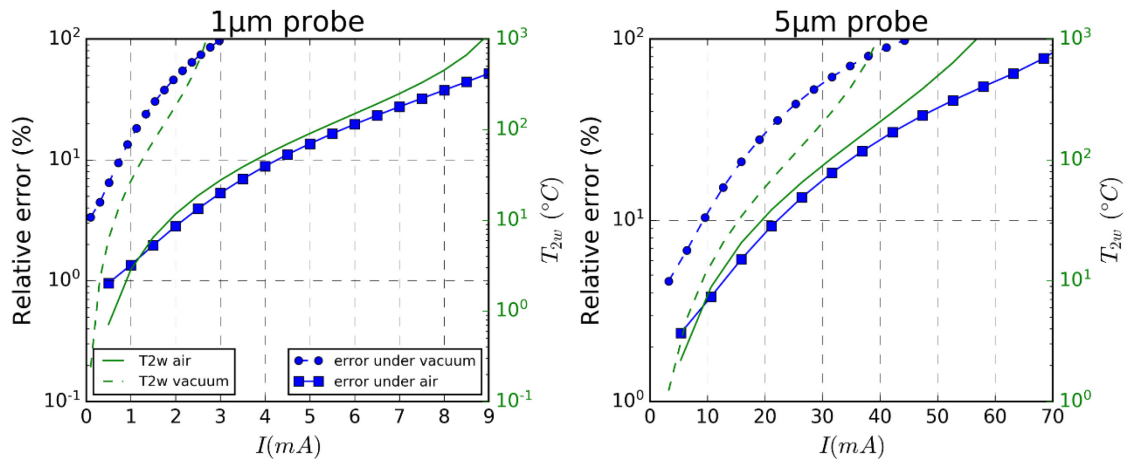


**Figure 5-13: Relative error between coupling model and identical wire analytical model for  $1.3\mu\text{m}$  and  $5\mu\text{m}$  thermocouple**

The error around 10% at normal operation condition permits to conclude that the identical wire analytical model is still valid. However, one must be careful to use the simple model and the probe should be operated at low temperature possible to minimize these errors. Figure 5-14 depicts the  $\Delta\theta/\theta$  ratio calculated when changing the probe length. The error increases when the probe length increases for the vacuum case due to the increase of the resistance and the rise of temperature in the wire element. This figure also shows that the optimization length  $L$  at which the ratio

attends a good sensitivity with small error is around 300 $\mu\text{m}$  for both 1 $\mu\text{m}$  and 5 $\mu\text{m}$  thermocouple.

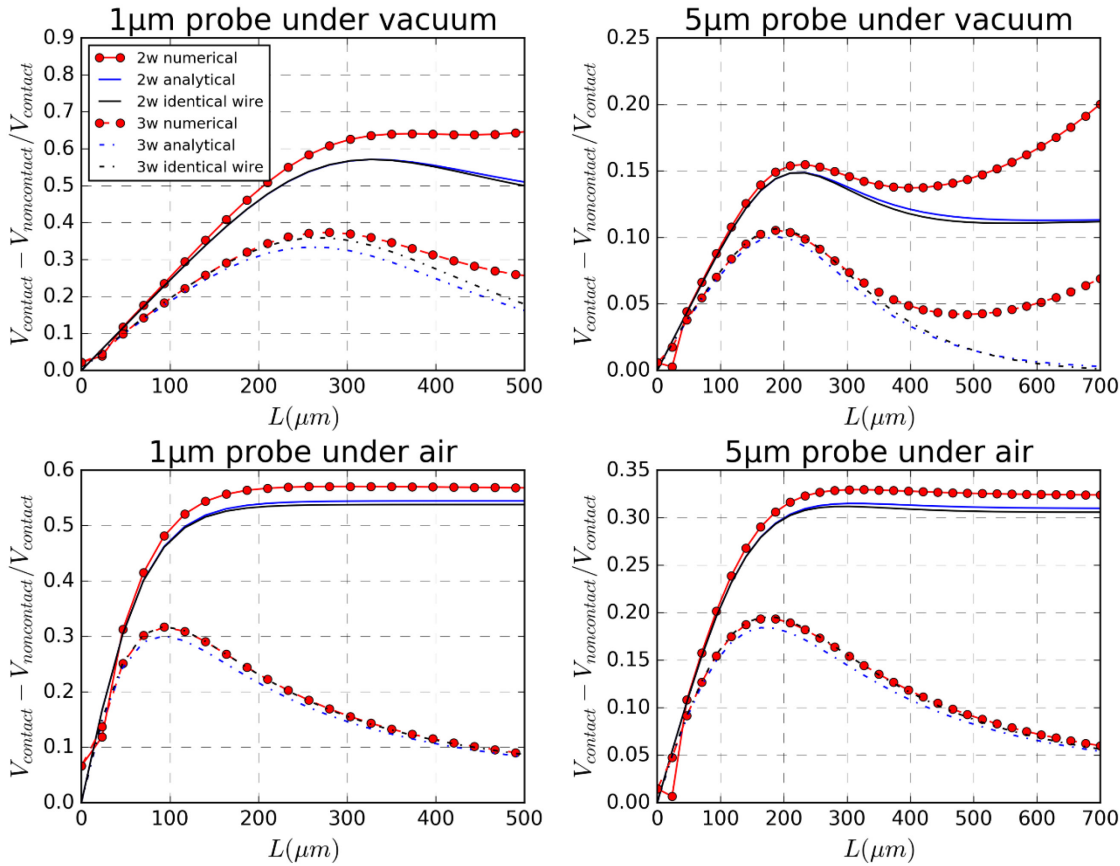


Figure 5-14:  $\Delta\theta/\theta$  ratio as function of probe length

### 5.3 Probe calibration using reference materials

In the last parts, we have described the AC thermal model (analytical and numerical models) of a thermocouple probe. Simulation parameters have been fitted using non-contact measurements. In this section, we will study the tip-sample heat transfer mechanism through a series of measurements under air and vacuum. By comparing with a simple model, these measurements will help to clarify the role of air and solid-solid heat transport.

#### 5.3.1 Calibrating materials

As an exercise of the Quantiheat project, a list of calibration materials has been proposed by the consortium to calibrate SThM probes in active mode and study the tip-sample heat transfer principle and the microscope efficiency (error, sensibility and

working range) for thermal conductivity measurements. Materials conductivities range from around 0.1 to 100 W/m.K. The samples are fabricated and polished by a specified protocol. The idea is to obtain a series of samples whose roughness stays comparable and below 10 nm typically ( $R_a$ ). These samples can be used as a calibration tool for SThM probes in order to measure thermal conductivity of any other bulk sample. The materials must also be insensitive (semiconductor and non-conductor materials) to the oxidation of ambient air environment. Sample size is chosen (10mm in diameter and 1 mm in thickness) so that their thermal conductivity can be verified by the other methods. Results of measured thermal conductivities by LNE are given in Table 5-4:

Material	Code	Thermal conductivity (W/m.K)	Heat capacity	Density (kg/m <sup>3</sup> )	Roughness $R_{ms}$ (nm)	Hardness (GPa)
PMMA	S-TH-cal1	0.187	1430	1180	6.43	0.2
POM-C	S-TH-cal2	0.329	1440	1400	15.7	0.32
Glass	S-TH-cal22	1.11	763	2197	1.90	6.21
Fused SiO <sub>2</sub>	S-TH-cal3	1.28	738	2190	0.73	5.10
ZrO <sub>2</sub>	S-TH-cal20	1.95	457	5855	1.58	1.22
TiO <sub>2</sub>	S-TH-cal18	9.15	698	4174	-	11.0
Al <sub>2</sub> O <sub>3</sub>	S-TH-cal9	29.8	765	3920	10.0	25.8
Al <sub>2</sub> O <sub>3</sub> mono	S-TH-cal21	36.9	769	4002	0.69	22.15
Ge	S-TH-cal16	52.0	310	5294	0.57	8.76
Si p++	S-TH-cal13	93.4	712	2330	1.47	13.9

**Table 5-4: Thermo-physical parameters of reference materials (provided by LNE)**

Thanks to the custom programmable microscope, measurements for all samples are automatically controlled and performed in a same day to maintain the maximum repeatability results with identical environmental conditions (laboratory environment, measurement devices...). The measurements for all samples listed were performed under vacuum ( $P=4\text{Pa}$ ) and under air ambient condition to compare and study the effect of air on the measurement. For every sample, the measurements were taken 25

times (5 times repeated at 5 different locations) by recording the  $2\omega, 3\omega$  voltages far away from the contact and during contact.

### 5.3.2 Under vacuum measurements

- *Calibration process*

Eleven different materials are placed together in the vacuum chamber. Thanks to the controllable motorized stage, the sample position can be predetermined and recorded, the measuring time distance between each sample is minimized around 10 minutes which can help to reduce the systematic error. It takes around 3 seconds on tip-in-contact position to guarantee the thermal stabilization. The contact force is estimated around 10nN. The same tip as in the Figure 5-6 were used with a supplied current of  $I=1\text{mA}$  and  $f=57\text{ Hz}$ . The  $2\omega$  voltage value far away from the contact (4 mm)  $V_0 = 232\mu\text{V}$  and the probe AC temperature is calculated around  $39^\circ\text{C}$  above ambient. Figure 5-15 depicts the ratio  $(V_0 - V_{\text{contact}})/V_0$  and  $V_{\text{contact}}/(V_0 - V_{\text{contact}})$  versus thermal conductivity and its inversion respectively.

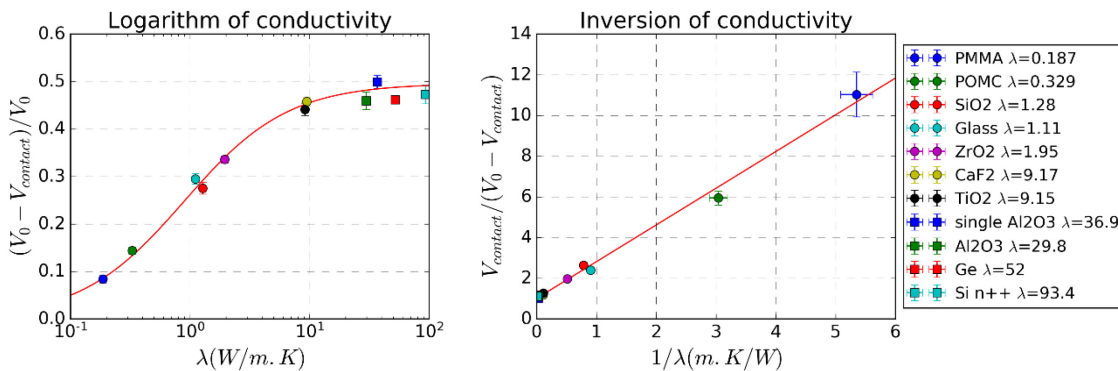


**Figure 5-15:  $\Delta V/V$  and  $V/\Delta V$  as function of thermal conductivity**

- *Modelling*

A linear dependence of the contact ratio  $V_{\text{contact}}/(V_0 - V_{\text{contact}})$  versus thermal conductivity  $1/\lambda_s$  have been observed from the Figure 5-15. A linear fit has been plotted in red in the figure, corresponding to the expression:

$$\frac{V_{\text{contact}}}{V_0 - V_{\text{contact}}} = \frac{A}{\lambda_s} + B \quad (5-26)$$

Where A and B are fitting constant, or in the Eq 5-27 if the ratio  $(V_0 - V_{contact})/V_0$  is considered.

$$\frac{V_0 - V_{contact}}{V_0} = \frac{\lambda_S}{(1+B)\lambda_S + A} \tag{5-27}$$

A least squares method has been used to calculate A and B constants. The results with statistical analysis value are given in the Table 5-5: Statistical results

Sample	A	$\sigma_A$	B	$\sigma_B$	R <sup>2</sup>
25 measurements x 11 samples	1.8030	0.01714	1.0181	0.03316	0.9897

**Table 5-5: Statistical results of the linear regression ( $V/\Delta V$  and  $1/\lambda$ )**

The linear behaviour between the ratio  $V_{contact}/(V_0 - V_{contact})$  and  $1/\lambda$  is also proved by the theoretical probe-sample theoretical model. As earlier mentioned, the equivalent tip-sample conductance can be decomposed into two parts: the sample spreading conductance  $G_s$  and the contact conductance  $G_c$ . As presented in the chapter 2, the contact resistance is composed of many terms (radiation, air conduction, water meniscus, tip-sample solid conduction).

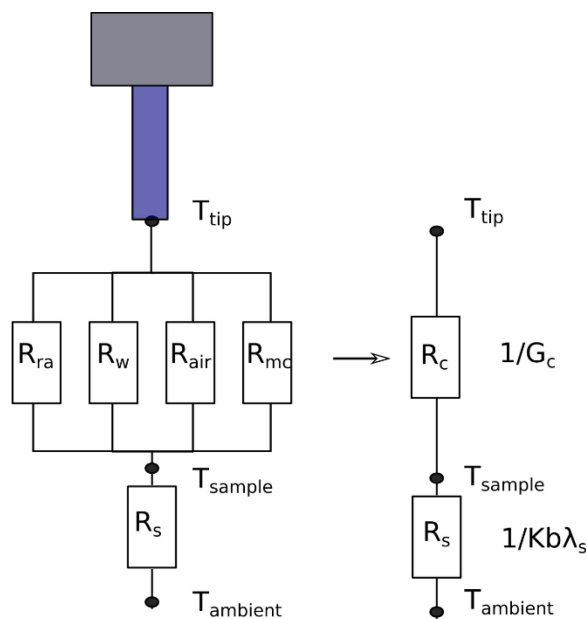


**Figure 5-16: Tip-sample heat transfer mechanism**

For vacuum conditions, the maximum tip temperature is  $T_{peak} = 106\text{ }^{\circ}\text{C}$ , only the tip-sample solid conduction is considered. The sample conductance follows thermal constriction relation  $G_e = Kb\lambda_s$ , where the K depends on the boundary conditions. The Table 5-6 presents the K factor for continuity boundary conditions of temperature and flux at the interface area.

Boundary condition	K
Constant temperature ( $0 < r < b$ )	2
Constant heat flux ( $0 < r < b$ )	$3\pi^2/16$

**Table 5-6: Boundary condition of thermal constriction**

Combining conductance parts ( $G_c$  and  $G_e$ ). The inversion of equivalent conductance  $1/G_{eq}$  therefore presents a linear dependence on the  $1/\lambda_s$ , we have:

$$\frac{1}{G_e} = \frac{1}{2b\lambda_s} + \frac{1}{G_c} \quad (5-28)$$

From the Eq 5-14, the  $G_{eq}$  can be converted directly from the ratio  $(V_{2\omega\ non\ contact} - V_{2\omega\ contact})/V_{2\omega\ contact}$  through  $\kappa$

$$\frac{V_{contact}}{V_0 - V_{contact}} = \frac{A}{\lambda_e} + B \quad (5-29)$$

$$\Rightarrow \frac{1}{G_e} = \frac{1}{\kappa} \frac{V_{contact}}{V_0 - V_{contact}} = \frac{1}{\kappa} \left( \frac{A}{\lambda_e} + B \right) \quad (5-30)$$

The equivalent conductance is calculated from the fit curve used in the Equation (5-30). The theoretical model proposed seems coherent with the experimental measurements. The error bars are calculated from the 15% error of  $\kappa$  (which is a rational approximation between coupling model and non-coupling model) and the standard error of 25 measurements for every sample.

From the fit curve values, the thermal contact radius  $b = 22.9 \pm 5\text{ nm}$  and the contact conductance  $G_c = 8.15 \pm 1.3 \times 10^{-7}\text{ W/K}$  are calculated. The b values seem to remain constant for every samples due to the surface polishing and the similar contact force.

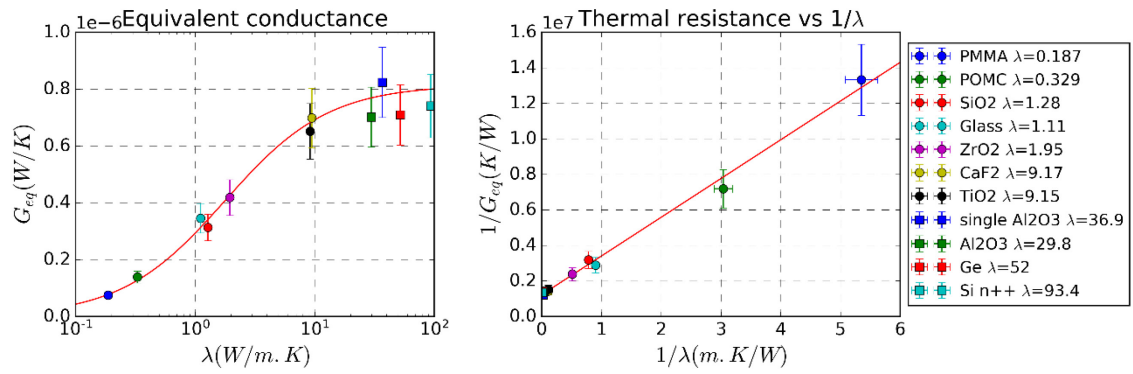


**Figure 5-17: Evolution of equivalent thermal conductance and resistance as function of sample conductivity**

- *Microscope working range under vacuum*

To calculate the maximum measurable thermal conductivity of the microscope, we recall the term  $\frac{V}{\Delta V} = \frac{A}{\lambda_s} + B$  as the microscope calibration curve under vacuum. The relative error  $\delta_{vacuum}$  of the microscope is defined by the error of the ratio  $V/\Delta V$ . The minimum ratio that the microscope can distinguish is  $B(1 + \delta_{vacuum})$ . Therefore, the maximum measurable value of conductivity can be written as:

$$\lambda_{s\ max} = \frac{A}{B(1 + \delta_{vacuum}) - B} = \frac{A}{B\delta_{vacuum}} \quad (5-31)$$

The relative error  $\delta_{vacuum}$  of ratio  $V/\Delta V$  is calculated from the standard deviation of the voltage measured giving the value of around 7.6%. This gives for the 1.3 $\mu$ m thermocouple under vacuum:  $\lambda_{s\ max} \approx 26$  W/mK.

- *Monte Carlo error analysis*

The consistency of the fitting parameters A, B is verified using a Monte Carlo estimation. Monte Carlo method permits to estimate the error of the fitted parameters regardless the complicated relationships of the parameters to the data[125]. The errors analysis process consists of 3 main steps:

1. Generate random number which satisfies the experimental results of the calibration sample. For example, 5000 random samples follow the normal distribution ( $mean(\lambda_s)$ );

$\sigma(\lambda_S)$  and  $(mean(V_{2\omega}); \sigma(V_{2\omega}))$  are generated for every reference sample (PMMA, POM-C, ... Si n++).

2. The A, B parameters of the fit curve are calculated 5000 times which is the number of the data set. The consistency of A, B parameters can be analysed through their data sets.

3. Relative errors of the microscope can be calculated depending on the measured voltage and its standard deviation.

The implement Python code of the simulation are shown in the Appendix 4. Using this program, the A and B distribution is plotted in the Figure 5-18, the standard deviation mean ratios are around 10% proves the consistency of the fitting model used.

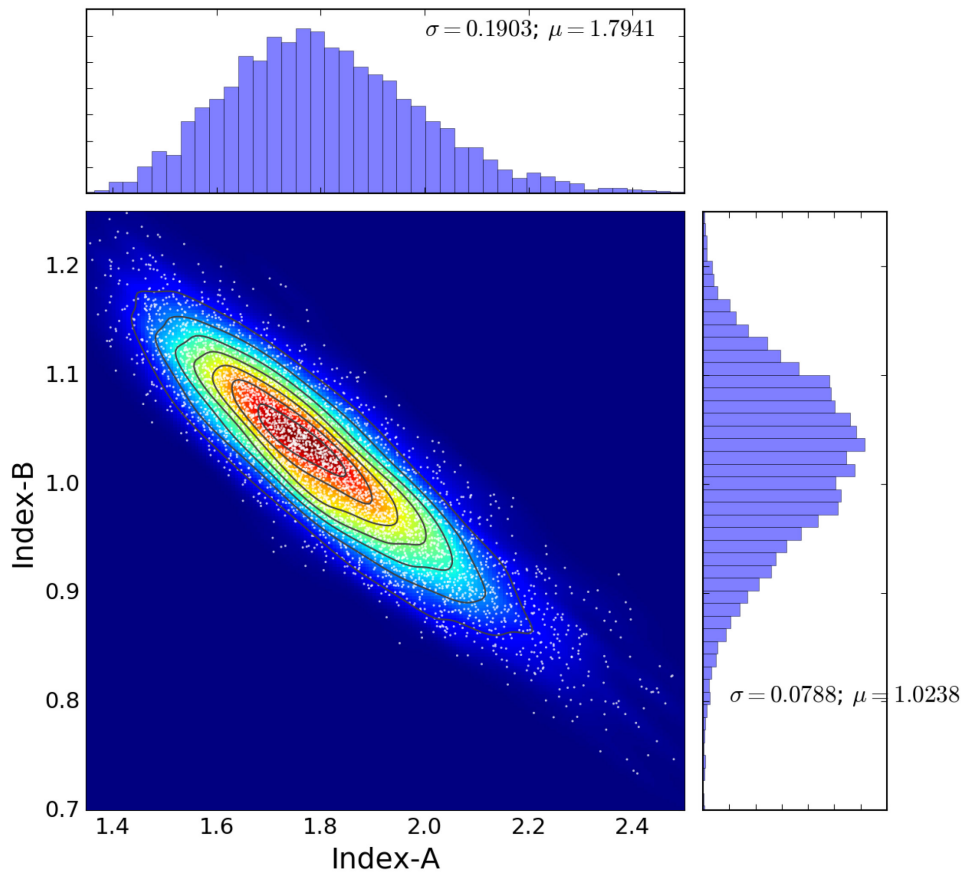


**Figure 5-18: Index-A and B distribution calculated by Monte Carlo method**

Figure 5-19 depicts the histogram of an error simulation at  $V_{2\omega} = 150 \pm 4 \mu V$  giving  $\lambda = 2.25 \pm 0.32 W/mK$ . The relative error calculated varies from 12% to 25% at the conductivity range of 0.11 – 5 W/mK.

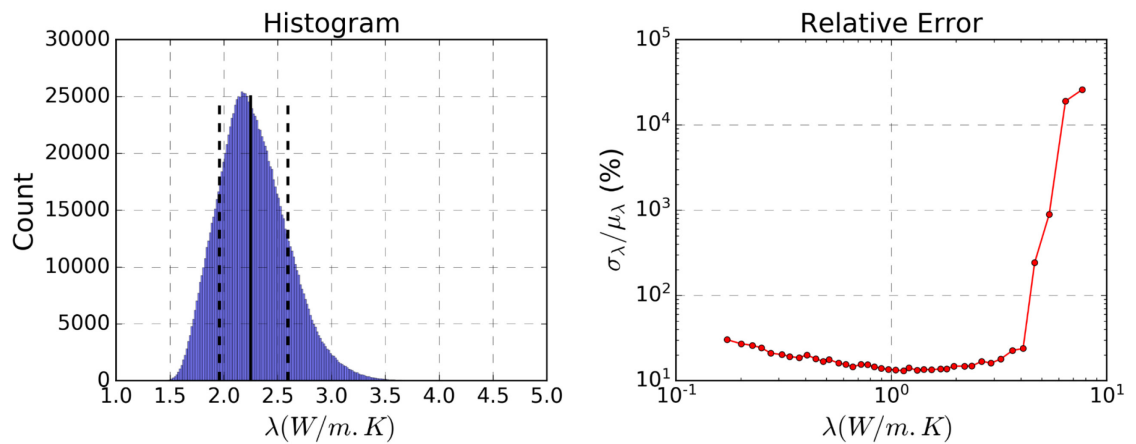


**Figure 5-19: An example of the error estimation ( $V=150\mu V$ ;  $\lambda=2.25$  W/mK) and relative error under vacuum calculated at different thermal conductivity**

The measurements on higher thermal conductivity materials are shown not reliable with the error estimated larger than 100%. However, measurements on high conductivity materials still present qualitative meaning, a Bayesian model can be used in the future for a better error estimation.

### 5.3.3 Ambient air measurements

The same measurements procedure was made in ambient conditions ( $P= 100000\text{Pa}$ ). The current supplied is at  $I=3\text{mA}$  and  $f=57\text{Hz}$ . The  $2\omega$  voltage at 4mm above the sample  $V_0 = 162\mu V$  ( $T_0 = 27^\circ\text{C} + T_{amb}$ ). The results are depicted in the Figure 5-24. There is no linearity between the ratio  $V_{contact}/(V_0 - V_{contact})$  and the  $1/\lambda_s$  on the data obtained. This non-linearity can be explained by the influence of air in the tip-sample heat transfer. Another contact model taking account the effect of air conduction on the non-linearity needs to be built.

- *Ambient air measurement modelling*

In his thesis [126], Lefèvre has shown that the thermal contact radius decreases when the sample thermal conductivity increases. This phenomenon can be explained by the

fact that when heat diffuses more efficiently from a point source, a similar relative temperature decrease requires less distance (Figure 5-20).

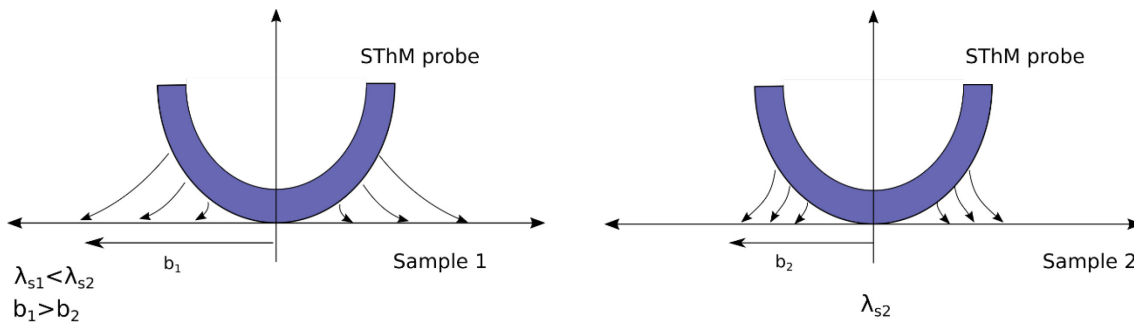


**Figure 5-20: Radius contact schematic on different conductivity samples**

The new contact model is built based on the assumption that the thermal radius  $b$  has a linear dependence over  $1/\lambda_s$ .

$$b = \frac{M}{\lambda_s} + b_0 \quad (5-32)$$

where  $M$  and  $b_0$  are constants which depend on the probe geometrical and the thermal conductivity of air.

A simple COMSOL FEM 2D axisymmetric model can verify the assumption. This is a steady-state model that demonstrates the dependence between the thermal contact radius and the sample thermal conductivity. As shown in Figure 5-19, the probe is represented by a conical platinum tip in a surround air environment. Constant temperature boundary conditions are used for the surrounding box and the probe base. The probe heat source is located along the central axis with a power of 4mW. Conduction heat transfer between different interfaces (probe-air, air-sample and tip-sample thermal conduction) using temperature and flux continuities are simulated and the result is depicted in the Figure 5-21.

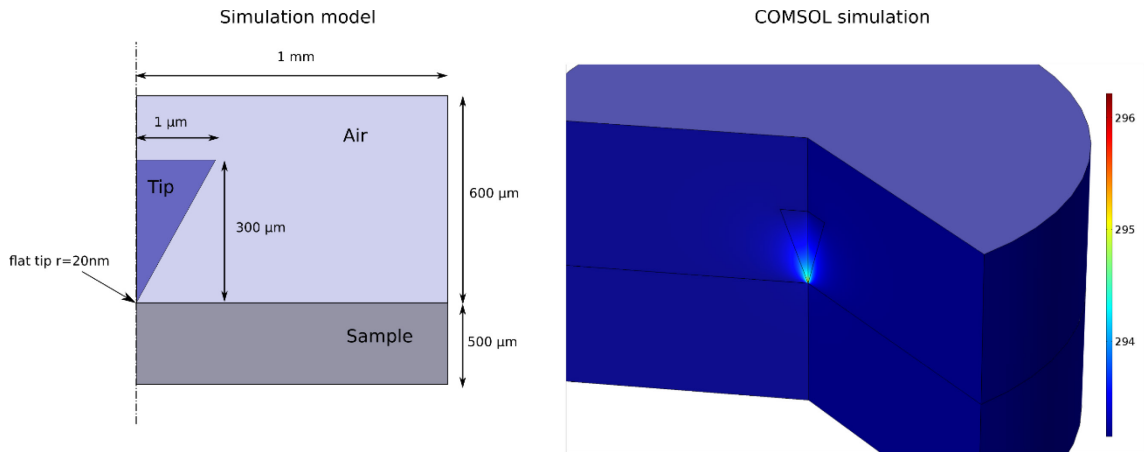


**Figure 5-21: COMSOL model of tip-sample heat transfer under air**

Simulations were made for different samples of which the thermal conductivity varies from 0.15 to 100 W/mK. Figure 5-22 shows the temperature distribution in two cases of sample: very low (left) and high thermal conductivity (right). These results illustrate the phenomenon schematic described in the Figure 5-20.

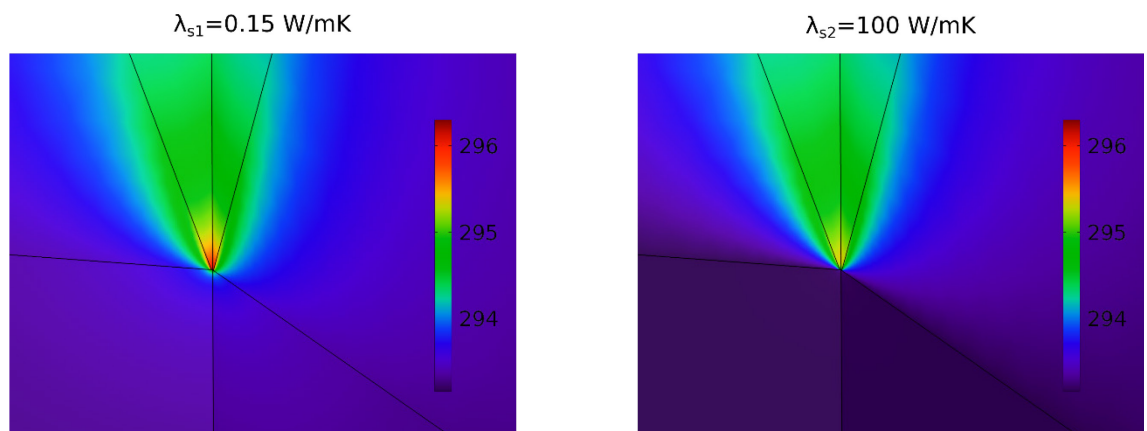


**Figure 5-22: System temperature simulations for low conductivity and high conductivity material**

Figure 5-23 presents the normalized temperature on the sample surface as a function of the distance to the tip contact point. To have an idea on the contact radius, we define here the thermal contact radius as the location where the temperature magnitude decreases of 90%. The evolution of thermal contact radius versus the sample thermal conductivity change is then depicted in the Figure 5-23b.

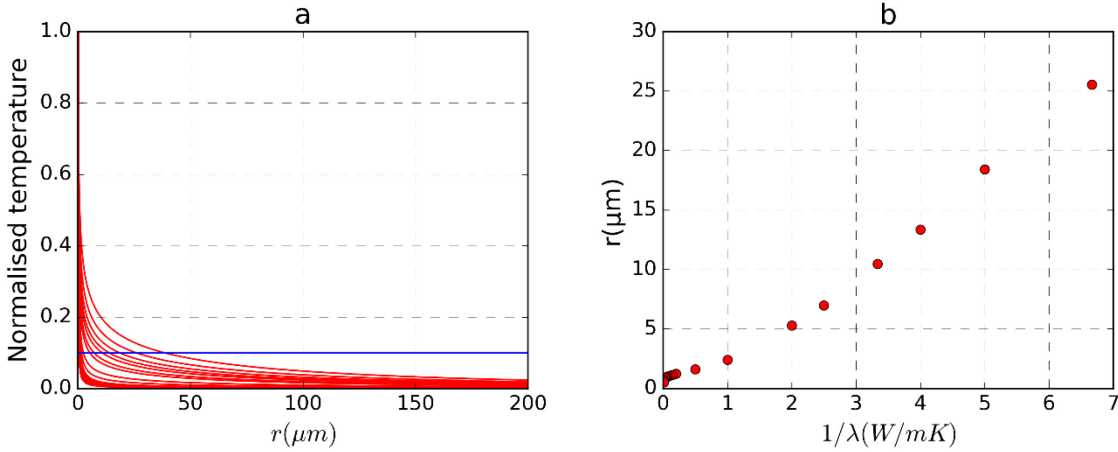


**Figure 5-23: Normalised temperature on the sample surface (a) and thermal radius (b) at different thermal conductivity**

As mentioned before, the thermal contact radius increases with the decreasing of sample thermal conductivity. The results obtained are almost linear for the low thermal conductivity materials however; there is still an uncertainty at higher thermal conductivity. The linear assumption (Eq 5-32) is therefore the simplest and effective way to simulate the thermal contact radius and introduce this term in an analytical model.

Using the same tip-sample equivalent conductance term (Eq 5-29) under vacuum, if the  $1/2b$  is considered as the slope (derivative) of the resistance  $1/G_{eq}$ , this term can be found by taking an integral of  $1/2b$ :

$$\frac{1}{G_{eq}} = \int \frac{1}{2b} d\left(\frac{1}{\lambda_s}\right) = \int \frac{1}{2\left(\frac{K}{\lambda_s} + b_0\right)} d\left(\frac{1}{\lambda_s}\right) \quad (5-33)$$

$$\begin{aligned} \Rightarrow \frac{1}{G_e} &= \frac{1}{2K} \ln\left(\frac{K}{\lambda_e} + b_0\right) + C \\ &= C_1 \ln\left(\frac{1}{\lambda_e} + C_2\right) + C_3 \end{aligned} \quad (5-34)$$

Knowing that

$$\frac{1}{G_{eq}} = \frac{1}{\kappa} \frac{V_{contact}}{V_0 - V_{contact}} \quad (5-35)$$

Therefore, the ratio  $V/\Delta V$  function is given by

$$\frac{V_{contact}}{V_0 - V_{contact}} = A \ln\left(\frac{1}{\lambda_e} + B\right) + C \quad (5-36)$$

Where A,B,C are constants of the fit curve.

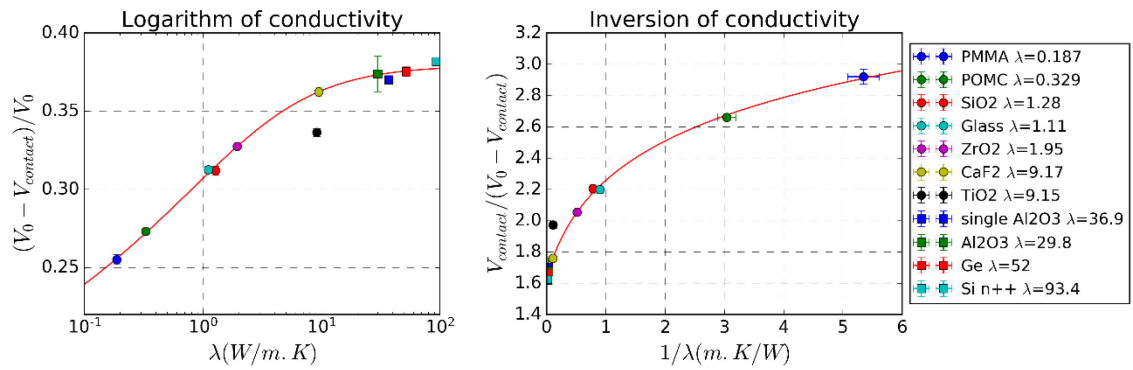


**Figure 5-24:  $\Delta V/V$  and  $V/\Delta V$  as function of thermal conductivity under air measurements and the fit curve**

From experimental results, the fitting parameters A,B,C are calculated by the least squares method for 250 measurements points (25 measurements x 10 samples except TiO<sub>2</sub>). Table 5-7: notes the fitting parameters of the calibration curve. The coefficient of determination  $R^2 = 0.991$  is closed to 1 (perfect fitting value) demonstrating the well-fitted results.

Sample	A	$\sigma_A$	B	$\sigma_B$	C	$\sigma_C$	$R^2$
25 measurements x 10 samples	0.4502	0.2053	0.3362	0.4140	2.1273	0.2849	0.9912

**Table 5-7: The fitting results and their statistical analysis**

The constants  $C_1 = A/\kappa, C_2 = B, C_3 = C/\kappa$  are calculated from the A, B, C values respectively to obtain the thermal conductance and resistance curve (demonstrated in the Figure 5-25).

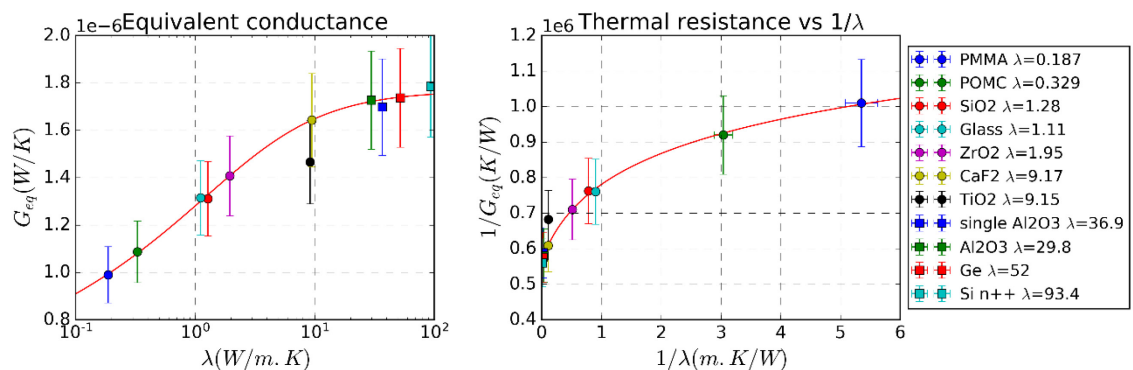


**Figure 5-25: Evolution of equivalent thermal conductance and resistance under air as function of sample conductivity and its inversion respectively**

The thermal contact diameter  $2b$  function is obtained by taking the derivative of the equivalent resistance  $1/G_e$ :

$$2b = \frac{1}{c_1 \lambda_s} + \frac{c_2}{c_1} \tag{5-37}$$

$$\Rightarrow M = \frac{1}{2c_1}; \quad b_0 = \frac{c_2}{2c_1} \tag{5-38}$$

C1	C2	C3	M	b0
155749	0.33622	735871	3.21e-6	1.08e-6

**Table 5-8: The parameters of the equation 5-34 and 5-36**

The constant values are given in the Table 5-8. From these constant, many parameters such as the sample conductance and the contact conductance can be extracted. The contact conductance and the sample spreading conductance are given by:

$$\frac{1}{G_s} = \frac{1}{(2b)\lambda_s} = \frac{1}{\left(\frac{1}{c_1 \lambda_s} + \frac{c_2}{c_1}\right)\lambda_s} \tag{5-39}$$

$$\frac{1}{G_c} = \frac{1}{G_{eq}} - \frac{1}{G_s} = C_1 \ln\left(\frac{1}{\lambda_e} + C_2\right) + C_3 - \frac{1}{\left(\frac{1}{c_1 \lambda_s} + \frac{c_2}{c_1}\right)\lambda_s} \tag{5-40}$$

Figure 5-26 depicts the resistance function and the contact diameter versus  $1/\lambda_s$ . These results are calculated from the parameters (C1, C2, C3). It is surprising that the contact radius  $b$  can increase to  $18\mu\text{m}$  for the lowest thermal conductivity material (PMMA). That value is much larger than the tip radius curvature (100nm) or even the tip size ( $1.3\mu\text{m}$ ).

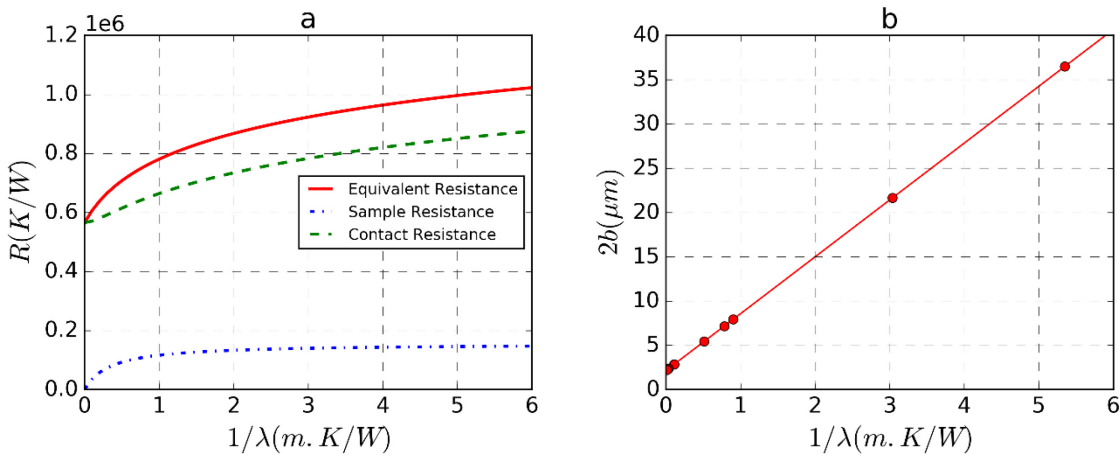


**Figure 5-26: The calculated conductance components (a) and evolution of thermal diameter as function of the inversion of sample conductivity**

These results give complementary information on the contact and the influence range of the thermal diffusion. This replies to one of the question asked in the introduction of this chapter. In Figure 5-2 the thermal signal is affected even at large distance range by the large range thermal radius  $b$ . The thermal measurements should then be corrected in the future with a thermal radius  $b$  corresponding to the effective conductivity of the sample.

- *Microscope working range under air*

As explained in vacuum, the minimum ratio that the microscope can distinguish is  $(1 + \delta_{air})(A \ln B + C)$  where  $\delta_{air}$  is the relative error of the ratio  $V/\Delta V$  of the whole system under air. The maximum measurable value of conductivity can be expressed by the following term:

$$\lambda_{s \max} = \left[ e^{\frac{(1 + \delta_{air})(A \ln B + C) - C}{A}} - B \right]^{-1} \quad (5-41)$$

The calculated relative error is  $\delta_{air} = 2.1\%$ . The sensitivity calculated for the  $1.3\mu\text{m}$  thermocouple under air is  $\lambda_{s \text{ air } \max} \approx 37.5 \text{ W/mK}$ . This can be considered as an ideal value in conditions for which the relative error is very low, the sample very flat and well-polished. One can expect lower value if the measurements are taken on rough surfaces for instance.

- *Monte Carlo error analysis*

Similar to the Monte Carlo analysis under vacuum, this error analysis under air uses 5000 random data sets following normalized distribution. The calculated A, B, C parameters give the standard deviation of 11%, 24%, 2% respectively comparing to their average values. The fitting model giving is therefore concluded consistent with the experimental results.

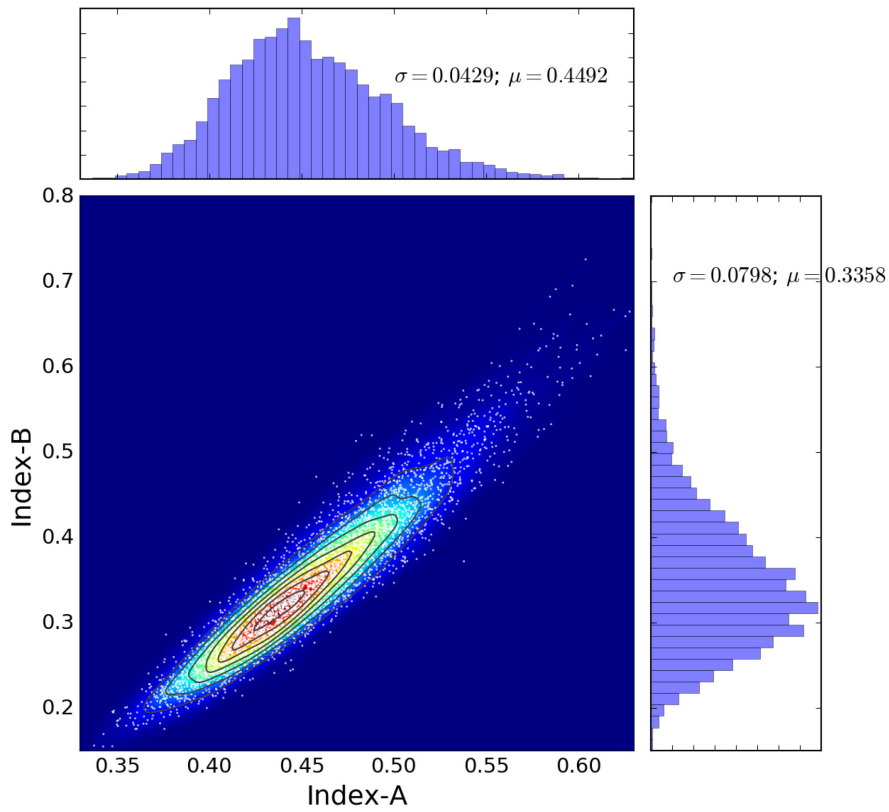


Figure 5-27: Index-A and B distribution calculated by Monte Carlo method

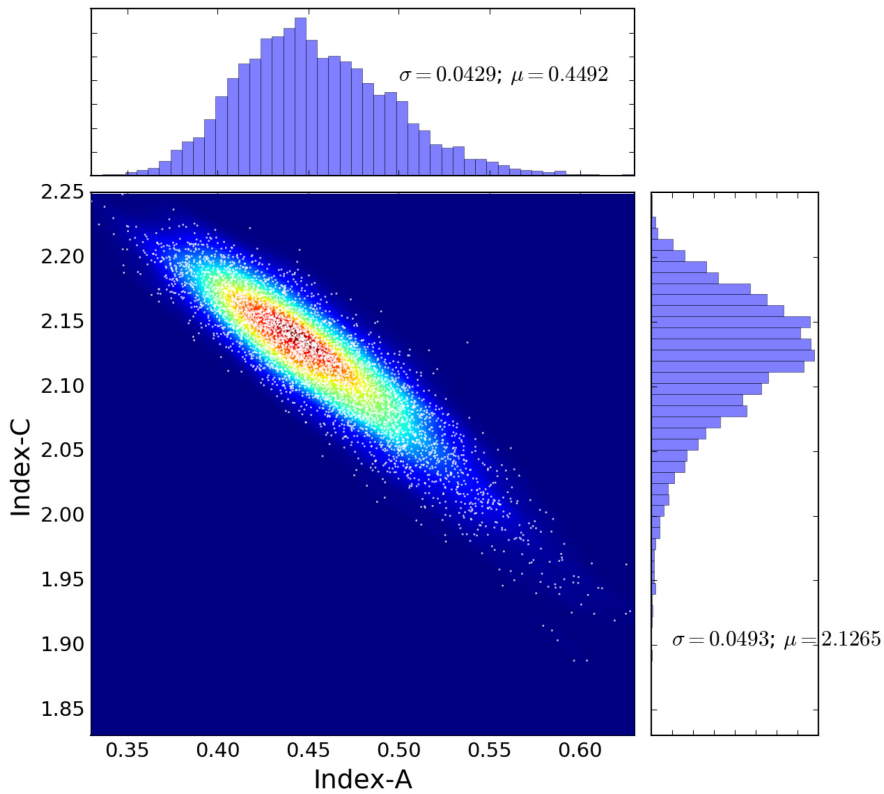
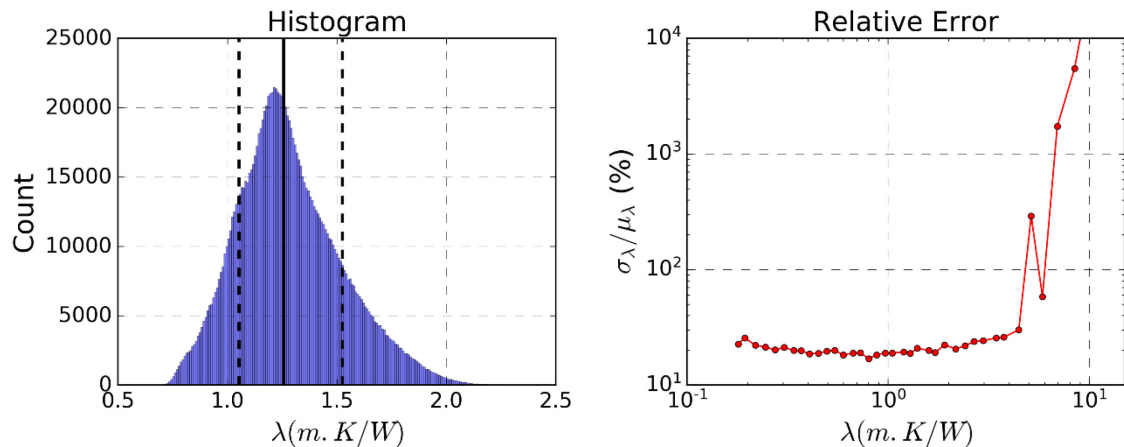


Figure 5-28: Index-A and C distribution calculated by Monte Carlo method

Figure 5-29 depicts the histogram of an error simulation at  $V_{2\omega} = 111 \pm 0.8 \mu V$  giving  $\lambda = 1.26 \pm 0.24 W/mK$  and the relative error calculated by dividing the standard deviation of thermal conductivity by its average values. The error varies from 20% to 28% at the conductivity range of 0 – 5 W/mK which is higher than the error under vacuum due to its lower sensitivity in air.



**Figure 5-29: An example of the error estimation ( $V=111\mu V$ ;  $\lambda=1.26$  W/mK) and relative error under vacuum calculated at different thermal conductivity**

The relative error plotted in the Figure 5-29 shows the uncertainty of the measurements which takes into account of the error sources:

- The signal-noise-ratio of the measurement setup which means the standard deviation of measured 2-omega voltage.
- The uncertainty of calibration samples due to the fact that the samples do not have the same roughness level, the same physico-thermal properties (hardness, hydrophobicity, thermal oxidation...). As a result, their thermal contact conductance remain uncertain.

Error sources from the system, calibration sample were taken into account. However, in reality, to measure an unknown sample, its unknown physical properties (hardness, hydrophobicity, thermal oxidation...) may lead to an uncontrollable thermal contact conductance in most serious case and cause a considerable error on the measurement. To eliminate these errors, a full investigation on the sample should be performed

before the measurement especially physico-chemical and thermodynamical properties of the tip-sample system.

## 5.4 Tip-sample heat transfer

### 5.4.1 Tip-sample heat transfer analyze

As previously described, the equivalent thermal conductance depends principally on the thermal contact radius and the contact conductance. The dominant heat transfer mechanisms are solid-solid conduction and conduction through the air environment (radiation and conduction through water meniscus are negligible for our measurement conditions). Measurements under vacuum are dedicated to study the solid-solid tip-sample heat conduction whereas measurements in ambient air are more complex cases due to air conduction. Figure 5-30 depicts the local contact between a heated tip and a sample.

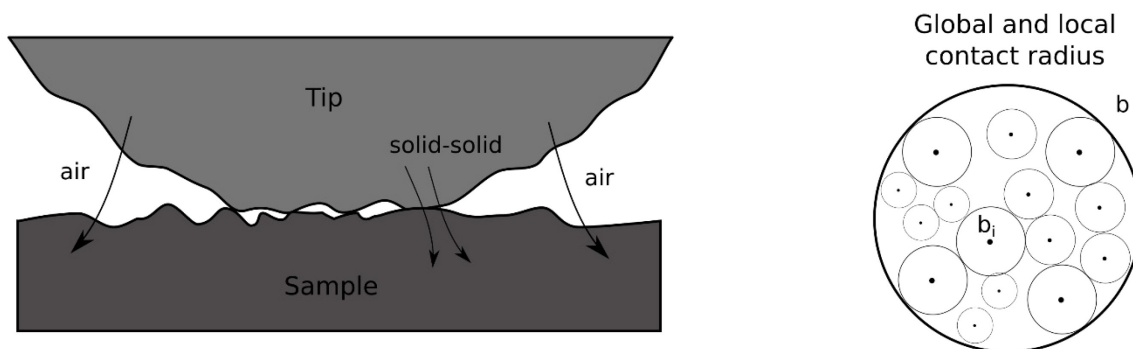


**Figure 5-30: Global and local tip-sample heat transfer**

In the Figure 5-30, the tip-sample mechanical contact and interaction through air are illustrated. In a real situation, the tip-sample contact radius  $b$  can be divided into many smaller local contact areas  $b_i$  due to the local roughness of the tip as well as the surface.

- *Solid-solid heat conduction*

To study solid-solid conduction, measurements under vacuum are considered. The solid mechanical contact radius can be estimated using Hertz contact by the following term for elastic deformation [115]

$$b_{s-s c} = \left( \frac{6RF}{E^*} \right)^{\frac{1}{3}} \quad (5-42)$$

where  $R$  is the curvature radius of the tip,  $F$  is the contact force,  $E^*$  is effective tip-sample Young's modulus and

$$b_{s-s c} = \left( \frac{4F}{\pi H} \right)^{\frac{1}{2}} \quad (5-43)$$

for plastic deformation, where  $H$  is the hardness of the material. The contact radius is estimated around 5nm with tip curvature  $R = 200\text{nm}$ ,  $F = 10\text{nN}$  and  $E^* = 100\text{GPa}$ . This mechanical contact radius is 5 times smaller the thermal radius measured under vacuum ( $b = 22.9 \pm 5 \text{ nm}$ ) and almost 100 times smaller than the one under air ( $1-16\mu\text{m}$ ). When the applied force increases, the sample conductance  $G_s$  may increase through the rise of thermal radius  $b$ . This change is only significant for vacuum measurements and negligible under air case because of the much larger thermal radius from air.

The contact conduction  $G_c$  may also increase due to the flattening of the local roughness [127] when plastic deformation occurs. In this case, local contact areas increase their sizes until the saturation  $\sum \pi b_i^2 \rightarrow \pi b^2$ . This phenomenon appears in the approach curve (Figure 5-31) with the emergence of thermal conductance saturation. The probe-sample stiffness calculated from QTF frequency shift (Figure 5-31a) can also give an indication on probe deformation.

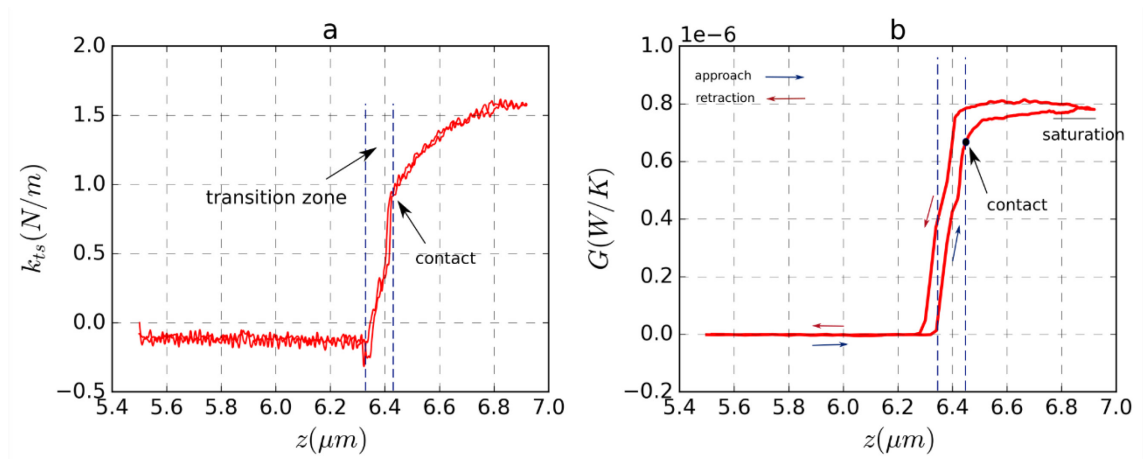


**Figure 5-31: Approach and retraction curves of the  $1.3\mu\text{m}$  thermocouple tip on the sample. a) tip-sample equivalent stiffness and b) tip-sample equivalent conductance**

- Heat conduction through air

An approach curve was performed far away from the sample (100 $\mu\text{m}$ ) down to contact (Figure 5-32) in order to point out the influence of air in the tip-to-sample heat transfer. The tip-sample equivalent resistance is also plotted versus its distance to a silicon surface. This probe had passed the calibration process (Bode curve, calibration with reference materials).

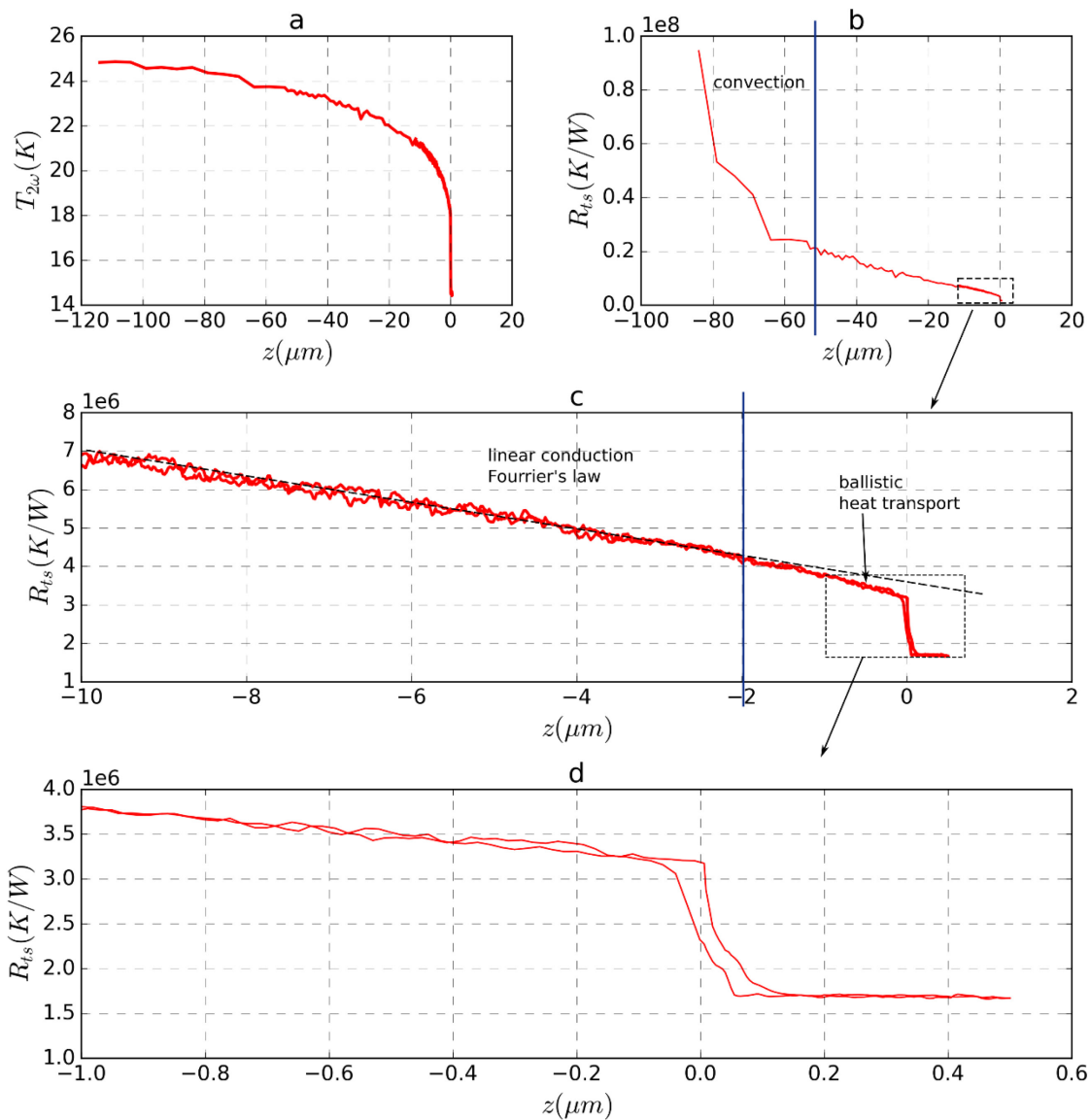


Figure 5-32: Approach curve 100 $\mu\text{m}$  above the sample a)  $2\omega$  temperature b) tip-sample thermal resistance and its zoom on the close contact zone c) and d)

In their works, Majumdar [74] and Lefèvre [71] presented different heat transfer domains through air based on the tip position above the surface. Air is considered as a transporting environment with the thermal conductivity  $\lambda_{air} = 0.025 \text{ W/mK}$ . When the tip is far from the surface ( $>40\mu\text{m}$ ) heat transfer by convection is dominant [71]. When the tip comes closer to the sample Li Shi proposed a 3 regimes theoretical approach [75], depending the tip-sample distance  $d$  compared the mean free path of air particle  $\Lambda$ . For  $d > 100\Lambda$ , a constant gradient of tip-sample resistance is detected. For  $\Lambda < d < 100\Lambda$ , a slip regime is defined due to a discontinuity of temperature at the boundaries of air and the solid material. For  $d < \Lambda$ , the regime is ballistic, the heat transport does not depend on tip's altitude.

Knowing the mean free path of air, around  $60\text{nm}$ [75], the ballistic regime starts to appear when the tip is at few hundred nanometres above the sample (Figure 5-32c). To simulate this regime, many advance tools have been used [128],[129].

Simply from experimental results, we have shown that the thermal contact radius  $b$  varies from  $1\mu\text{m}$  to  $15\mu\text{m}$  which is a 16-200 times larger than  $\Lambda$  (depending on the thermal conductivity of the sample). Following the thermal constriction equation consisting of ballistic and diffuse components proposed by Prasher et al [80]:

$$R_s = \frac{1}{2b\lambda_s} \left( 1 + \frac{8}{3\pi} Kn \right) \quad (5-44)$$

where  $Kn$  is the Knudsen number  $\Lambda/b$ .

The ballistic component only represents 0.5% (for low conductivity sample) to 5% (for high conductivity sample) of the total spreading resistance. Taking into account of the ballistic regime, the calibration curve may slightly change its form different from the curve presented on Figure 5-25 (especially at the high thermal conductivity zone) but not significantly. A more precise fitting model with 4 parameters can be considered but it may be useless due to the low sensitivity of the microscope in the high thermal conductivity zone.

The ballistic regime can also play an important role in the contact conductance  $G_c$  value. The solid-solid conductance under air is represented by a conductance step (jump to contact)  $\Delta G$  in the Figure 5-33.  $\Delta G$  in air is slightly higher than in vacuum, which can be explained from the calculation error, from ballistic regime in air or even

the change of convection coefficient  $h$  during the approach, at the moment we do not have enough information to conclude.

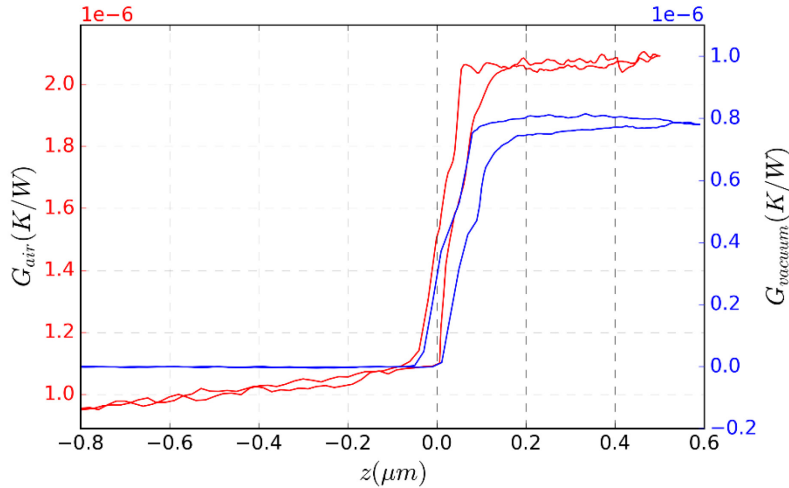


**Figure 5-33: Comparison of conductance approach curve under air and vacuum measured by 1.3µm thermocouple probe on a Silicon substrate**

By combining the two calibration experimental results (Section 5.3) (under vacuum and under air), if we consider that the contact conductance under vacuum is equal to the solid-solid heat conduction  $G_{c\ vacuum} = G_{s-s\ c\ air} = 8.15 \pm 1.3 \times 10^{-7} W/K$ , the air contact conduction  $G_{air\ c}$  can be extracted by subtracting the total contact conductance  $G_c$  by  $G_{s-s\ c}$ .

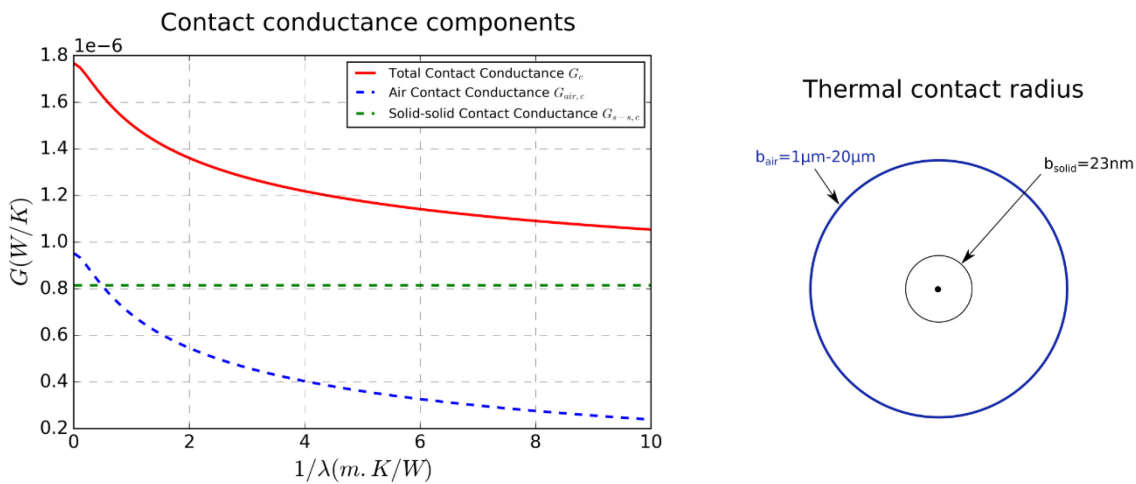


**Figure 5-34: The contact conductance components (air, solid-solid) and the thermal radius produced by air and solid-solid contact**

Environment	Conductance (W/K)	PMMA	Si n++
Vacuum	$G_{eq \text{ vacuum}}$	$7.5 \times 10^{-8}$	$7.45 \times 10^{-7}$
	$G_{C \text{ vacuum}}$	$8.15 \times 10^{-7}$	$8.15 \times 10^{-7}$
	$G_{S \text{ vacuum}}$	$8.26 \times 10^{-8}$	$8.11 \times 10^{-6}$
Air	$G_{eq}$	<b><math>9.89 \times 10^{-7}</math></b>	<b><math>1.78 \times 10^{-6}</math></b>
	$G_C$	<b><math>1.16 \times 10^{-6}</math></b> (100%)	<b><math>1.8 \times 10^{-6}</math></b> (100%)
	$G_{S-S} = G_{C \text{ vacuum}}$	$8.15 \times 10^{-7}$ (70%)	$8.15 \times 10^{-7}$ (45%)
	$G_{air C} = G_C - G_{C \text{ vacuum}}$	$3.45 \times 10^{-7}$ (30%)	$9.85 \times 10^{-7}$ (55%)
	$G_S$	<b><math>6.82 \times 10^{-6}</math></b> (100%)	<b><math>2.08 \times 10^{-4}</math></b> (100%)
	$G_{S-S} = G_{S \text{ vacuum}}$	$8.26 \times 10^{-8}$ (2%)	$8.11 \times 10^{-6}$ (4%)
	$G_{air S} = G_S - G_{S \text{ vacuum}}$	$6.74 \times 10^{-6}$ (98%)	$2.00 \times 10^{-4}$ (96%)

**Table 5-9: Thermal conductance components extracted from the measurements of PMMA and Si doped n++**

Table 5-9 summarises the different heat conductance components for 2 samples: PMMA (the lowest thermal conductivity on the calibration materials) and Si n++ (the highest). We assume that the conductance values under vacuum are equal to the solid-solid conduction components in air even if the two experiments may not have exactly the same solid-solid contact and the vacuum used (4Pa) may not eliminate totally the conduction from air.

The obtained results show that the air plays an important role in the transportation of heat. The constriction conductance (spreading conductance to the sample) by air represents 96-98% of total due to very large thermal contact radius generated by air  $b_{air} > 50b_{solid}$ . The air contact conductance ranges from 30-55% of total contact conductance. If we compare the equivalent conductance under vacuum and under air, we note that the conductance under vacuum (solid-solid conductance) takes 7.6% and 41.8% of the equivalent conductance under air for PMMA and Si dope n++. This means that the conductance by air represent 92.4% of total conductance for PMMA (low thermal conductivity material) and 59.2% for Si dope n++ (high thermal conductivity). We have shown that the air helps to increase the thermal conductance by increasing

the thermal contact radius. However, this can reduce significantly the SThM lateral thermal resolution that will be discussed in a further part of this chapter.

### 5.4.2 Influence of different factors on the measurement

- *Statistical method to study the influence of different factor (LNE)*

The ratio  $\Delta T/T$  or  $\Delta V/V$  is plotted for 3 different probe sizes S1, S2, S3 corresponding to 1.3 $\mu\text{m}$ , 2.5 $\mu\text{m}$  and 5 $\mu\text{m}$  TC probe respectively. The results obtained for  $\text{SiO}_2$  are depicted in Figure 5-35.

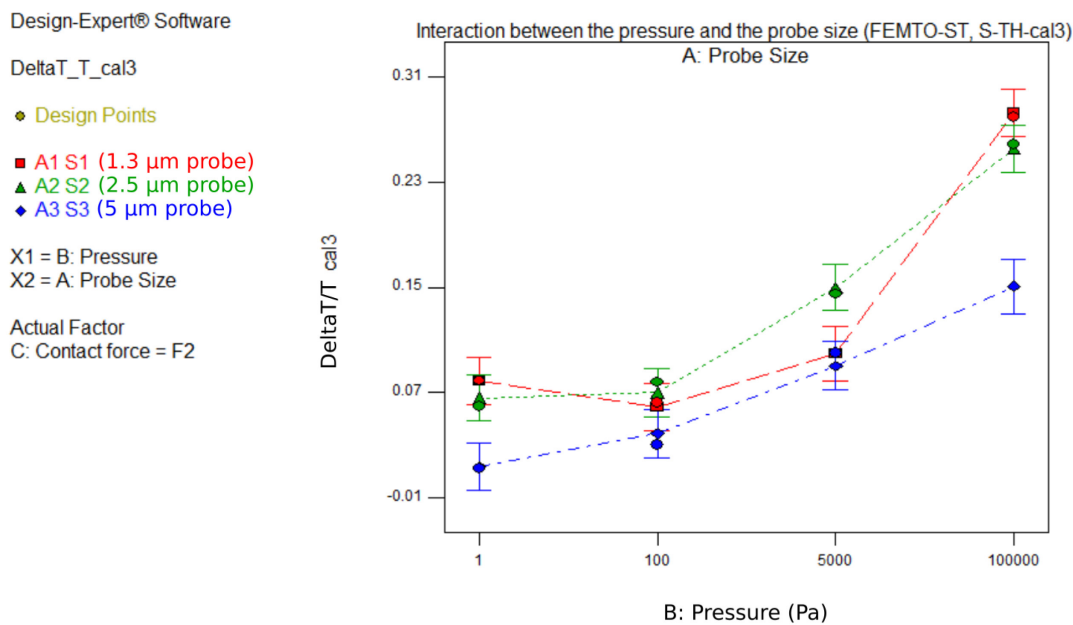


**Figure 5-35: Visualization of the interaction effect between the probe size and the pressure**

A Fisher's test analysis was performed at LNE in order to point out the influence of a given set of factors on the measured ratio  $\Delta T/T$ . The three factors have a significant effect but the pressure is the most influential (with a lower associated p-value). The probe size, the pressure and the contact force have a significant influence on the measured temperature. However, the main effect is the air pressure.

ANOVA for selected factorial model - $\Delta T/T$ - Cal3					
Analysis of variance table [Classical sum of squares - Type II]					
Source	Sum of Squares	df	Mean Square	F Value	p-value Prob > F
Model	0.21	17	0.01	60.6	< 0.0001
A-Probe Size	0.01	2	0.00	20.4	0.0002
B-Pressure	0.15	3	0.05	246.0	< 0.0001
C-Contact force	0.01	2	0.00	19.4	0.0002
AB	0.01	6	0.00	8.7	0.0012
AC	0.00	4	0.00	4.1	0.0275
Residual	0.00	11	0.00		
Cor Total	0.21	28			

**Table 5-10: ANOVA table for  $\Delta T/T$  for the DOE applied to S-TH-Cal3**

- *Thin film effect*

To study the influence of thin film effect on the SThM measurement, a sample of multi-thickness layers is used. This sample is provided by Glasgow University/KNT technology as a reference sample in the frame of Quantiheat project. It is composed of  $\text{SiO}_2$  layers of different thickness deposited on a Silicon substrate. Nine different thickness levels are available (7, 12, 30, 65, 145, 237, 330, 530, 950nm). Measurements were performed using the calibrated probe presented in the last section. The topography and the thermal signal  $V_{2\omega}$  scans are illustrated in Figure 5-36.

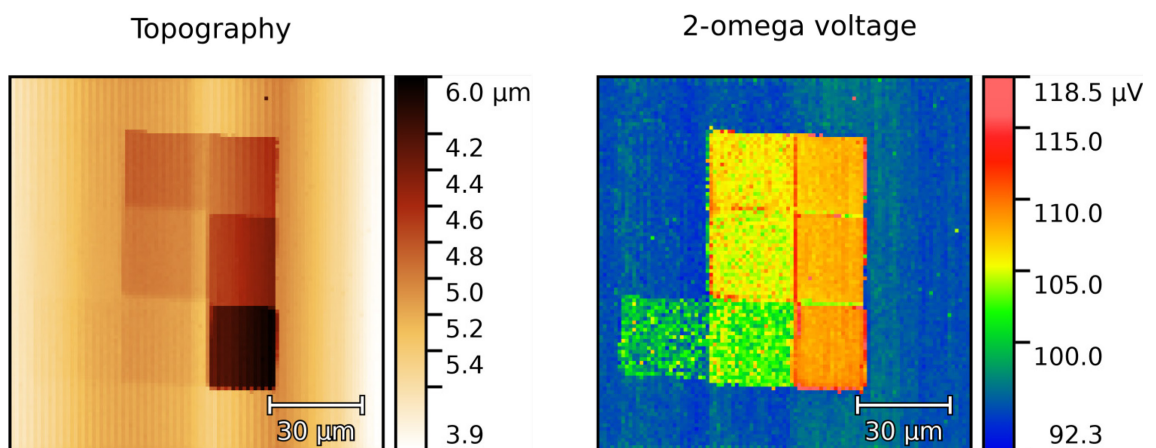


**Figure 5-36: Topography and 2-omega thermography**

As seen in the figure, the microscope is only sensitive to the thicknesses higher than 30nm. There is a saturation value when the thickness increases which converges to the bulk value of SiO<sub>2</sub>.

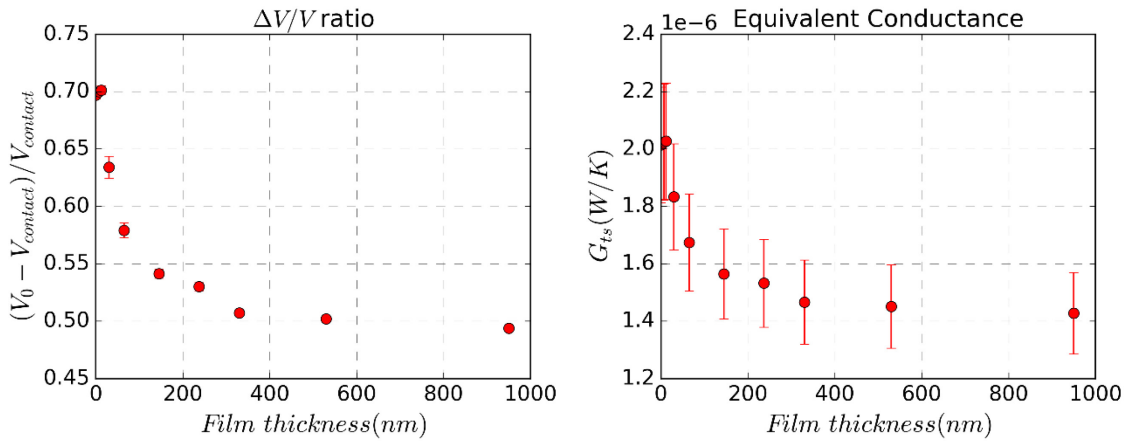


**Figure 5-37: The thermal ratio and equivalent conductance on every layer step**

The equivalent tip-sample conductance is extracted thanks to the calibrating parameter  $\kappa$  presented in the last section. From the calibration curve (eq 5-36, Figure 5-24), the equivalent thermal conductivity can also be determined.

$$\lambda_{seq} = \left[ e^{\frac{V/\Delta V - C}{A}} - B \right]^{-1} \quad (5-45)$$

Where A, B, C are fitting parameters of calibration curve under air.

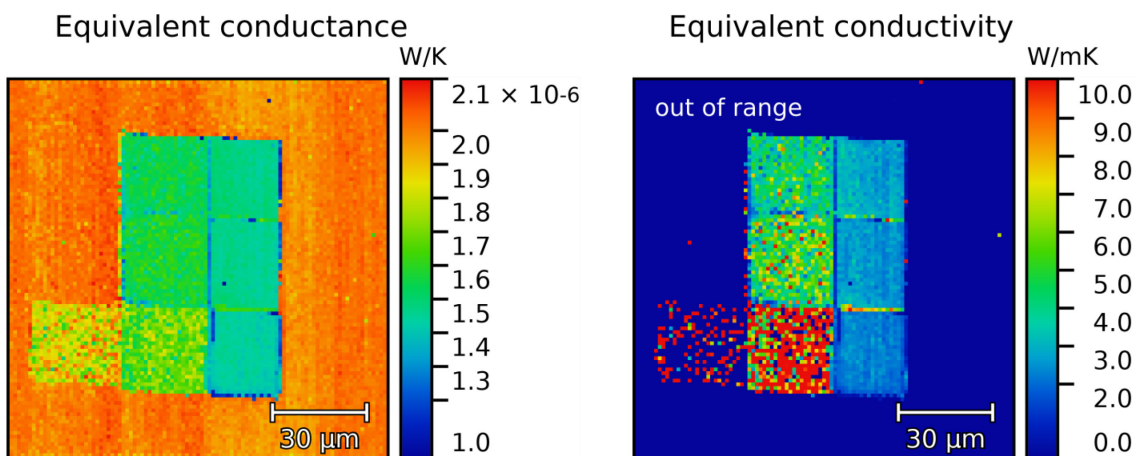


**Figure 5-33: The conductance map and thermal conductivity map on the sample**

The equivalent conductance and conductivity values are summarised in the Table 5-11. The out of range obtained results (negative values on the Table 5-11 for the four thinnest steps) correspond to measured thermal conductivities higher than the maximum measurable thermal conductivity value (66 W/mK) of the microscope. The conductivity of the thickest layer is 2.17 (W/mK) which is close to the SiO<sub>2</sub> bulk value (1.28 W/mK).

d(nm)	0	7	12	30	65	145	237	330	530	950
G(μW/K)	2.014	2.024	2.027	1.833	1.674	1.565	1.532	1.466	1.451	1.428
λ(W/mK)	-8.24	-8.03	-7.96	-24.0	13.41	4.98	4.00	2.69	2.47	2.17

**Table 5-11: Equivalent conductivity calculated for every step**

Figure 5-38 plots the equivalent conductivity as function of film thickness with 20% error

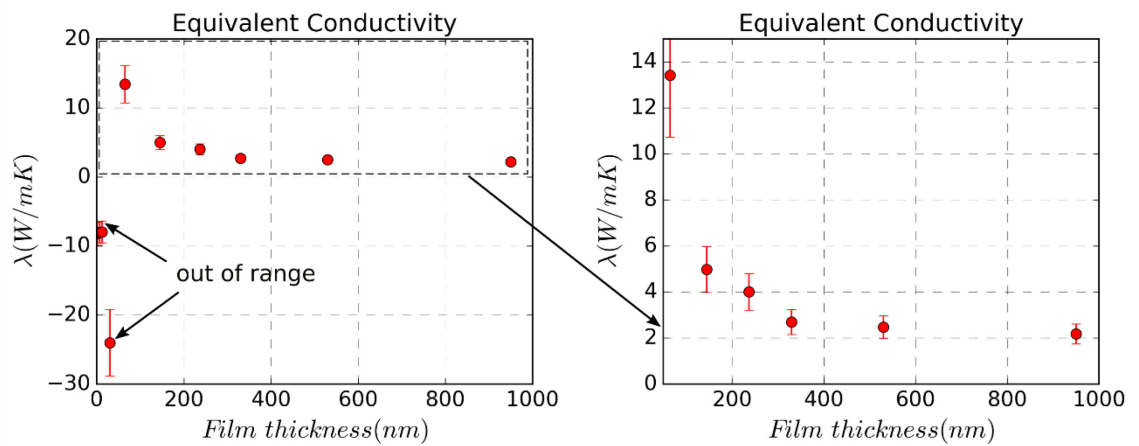


**Figure 5-38: Equivalent conductivity for every layer step**

- *Thermal resolution*

A topography free sample fabricated from Glasgow University is used to study SThM thermal lateral resolution by eliminating the topography artifact[79].

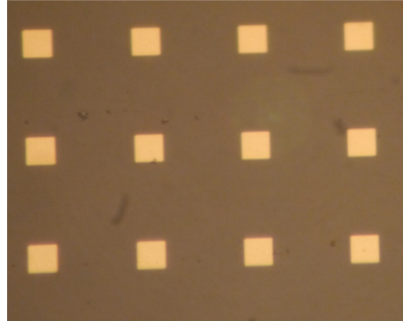


**Figure 5-39: Optical image of the sample**

This sample consist of thin film  $5\mu\text{m} \times 5\mu\text{m}$  gold layers of around 20nm thickness buried in 400nm of silicon nitride ( $\text{SiN}_x$ ) [79]. A scan ( $10\mu\text{m} \times 10\mu\text{m}$ ) has been performed around a square. The topography and the thermal signal are depicted in the Figure 5-41. The topography image shows the lack of significant geometrical details on the surface. The layer is so thin that the 2-omega voltage is very noisy the contrast between 2 materials is no so high. Here, we will use 3-omega signal to study lateral resolution due to its more stable signal. The microscope resolution is studied by scanning over the boundary of two materials.

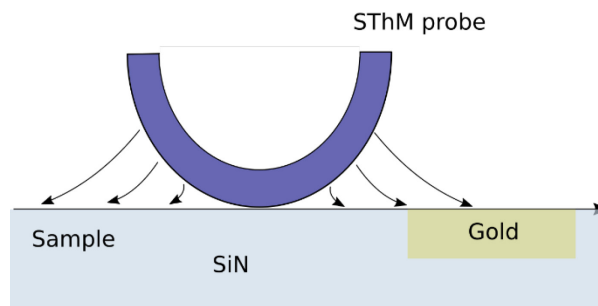


**Figure 5-40: Probe scanning schematic**

As seen from the Figure 5-41, the temperature gradient is detected at least  $2\mu\text{m}$  far from the gold square which is coherent with an estimated thermal contact radius  $b=4\mu\text{m}$  (Figure 5-26b) corresponding to the  $\text{SiN}_x$  thermal conductivity of around  $10\text{W/mK}$ . Besides, thermal spatial resolution is also subjected to depend on the frequency. This is why measurements have been performed at different excitation

frequencies, as shown in Figure 5-41 and 5-48 in which it is confirmed that no significant topographical detail are detected. Besides, without surprise, phase contrast only appears at higher frequencies (Figure 5-42).

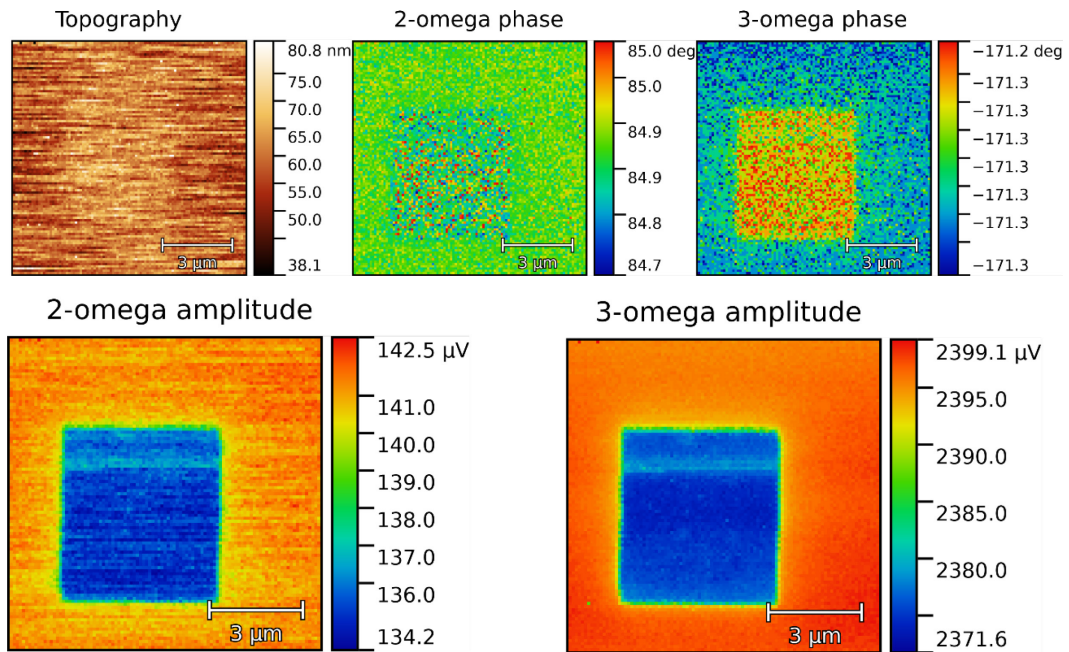


Figure 5-41: Topography, amplitude and phase of  $2\omega$  and  $3\omega$  harmonics at 57Hz

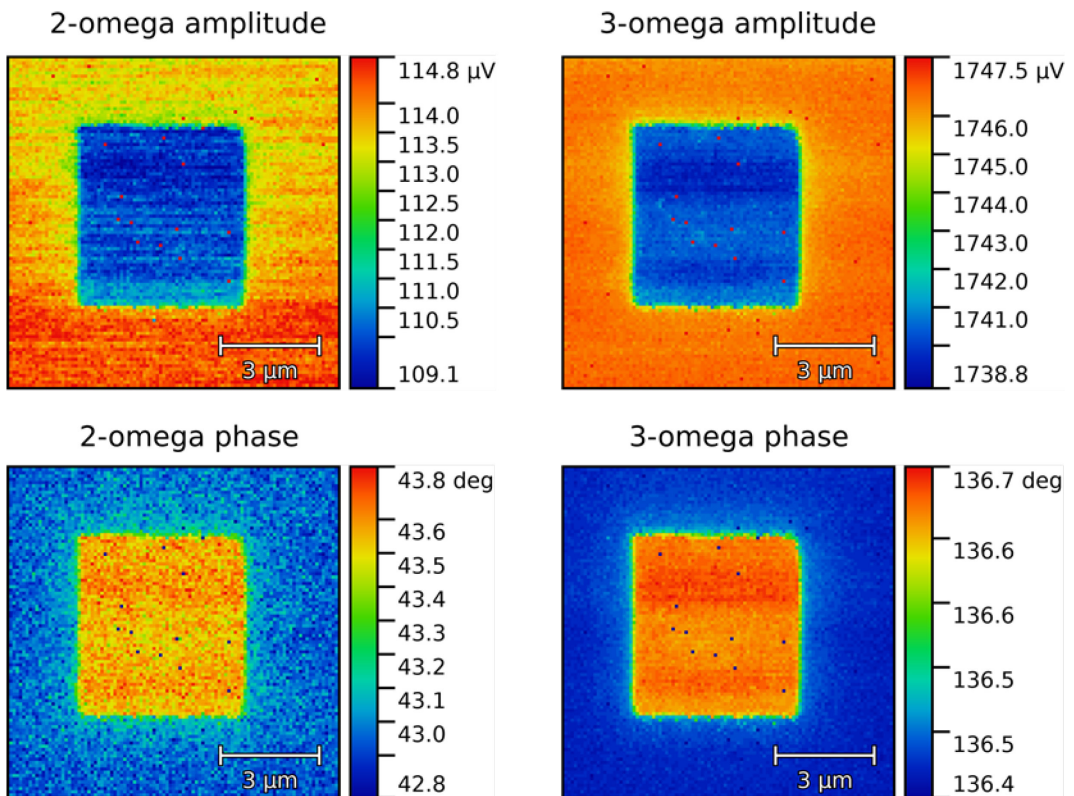
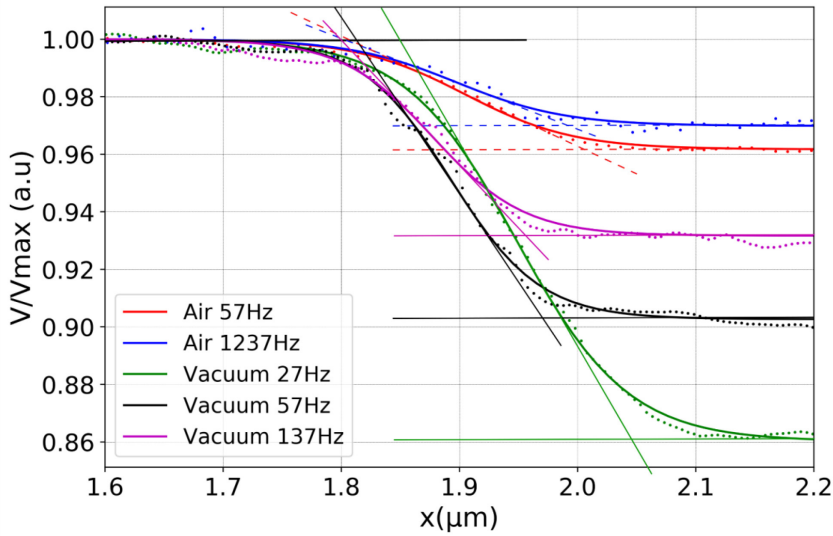


Figure 5-42: amplitude and phase of  $2\omega$  and  $3\omega$  harmonics at 1237Hz

To have an idea on the lateral resolution of the probe, measuring lines crossing the boundary of two materials have been extracted under air and vacuum at different excitation frequencies. Results are plotted in Figure 5-43 revealing an increasing of apparent resolution with the increase of frequency. The experimental data is fitted with a sigmoid function  $y = \frac{c}{1+\exp(-k(x-x_0))} + y_0$ .



**Figure 5-43: Normalized amplitude and phase at different frequencies**

The thermal resolution of the image can be represented as the transition zone width of thermal signal when the tip crosses the boundary of two different materials.

Frequency	57 (Air)	1237(Air)	27(Vacuum)	57(Vacuum)	137(Vacuum)
Resolution (nm)	200	180	200	160	150

**Table 5-12: Apparent resolution at different frequency**

As can be seen in the Figure 5-43, the transition zone width decreases when the excitation frequency increases. A 1D semi-infinite thermal model can explain this effect. Considering a heat source  $\phi = \phi_0 \cos(\omega t)$  at the interface that diffuses into the semi-infinite environment, standard heat diffusion equation:

$$\lambda \frac{\partial^2 T(x,t)}{\partial x^2} - \rho c \frac{\partial T(x,t)}{\partial t} = 0 \tag{5-46}$$

The resolution in periodic regime gives after separation of time [130]:

$$\Delta T(x, t) = \frac{\phi_0}{\lambda} \sqrt{\frac{2a}{\omega}} \exp\left(-x \sqrt{\frac{\omega}{2a}}\right) \cos\left(\omega t - x \sqrt{\frac{\omega}{2a}} - \frac{\pi}{4}\right) \quad (5-47)$$

where  $a$  is the thermal diffusivity.

Thermal wave is therefore a damping wave propagating in  $x$  direction with the speed  $v = \sqrt{2a\omega}$ . Its amplitude is reduced by a factor of  $e$  at the depth  $x = \sqrt{2a/\omega}$  called  $\delta$  or “thermal diffusion length”. The amplitude wave is considered totally damped at the depth of  $5\delta$  or  $6\delta$ . This effect may therefore decrease the thermal contact radius occurred by surrounding air  $b_{air}$  and the depth penetration to the sample.

## 5.5 Summary

This chapter has presented the  $2\omega$  active mode for thermocouple probe measurements. Together the thermal model of the probe and tip-sample heat transfer model is coherent with the experimental results. Vacuum and ambient air environments were studied. The comparison of these cases has shown that air conduction plays a dominant role. The thermal contact radius presents a linear dependence to the inversion of sample’s thermal conductivity. It can vary from  $b_0 \approx 1\mu m$  at high thermal conductivity to  $b \approx 16\mu m$  for the lowest thermal conductivity. This can influence seriously the lateral resolution of the microscope.

Demonstrations on different film thicknesses reference sample have also shown a microscope sensitivity on the layer thickness ( $>20$  nm). In term of resolution the first demonstration showed that the lateral resolution is degraded by air conduction but can be improved by increasing excitation frequency.

# 6 CONCLUSIONS AND PERSPECTIVES

## 6.1 Conclusions

Local thermal probing has become a major tool for studying transport phenomena at micro and nanoscale levels. SThM techniques have been developed for 30 years and obtained many breakthroughs. Among existing systems, our homemade micro-wire thermocouple probe system presents many advantages.

The use of a QTF force detector solves many problems compared to conventional cantilever force detector principles such as:

- The thermal distortion due to the heat conduction through the air gap along the cantilever.
- The perturbation of the laser probe.
- A flexible system allowing short periods of measurement in order to guarantee the same condition for every sample.

The QTF detection is however an indirect technique of force detection which relates only to the force gradient not the force itself.

The point by point scanning technique (the probe is put in and taken out of contact for every pixel) is presently a limiting factor since the scanning speed still rest limited (several hours for a full scan of 101x101 pixels). This might be improved in the future.

The thermocouple probe can work well in active mode and passive mode. Thanks to the coupling between simple model and calibration method, the measurements obtained are close to quantitative.

In the chapter 4, a new series of calibration devices ( $\text{SiN}_x$  membrane and Pt heater) are presented. These are high temperature devices with a central maximum temperature higher than  $500^\circ\text{C}$ . They also permit to obtain a reference temperature by two different techniques (localised RTD and NIR method). Probe calibration on different devices has proved their ability for probe evaluation providing a convenient tool for thermal probe study. The optimised last generation of active device (v2RTD) is used to study the tip-sample heat transfer in passive mode. Influence of different parameters was studied by a Fisher's test. A comparison between  $1.3\mu\text{m}$  thermocouple and  $5\mu\text{m}$  thermocouple on a heated sub-micron Platinum wire on Silicon substrate has shown a much higher resolution of  $1.3\mu\text{m}$  comparing to  $5\mu\text{m}$  probe. A coupling probe-device system is also used for thermal characterization of micro-scale structure. The probe design has proved its efficiency since its temperature resolution is near  $0.1\text{K}$  and its spatial thermal resolution is around  $100\text{nm}$ , which is comparable to other commercialized SThM probes. In mean times, its geometry (long wires) allows maintaining the reference junction at ambient and insures that the probe is not perturbed by other factors (air artefact to the QTF prong, laser perturbation).

In active mode (chapter 5), the analytical model allows us to calculate the tip-sample conductance through a very simple conversion  $G = \kappa\Delta V/V$ . A series of measurements on passive bulk samples were performed. The proposed theoretical model of microscale probe-sample heat transfer in air and under vacuum is coherent with experimental results. The influence of air and solid-solid conduction on measurements has also been quantified. For the first time, all the conductance terms (spreading conductance, contact conductance through air and solid-solid conduction) have been quantified by experiment using a combination between vacuum and air measurements of the same probe on well-prepared reference samples. The thermal contact radius is estimated from  $1\mu\text{m}$  to  $15\mu\text{m}$  in ambient conditions and around  $23\text{nm}$  in primary vacuum, which demonstrates the role of air on the tip-sample thermal coupling. Measurements on reference samples (different thicknesses  $\text{SiO}_2$  and topography free

sample) have shown the capabilities of the probe and its resolution without topography artifact.

In this dissertation, a SThM probe based on micro-wire thermocouple associated QTF as force detector and its performances have been described. Thanks to the devices and calibration samples, all provided by Quantiheat partners, the thermocouple probe has been fully calibrated. However, such homemade probe cannot be strictly identical so that each fabricated probe must be individually calibrated.

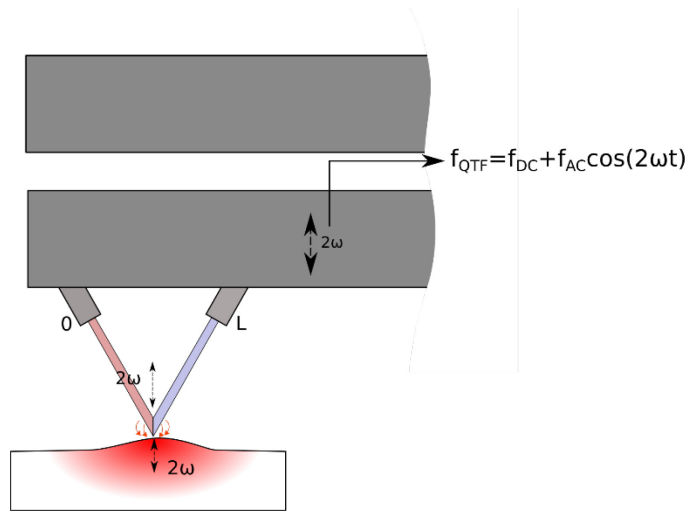
In conclusion, because this is a work to obtain the degree “Doctor of Philosophy”, I would like to cite classical Plato words in Parmenides: “ce qui est, est ce qui n’est pas” which means things in reality are always influenced by the other things. In our cases, our studies take us closer to the reality but never attend a perfect understanding. The quantification of thermal measurements by thermocouple probes is obtained through the calibration processes. However, there are still many interesting things out there may bring us even closer to the true understanding of nano/micro scale physico-thermal phenomena. Some of them will be presented in the perspectives part about the possible future experiments of the thermocouple probe and the system.

## 6.2 Perspectives

### 6.2.1 Thermo-mechanical measurements

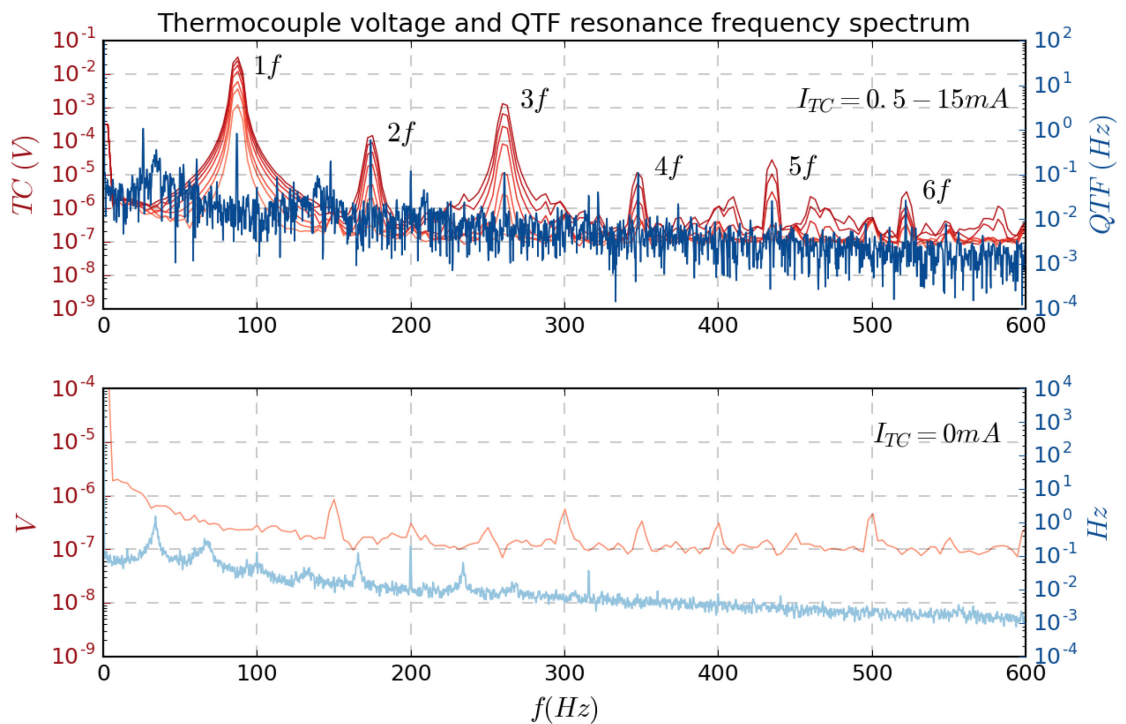
Tip-sample thermal interaction always leads to a thermal mechanical interaction through a thermal expansion coefficient. Therefore, the thermal variation at  $2\omega$  produces mechanical variation at  $2\omega$ . The frequency shift of the QTF depends on the mechanical interaction. Since the thermocouple probe is associated directly on the QTF, a thermo-mechanical modulation can be measured through the  $2\omega$  component of the QTF frequency shift (Figure 6-1).

$$\Delta f_{QTF} = \Delta f_{DC} + \Delta f_{AC} \cos(2\omega t) \quad (6-1)$$



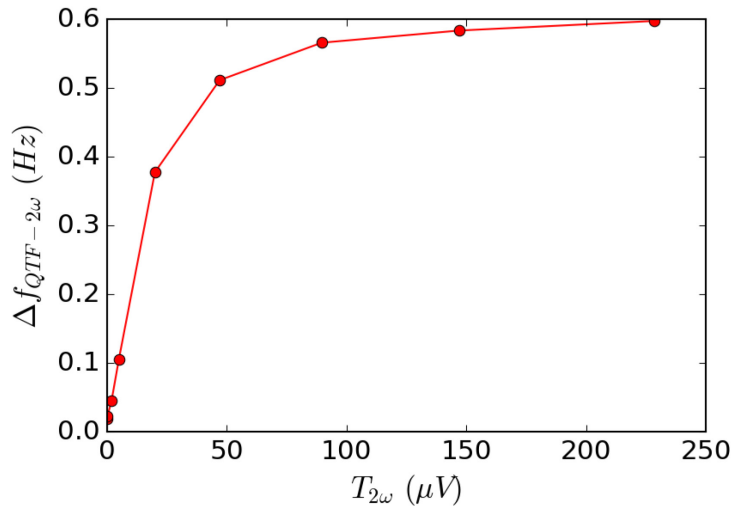
**Figure 6-1: Thermo-mechanical coupling effect**

Figure 6-2 depicts the  $5\mu\text{m}$  thermocouple voltage and the QTF frequency shift spectrum measured using a double lock-in with PLL option at different current excitations when the probe is in contact with a Silicon substrate. The results obtained are coherent with the predicted phenomena. However, not only  $2\omega$  peak appears but also other peaks of the voltage spectrum ( $\omega, 3\omega, 4\omega, 5\omega, 6\omega \dots$ ).



**Figure 6-2: Thermocouple voltage spectrum (in red) and QTF frequency shift spectrum in blue at different excitation current 0.5 – 15mA (upper plot) and 0mA (lower plot)**

The correlation between the thermocouple voltage and QTF frequency shift at  $2\omega$  is shown in Figure 6-3.



**Figure 6-3: The correlation between QTF  $2\omega$  component frequency shift and  $2\omega$  voltage of thermocouple in contact with a silicon substrate**

The explanation of these phenomena requires further studies and experiments. Thermo-mechanical images (amplitude, phase of QTF frequency shift at  $2\omega$ ) can be easily obtained simultaneously with the topography, thermography images... which can give a complete indication on the physico-thermal characteristics of the sample.

### 6.2.2 Square wave frequency synthesis technique for thermal penetration measurement

Previously, in chapter 5, every measurement uses a sinusoid excitation, which can give the tip-sample thermal conductance at the double or triple frequency only. As described in chapter 5, the thermal resolution is also depending on the excitation frequency due to the diffusion of thermal wave. A 50%-50% square wave may be interesting due to its odd harmonics components (1f, 3f, 5f, 7f...) (Figure 6-4). The use of a squares form signal excitation opens a possibility to access to thermoelectric voltages generated at the double harmonics (2f, 6f, 10f...). These measurements can give information on the diffusion of thermal wave or the diffusivity of the sample if the results are interpreted correctly.

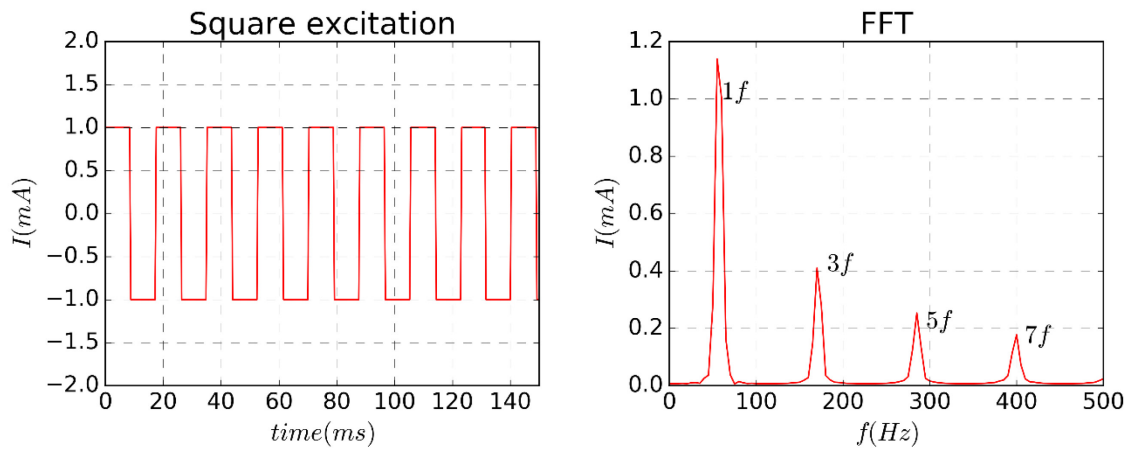


**Figure 6-4: Square wave signal and its frequency component**

### 6.2.3 Towards quantitative temperature measurements by a correction of thermal resistance

The main objective of SThM techniques is quantitative measurements. In chapter 4, we have presented temperature measurements through calibration process. These calibrations are still not practical. In chapter 5, tip-sample thermal resistance can be measured using  $2\omega$  method. The next step is a combination of passive temperature measurement (chapter 4) with active mode tip-sample conductance measurement (chapter 5) to deduce the actual sample temperature.

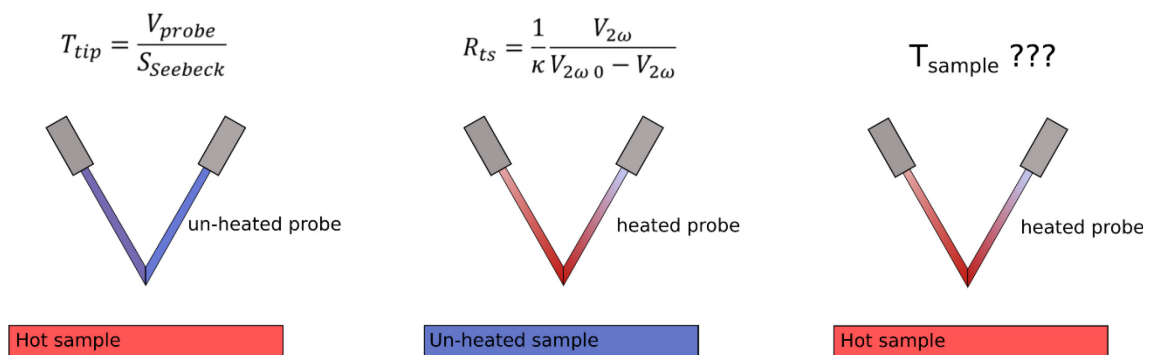


**Figure 6-5: Different measuring schematics, from the left to the right: active sample measured by passive probe, passive sample measured by active probe and active sample measured by active probe in the future**

- *Un-heated sample*

As presented in chapter 5 using  $2\omega$  method, when the sample is not heated, the tip-sample thermal resistance has linear dependence with  $T/\Delta T$

$$R_{ts} = k \frac{T_{AC}}{T_{AC noncontact} - T_{AC}} = \frac{T_{AC}}{Q_{ts}} \quad (6-2)$$

Where k is a constant depend only on the probe geometrical parameters and the coefficient of convection.

- *Hot sample*

If the sample is heated ( $T_{sample} > T_{ambient}$ ), supposing the tip-sample thermal resistance does not change, the tip-sample resistance is given

$$R_{ts} = \frac{[T'_{AC} + T_{DC}]_{probe} - [T_{DC}]_{sample}}{Q'_{ts}} \quad (6-3)$$

$$[T_{DC}]_{sample} = [T'_{AC} + T_{DC}]_{probe} - R_{ts} \times Q'_{ts} \quad (6-4)$$

where the  $T'_{AC}$  is  $2\omega$  temperature and  $T_{DC}$  is DC temperature measured when the sample is heated.

Due to the influence of hot surface, we define an apparent tip-sample resistance following the same principle for ambient temperature sample. If we consider k does not change for a hot surface and  $Q'_{ts}$  is considered as the RMS value of DC and AC flux.

$$R'_{ts} = k \frac{T'_{AC}}{T_{AC noncontact} - T'_{AC}} = \frac{[T'_{AC}]_{probe}}{Q'_{ts}} \quad (6-5)$$

With the conditions defined, we obtain finally the following term of sample temperature

$$[T_{DC}]_{sample} = [T'_{AC} + T_{DC}]_{probe} - \frac{T_{AC}(T_{AC noncontact} - T'_{AC})}{T_{AC noncontact} - T_{AC}} \quad (6-6)$$

Two scans (active probe scan on ambient temperature sample, active scan on hot sample) at the same location are needed. This principle is in development and should be studied carefully. An important point relies on the optimization of the signal-to-noise ratio that requires new measurement setup for correctly extracting DC and AC signal simultaneously.

#### 6.2.4 New probe generation based on optical fibre

As it is hard to guarantee the reproducibility of micro-wire thermocouple probe, every probe must be calibrated before performing measurement. A new probe conception is based on an optical fibre. The probe is also connected to the quartz tuning fork for contact detection. Instead of Joule heating by electrical current, a modulated laser beam is injected into the fibre core to be absorbed into the taper, which is more flexible in terms of excitation signal (Dirac pulse, square signal...) and more stable in terms of signal to noise ratio.

## 7 REFERENCES

- [1] G. E. Moore, "Lithography and the future of Moore's law," *Proc. SPIE*, vol. 2438, pp. 2–17, 1995.
- [2] A. a Balandin, "Thermal properties of graphene and nanostructured carbon materials.," *Nat. Mater.*, vol. 10, no. 8, pp. 569–81, Aug. 2011.
- [3] R. Prasher, X. Hu, Y. Chalopin, N. Mingo, K. Lofgreen, S. Volz, F. Cleri, and P. Keblinski, "Turning Carbon Nanotubes from Exceptional Heat Conductors into Insulators," *Phys. Rev. Lett.*, vol. 102, no. 10, p. 105901, Mar. 2009.
- [4] Y. Ni, H. Le Khanh, Y. Chalopin, J. Bai, P. Lebarney, L. Divay, and S. Volz, "Highly efficient thermal glue for carbon nanotubes based on azide polymers," *Appl. Phys. Lett.*, vol. 100, no. 19, p. 193118, 2012.
- [5] D. G. Cahill, W. K. Ford, K. E. Goodson, G. D. Mahan, A. Majumdar, H. J. Maris, R. Merlin, and S. R. Phillpot, "Nanoscale thermal transport," *J. Appl. Phys.*, vol. 93, no. 2, p. 793, 2003.
- [6] D. G. Cahill, P. V. Braun, G. Chen, D. R. Clarke, S. Fan, K. E. Goodson, P. Keblinski, W. P. King, G. D. Mahan, A. Majumdar, H. J. Maris, S. R. Phillpot, E. Pop, and L. Shi, "Nanoscale thermal transport. II. 2003-2012," *Appl. Phys. Rev.*, vol. 1, no. 1, 2014.
- [7] D. Teyssieux, L. Thiery, and B. Cretin, "Near-infrared thermography using a charge-coupled device camera: Application to microsystems," *Rev. Sci. Instrum.*, vol. 78, no. 3, p. 34902, 2007.
- [8] D. Teyssieux, D. Briand, J. Charnay, N. F. de Rooij, and B. Cretin, "Dynamic and

- static thermal study of micromachined heaters: the advantages of visible and near-infrared thermography compared to classical methods," *J. Micromechanics Microengineering*, vol. 18, no. 6, p. 65005, Jun. 2008.
- [9] J. Christofferson and A. Shakouri, "Thermoreflectance based thermal microscope," *Rev. Sci. Instrum.*, vol. 76, no. 2, 2005.
- [10] G. Tessier, S. Holé, and D. Fournier, "Quantitative thermal imaging by synchronous thermoreflectance with optimized illumination wavelengths," *Appl. Phys. Lett.*, vol. 78, no. 16, pp. 2267–2269, 2001.
- [11] R. B. Wilson, B. a Apgar, L. W. Martin, and D. G. Cahill, "Thermoreflectance of metal transducers for optical pump-probe studies of thermal properties.," *Opt. Express*, vol. 20, no. 27, pp. 28829–38, Dec. 2012.
- [12] D. Luerssen, J. A. Hudgings, P. M. Mayer, and R. J. Ram, "Nanoscale thermoreflectance with 10mK temperature resolution using stochastic resonance," in *Semiconductor Thermal Measurement and Management IEEE Twenty First Annual IEEE Symposium, 2005.*, 2005, pp. 253–258.
- [13] M. Malyj and J. E. Griffiths, "Stokes/Anti-Stokes Raman Vibrational Temperatures: Reference Materials, Standard Lamps, and Spectrophotometric Calibrations," *Appl. Spectrosc.*, vol. 37, no. 4, pp. 315–333, 1983.
- [14] M. Kuball, J. M. Hayes, M. J. Uren, I. Martin, J. C. H. Birbeck, R. S. Balmer, and B. T. Hughes, "Measurement of temperature in active high-power AlGaIn/GaN HFETs using Raman spectroscopy," *IEEE Electron Device Lett.*, vol. 23, no. 1, pp. 7–9, Jan. 2002.
- [15] A. Soudi, R. D. Dawson, and Y. Gu, "Characteristics in Current-Carrying GaN Scanning Thermal Microscopy and," vol. 5, no. 1, pp. 255–262, 2011.
- [16] P. Kolodner and J. A. Tyson, "Microscopic fluorescent imaging of surface temperature profiles with 0.01 °C resolution," *Appl. Phys. Lett.*, vol. 40, no. 9, pp. 782–784, 1982.
- [17] P. Kolodner, "Remote thermal imaging with 0.7- $\mu$ m spatial resolution using temperature-dependent fluorescent thin films," *Appl. Phys. Lett.*, vol. 42, no. 1, p. 117, 1983.
- [18] B. Cretin, S. Gomès, N. Trannoy, and P. Vairac, "Scanning Thermal Microscopy," in *Microscale and Nanoscale Heat Transfer*, Springer-V., vol. 238, no. 2007, pp.

181–238.

- [19] S. Gomès and S. Lefèvre, “Chapter 5 : Scanning thermal microscopy (STHM): Advances of the technique for the characterization of the thermo-physical properties of solid materials,” in *Advanced Techniques and Applications on Scanning Probe Microscopy*, F.H. Lei, Ed. Research Signpost, 2008, pp. 157–195.
- [20] a Bontempi, L. Thiery, D. Teysieux, D. Briand, and P. Vairac, “Quantitative thermal microscopy using thermoelectric probe in passive mode.,” *Rev. Sci. Instrum.*, vol. 84, no. 10, p. 103703, Oct. 2013.
- [21] L. Thiery, E. Gavignet, B. Cretin, L. Thiery, E. Gavignet, and B. Cretin, “Two omega method for active thermocouple microscopy Two omega method for active thermocouple microscopy,” vol. 34901, no. 2009, 2012.
- [22] G. Binnig, H. Rohrer, C. Gerber, and E. Weibel, “Surface Studies by Scanning Tunneling Microscopy,” *Phys. Rev. Lett.*, vol. 49, no. 1, pp. 57–61, 1982.
- [23] G. Binnig and H. Rohrer, “Scanning tunneling microscopy,” *Surf. Sci.*, vol. 126, pp. 236–244, 1983.
- [24] G. Binnig, C. F. Quate, and C. Gerber, “Atomic Force Microscope,” *Phys. Rev. Lett.*, vol. 56, no. 9, pp. 930–933, Mar. 1986.
- [25] “<http://www.nanoworld.com>.” .
- [26] R. Garcia and A. San Paulo, “Attractive and repulsive tip-sample interaction regimes in tapping-mode atomic force microscopy,” *Phys. Rev. B*, vol. 60, no. 7, pp. 4961–4967, 1999.
- [27] J. Tamayo and R. García, “Deformation, Contact Time, and Phase Contrast in Tapping Mode Scanning Force Microscopy,” *Langmuir*, vol. 12, no. 18, pp. 4430–4435, 1996.
- [28] N. Sasaki and M. Tsukada, “Theory for the effect of the tip–surface interaction potential on atomic resolution in forced vibration system of noncontact AFM,” *Appl. Surf. Sci.*, vol. 140, no. 3, pp. 339–343, 1999.
- [29] T. R. Albrecht, P. Grütter, D. Horne, and D. Rugar, “Frequency modulation detection using high-Q cantilevers for enhanced force microscope sensitivity,” *J. Appl. Phys.*, vol. 69, no. 2, p. 668, 1991.
- [30] B. Gotsmann and H. Fuchs, “Dynamic AFM using the FM technique with constant excitation amplitude,” *Appl. Surf. Sci.*, vol. 188, no. 3–4, pp. 355–362,

- Mar. 2002.
- [31] F. Giessibl, "Forces and frequency shifts in atomic-resolution dynamic-force microscopy," *Phys. Rev. B*, vol. 56, no. 24, pp. 16010–16015, Dec. 1997.
- [32] Y. Martin and H. K. Wickramasinghe, "Magnetic imaging by "force microscopy" with 1000 Å resolution," *Appl. Phys. Lett.*, vol. 50, no. 20, p. 1455, 1987.
- [33] P. Vairac and B. Cretin, "Scanning microdeformation microscopy in reflection mode," *Appl. Phys. Lett.*, vol. 68, no. 4, pp. 461–463, 1996.
- [34] M. Nonnenmacher, M. P. O'Boyle, and H. K. Wickramasinghe, "Kelvin probe force microscopy," *Appl. Phys. Lett.*, vol. 58, no. 25, pp. 2921–2923, 1991.
- [35] a. Majumdar, J. P. Carrejo, and J. Lai, "Thermal imaging using the atomic force microscope," *Appl. Phys. Lett.*, vol. 62, no. 20, p. 2501, 1993.
- [36] C. C. Williams and H. K. Wickramasinghe, "Scanning thermal profiler," *Appl. Phys. Lett.*, vol. 49, no. 23, p. 1587, 1986.
- [37] M. Nonnenmacher and H. K. Wickramasinghe, "Scanning probe microscopy of thermal conductivity and subsurface properties," *Appl. Phys. Lett.*, vol. 61, no. 2, pp. 168–170, 1992.
- [38] R. J. Pylkki, P. J. Moyer, and P. E. West, "Scanning Near-Field Optical Microscopy and Scanning Thermal Microscopy," *Jpn. J. Appl. Phys.*, vol. 33, no. 6S, p. 3785, 1994.
- [39] B. A. Nelson and W. P. King, "Measuring material softening with nanoscale spatial resolution using heated silicon probes," *Rev. Sci. Instrum.*, vol. 78, no. 2, 2007.
- [40] I. W. Rangelow, T. Gotszalk, N. Abedinov, P. Grabiec, and K. Edinger, "Thermal nano-probe," *Microelectron. Eng.*, vol. 57–58, pp. 737–748, 2001.
- [41] G. Mills, J. M. . Weaver, G. Harris, W. Chen, J. Carrejo, L. Johnson, and B. Rogers, "Detection of subsurface voids using scanning thermal microscopy," *Ultramicroscopy*, vol. 80, no. 1, pp. 7–11, Aug. 1999.
- [42] P. S. Dobson, J. M. R. Weaver, and G. Mills, "New Methods for Calibrated Scanning Thermal Microscopy (SThM)," in *2007 IEEE Sensors*, 2007, pp. 708–711.
- [43] "[https://www.kelvinnanotechnology.com/scanning-thermal-probes.](https://www.kelvinnanotechnology.com/scanning-thermal-probes)" .
- [44] G. Wielgoszewski, P. Sulecki, T. Gotszalk, P. Janus, D. Szmigiel, P. Grabiec, and E.

Zschech, "Microfabricated resistive high-sensitivity nanoprobe for scanning thermal microscopy," *J. Vac. Sci. Technol. B Microelectron. Nanom. Struct.*, vol. 28, no. 6, p. C6N7, 2010.

- [45] W. P. King, T. W. Kenny, K. E. Goodson, A. Member, G. L. W. Cross, M. Despont, U. T. Dürig, H. Rothuizen, G. Binnig, and P. Vettiger, "Design of Atomic Force Microscope Cantilevers for Combined Thermomechanical Writing and Thermal Reading in Array Operation," vol. 11, no. 6, pp. 765–774, 2002.
- [46] M. Hinz, O. Marti, B. Gotsmann, M. A. Lantz, U. Dürig, and U. Durig, "High resolution vacuum scanning thermal microscopy of HfO<sub>2</sub> and SiO<sub>2</sub>," *Appl. Phys. Lett.*, vol. 92, no. 4, p. 3, 2008.
- [47] F. Menges, H. Riel, A. Stemmer, and B. Gotsmann, "Quantitative thermometry of nanoscale hot spots.," *Nano Lett.*, vol. 12, no. 2, pp. 596–601, Feb. 2012.
- [48] F. Menges, P. Mensch, H. Schmid, H. Riel, A. Stemmer, and B. Gotsmann, "Temperature mapping of operating nanoscale devices by scanning probe thermometry," *Nat. Commun.*, vol. 7, p. 10874, 2016.
- [49] B. a. Nelson and W. P. King, "Measuring material softening with nanoscale spatial resolution using heated silicon probes," *Rev. Sci. Instrum.*, vol. 78, no. 2, p. 23702, 2007.
- [50] L. Thiery, "Application des microcapteurs thermoelectriques en metrologie opto-thermique et en microscopie photothermique," Université de Franche-Comté, 1994.
- [51] L. Thiery, S. Toullier, D. Teyssieux, and D. Briand, "Thermal Contact Calibration Between a Thermocouple Probe and a Microhotplate," *J. Heat Transfer*, vol. 130, no. 9, p. 91601, 2008.
- [52] A. Bontempi, T. P. Nguyen, R. Salut, L. Thiery, D. Teyssieux, and P. Vairac, "Scanning thermal microscopy based on a quartz tuning fork and a micro-thermocouple in active mode ( $2\omega$  method)," *Rev. Sci. Instrum.*, vol. 87, no. 6, 2016.
- [53] Y. Zhang, Y. Zhang, J. Blaser, T. S. Sriram, A. Enver, and R. B. Marcus, "A thermal microprobe fabricated with wafer-stage processing," *Rev. Sci. Instrum.*, vol. 69, no. 5, p. 2081, 1998.
- [54] G. Mills, H. Zhou, a. Midha, L. Donaldson, and J. M. R. Weaver, "Scanning

- thermal microscopy using batch fabricated thermocouple probes," *Appl. Phys. Lett.*, vol. 72, no. 22, p. 2900, 1998.
- [55] L. Shi and A. Majumdar, "Thermal transport mechanisms at nanoscale point contacts," *J. Heat Transfer*, vol. 124, no. 2, pp. 329–337, 2002.
- [56] L. Shi, J. Zhou, P. Kim, A. Bachtold, A. Majumdar, and P. L. McEuen, "Thermal probing of energy dissipation in current-carrying carbon nanotubes," *J. Appl. Phys.*, vol. 105, no. 10, p. 104306, 2009.
- [57] K. Kim, J. Chung, J. Won, O. Kwon, J. S. Lee, S. H. Park, and Y. K. Choi, "Quantitative scanning thermal microscopy using double scan technique," *Appl. Phys. Lett.*, vol. 93, no. 20, p. 203115, 2008.
- [58] J. Chung, K. Kim, G. Hwang, O. Kwon, Y. K. Choi, and J. S. Lee, "Quantitative temperature profiling through null-point scanning thermal microscopy," *Int. J. Therm. Sci.*, vol. 62, pp. 109–113, 2012.
- [59] L. Thiery, C. Bainier, and M. Spajer, "New opto-thermal probes on near-field optical fibre tips," in *OPTO 2002 International Conference Proceedings*, 2002, pp. 193–196.
- [60] D. W. Pohl, W. Denk, and M. Lanz, "Optical stethoscopy: Image recording with resolution  $\lambda/20$ ," *Appl. Phys. Lett.*, vol. 44, no. 7, pp. 651–653, 1984.
- [61] Kenneth E. Goodson and Mehdi Ashegh, "Near-Field Optical Thermometry," *Microscale Thermophys. Eng.*, vol. 1, no. 3, pp. 225–235, 1997.
- [62] L. Aigouy, G. Tessier, M. Mortier, and B. Charlot, "Scanning thermal imaging of microelectronic circuits with a fluorescent nanoprobe," *Appl. Phys. Lett.*, vol. 87, no. 18, p. 184105, 2005.
- [63] B. Samson, L. Aigouy, R. Latempa, G. Tessier, M. Aprili, M. Mortier, J. Lesueur, and D. Fournier, "Scanning thermal imaging of an electrically excited aluminum microstripe," *J. Appl. Phys.*, vol. 102, no. 2, p. 24305, 2007.
- [64] A. Assy, H. J. Lin, M. Schoenauer-Sebag, P. Gredin, M. Mortier, L. Billot, Z. Chen, and L. Aigouy, "Nanoscale thermometry with fluorescent yttrium-based Er/Yb-doped fluoride nanocrystals," *Sensors Actuators, A Phys.*, vol. 250, pp. 71–77, 2016.
- [65] S. Gomès, A. Assy, and P. O. Chapuis, "Scanning thermal microscopy: A review," *Phys. Status Solidi Appl. Mater. Sci.*, vol. 212, no. 3, pp. 477–494, 2015.

- [66] Y. Ge, Y. Zhang, J. A. Booth, J. M. R. Weaver, and P. S. Dobson, "Quantification of probe-sample interactions of a scanning thermal microscope using a nanofabricated calibration sample having programmable size," *Nanotechnology*, vol. 27, no. 32, p. 325503, 2016.
- [67] K. Kim, W. Jeong, W. Lee, and P. Reddy, "Ultra-High Vacuum Scanning Thermal Microscopy for Nanometer Resolution Quantitative Thermometry," no. Step 3.
- [68] P. D. Tovee and O. V Kolosov, "Mapping nanoscale thermal transfer in-liquid environment-immersion scanning thermal microscopy.," *Nanotechnology*, vol. 24, no. 46, p. 465706, 2013.
- [69] S. Gomes, N. Trannoy, P. Grossel, and F. Depasse, "D . C . scanning thermal microscopy : Characterisation and interpretation of the measurement," *Int. J. Therm. Sci.*, vol. 729, pp. 949–958, 2001.
- [70] S. Lefèvre, S. Volz, J.-B. Saulnier, C. Fuentes, and N. Trannoy, "Thermal conductivity calibration for hot wire based dc scanning thermal microscopy," *Rev. Sci. Instrum.*, vol. 74, no. 4, p. 2418, 2003.
- [71] S. Lefèvre, S. Volz, and P.-O. Chapuis, "Nanoscale heat transfer at contact between a hot tip and a substrate," *Int. J. Heat Mass Transf.*, vol. 49, no. 1–2, pp. 251–258, Jan. 2006.
- [72] S. Gomès, N. Trannoy, F. Depasse, and P. Grossel, "A . C . scanning thermal microscopy : Tip – sample interaction and buried defects modellings 1," vol. 729, no. 57, pp. 526–531, 2000.
- [73] S. Gomès, N. Trannoy, and P. Grossel, "DC thermal microscopy: study of the thermal exchange between a probe and a sample," *Meas. Sci. Technol.*, vol. 10, no. 9, pp. 805–811, Sep. 1999.
- [74] a. Majumdar, "Scanning Thermal Microscopy," *Annu. Rev. Mater. Sci.*, vol. 29, no. 1, pp. 505–585, Aug. 1999.
- [75] L. Shi and A. Majumdar, "Thermal Transport Mechanisms at Nanoscale Point Contacts," *J. Heat Transfer*, vol. 124, no. 2, p. 329, 2002.
- [76] A. Assy, S. Lefèvre, P.-O. Chapuis, and S. Gomès, "Analysis of heat transfer in the water meniscus at the tip-sample contact in scanning thermal microscopy," *J. Phys. D. Appl. Phys.*, vol. 47, no. 44, p. 442001, 2014.
- [77] K. Luo, Z. Shi, J. Varesi, and A. Majumdar, "Sensor nanofabrication,

- performance, and conduction mechanisms in scanning thermal microscopy," *J. Vac. Sci. Technol. B Microelectron. Nanom. Struct.*, vol. 15, no. 2, p. 349, 1997.
- [78] P. Klapetek, I. Ohlidal, and J. Bursik, "Applications of scanning thermal microscopy in the analysis of the geometry of patterned structures," *Surf. Interface Anal.*, vol. 38, no. c, pp. 383–387, 2006.
- [79] Y. Ge, Y. Zhang, J. M. R. Weaver, H. Zhou, and P. S. Dobson, "Topography-free sample for thermal spatial response measurement of scanning thermal microscopy," *J. Vac. Sci. Technol. B, Nanotechnol. Microelectron. Mater. Process. Meas. Phenom.*, vol. 33, no. 6, p. 06FA03, 2015.
- [80] R. S. Prasher and P. E. Phelan, "Microscopic and macroscopic thermal contact resistances of pressed mechanical contacts," *J. Appl. Phys.*, vol. 100, no. 6, 2006.
- [81] R. Prasher, T. Tong, and A. Majumdar, "Diffraction-limited phonon thermal conductance of nanoconstrictions," *Appl. Phys. Lett.*, vol. 91, no. 14, pp. 1–4, 2007.
- [82] P.-O. Chapuis, "Chapter 3 Introduction to Heat Transfer at the Nanoscale," in *Thermometry at the Nanoscale: Techniques and Selected Applications*, The Royal Society of Chemistry, 2016, pp. 39–81.
- [83] A. Bontempi, T. P. Nguyen, E. Lemaire, L. Thiery, D. Teyssieux, S. Euphrasie, D. Briand, and P. Vairac, "Micromachined temperature calibration tool for contact Scanning Thermal Microscope probes," *THERMINIC 2015 - 21st Int. Work. Therm. Investig. ICs Syst.*, vol. 2015, no. October, pp. 1–5, 2016.
- [84] A. Bontempi, "Microscopie thermique par sonde thermoélectrique," Université de Franche-Comté, 2015.
- [85] D. G. Cahill, "Thermal conductivity measurement from 30 to 750 K: The  $3\omega$  method," *Rev. Sci. Instrum.*, vol. 61, no. 2, pp. 802–808, 1990.
- [86] F. Depasse, S. Gomès, N. Trannoy, and P. Grossel, "AC thermal microscopy: a probe - sample thermal coupling model," *J. Phys. D. Appl. Phys.*, vol. 30, no. 24, pp. 3279–3285, Dec. 1997.
- [87] S. Lefèvre, J.-B. Saulnier, C. Fuentes, and S. Volz, "Probe calibration of the scanning thermal microscope in the AC mode," *Superlattices Microstruct.*, vol. 35, no. 3–6, pp. 283–288, Mar. 2004.
- [88] S. Lefèvre and S. Volz, " $3\Omega$ -Scanning Thermal Microscope," *Rev. Sci. Instrum.*,

vol. 76, no. 3, p. 33701, 2005.

- [89] L. Thiéry, Y. Bailly, F. Lanzetta, H. Gualous, and É. Gavignet, “Évolution des techniques de micromesures thermiques au travers de quelques applications,” *Rev. Générale Therm.*, vol. 37, no. 1, pp. 60–73, 1998.
- [90] R. a. Secco and R. F. Tucker, “Thermocouple butt-welding device,” *Rev. Sci. Instrum.*, vol. 63, no. 11, p. 5485, 1992.
- [91] K. Karrai and R. D. Grober, “Piezo-electric tuning fork tip-sample distance control for near field optical microscopes,” *Ultramicroscopy*, vol. 61, no. 1995, pp. 197–205, 1996.
- [92] K. Karrai and R. D. Grober, “Piezoelectric tip-sample distance control for near field optical microscopes,” *Appl. Phys. Lett.*, vol. 66, no. 14, p. 1842, 1995.
- [93] a Castellanos-Gomez, N. Agraït, and G. Rubio-Bollinger, “Dynamics of quartz tuning fork force sensors used in scanning probe microscopy.,” *Nanotechnology*, vol. 20, no. 21, p. 215502, May 2009.
- [94] A. G. T. Ruiter, J. A. Veerman, K. O. Van Der Werf, and N. F. Van Hulst, “Dynamic behavior of tuning fork shear-force feedback,” vol. 71, no. January, pp. 28–30, 1997.
- [95] S. Park, M. B. Goodman, and B. L. Pruitt, “Analysis of nematode mechanics by piezoresistive displacement clamp,” vol. 2007, 2007.
- [96] F. Beyeler, S. Muntwyler, and B. J. Nelson, “A Six-Axis MEMS Force-Torque Sensor With Micro-Newton and Nano-Newtonmeter Resolution,” *J. Microelectromechanical Syst.*, vol. 18, no. 2, pp. 433–441, 2009.
- [97] Y. H. Jeong, D. J. Bae, T. W. Kwon, and I. K. Moon, “Dynamic specific heat near the Curie point of Gd,” *J. Appl. Phys.*, vol. 70, no. 10, p. 6166, 1991.
- [98] G. Cross, A. Schirmeisen, A. Stalder, and P. Grütter, “Adhesion Interaction between Atomically Defined Tip and Sample,” pp. 4685–4688, 1998.
- [99] F. J. Giessibl, “Atomic resolution on Si(111)-(7×7) by noncontact atomic force microscopy with a force sensor based on a quartz tuning fork,” *Appl. Phys. Lett.*, vol. 76, no. 11, p. 1470, 2000.
- [100] Y. U. SUN and B. J. NELSON, “MEMS for cellular force measurements and molecular detection,” *Int. J. Inf. Acquis.*, vol. 1, no. 1, pp. 23–32, 2004.
- [101] J. C. Acosta, G. Hwang, J. Polesel-Maris, and S. Régnier, “A tuning fork based

- wide range mechanical characterization tool with nanorobotic manipulators inside a scanning electron microscope.," *Rev. Sci. Instrum.*, vol. 82, no. 3, p. 35116, Mar. 2011.
- [102] P. G. Gucciardi, G. Bachelier, A. Mlayah, and M. Allegrini, "Interferometric measurement of the tip oscillation amplitude in apertureless near-field optical microscopy," *Rev. Sci. Instrum.*, vol. 76, no. 3, p. 36105, 2005.
- [103] U. Rabe, "Atomic Force Acoustic Microscopy," in *Applied Scanning Probe Methods II: Scanning Probe Microscopy Techniques*, B. Bhushan and H. Fuchs, Eds. Berlin, Heidelberg: Springer Berlin Heidelberg, 2006, pp. 37–90.
- [104] A. Bontempi, D. Teyssieux, J.-M. Friedt, L. Thiery, D. Hermelin, and P. Vairac, "Photo-thermal quartz tuning fork excitation for dynamic mode atomic force microscope," *Appl. Phys. Lett.*, vol. 105, no. 15, p. 154104, Oct. 2014.
- [105] R. D. Grober, J. Acimovic, J. Schuck, D. Hessman, P. J. Kindlemann, J. Hespanha, a. S. Morse, K. Karrai, I. Tiemann, and S. Manus, "Fundamental limits to force detection using quartz tuning forks," *Rev. Sci. Instrum.*, vol. 71, no. 7, p. 2776, 2000.
- [106] M. González, P. Zheng, E. Garcell, Y. Lee, and H. B. Chan, "Comb-drive micro-electro-mechanical systems oscillators for low temperature experiments.," *Rev. Sci. Instrum.*, vol. 84, no. 2, p. 25003, Feb. 2013.
- [107] T. Akiyama, N. F. de Rooij, U. Staufer, M. Detterbeck, D. Braendlin, S. Waldmeier, and M. Scheidiger, "Implementation and characterization of a quartz tuning fork based probe consisted of discrete resonators for dynamic mode atomic force microscopy.," *Rev. Sci. Instrum.*, vol. 81, no. 6, p. 63706, Jun. 2010.
- [108] F. J. Giessibl, "High-speed force sensor for force microscopy and profilometry utilizing a quartz tuning fork," *Appl. Phys. Lett.*, vol. 73, no. 26, p. 3956, 1998.
- [109] J. Berger, M. Svec, M. Müller, M. Ledinský, A. Fejfar, P. Jelínek, and Z. Majzik, "Characterization of the mechanical properties of qPlus sensors.," *Beilstein J. Nanotechnol.*, vol. 4, pp. 1–9, Jan. 2013.
- [110] S. Jesse, S. V Kalinin, B. J. Rodriguez, C. Callahan, and S. V Kalinin, "Dual-frequency resonance-tracking atomic force microscopy," 2007.
- [111] J. E. Sader and S. P. Jarvis, "Accurate formulas for interaction force and energy in

frequency modulation force spectroscopy," *Appl. Phys. Lett.*, vol. 84, no. 10, p. 1801, 2004.

- [112] F. J. Giessibl, "A direct method to calculate tip-sample forces from frequency shifts in frequency-modulation atomic force microscopy," *Appl. Phys. Lett.*, vol. 78, no. 1, p. 123, 2001.
- [113] U. Rabe, S. Amelio, E. Kester, V. Scherer, S. Hirsekorn, and W. Arnold, "Quantitative determination of contact stiffness using atomic force acoustic microscopy," vol. 38, pp. 430–437, 2000.
- [114] G. Stan, S. W. King, and R. F. Cook, "Nanoscale mapping of contact stiffness and damping by contact resonance atomic force microscopy," *Nanotechnology*, vol. 23, no. 21, p. 215703, Jun. 2012.
- [115] K. L. Johnson, *Contact Mechanics*. Cambridge University Press, 1985.
- [116] F. J. Giessibl, "A direct method to calculate tip-sample forces from frequency shifts in frequency-modulation atomic force microscopy," *Appl. Phys. Lett.*, vol. 78, no. 1, p. 123, 2001.
- [117] a Castellanos-Gomez, N. Agraït, and G. Rubio-Bollinger, "Dynamics of quartz tuning fork force sensors used in scanning probe microscopy," *Nanotechnology*, vol. 20, no. 21, p. 215502, May 2009.
- [118] R. Lévy and M. Maaloum, "Measuring the spring constant of atomic force microscope cantilevers: thermal fluctuations and other methods," *Nanotechnology*, vol. 13, no. 1, p. 33, 2002.
- [119] J. P. Cleveland, B. Anczykowski, A. E. Schmid, and V. B. Elings, "Energy dissipation in tapping-mode atomic force microscopy," *Appl. Phys. Lett.*, vol. 72, no. 20, p. 2613, 1998.
- [120] J. C. Acosta, "Atomic Force Microscopy Based Micro/Nanomanipulation," University Pierre et Marie Curie, 2011.
- [121] C. Rossi, D. Briand, M. Dumonteuil, T. Camps, P. Q. Pham, and N. F. De Rooij, "Matrix of  $10 \times 10$  addressed solid propellant microthrusters: Review of the technologies," *Sensors Actuators, A Phys.*, vol. 126, no. 1, pp. 241–252, 2006.
- [122] I. Simon, N. Bârsan, M. Bauer, and U. Weimar, "Micromachined metal oxide gas sensors: Opportunities to improve sensor performance," *Sensors Actuators, B Chem.*, vol. 73, no. 1, pp. 1–26, 2001.

- [123] S. R. Pettersen, S. Nagao, H. Kristiansen, S. Helland, J. Njagi, K. Suganuma, Z. Zhang, and J. He, "Investigation of thermal transport in polymer composites with percolating networks of silver thin films by the flash diffusivity method," *J. Appl. Phys.*, vol. 121, no. 2, 2017.
- [124] L. Thiery, "chapitre R2765 : Micro-sondes thermoélectriques," in *Techniques de l'Ingénieur, Traité de Mesures Physiques*, 2006.
- [125] L. Ramiandrisoa, A. Allard, B. Hay, and S. Gomés, "Uncertainty assessment for measurements performed in the determination of thermal conductivity by scanning thermal microscopy," *Meas. Sci. Technol.*, vol. 28, no. 11, p. 115010, 2017.
- [126] S. Lefèvre, "Modélisation et élaboration des métrologies de microscopie thermique à sonde locale résistive," Université de Poitiers, 2002.
- [127] B. Gotsmann and M. a. Lantz, "Quantized thermal transport across contacts of rough surfaces," *Nat. Mater.*, vol. 12, no. 1, pp. 59–65, 2012.
- [128] P.-O. Chapuis, J.-J. Greffet, K. Joulain, and S. Volz, "Heat transfer between a nano-tip and a surface," *Nanotechnology*, vol. 17, pp. 2978–2981, 2006.
- [129] N. D. Masters, W. Ye, and W. P. King, "The impact of subcontinuum gas conduction on topography measurement sensitivity using heated atomic force microscope cantilevers," pp. 1–9, 2005.
- [130] H. . Carslaw and J. . Jaeger, *Conduction of heat in solids*. Oxford, 1959.
- [131] D. D. Pollock, *Handbook of Thermoelectrics*. 1995.

## 8 APPENDICES

Appendix 1 Thermocouple principles	175
Appendix 2 Fabrication of calibration devices	179
Appendix 3 Fisher's Test	181
Appendix 4 Uncertainty propagation	183
Appendix 5 Coupling model and python simulation code	185

## APPENDIX 1 THERMOCOUPLE PRINCIPLES

### Seebeck effect

The temperature is converted directly to electrical potential by Seebeck effect which is discovered by Thomas Johann Seebeck. In 1820, Seebeck discovered an electromotive force when close loop of two different metals joined by two junctions with a difference in temperature[131].

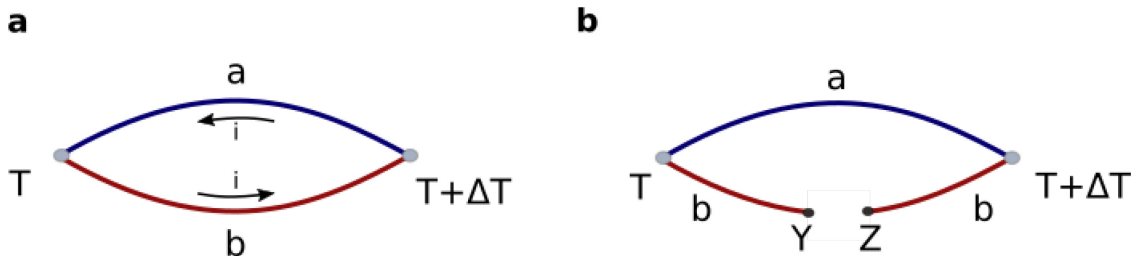


**Figure 8-1: Seebeck effect**

This electromotive force is generated by a local current density from a local electrical field. In an open circuit

$$S_{ab} = \frac{dV}{dT} = \frac{V_Z - V_Y}{\Delta T} \quad (8-1)$$

Where S is Seebeck coefficient

$$S_{ab} = S_b - S_a \quad (8-2)$$

The Seebeck coefficient of a couple comprise the absolute Seebeck coefficient of the material a and b. The table below present a list of absolute Seebeck coefficient for different materials

Material	S	Material	S	Material	S	Material	S
Bismuth	-76.5	Platinum	-4.5	Rhodium	1	Titanium	7.5
Constantan	-37.3	Carbon	-1.5	Silver	1.4	Fer	12.7
Nickel	-19.5	Aluminium	-1	Copper	1.7	Chrome	18.5
Alumel	-17.3	Tungsten	0.1	Gold	1.8	Chromel	21.7
Palladium	-9	Iridium	1	Molybdenum	4.7	Antimonies	42.5

**Table 8-1: Absolute Seebeck coefficient of materials at 0°C**

The widest application of Seebeck effect is thermometry based on thermocouple. The results of the equations above allow us to convert electrical voltage to temperature.

Peltier effect

Peltier effect was discovered by Jean Charles Peltier in 1834. When a current cross the interface of two different materials, Peltier has noticed a heat exchange at the junction. A heat amount is absorbed or liberated depends on the sign of the current and the materials used.

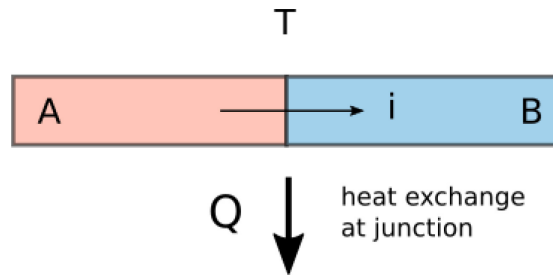


**Figure 8-2: Peltier effect**

$$Q = (\Pi_b - \Pi_a)I \quad (8-3)$$

With  $Q$  is the heat exchanged at the interface,  $\Pi$  is Peltier coefficient and  $I$  represent the current through interface. The Peltier coefficient is only depended on the materials and the temperature.

Thompson effect

In 1851, William Thomson noticed that there is a change of heat content within a single homogenous under a temperature gradient when a current pass through it. On contrary to Peltier effect in which the heat exchange occurs only at the junction, the heat absorption or emission occurs along the conductor in Thompson effect.

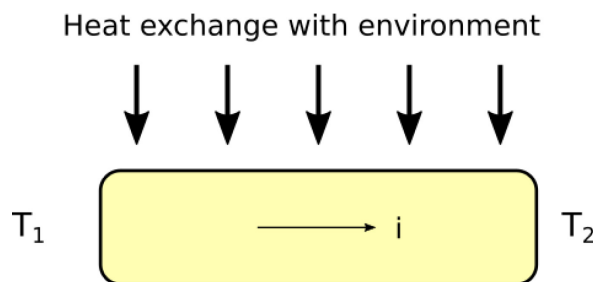


**Figure 8-3: Thomson effect**

$$dQ_T = \int_{T_1}^{T_2} \tau_A dTidt \tag{8-4}$$

Thomson also found the relation between Seebeck effect, Peltier effect and Thomson effect through the equation below. In fact, they are different manifestations of the same physical phenomenon:

$$\Pi_{ab} = S_{ab}T \tag{8-5}$$

$$\tau_a = T \frac{TdS_a}{dT} \tag{8-6}$$

Thermometry using thermocouple

As indicated earlier, the thermocouple use Seebeck voltage to measure the temperature. A temperature gradient between two junctions (hot and cold) generates an electrical field within the conductor material. The temperature different between two junctions is quantified due to the Seebeck coefficient (Equation 2-10).

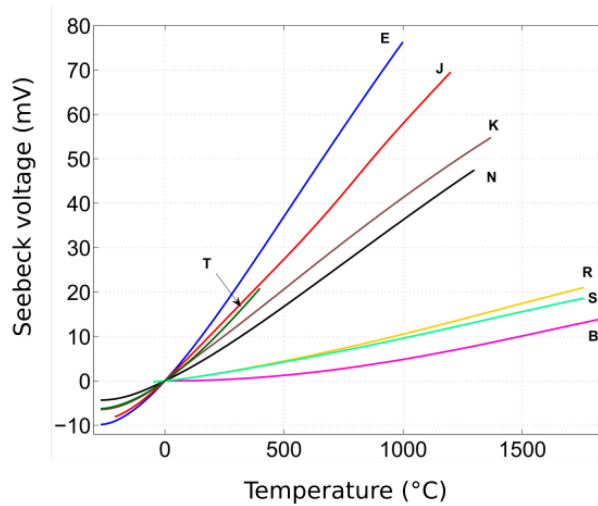


**Figure 8-4: Seebeck voltage of different type thermocouple in function of temperature (source: NIST)**

The Seebeck coefficient of different types thermocouple at 0°C is presented in the table below.

Name	Composition	Temperature range (°C)	Seebeck coefficient (μV/K)
B	Platinum-30% Rhodium/ Platinum-6%Rhodium	0 - 1820	0
E	Chromel/Constantan	-270 - 1000	60.5

J	Iron/Constantan	-210 - 1200	51.5
K	Chromel/ Alumel	-270 - 1372	40.3
N	Nicrosil/Nisil	-270 – 1300	26.6
R	Platinum/Platinum-13%Rhodium	-50 - 1768	6
S	Platinum/Platinum-10%Rhodium	-50 - 1768	6
T	Bronze/Constantan	-270 - 400	40.3

**Table 8-2: Characteristics of different types thermocouple**

Thomson, Peltier and Joule effect can also generate a small heat exchange in close loop when there is a small current within the conductor. This can make a measurement error. To avoid these effects, the Seebeck voltage is measured in open loop with a very high input impedance instrument.

A well-known temperature measurement setup using a thermocouple is depicted in the Figure 8-5. The cold junction is emerged in a melting ice tank as 0°C reference. The hot junction is put in contact with a hot object. The temperature measuring is directly the object temperature.

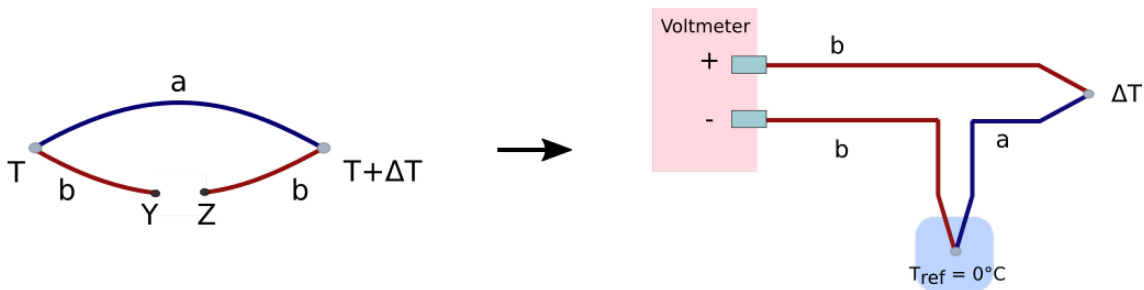


**Figure 8-5: Temperature calibration with 0°C**

## APPENDIX 2 FABRICATION OF CALIBRATION DEVICES

The complete fabrication process for the manufacturing of the RTD and OPT devices is developed at EPFL by E.Lemaire and D.Briand and depicted on Figure 8-6. The calibration chips are made by combining a silicon nitride membrane with a layer of evaporated platinum to achieve the functional thermal elements. For the RTD devices, an extra platinum deposition step is required for the RTDs when patterned using e-beam lithography. For the OPT devices, an etching step is a necessary step to remove the first silicon nitride in the area underneath of the standalone platinum membrane.

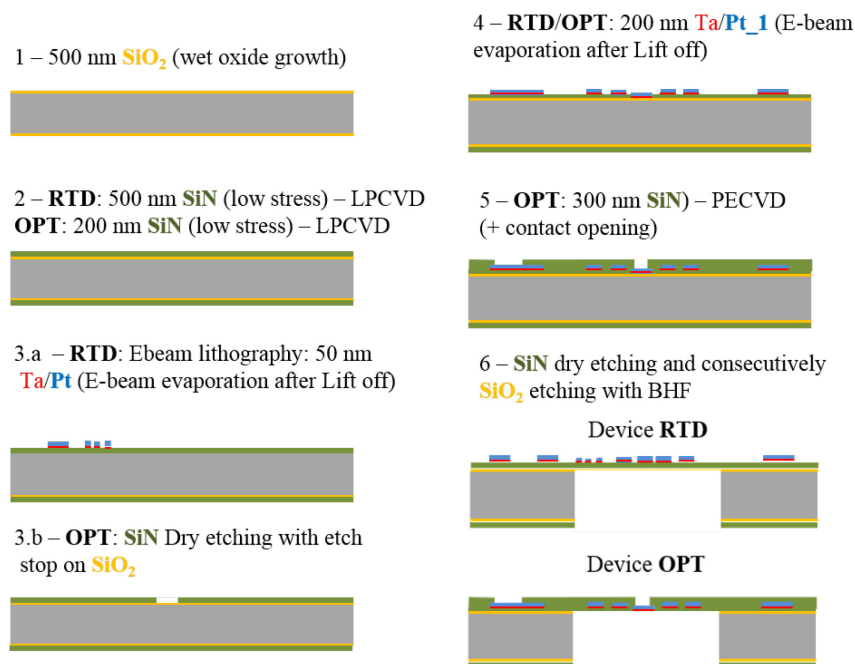


**Figure 8-6: Illustration of the fabrication process detailing the two variations of designs: RTD and OPT device**

The micro-hotplates calibration chips were micromachined on 390  $\mu\text{m}$ -thick double side polished silicon wafers. First, a 500 nm-thick silicon oxide was thermally grown on the wafers to be used as etch-stop during the silicon etching process (Figure 2 step 1). During the second step, 500 nm thick and a 200 nm thick low-stress Low Pressure Chemical Vapor Deposition (LPCVD) silicon nitride ( $\text{SiN}$ ) layer was deposited for the RTD and OPT devices, respectively (Figure 8-6 step 2). Then, for the RTD devices, high resolution RTDs with a linewidth of 1.2  $\mu\text{m}$  were structured using e-beam lithography to lift-off a thin platinum film (5 nm Ta/45 nm Pt) deposited by e-beam evaporation (Figure 8-6 step 3a). In the case of the OPT devices, the area of the standalone Pt-

membrane was defined by etching the SiN layer by reactive ion etching (RIE) in order to structure 10  $\mu\text{m}$ -wide circular holes (Figure 8-6 step 3b). This was followed by the deposition of a 15 nm Ta/150 nm Pt thin film by e-beam-evaporation, which was patterned via a lift-off process using UV photolithography in order to define the resistive heating elements, and, at the same time in the case of the RTD devices, resistive temperature sensors (Figure 8-6 step 4). OPT devices were coated with another SiN layer by Plasma Enhanced Chemical Vapor Deposition (PECVD). Another etching by RIE was performed to remove the SiN on top of the Pt-membrane itself and the contact pads of the heater (Figure 8-6 step 5). Finally, the SiN membranes were defined by deep reactive ion etching (DRIE) of silicon. The SiO<sub>2</sub> layer underneath the membrane, used as etch-stop, was then removed by wet etching (Figure 8-6 step 6). Optical images of the released membrane and RTD structured by e-beam lithography are presented on Figure 4-5.

## APPENDIX 3 FISHER'S TEST

Each DoE is analyzed independently. The goal is to determine a statistical model which explains the influence of a given set of factors on an output quantity called the response variable (denoted as  $y$ ). The resulting statistical model is only a statistical relationship and does not represent a particular physical relationship. For example, the considered statistical model with 3 factors  $x_1$ ,  $x_2$  and  $x_3$  is :

$$y = b_0 + b_1x_1 + b_2x_2 + b_3x_3 + b_{12}x_1x_2 + b_{13}x_1x_3 + b_{23}x_2x_3$$

In which the products terms represent the potential interactions between two factors and the coefficients  $b_0, b_1, b_2, b_3, b_{12}, b_{13}, b_{23}$  are the coefficients which can be estimated thanks to the results of the experiments in the DoE. In this exercise, we are more interested in the significance of the coefficients than in their estimated value as this latter is likely to be very high due to the small number of experiments. The goal is to detect the coefficients that are significantly different from 0. Indeed, in this case, it means that the associated effect (of first order or interaction effect) is significant and that the measurement of the response quantity differs according to the value of the effect.

In the final statistical model, only the significant effects are taken into account. A (multiple) Analysis Of Variance is performed in order to test whether the deviations due to each effect are significant with regards with the residual dispersion. In particular, a Fisher's test is performed for each effect to be tested. **Table 8.3** summarizes the ANOVA table for the DoE with several factors.

Analysis of Variance for a DoE					
Source	Sum of Squares	Degrees of freedom	Mean squares	F-statistic	p-value
					Prob > F
Model	$SS_M$	$n - \nu_R - 1$	$MS_M$	$\frac{MS_M}{MS_R}$	$P(F < F_{p-1; N-p}^\alpha)$
Factor A	$SS_A$	$q_A - 1$	$MS_A$	$\frac{MS_A}{MS_R}$	
Factor B	$SS_B$	$q_B - 1$	$MS_B$	$\frac{MS_B}{MS_R}$	
Factor C	$SS_C$	$q_C - 1$	$MS_C$	$\frac{MS_C}{MS_R}$	
Interaction AB	$SS_{AB}$	$(q_A - 1)(q_B - 1)$	$MS_{AB}$	$\frac{MS_{AB}}{MS_R}$	
Residuals	$SS_R$	$\nu_R = \nu_{LF} + \nu_{PE}$	$MS_R$		
Lack of fit	$SS_{LF}$	$\nu_{LF}$	$MS_{LF}$		
Pure error	$SS_{PE}$	$\nu_{PE}$	$MS_{PE}$		
Total	$SS_T$	$n - 1$			

**Table 8-3: Analysis of variance**

## APPENDIX 4 UNCERTAINTY PROPAGATION

- *Uncertainty propagation by analytical calculation*

Uncertainty of a quantity  $V$  can be defined as its standard error

$$\sigma_{\bar{V}} = \sigma_V / \sqrt{N} \quad (8-7)$$

where  $\sigma_V$  is the standard deviation of  $N$  measurements.

The propagation of uncertainties between independent random errors are defined as []

$$\sigma_{\bar{z}} = \sqrt{\sigma_{\bar{x}}^2 + \sigma_{\bar{y}}^2} \quad (8-8)$$

if  $z = x \pm y$  and

$$\delta_z = \sqrt{\delta_x^2 + \delta_y^2} \quad (8-9)$$

if  $z = x * y$  or  $x/y$ , where  $\delta_z = \sigma_{\bar{z}}/|\bar{z}|$ ,  $\delta_x = \sigma_{\bar{x}}/|\bar{x}|$ ,  $\delta_y = \sigma_{\bar{y}}/|\bar{y}|$  are the relative error of the quantities  $x, y, z$  respectively.

$$\sigma_{\bar{z}} = \left| \frac{dz}{dx} \right| \sigma_{\bar{x}} \quad (8-10)$$

if  $z$  is a function of  $x, z(x)$ .

Using the terms given in 8-7, 8, 9. The relative error of the microscope can be considered as the uncertainty of the quantity  $\frac{V_0 - V}{V}$  are given:

$$\delta = \left| \frac{V_0}{V_0 - V} \right| \sqrt{\frac{\sigma_{V_0}^2}{|V_0|} + \frac{\sigma_V^2}{|V|}} \quad (8-11)$$

The uncertainty of the coefficient  $\kappa$  in **Erreur ! Source du renvoi introuvable.**, is also determined

$$\delta_{\kappa} = \sqrt{(\delta_{mS})^2 + \left( \left| \frac{d(\tanh(mL))}{d(mL)} \right| \sigma_{mL} \right)^2} \quad (8-12)$$

$$\Rightarrow \delta_{\kappa} = \sqrt{(\delta_{mS})^2 + \left( \left| \frac{mL}{\tanh(mL)} [1 - \tanh^2(mL)] \right| \delta_{mL} \right)^2} \quad (8-13)$$

- *Monte Carlo error estimation code for the fitting model*

```

# calculated A,B,C distribution
nTrials = 5000 # number of random set measurement
airFitPars = array([]) # A,B,C matrix
nMeasure = size(k_2)
xTrial = empty([nMeasure])
yTrial = empty([nMeasure])
p0 = [0.4, 0.1, 1]

for iTrial in range(nTrials):
    for i in range(0,nMeasure): #loop for ith materials
        # random number for thermal conductivity
        xTrial[i] = 1/(k_2[i] + random.normal(scale=k_2[i]*0.05,size=1))
        # random number for simulated voltage
        yTrial[i] = mean(data_air_2w_2[i]) + random.normal(scale=std(data_air_2w_2[i]),size=1)
        # ratio DeltaV/V calculated
        yTrial[i] = yTrial[i]/(V_nc_air-yTrial[i])

        try:
            vTrial, aCova, infodict, errmsg, success = leastsq(residuals, p0, args=(yTrial,
xTrial),full_output=1)

        except:
            dumdum=1
            continue # This moves us to the next loop without stacking.

        if size(airFitPars) < 1:
            airFitPars=copy(vTrial)
        else:
            airFitPars = vstack(( airFitPars, vTrial ))

#function simulates thermal conductivity distribution from the ratio, and A, B, C calculated
def measTrial_3(ratio, A, B, C):
    return 1/(exp((ratio-C)/A)-B)

#function simulates thermal conductivity distribution from the V measured, V standard deviation and A, B,
C data
def measErrMonteCarlo_3(V,error,measNum, A, B, C,V0):
    measMontCarlo = array([])
    for i in range(0,measNum):
        V_measured = V + random.normal(scale=V*error,size=1)
        oneMontCarlo = measTrial_3(V_measured/(V0-V_measured),A, B, C)
    if size(measMontCarlo) < 1:
        measMontCarlo=copy(oneMontCarlo)
    else:
        measMontCarlo = vstack(( measMontCarlo, oneMontCarlo ))
    return measMontCarlo

#plot the thermal conductivity result
fig, ((ax1,ax2)) = plt.subplots(1,2)
meas_sample_k=
measErrMonteCarlo_3(111,0.008,250,airFitPars[:,0], irFitPars[:,1],airFitPars[:,2],V_nc_air).flatten()
ax1.hist(meas_sample_k,edgecolor='k',linewidth=0.4,bins=200,alpha=0.5)

```

## APPENDIX 5 COUPLING MODEL AND PYTHON SIMULATION CODE

$$\lambda S \frac{\partial^2 T(x,t)}{\partial x^2} - hp(T(x,t) - T_0) + \frac{\sigma_0(1+\alpha(T(x,t)-T_0))}{s} I(t)^2 = \rho c S \frac{\partial T(x,t)}{\partial t} \quad (8-14)$$

With an excitation  $I(t) = I_0 \exp(i\omega t)$ , the temperature in thermocouple can be given by  $T(x,t) = T_0 + T_{2\omega} \exp(2i\omega t) + T_{4\omega} \exp(4i\omega t) + \dots + T_{2n\omega} \exp(2ni\omega t)$

Similar to the model proposed by Gomes et al [] for Wollaston probe, from Eq 8-14, the equations for thermocouple probe becomes

$$\begin{aligned} \frac{\partial^2 \theta_0}{\partial x^2} - \frac{hp\theta_0}{\lambda S} + \frac{\sigma_0 I_0^2}{2\lambda S^2} (1 + \alpha\theta_0 + \frac{\alpha}{2}\theta_0) &= 0 \\ \frac{\partial^2 \theta_2}{\partial x^2} - \frac{hp\theta_2}{\lambda S} + \frac{\sigma_0 I_0^2}{2\lambda S^2} (1 + \alpha\theta_0 + \alpha\theta_2 + \frac{\alpha}{2}\theta_4) &= \frac{2i\omega}{a} \theta_2 \\ \frac{\partial^2 \theta_4}{\partial x^2} - \frac{hp\theta_4}{\lambda S} + \frac{\sigma_0 I_0^2}{2\lambda S^2} (\alpha\theta_4 + \frac{\alpha}{2}(\theta_2 + \theta_6)) &= \frac{2i\omega}{a} \theta_2 \\ &\dots \\ \frac{\partial^2 \theta_{2n}}{\partial x^2} - \frac{hp\theta_{2n}}{\lambda S} + \frac{\sigma_0 I_0^2}{2\lambda S^2} (\alpha\theta_{2n} + \frac{\alpha}{2}(\theta_{2(n-1)} + \theta_{2(n+1)})) &= \frac{2i\omega}{a} \theta_{2n} \end{aligned} \quad (8-15)$$

The Eq 8-15 presents a form of ordinary differential equation system (8-16) with the vector  $X = (\theta_0, \theta_2, \dots, \theta_{2n})$  can be solved numerically by Runge-Kutta methods or analytically by eliminate the high order harmonics to obtain the amplitude and phase of the harmonics.

$$\frac{d^2 X}{dx^2} + A.X = B \quad (8-16)$$

In the thesis, the solution of every harmonic is not presented but a space-time finite-volume simulation is made instead. This simulation is chosen due to the possibility to modify the physical phenomena. The simulation is made using Crank-Nicolson implementation. The probe temperature simulation implementation is presented in the following Python function.

```

from numpy import *
def solve_tc_numerique(k1, k2, rho1, rho2, c1, c2, L, R, f, sigma1, sigma2, h, Rj, I0, alpha, G, T_amb,
N,J):
    #constant values
    S = pi*R**2; p = 2*pi*R; w = 2*pi*f
    rhoc_moyen = (rho1*c1 + rho2*c2)/2
    sigma = (sigma1 + sigma2)/2

    #setup grids
    dx = L/(N-1)
    x_grid = array([j * dx for j in range(N)])

    # setup t grid
    time = 20 / f
    dt = float(time) / float(J - 1)
    t_grid = array([n * dt for n in range(J)])

    # initial condition
    T = zeros((N, J))
    T[:, 0] = T_amb * ones(N)
    T2w_amb = zeros(N)
    # setup matrix B and solve linear system
    b = zeros(N)

    for j in range(0, J - 1):
        I = I0*cos(w*j*dt)

        # setup matrix A
        Aii1 = 1 + k1*dt/(rho1*c1*(dx** 2)) + h*p*dt/(rho1*c1*S**2) -
sigma1*alpha*I**2*dt/(2*rho1*c1*S**2)
        Aii2 = 1 + k2*dt/(rho2*c2*(dx** 2)) + h*p*dt/(rho2*c2*S**2) -
sigma2*alpha*I**2*dt/(2*rho2*c2*S**2)
        Aii1_m1 = -k1 * dt / (2 * rho1 * c1 * (dx ** 2))
        Aii2_m1 = -k2 * dt / (2 * rho2 * c2 * (dx ** 2))
        Aii1_p1 = -k1 * dt / (2 * rho1 * c1 * (dx ** 2))
        Aii2_p1 = -k2 * dt / (2 * rho2 * c2 * (dx ** 2))
        AN2 = 1 + (k2 + k1)*dt/(2*(dx**2)*rhoc_moyen) + h*p*dt/(rhoc_moyen*S**2) +
G*dt/(2*rhoc_moyen*S*dx) - sigma*alpha*I**2*dt/(2*rhoc_moyen*S**2)#
        AN2_m1 = -k1 * dt / (2 * (dx ** 2) * rho1 * c1)
        AN2_p1 = -k2 * dt / (2 * (dx ** 2) * rho2 * c2)

        A = diagflat([0] + [Aii1_m1 for i in range(int((N - 1) / 2) - 2)] + [AN2_m1] + [Aii2_m1 for i
in range(int((N - 1) / 2)],1) + diagflat([1] + [Aii1 for i in range(int((N - 1) / 2) - 1)] + [AN2] + [Aii2 for i in
range(int((N - 1) / 2) - 1)] + [1]) + diagflat([Aii1_p1 for i in range(int((N - 1) / 2))] + [AN2_p1] + [Aii2_p1 for i
in range(int((N - 1) / 2) - 2)] + [0], -1)

        # setup vector b
        b[0] = T[0, j]
        for i in range(1, N - 1):
            # metal wire 1
            if i < (N - 1) / 2:
                b[i] = T[i, j] + k1 * dt * (T[i - 1, j] + T[i + 1, j] - 2 * T[i, j]) / (2 * (dx ** 2) *
rho1 * c1) + sigma1 * I ** 2 * dt / (rho1 * c1 * S ** 2) + dt * h * p * (2 * T_amb - T[i, j]) / (2 * rho1 * c1 * S) +
sigma1*alpha*(T[i, j]-2*T_amb)*I**2*dt/(2*rho1*c1*S**2)
            # metal wire 2
            elif i > (N - 1) / 2:
                b[i] = T[i, j] + k2 * dt * (T[i - 1, j] + T[i + 1, j] - 2 * T[i, j]) / (2 * (dx ** 2) *
rho2 * c2) + sigma2 * I ** 2 * dt / (rho2 * c2 * S ** 2) + dt * h * p * (2 * T_amb - T[i, j]) / (2 * rho2 * c2 * S) +
sigma2*alpha*(T[i, j]-2*T_amb)*I**2*dt/(2*rho2*c2*S**2)
            # thermocouple junction
            else:
                b[i] = T[i, j] + (k2 * dt * (T[i + 1, j] - T[i, j]) + k1 * dt * (T[i - 1, j] - T[i, j])) /
(2 * (dx ** 2) * rhoc_moyen) + sigma * I ** 2 * dt / (rhoc_moyen * S ** 2) + (Rj * I ** 2) * dt / (rhoc_moyen *
S * dx)+ dt * h * p * (2 * T_amb - T[i, j]) / (2 * rhoc_moyen * S) + G * (2 * T_amb - T[i, j]) * dt / (2 *
rhoc_moyen * S * dx) + sigma*alpha*(T[i, j]-2*T_amb)*I**2*dt/(2*rhoc_moyen*S**2)
                b[N - 1] = T[N - 1, j]
                T[:, j + 1] = linalg.solve(A, b) #solve T at the time jth

```

return

T





**Titre :** Progrès en thermométrie quantitative aux échelles micro et nanométriques par microscopie thermique à balayage (S<sub>Th</sub>M)

**Mots clés :** thermométrie, quantitative, échelles micro et nanométriques, S<sub>Th</sub>M, thermocouple

**Résumé :** Les caractérisations thermiques à l'échelle nanométrique restent un défi depuis l'émergence de dispositifs nano structurés. Ayant des avantages en termes de résolution latérale par rapport aux techniques de champ lointain, la microscopie thermique à balayage est devenue un outil essentiel pour la caractérisation locale des propriétés thermiques des matériaux. Dans le cadre du projet européen « Quantiheat », plusieurs laboratoires ont travaillé ensemble pour essayer de comprendre et d'obtenir des mesures quantitatives couvrant les échelles spatiales allant du micro au nanomètre.

Ce document contient six chapitres avec quatre parties principales, dans lesquelles des sondes S<sub>Th</sub>M à thermocouples microfilaires ont été utilisées pour améliorer nos connaissances en thermométrie quantitative à cette échelle. Ce type de sonde a été développé et amélioré pendant plusieurs années. Nous démontrons qu'il est adapté pour mesurer la température d'échantillons actifs ainsi que la conductivité thermique d'échantillons passifs.

Grâce à la thèse, la dernière version du microscope (matériel, logiciel) et la conception de la sonde sont présentés. Fixé sur un diapason en quartz, la force de contact pointe-échantillon peut être quantifiée. Placé dans une chambre à vide, ce système permet un contrôle complet des paramètres prédominants sur la mesure, tels que la pression de l'air et la force de contact. Les mesures en modes actif et passif ont pu être menées grâce aux échantillons fournis par les partenaires du projet « Quantiheat » afin de démontrer que des mesures quantitatives sont envisageables. En changeant les conditions ambiantes allant du vide primaire à la pression ambiante, les mécanismes de transfert de chaleur de l'échantillon-pointe ont été analysés en détail pour mettre en évidence le rôle prépondérant de l'air et des conductions de contact solide-solide.